



University  
of Glasgow

Zhang, Cui (2017) *Integrated waveguide optical isolator*. PhD thesis.

<http://theses.gla.ac.uk/7994/>

Copyright and moral rights for this work are retained by the author

A copy can be downloaded for personal non-commercial research or study, without prior permission or charge

This work cannot be reproduced or quoted extensively from without first obtaining permission in writing from the author

The content must not be changed in any way or sold commercially in any format or medium without the formal permission of the author

When referring to this work, full bibliographic details including the author, title, awarding institution and date of the thesis must be given

Glasgow Theses Service

<http://theses.gla.ac.uk/>

theses@gl.a.ac.uk

# Integrated Waveguide Optical Isolator



Cui Zhang

School of Engineering

University of Glasgow

*A thesis submitted in fulfilment of the requirements*

*for the degree of*

**Doctor of Philosophy**

March, 2017

©Cui Zhang, 2017

## Abstract

This project is aimed at the integration of a polarisation-insensitive optical waveguide isolator on a Silicon-on-Insulator platform. The final device must provide comparable performance for both Transverse Electric and Transverse Magnetic modes at a wavelength of 1550 nm. This is achieved through two core components, a 45° Nonreciprocal Polarisation Mode Converter, and a 45° Reciprocal Polarisation Mode Converter.

In order to realise the Nonreciprocal Polarisation Mode Converter, several materials were investigated, all consisting of Silicon-on-insulator substrates with various thicknesses of the core layer that were coated with films of Magneto-Optic garnet materials. A wide number of Magneto-Optic garnet materials were tested. Among them, the Cerium-Terbium Iron Garnet proved the most promising for two reasons: first, it has a considerable Faraday rotation coefficient; secondly, it can be grown in crystalline form without the need for a buffer/seed layer, necessary for growing most other garnets.

Simulations were carried out for all grown materials in order to identify the most promising design. The simulated designs, however, could not always be translated into fabricated devices, as sometimes growth challenges would hinder the quality of the material. Since the growths on the 340 nm and 500 nm Silicon-on-Insulator platforms provided the best material quality, devices on these material systems were fabricated and optically characterised.

Nonreciprocal isolation performance was observed in all fabricated devices, independently of the Magneto-Optic garnet used. On the 340 nm Silicon-on-Insulator platform, the best performance was obtained when Bismuth-Terbium Iron Garnet, either on its own or in combination with Terbium Iron Garnet, was used as Magneto-Optic periodic cladding, leading to more than  $3/4\pi$  Stokes vector angle. On the 500 nm Silicon-on-Insulator platform instead, Cerium-Yttrium Iron Garnet, either by Magnesium Oxide or on Yttrium Iron Garnet, provided a calculated isolation ratio of 11.6 dB. The length of the fabricated devices ranged between 3 mm and 6 mm.

A reproducible device fabrication process, optical characterisation method and dedicated data analysis process had to be developed for this project. Nonreciprocal Polarisation Mode Conversion was demonstrated for devices on both the 500 nm and 340 nm Silicon-on-Insulator platforms. Moreover, in order to

achieve integration of Magneto-Optic garnet materials on Silicon-on-Insulator substrates, Radio-Frequency sputtering was preferred to wafer bonding as it improves the controllability and lends itself better to scaling up production.

With regard to the Reciprocal Polarisation Mode Converter, an asymmetric structure consisting of an L-shaped waveguide was chosen. In such a structure, the rotation of the optical axis enables an injected linear polarisation mode to excite hybrid modes and reciprocal mode conversion. The research carried out in this project for the reciprocal polarisation mode converter helped identify major issues with fabrication and characterisation, and lead to the proposal of a new design for further research.

This work successfully realised the first integrated polarisation-independent Faraday rotator showing comparable performance for both Transverse Electric and Transverse Magnetic modes. Device operation was based on nonreciprocal polarisation mode conversion, and it was demonstrated on both 500 nm and 340 nm Silicon-on-Insulator platforms. The results shown in this work in terms of performance and footprint prove the technology is suitable for optical integration.

## Publications

Hutchings, D. C., Zhang, C., Holmes, B. M., Dulal, P., Block, A. D., and Stadler, B. J. H. (2016) Faraday Polarisation Mode Conversion in Semiconductor Waveguides Incorporating Periodic Garnet Claddings. In: *Integrated Optics: Devices, Materials, and Technologies XX*, San Francisco, CA, USA, 13 Feb 2016, ISBN 9781628419856 (doi:10.1117/12.2211628)

C. Zhang, B. M. Holmes, and D. C. Hutchings, “Faraday Polarisation Rotation in Semiconductor Waveguides Incorporating Periodic Garnet Claddings,” *Conf. Lasers Electro-Optics 2014*, vol. SM4G.3, pp. 4-5, San Francisco, CA, USA, 2014.

D. C. Hutchings, B. M. Holmes, C. Zhang, P. Dulal, A. D. Block, S.-Y. Sung, N. C. a. Seaton, and B. J. H. Stadler, “Quasi-Phase-Matched Faraday Rotation in Semiconductor Waveguides With a Magneto-optic Cladding for Monolithically Integrated Optical Isolators,” *IEEE Photonics J.*, vol. 5, no. 6, pp. 6602512-6602512, Dec. 2013.

A journal paper is under draft.

# Table of Contents

## Contents

Abstract.....	ii
List of Tables .....	viii
List of Figures .....	ix
Acknowledgement .....	xviii
Author’s Declaration .....	xx
Abbreviation .....	xxi
1 Chapter 1— Introduction.....	1
1.1 Integrated optics.....	1
1.2 Isolators.....	4
1.2.1 Bulk Isolators.....	4
1.2.2 What is an isolator .....	6
1.3 Obstacles of Integration of Magneto-Optical Garnets on SOI platforms .....	8
1.4 Literature Review about Current Research conducted on SOI substrate.....	11
1.5 Approach adopted in this project .....	16
1.5.1 NR-PMC (Non-Reciprocal Polarisation Mode Converter) .....	16
1.5.2 R-PMC (Reciprocal Polarisation Mode Converter).....	18
1.5.3 Integrated Waveguide Optical Isolator .....	18
2 Chapter 2 – Magneto-optic Effects.....	20
2.1 Magneto-optic Effects.....	20
2.1.1 Nonreciprocal Polarisation Mode Conversion (NR-PMC) - Longitudinal approach of Faraday Rotation Effect .....	25
2.1.2 Nonreciprocal Phase Shift (NPS) - Transverse approach of Faraday Rotation Effect	29
2.2 Magneto-optic Materials .....	32
2.3 Magneto-optical Garnets.....	34
2.3.1 Basics of Magneto-optic Garnets.....	35
2.3.2 Radio Frequency Sputtering Deposition .....	38
2.3.3 Characterisation of the garnet thin film .....	39
3 Chapter 3—Simulation and Design of Nonreciprocal Polarisation Mode Converter .....	50
3.1 Introduction .....	50
3.1.1 Stokes Parameters and Poincare Sphere .....	51
3.1.2 Simulation Methods.....	54
3.2 Faraday Rotation Effect Simulation .....	56

3.3	Effect of Seed/Buffer Layer of Different Thicknesses on the Faraday Rotation .....	63
4	Chapter 4 - Fabrication of Nonreciprocal Polarisation Mode Converter .....	71
4.1	Introduction .....	71
4.2	Whole Fabrication Process.....	72
4.2.1	Electron-Beam Resist: PMMA (Polymethyl Methacrylate) and HSQ (Hydrogen silsesquioxane) .....	73
4.2.2	Whole Fabrication Process.....	75
4.2.3	Lift-off.....	81
4.2.4	RTA (Rapid Thermal Annealing) .....	84
4.2.5	Garnet Material Characterisation .....	89
4.2.6	Effect of MgO Buffer Layer on the Crystallisation of the Magneto-optical Garnets	95
5	Chapter 5 — Optical Measurement for Nonreciprocal Polarisation Mode Converter .....	100
5.1	Introduction .....	101
5.1.1	Coupling Method .....	101
5.1.2	Propagation Loss Measurement – The Fabry-Perot Measurement Method.....	101
5.2	Measurements with Permanent Magnets .....	110
5.2.1	Setup of the Whole Measurement Rig .....	110
5.2.2	Measurement Process .....	112
5.2.3	Analysis of the Results – Poincare Sphere and Angle Between Two Stokes Vectors	120
5.2.4	Observed Promising Results on Both 500 nm SOI and 340 nm SOI Platforms with Different Garnets on Top .....	124
5.2.5	Summary of the Observed Promising Results.....	129
6	Chapter 6—Design, Fabrication, and Optical Measurement for Reciprocal Polarisation Mode Converter .....	134
6.1	Introduction .....	134
6.2	Simulation and Design on 500 nm SOI and 340 nm SOI .....	135
6.2.1	500 nm SOI.....	135
6.2.2	340 nm SOI.....	140
6.3	Fabrication .....	142
6.4	Optical Measurements.....	144
6.5	Discussion and Future Work .....	147
7	Chapter 7—Discussions, Conclusions, and Future Work.....	150
7.1	Nonreciprocal Polarisation Mode Converter (NR-PMC) .....	152
7.1.1	Conclusions .....	152
7.1.2	Future Work .....	154
7.2	Reciprocal Polarisation Mode Converter (R-PMC).....	155

- 7.2.1 Conclusions .....155
- 7.2.2 Future Work .....156
- 7.3 Integration of the NR-PMC Part and R-PMC Part .....157
- 7.4 Conclusions .....158
- Appendix A – Observed Promising Results on 340 nm SOI Platforms with Different Garnets on Top .....160
- Appendix B – Failed Fabrication on 220 nm SOI, 340 nm SOI, and 400 nm SOI .....168
- List of References .....170

## List of Tables

Table 1-1. Contribution of each party in this project. ....	11
Table 1-2. SOI-based Magneto-optical Isolator .....	13
Table 3-1. The effective refractive index of all the guided modes (fundamental modes, 1 <sup>st</sup> order modes, and 2 <sup>nd</sup> order modes) in 500 nm-wide waveguides on a 500 nm SOI platform for the Si <sub>x</sub> N <sub>y</sub> -Garnet-SOI model and the Si <sub>x</sub> N <sub>y</sub> -SOI model, respectively. ....	59
Table 3-2. The Faraday rotation coefficient, $\epsilon_{xy}$ , and thickness for optimal performance of different garnet layers. ....	65
Table 4-1. [23] The characteristics of different ratios of developers. ....	83
Table 4-2. The effect of a seed layer (MgO/YIG) on the crystallisation of various garnets. ....	98
Table 5-1. Different types of losses and the origin of them. ....	102
Table 5-2. Summary of the measurement results of all the NR-PMC devices fabricated on both 500 nm SOI and 340 nm SOI. In the table, $L_m$ - Measured Device Length, $\Theta_m$ - Measured Stokes vectors angle, $d_c$ - Calculated Isolation ratio based on $\Theta_m$ , $L_{optimal}$ - Device Length Needed to achieve $\pi$ between Stokes vectors. The best results are highlighted in red. ....	131
Table 6-1. The optimised parameters of the L-shaped waveguide of each specific width to achieve a 50% mode conversion on 500 nm SOI. ....	138
Table 6-2. The optimised parameters of the L-shaped waveguide of each specific width to achieve a 50% mode conversion on a 340 nm SOI. ....	141

## List of Figures

Figure 1-1. Work flow of bulk magneto-optical isolator. ....	5
Figure 1-2. Structure of Bulk Component Optical Isolator. ....	5
Figure 1-3. Schematic of how the reflected signal is isolated in the integrated system that this project aims to achieve. ....	6
Figure 1-4. Structure of Waveguide Isolator. ....	8
Figure 1-5. Layer structure of waveguide-type isolator with Si as the core layer and the magneto-optical garnet as the upper cladding layer. All the refractive index of the material is given at 1.55 $\mu\text{m}$ wavelength. ....	9
Figure 1-6. (a) The periodic loading structure of NR-PMC with alternating half beat-length long ( $L\Delta B$ ) MO segments and Non-MO segments; (b) The difference in rotation between QPM and Phase Mismatching. ....	10
Figure 1-7. Schematic of a typical isolator with MZI structure based on nonreciprocal phase shift. ....	15
Figure 1-8. The constructive and destructive interference in the forward and backward direction of the isolator system described in figure 1-7. ....	15
Figure 1-9. Top view and cross-section view of the Si <sub>3</sub> N <sub>4</sub> rings with sidewall coated with Ce-YIG[84]. ....	16
Figure 1-10. Changes in resultant polarisation from two modes propagating in anisotropic media, where $\psi$ is the phase difference between the TE and TM components. ....	17
Figure 1-11. Trench structure realised by Electrical Beam Lithography (EBL) and Reactive Ion Etching (RIE) lag effect [96]. Got permission from Dr. Barry Holmes to reprint. ....	18
Figure 1-12. The schematic of the integrated waveguide optical isolator device proposed in this thesis. ....	19
Figure 2-1. Illustration of possible magnetisation direction. Light propagation is along the z axis and (a) (b) (c) describe the external magnetic field along z axis, y axis and x axis respectively. ....	23
Figure 2-2. Summary of the relationship between different kinds of magneto-optical effects. The NR-PMC effect has been highlighted as it has been employed in this thesis. ....	25
Figure 2-3. Illustration of the ferromagnetic resonance splitting process in presence of a static internal magnetic field $H_i$ . ....	26

Figure 2-4. (a) Under magnetic field, because of the Zeeman Effect, the wave splits into two circularly polarised waves, right-hand polarised and left-hand polarised. (b) By the Kramers-KrÖnig relations the corresponding refractive indices are modified. ....	27
Figure 2-5. Schematic of a three-layer slab waveguide with MO garnet as cladding layer. The light wave propagates along the z axis, while the external magnetic field is applied along the y axis. ....	30
Figure 2-6. Two possible presentations of a unit cell, showing both the location of all the cations within the cubic structure (top right), and their bonds with O <sup>2-</sup> ions (bottom left). ....	36
Figure 2-7. Schematic illustrating the change of direction in the sub-lattice magnetisation below and above compensation temperature. ....	37
Figure 2-8. Schematic showing the structure of the deposition chamber and the deposition process.....	39
Figure 2-9. Describes that in the SEM chamber different forms of signals are emitted based on the differences in interaction depth between the electron beam and the specimen and the energy the excited signal carries. ....	42
Figure 2-10. Illustration of Bragg's condition, where the difference between the distances travelled by two beams that interfere constructively is an integer multiple of the wavelength, $2d\sin\theta = n\lambda$ .....	43
Figure 2-11. XRD spectra of: (a) Bi:YIG layers grown with or without seed layer; (b) Ce:YIG layers grown with or without seed layer[35]. ....	44
Figure 2-12. Schematic showing how the chance of electrons escaping from the surface increases by tilting the specimen. ....	44
Figure 2-13. Illustration of the EBSD Kikuchi pattern formation. ....	46
Figure 2-14. EBSP patterns of: (a) garnet, with the blue lines outlining the crystalline structure which agrees with that in the database; (b) Si, with the red lines outlining the crystalline structure which agrees with that in the database	47
Figure 2-15. VSM hysteresis curve of Ce-TIG. A 1.5k Oe-2k Oe magnetic field is needed to saturate all these garnets. ....	48
Figure 2-16. Faraday rotation coefficient measurement rig. ....	49
Figure 3-1. The rotation degree/azimuth ( $\psi$ ) and the ellipticity angle ( $\chi$ ) of a normal elliptically polarized lightwave in an x-y coordinate system. ....	51
Figure 3-2. The Poincaré sphere is a sphere used to visualise ( $S_1, S_2, S_3$ ). Points on the equator stand for all orientations of linearly polarized light; the north and	

south poles stand for right and left circular polarization, respectively. All other points on the sphere represent elliptically polarised states, with ellipticity increasing with the distance from the equator. ....	54
Figure 3-3. The Si core is cladded by garnet segments alternating with SixNy segments. ....	56
Figure 3-4. a) A cross-sectional profile of the Si Waveguide on SiO <sub>2</sub> with garnet segment claddings capped in SixNy; b) A cross-sectional profile of the Si Waveguide on SiO <sub>2</sub> with SixNy capped on top. ....	57
Figure 3-5. How the effective refractive index of the two single-lobed fundamental modes changes with width for the SixNy-Garnet-SOI model and the SixNy-SOI model, respectively, at a working wavelength of 1550 nm. ....	60
Figure 3-6. The relationship between $L_{\pi}$ and the width for both of the two models for the 500nm SOI platform at a working wavelength of 1550 nm. ....	61
Figure 3-7. The relationship between $L_{\pi}$ and the width for both the SixNy-Garnet-SOI and SixNy-SOI models on 400 nm SOI, 340 nm SOI, and 220 nm SOI platforms, respectively. ....	63
Figure 3-8. The Si core is cladded by garnet segments MO(+) alternating with MO(-) segments. ....	64
Figure 3-9. How different thickness of the garnet layer affect the Average $S_3$ parameters of the quasi-TE and quasi-TM mode. As the absolute value of the Faraday coefficient of TIG and Bi-TIG is the same, they are presented together; the same applies to Ce-TIG and Ce-YIG. It is clear that the garnet layer of the bigger Faraday rotation coefficient gets bigger absolute Average $S_3$ parameters, and it increases with the increase of the thickness of the garnet layer until it reaches an optimal thickness and goes steady. The optimal thickness for the YIG layer is 110 nm, for TIG/Bi-TIG it is 150 nm, and for Ce-TIG/Ce-YIG it is 200 nm. ....	66
Figure 3-10. The existence and different thickness of the MgO buffer layer on the performance of all the garnets. It is demonstrated that the MgO does severely decrease the Average $S_3$ parameters. Compared to the quasi-TE mode, the quasi-TM mode is more sensitive to the MgO layer. Only 10nm of the MgO layer will weaken the $S_3$ component by more than half of the original value. Also, the $S_3$ component completely vanishes when the MgO layer reaches 100 nm. ....	68
Figure 3-11. The presence and different thicknesses of the YIG layer underneath the Ce-YIG layer, and on top of the Ce-YIG layer on the performance of Ce-YIG. It	

is seen that it will not affect the magneto-optical effect of the Ce-YIG layer when the YIG layer acts as a cap layer put on top of it. .... 70

Figures 4-1 (a) and (b). The layer structure of a waveguide-type isolator with Si as the core layer and the magneto-optical garnet as the upper cladding layer indicates the structures of NR-PMC alternating between MO segments and Non-MO segments, and between MO(+) and MO(-), respectively, All of the refractive index of the material is given at a 1.55 $\mu$ m wavelength. (c) demonstrates the difference in rotation efficiency between QPM (MO+ Non-MO structure and MO(+)+MO(-) structure) and Phase Mismatching. .... 72

Figure 4-2. Two kinds of electron-beam resist are used in the fabrication process: PMMA (Polymethyl Methacrylate, positive-tone resist) and HSQ (Hydrogen silsesquioxane, negative tone resist). .... 73

Figure 4-3. The two kinds of bilayer structures. .... 74

Figure 4-4. The network structures and Cage structures before and after exposure [14]. .... 75

Figure 4-5. The whole device fabrication process: Sample clean – Spin PMMA on – E-beam exposure – Development – Etch markers down – PMMA removed – Spin bi-layer PMMA for lift off – E-beam exposure – Sent to US – Garnet deposition – Lift-off – RTA – SixNy coating – Spin HSQ on to – E-beam exposure – Si<sub>x</sub>N<sub>y</sub> etch – Si etch. .... 76

Figure 4-6. Sample cleave and clean process. .... 77

Figure 4-7. Contaminated surface and ‘grass’ after etch. .... 78

Figure 4-8 (a). The cross section of a waveguide on the Bi-TIG sample. From top to bottom, HSQ, SixNy, Bi-TIG, and Si are clearly shown in the micrograph. Figures 4-8 (b), (c), and (d) show the octant and the cross section of the structure with SixNy removed by HF. .... 81

Figure 4-9. Cross section undercut profile of two layers of PMMA for the garnet lift-off. .... 82

Figure 4-10. Left a) is the optical micrograph for the garnet islands after lift-off, and right b) is the 2.2  $\mu$ m-wide garnet islands under SEM when written with the dose of 976  $\mu$ C/ cm<sup>2</sup>. .... 82

Figure 4-11. Buttresses are found at the corners of the segments after lift-off. 84

Figure 4-12. Edges instead of buttresses are found around the islands. .... 84

Figures 4-13 (a), (b), and (c). 100x100 $\mu$ m square of Bi-TIG, Ce-TIG, and Ce-YIG on MgO material after annealing at 900 $^{\circ}$ C for 2 mins. Cracks exist in all of the three

patterns and the square of Ce-YIG on MgO even starts to peel off, which means that the stress is beyond the limit. ....	86
Figure 4-14. The simulated process (a) and the actual annealing process (b) for 900 °C, respectively. ....	88
Figure 4-15. The simulated process (a) and the actual annealing process (b) for 950 °C, respectively. ....	89
Figure 4-16. The X-ray emission spectrum on the bright spot where the crystalline phase of Ce-YIG was found, from which we can confirm the existence of O, Fe, Y, Ce, and also an Si signal from the substrate surface on which the Ce-YIG islands sit. The ratio of all the elements can help work out the stoichiometry of the Ce-YIG garnet. (Courtesy to Mr. Peter Chung in ISAAC from the School of Geographical and Earth Sciences, University of Glasgow, for the pics).....	90
Figure 4-17. The upper two pics show the position of the segment in an e-beam mask taken under SEM. The upper SEM micrograph is the Ce-TIG segments after lift-off. The lower SEM micrograph is the Ce-TIG segments after annealing three times at 900 deg at 120 mbar in an oxygen atmosphere for 2 mins. ....	92
Figure 4-18. The three micrographs taken in a 3-in-1 Multi-beam (gallium, neon, and helium ion beams) Ion Microscope indicate the crystallisation of Ce-TIG in thicker segments; the white spots are crystallised while the grey areas are not. It can also be seen that the garnet has grown in different directions, making it polycrystalline with the grain size ranging from 20-50 nm. (Courtesy to Mr. Peter Chung in ISAAC from the School of Geographical and Earth Sciences, University of Glasgow for the micrographs). ....	93
Figure 4-19. The upper two micrographs are the Bi-TIG segments after lift-off. The lower two micrographs are the Bi-TIG segments after annealing three times at 900 deg at 120 mbar in an oxygen atmosphere for 2 mins. The clear crystalline garnet phase can be easily seen from the micrographs after annealing. ....	93
Figure 4-20. EBSD results of annealed Bi-TIG: (a) shows the EBSD diffraction pattern for both the Si substrate and the Garnet segments pattern; (b) shows the EBSD mapping results in the grating pattern in (a); the coloured spots are crystallised. It is clearly seen that it is polycrystalline and partially crystallised. ....	94
Figure 4-21. The micrographs (a) and (b) show the periodic alternating garnet segments with bare Si or SixNy; micrograph (c) shows the cross-section profile of all the layers: Si core layer, garnet cladding layer, and SixNy layer. ....	95

Figure 4-22. 1a) and 1b): the Optical microscope and SEM micrograph for YIG were annealed at 800oC; 2a) and 2b): the Optical microscope and SEM micrograph for YIG on the MgO seed layer were annealed at 800oC; 3a) and 3b): the Optical microscope and SEM micrograph for YIG on the MgO seed layer were annealed at 825°C; and 4a) and 4b): the Optical microscope and SEM micrograph for YIG on the MgO seed layer were annealed at 900°C. ....	96
Figure 4-23. 1a) and 1b): the Optical microscope and SEM micrograph for Tb-YIG on MgO (120nm/5nm) annealed at 900oC; 2a) and 2b): the Optical microscope and SEM micrograph for Tb-YIG alone annealed at 800oC; and 3a) and 3b): the Optical microscope and SEM micrograph for Ce-YIG on MgO annealed at 900°C. ....	97
Figure 4-24. General map of well-aligned garnet islands segments on substrate. ....	99
Figure 5-1. The transmission spectra, associated FFTs, and FFT-filtered spectra of (a) the TE mode and (b) the TM mode of HSQ-cladded waveguides, respectively. ....	107
Figure 5-2. The transmission spectra and associated FFTs of (a) TE mode and (b) TM mode of YIG-cladded waveguides, respectively. ....	109
Figure 5-3. Measurements rig set-up using permanent magnets. ....	111
Figure 5-4. The right pic shows that TE-polarised radiation was coupled with the guides using an in-line polariser followed by an in-line TM-TE converter, and the output passed through a polarising beam-splitting cube in order to separate the TE- and TM-polarised components; the left pic shows that a collimated objective lens was used to inject TE-polarised light into the millimetre scale long waveguides. ....	112
Figure 5-5. A photodiode detector linked with lock-in amplifier modulated by a mechanical chopper (left) or a polarimeter (right) was used to receive the signal out of the waveguides. ....	112
Figure 5-6. The steps for the whole measurement process. ....	113
Figure 5-7. The optical characterisation results of Ce-YIG on the MgO sample. (a) displays that substantially bigger peaks occur after saturating the sample both negatively and positively, while there is a small peak before saturation, most likely due to the small mis-alignment between lithography mask writings. (b) shows that the azimuth of the light turns in the opposite direction when saturated in different directions at the same wavelength peak, as found in the upper graph. (c) shows traces of the $S_1$ , $S_2$ , and $S_3$ Stokes parameters of the two saturated directions. It	

is clearly seen that there is no difference in the Stokes parameters of two opposite directions of saturation..... 117

Figure 5-8. The optical characterisation results of the Ce-TIG sample. (a) displays that good peaks occur after saturating the sample both negatively and positively, while there is no peak at all before saturation. (b) shows that the azimuth of the light turns in the opposite direction when saturated in different directions at the same wavelength peak, as found in the left graph. The waveguide is with the beat length of Ce-TIG/HSQ=10.5/10.5  $\mu\text{m}$ . (c) shows traces of the  $S_1$ ,  $S_2$ , and  $S_3$  Stokes parameters of the two saturated directions. It is observed that at  $\lambda=1511$  nm there is an opposite change in the sign of the  $S_2$  and  $S_3$  Stokes parameters of the two opposite saturation directions, which indicates that both the orientation of the major axis *and* the sense of the ellipse of the transmitted polarisation state have reversed with the reversal of the longitudinal magnetic saturation direction. . 119

Figure 5-9. The optical characterisation result of the Bi-TIG device. The first plot shows the relative fraction of the TM-polarised output as a function of the input wavelength; a peak at  $\lambda=1530$  nm is observed. The second plot displays the position of the peak points on the Poincare sphere. It is clearly seen that they are situated on different sections of the sphere while saturated in different directions. The third graph shows the angle between the two Stokes vectors in opposite directions of saturation. The maximum angle is around  $55^\circ$ . ..... 121

Figure 5-10. The optical characterisation result of the Ce-TIG device. The first plot shows the relative fraction of the TM-polarised output as a function of the input wavelength; a peak at  $\lambda=1511$  nm is observed. The second plot displays the position of the peak point on the Poincare sphere. It is clearly seen that they are situated on different spheres while saturated in different directions. The third graph shows the angle between the two Stokes vectors in opposite directions of saturation. The angle is nearly  $180^\circ$ , which indicates that the number of quasi-phase matching periods on this device is near the ideal for an optical isolator implementation..... 122

Figure 5-11. Device with Ce-YIG on YIG cladding on a 500nm SOI platform: the relative fraction of the TM-polarised output as a function of input wavelength when the sample is not saturated, and saturated in a forward direction and back direction; a peak at  $\lambda=1612$  nm is observed. .... 125

Figure 5-12. Device with Ce-YIG on YIG cladding on a 500 nm SOI platform: it presents the Stokes vector angle of opposite magnetic saturation at resolutions of

0.01 nm, where an angle of nearly $3/4\pi$ is observed and there is fringe-like noise. ....	126
Figure 5-13. Device with Ce-YIG on YIG cladding on a 500nm SOI platform: (a) and (b) compare the experiment results of the QPM period length to the simulation results of QPM period length on 900 nm-wide devices and 800 nm-wide devices, respectively. ....	127
Figure 5-14. Device with Ce-YIG on MgO cladding on a 500 nm SOI platform: the relative fraction of the TM-polarised output as a function of input wavelength when the sample is not saturated, and saturated in a forward direction and back direction; a peak at $\lambda=1612$ nm is observed. ....	128
Figure 5-15. Device with Ce-YIG on MgO cladding on a 500 nm SOI platform: it presents the Stokes vector angle of opposite magnetic saturation at a 0.5 nm resolution, where an angle of about $1/2\pi$ is observed. ....	129
Figure 5-16. (a), (b), (c), and (d). The relationship between isolation vs wavelength for the four best results highlighted in red in Table 5-2. The isolation was calculated by the method and equation 5.11 described in 5.4.4. ....	132
Figure 5-17. (a) describes the relationship between the Isolation Ratio and Stokes Vector Angle according to equation 5.11, which clearly shows a periodic trend with the period of $2\pi$ . The maximum value, which tends to be infinite, is obtained at Stokes Vector Angle = $(2n+1)\pi$ , $n=0,1,2,\dots$ , where the two modes are orthogonal to each other. (b) presents the relationship between the isolation ratio and Stokes vector angle for half a period, and points out the best results described in Table 5-2. ....	133
Figure 6-1. The left pic of Figure 6-1 presents the cross-section profile of trenches of different widths after being deep etched for 20 mins, where it is clear that not much difference in etched depth is obtained. The 5 $\mu\text{m}$ -wide trench is etched down 54 $\mu\text{m}$ , while the 10 $\mu\text{m}$ -wide trench is etched down 60 $\mu\text{m}$ . The right pic of Figure 6-1 includes four sets of data reflecting the change of etch depth of different trench widths after being etched for 20 mins, 60 mins, 80 mins, and 100 mins, respectively. These results are reprinted with the kind permission of Dr. Haiping Zhou [158]. ....	135
Figure 6-2. (a) The Cross-Section Profile of a 500 nm-thick single-moded waveguide, while (b) is the Cross-Section Profile of the L-shaped design. ....	137
Figure 6-3. The relationship between the effective refractive index of the two fundamental modes and the width of the waveguide. ....	138

Figure 6-4. The structure of the L shape with Si adiabatic taper coupler. ....	139
Figure 6-5. The triangle and the quarter circle added to both ends of the L-part to avoid the sudden change and in-continuity. ....	139
Figure 6-6. The relationship between the effective refractive index of the two fundamental modes and the width of the waveguide.....	141
Figure 6-7. The structure of the L-shape under SEM. The left and the middle pics show the top-down view of the L-part with a triangle and quarter-circle taper, respectively, while the right pic presents the cross-section profile of the L-part. ....	143
Figure 6-8. Field stitch errors .....	144
Figure 6-9. Measurement rig set-up for the R-PMC part. ....	145
Figure 6-10. The measurement results of TM output vs wavelength of three devices on a 500 nm SOI.....	146
Figure 6-11. The measurement results of TM output vs wavelength of three devices on a 340 nm SOI.....	147
Figure 6-12. The existence of the anti-reflection coating layer creates a double interface, which, thus, leads to two reflected waves. ....	148
Figure 6-13. The structure of a potential working L-shaped R-PMC device; a wider second layer can be added to the coupler to avoid the total square waveguide. ....	149

## Acknowledgement

I am deeply grateful for my supervisors Professor David C. Hutchings, Dr. Barry M. Holmes and Professor Marc Sorel. First, thanks Dave for accepting me as a PhD student here to have the opportunity to work on this novel project and his knowledge, guidance and support on both the project and life has been invaluable in my PhD life. I still have fresh memories when we crossed the needle on Cobbler with him, which is a very risky and exciting moment. I just followed his lead and his word 'make sure you have every step' meant a lot to me in that situation. Meanwhile, huge thanks goes to Barry. Thanks very much for your nearly day-to-day supervisor, guidance and encouragement for the first three years of my PhD. Even though he left this field and moved to other place, he still offers help and guidance on both project and completing the thesis. He is a great researcher and also a very cheerful person. His encouragement has been the sunshine through the dark moments and frustrations of the progress of this project. I also appreciate Professor Marc Sorel's help and guidance as my second supervisor in the final stage of my PhD. He has widespread knowledge in both theory, fabrication and measurement and can always give some helpful suggestions.

I would also like to thank school of Engineering at University of Glasgow and China Scholarship Council for the financial support during my PhD.

I also like to express my gratitude to our collaborators at University of Minnesota - Professor Bethanie Stadler, Prabesh Dulal, Dr. Andrew Block, Dr. Sang-Yeob Sung for providing the best quality Magneto-Optical Garnet and XRD/EBSD characterisation of the garnet on top of our samples.

Special thanks to Vince for proof-reading some chapters of this thesis.

Special thanks to the technical assistance provided by the staff in James Watt Nanofabrication Center (JWNC), Stephen Thoms, Ronnie Roger, Mark Dragsnes, Ronnie Roger, Douglas Lang, Eve Aitkenhead, Susan Ferguson, Rachel Love, Haiping Zhou, Helen McLelland, Robert Harkins, Linda Pollock, Lesley Donaldson, Elizabeth Wyllie, Donald Nicholson, David Gourlay, Vanda Brash, Margaret McCann, Colin Roberts, Michael Duffy, Michael Turmey. Also substantial help has been provided by Bill ward for all the lab facilities and Thomas Reilly for thin-film evaporation and rapid thermal annealing, which is much appreciated.

I am also thankful for all the officemates and the nice colleagues in this department, Vince, Olesya, Ifeoma, Ope, Tania, Ili, Jharna, Ameze, Khaled, Alex, Andy, Alistair, Lianping, Ying, Xu, Jue, Chengzhi, Johnny, Kevin, Bhavana. There have been so many great happy moments with you guys, which are one of the highlights and precious parts during these PhD years.

Last but not the least, I owe huge debt to all my families, my parents, my brother and my sister-in-law. Thanks for all the emotional support over all these years and I feel sorry not being able to offer the support in action for you guys while I am this far away. Hopefully I can stay nearer to you guys so that family reunions can happen more often in the future.

## **Author's Declaration**

I declare that all the work presented in this thesis has been carried out by me unless otherwise acknowledged or referred to.

**Cui Zhang**

March 2017

## Abbreviation

Bi-YIG - Bismuth Yttrium Iron Garnet  
 Bi-TIG - Bismuth Terbium Iron Garnet  
 BPM - Beam Propagation Method  
 BSE - Backscattered Electrons  
 BSS - Beam Step Size  
 CMOS - Complementary metal-oxide-semiconductor  
 CM - Cotton-Mouton  
 CRT - Cathode Ray Tube  
 Ce-TIG - Cerium Terbium Iron Garnet  
 Ce-YIG - Cerium Yttrium Iron Garnet  
 DWDM - Dense Wavelength Division Multiplexing  
 EBL - Electron Beam Lithography  
 EBSD - Electron Backscattered Diffraction  
 EDFA - Erbium-Doped Fibre Amplifier  
 EDX - Energy Dispersive X-ray Diffraction  
 EM - Electromagnetic  
 EME - Eigen-mode Expansion  
 E-T Detector - Everhart and Thornley Detector  
 FDM - Finite Difference Methods  
 FDTD - Finite-Difference Time Domain  
 FEG - Field Emission Gun  
 FMR - Ferromagnetic Resonance  
 FP - Fabry-Perot  
 GGG- Gadolinium Gallium Garnet,  $Gd_3Ga_5O_{12}$   
 HSQ - Hydrogen Silsesquioxane  
 ICP-CVD Inductively Coupled Plasma -Chemical Vapour Deposition  
 ICP-RIE Inductively Coupled Plasma - Reactive Ion Etching  
 IPA - Isopropyl alcohol  $C_3H_8O$  or  $C_3H_7OH$  or  $CH_3CHOHCH_3$   
 IPC - Integrated Optical Circuits  
 JWNC - James Watt Nanofabrication Centre  
 LCP - Left Circularly Polarized  
 LHCP - Left-Hand Circular Polarization  
 LPE - Liquid Phase Epitaxy  
 MBE - Molecular Beam Epitaxy  
 MCB - Magnetic Circular Birefringence  
 MIBK - Methyl isobutyl ketone,  $(CH_3)_2CHCH_2C(O)CH_3$   
 MLB - Magnetic Linear Birefringence  
 MMI - Multi-Mode Interference  
 MO - Magneto-Optical  
 MOCVD - Metal Organic Chemical Vapor Deposition  
 MOE - Magneto-optic effect  
 MOKE - Magneto-Optic Kerr Effect  
 MZI - Mach-Zehnder interferometer  
 NPS - Nonreciprocal Phase Shift  
 NR-PMC - Non-Reciprocal Polarisation Mode Converter/ Conversion  
 OADM - Optical Add-Drop Multiplexer  
 OEIC - Opto-electronic Integrated Circuits  
 PEC - Proximity Effect Correction  
 PECVD Plasma Enhanced Chemical Vapour Deposition  
 PIC - Photonic Integrated Circuits

PLD - Pulsed laser deposition  
PM - Polarisation Maintaining  
PMMA - Polymethyl Methacrylate  
PSF - Point Spread Function  
QPM - Quasi-Phase Matching  
QWP - Quarter Wave-Plate  
RCP - Right Circularly Polarized  
REIG - Rare Earth Iron garnets  
RE-TM Rare Earth - Transition Metal  
RF - Radio Frequency  
RHCP - Right-Hand Circular Polarization  
RIE - Reactive Ion Etching  
R.O water - Deionized  
R-PMC - Reciprocal Polarization Mode Converter/Conversion  
RTA - Rapid Thermal Annealing  
RTP - Rapid Thermal Processor  
SE - Secondary Electrons  
SEM - Scanning Electron Microscope  
SOI - Silicon on Insulator  
SRS - Stimulated Raman Scattering  
TE - Transverse Electrical  
TEM - Transmission Electron Microscopy  
TM -Transverse Magnetic  
TIG - Terbium Iron Garnet  
TMAH Tetramethylammonium Hydroxide  
TTL Detector - Through-the-lens detector  
VRU - Variable Resolution Units  
VSLI - Very large scale Integration  
VSM - Vibrating Sample Magnetometer  
XRD - X-ray Diffraction  
YIG - Yttrium Iron Garnet

# 1 Chapter 1— Introduction

## 1.1 Integrated optics

The concept of integrated optics was proposed by S. E. Miller in 1969[1]. It is a technology aiming to construct integrated optical devices, integrated optical circuits (IOC) (also called photonic integrated circuits or PICs) or planar lightwave circuits composed of specific optical components to realise complex functions. Since then, the fields of Opto-electronic Integrated Circuits(OEIC) [2]-[4] and of PICs[2][5]-[8] have been steadily growing, as part of an inevitable trend towards miniaturisation and the attainment of an ‘information superhighway’ [2]. In order to reach that goal faster signal processing and transmission is required and dense wavelength division multiplexing (DWDM) PICs seem extremely promising for improving data processing and transmission, and for increasing bandwidth substantially with a great number of signals being de/multiplexed from a single channel.

In comparison with bulk optical systems, composed of relatively large discrete optical elements and conventional integrated electronics, integrated optical systems perform better in nearly all aspects: they are alignment-free, vibration-proof, more stable, light-weight, portable, low-cost and, most importantly, have lower power consumption. Furthermore, they are suitable for signal processing and transmission with higher bandwidth and lower loss. Nowadays, it is common to get single-mode fibres with attenuation less than 0.4 dB/km at 1.3  $\mu\text{m}$  and 0.2 dB/km at 1.55  $\mu\text{m}$  [2][9]. As silica fibres have their lowest attenuation at 1550 nm, the device designed in this work is intended to work at such wavelength.

The development of extremely effective micro- and nano-fabrication methods, most of them borrowed from the electronics industry, has encouraged and made possible the advancement of new integrated optic devices and substrate structures. For example, thin film growth techniques allowed the creation of

quantum-well devices [2][10][11], while plasma processing has been applied to realise two- and three-dimensional photonic crystal structures[12][13].

Any integrated optical system is composed of active and passive optical devices. Active devices include lasers, optical amplifiers, modulators, switches, and photodetectors, whereas passive ones range from simple waveguide interconnects to isolators/circulators, couplers, and splitters. The function achieved by the integrated optical system will depend on the particular combination of active and passive optical devices used. Depending on the type of device needing integration, different materials will be suitable. Some semiconductor materials, thanks to their direct bandgap, are capable of light generation, and they include gallium arsenide (GaAs), gallium aluminium arsenide (GaAlAs), gallium arsenide phosphide (GaAsP), indium phosphide (InP) and gallium indium arsenide (GaInP). Other III-V&II-VI semiconductors have an indirect bandgap, and are thus incapable of light generation, like silicon(Si), silicon on insulator (SOI), silicon nitride(Si<sub>3</sub>N<sub>4</sub>), silica/quartz(SiO<sub>2</sub>), polymers, and lithium niobate (LiNbO<sub>3</sub>)[2]. No specific material has been found so far that can accommodate the requirements of both active and passive optical devices, and that can be used to fabricate all components with optimal performance. A compromise needs therefore to be made when choosing a material as the substrate platform for the corresponding integrated system.

Currently, despite some research carried out on some exotic material platforms, mainly three materials are used commercially as substrates for PICs: they are InP, Si/SOI, and TriPleX™ (alternating layers of Si<sub>3</sub>N<sub>4</sub> and SiO<sub>2</sub>) [7][14]-[16]. As Si/SOI and TriPleX™ are passive substrate platforms, difficulties arise with regard to the integration of active devices, such as lasers and optical amplifiers. On the contrary, InP based PICs seem to be able to integrate both active and passive optical components, but due to their large footprint, high cost and poor CMOS (Complementary metal-oxide-semiconductor) compatibility they present undesired and unavoidable limits to commercialisation. Future VLSI (Very-large-scale Integration) for integration with the mature CMOS ICs is challenging, thus will not be able to take advantage of the mighty functions of the existing CMOS IC system. Comparing the two passive platforms (TriPleX™ and Si/SOI) that share the same obstacles regarding the integration of active devices, the high-index-contrast platform of SOI, which enables further miniaturisation, makes it preferable.

So far, in order to integrate laser sources and other active devices in Si/SOI substrates, two main approaches are adopted: the monolithic approach, in which the same substrate material is used for all devices; and the hybrid approach, exploiting other active substrate materials bonded on top of the Si/SOI substrate to take advantage of the existing developed technology [2][17].

In the monolithic case, Stimulated Raman Scattering (SRS) can be used to fabricate a silicon Raman laser in the presence of a light pumping source [17]-[19]; rare-earth doped (Er, erbium) Si is able to integrate both light emitting devices and optical amplifiers [17]; Epitaxial growth of III-V/II-VI materials on silicon surface, like GaAs, InP and Ge, is another option for monolithic integration [20][21].

In the hybrid case instead, direct bonding and adhesive bonding have both been employed to bond the active devices made of III-V/II-VI material on Si/SOI platforms [22]-[28]. However, the hybrid integration is sensitive to the alignment of bonding, vibration and even thermal expansion between the bonding interfaces [2] and also is not suitable for mass production. Eventually, the monolithic approach will be needed for automated mass production. Until then, great financial and technical efforts will be devoted to developing new ways to make active devices on Si/SOI platforms, thus creating new fabrication methods.

Except for the lack of active devices on Si/SOI platforms, there is one passive device not fully integrated and deployed in commercial systems yet: the optical isolator or circulator. More precisely, it is not integrated in any of the common substrate platforms. Currently, an integrated TE/TM mode isolator has not been realised and most integrated optical isolators that have been reported can only work with TM mode [29][30]. TM-mode operation cannot accommodate the isolation needs of integrated optical systems as the vast majority of semiconductor lasers emit TE rather than TM, due to quantum mechanical selection rules. (A detailed literature review on the current research will be presented later in this chapter).

To date only two TE polarised light optical isolators were realised by Ghosh etc. [31] and Shoji etc. [32]. Despite this approach being able to achieve TE isolation, it does not work on TM modes and has a rather large footprint. Also the controllability of the thickness of the adhesive bonding layer remains an issue of concern. Due to the lack of integrated optical isolators able to work with both modes, this project aims to make an integrated waveguide TE/TM optical isolator.

## 1.2 Isolators

### 1.2.1 Bulk Isolators

Optical Isolators are an indispensable and important component in many optical systems. By placing them between the light source and the rest of the system, they can prevent and block the reflected light signals which occur at interfaces, and also prevent undesired interference from coming back to the optical source, which would lead to instabilities. This ‘injection noise’ from the back-reflected signal may broaden the optical laser line width and increase the amplitude of noise[33][34], potentially leading to severe system degradation[35][36].

Traditionally bulk/discrete optical isolators are used[35][36], employing Faraday rotation to eliminate spurious reflections and keep the systems operating stably[37]. The bulk optical isolators generally consist of a polariser, a 45° Faraday rotator and an analyser, as depicted in Figure 1-1. The angle between the polarizer and the analyser is 45°. When the light comes out from the laser it is linearly polarized and set at an angle of 0°, so that it is able to pass through a polariser aligned with it. Upon passing through the Faraday rotator, the plane of the light’s electric vector (its polarisation) rotates 45°, making it parallel to the axis of the analyser so that the light can therefore pass through it. When any light is reflected back, it goes through the Faraday rotator and the electric vector rotates another 45°, thus becoming perpendicular to the optical axis of the polariser, which therefore blocks light propagation. The 45° rotator is made from garnet based media, employing Faraday rotation theory, while the polariser is usually a plastic-based thin film in contact with the sides of the garnet rotator. In addition, a ring-shaped permanent magnet is placed in a way where the direction of the magnetic field is parallel to that of linearly polarised light(see Figure 1-2)[38].

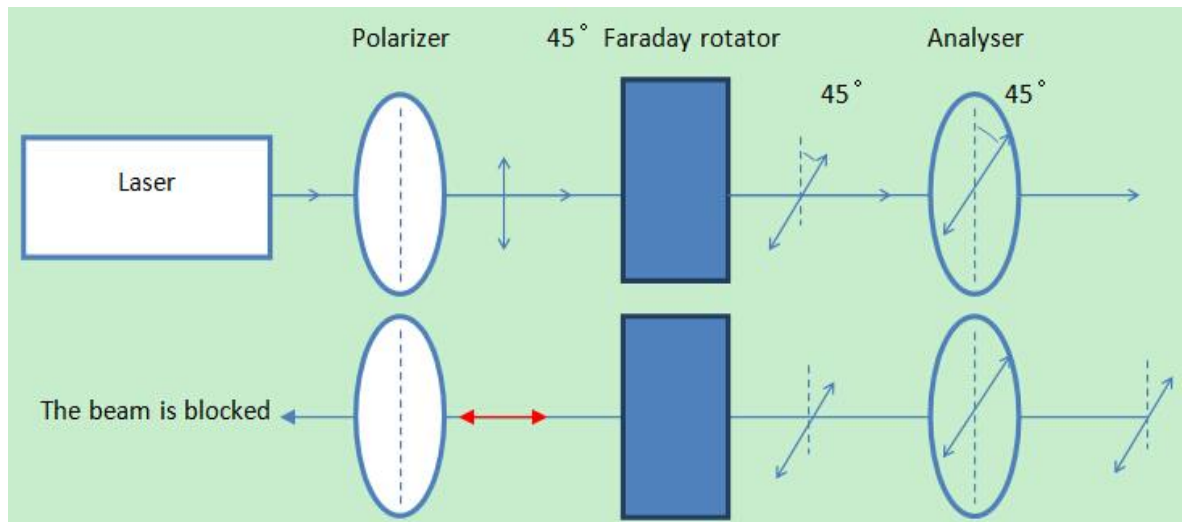


Figure 1-1. Work flow of bulk magneto-optical isolator.

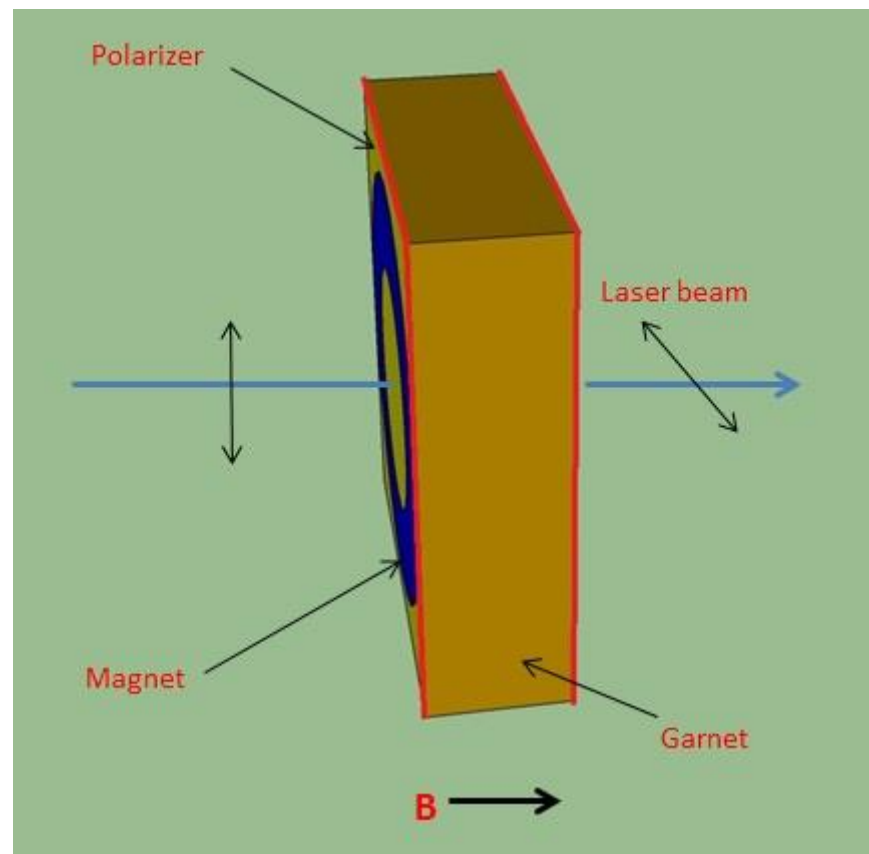


Figure 1-2. Structure of Bulk Component Optical Isolator.

Commercially available 1550 nm polarisation-independent bulk isolators on the market can achieve 30 - 40 dB isolation with about 1 dB insertion loss, and cost approximately £1000 - 1500[39]-[41]. However, the assembly and alignment of these bulk systems is a rather time- and labour-consuming task, which leads to the reduced throughput and increased production cost. Therefore, the integrated

optical isolator has become an irresistible trend for the sake of high level of integration system, small format and low cost.

Here in this project we intend to put the isolator in waveguide form so that it can be part of an integrated optical system. When light from a TE-polarised laser (as previously mentioned the vast majority of semiconductor lasers emit TE) propagates in the forward direction along the isolator, the polarisation angle will rotate by  $+45^\circ$  after traversing the Non-Reciprocal Polarisation Mode Converter (NR-PMC) and then rotate  $-45^\circ$  after passing through the Reciprocal Polarisation Mode Converter (R-PMC), so the two rotations cancel one another. When the light propagates backwards, it will first rotate  $+45^\circ$  after the R-PMC but then another  $+45^\circ$  after the NR-PMC, adding to a total polarisation change by  $+90^\circ$ . As such, it converts to a TM mode, which does no harm to the laser source that emits TE-polarised light, as it is essentially transparent at the TM mode's wavelength (which is longer than the TE's wavelength in the structure, as the two modes have different effective indexes, due to the birefringence discussed previously). The whole process for the device we intend to achieve in this project is described in Figure 1-3.

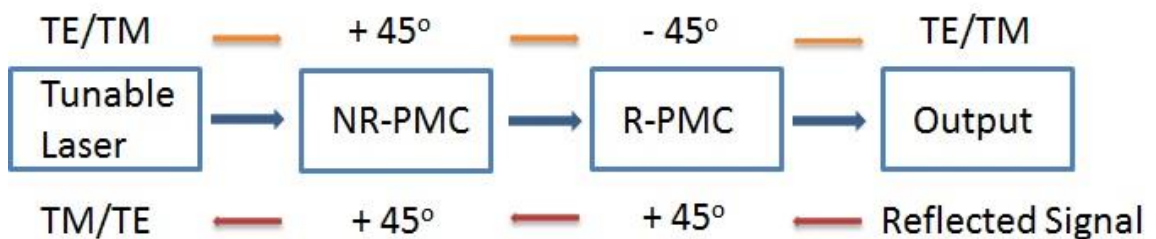


Figure 1-3. Schematic of how the reflected signal is isolated in the integrated system that this project aims to achieve.

## 1.2.2 What is an isolator

An optical isolator allows light to pass in one direction while blocking the light in the opposite direction. It is thus useful between the laser source and the rest of the optical system to prevent the reflected light from the rest of the optical system to cause disturbance to the laser source. The intrinsic characteristic of an isolator is the non-reciprocity.

Research has been carried out to develop isolators based on various structures and materials. Among them, some isolators have been developed which

although reciprocal, are claimed to be non-reciprocal [42][43]; in them asymmetric structures are used to achieve asymmetrical total power transmission, rather than true asymmetrical modal properties.

When an ‘isolator’ based on asymmetrical total power transmission is implemented in the system, the reflected signal is reduced but has the same polarisation as the laser source, meaning the source will still be affected and the ‘isolator’ cannot provide sufficient protection. Comparatively, when an ‘isolator’ based on asymmetrical modal properties is implemented in the system, even though the reflected signal is not reduced at all, it has a different polarisation from the laser source, thus it is transparent to the laser source and can offer sufficient protection.

In order to remove the confusion about the requirement for a ‘true’ optical isolator, Dirk etc.[44] defines that a ‘true’ isolator needs to break Lorentz reciprocity[45], where the relationship between an oscillating current and the resulting electric field will not change with the interchange of the place of the current and the detector. Breaking spatial structure symmetry and demonstrating asymmetrical power transmission is not sufficient to indicate the break of Lorentz reciprocity. The following equation describes the linear relationship between the incoming waves and outgoing waves of a linear, time-independent and passive system or device:

$$\vec{B} = S\vec{A} \quad (1-1)$$

Where  $\vec{A}$ ,  $\vec{B}$  are the incoming and outgoing waves, respectively, and  $S$  is the scattering matrix.

In order to break Lorentz reciprocity, the scattering matrix needs to be asymmetric. There are generally three cases that can break Lorentz reciprocity[44]. The first is magneto-optical materials with asymmetric permittivity tensor  $\epsilon$ ; the second option is nonlinear materials, where the permittivity  $\epsilon$  is a function of the electric-field strength; and finally there are the time-dependent structures where permittivity  $\epsilon$  or permeability  $\mu$  or both depend on time. In our case, the magneto-optical material is used to break the Lorentz reciprocity to achieve non-reciprocity with asymmetric permittivity tensor.

### 1.3 Obstacles of Integration of Magneto-Optical Garnets on SOI platforms

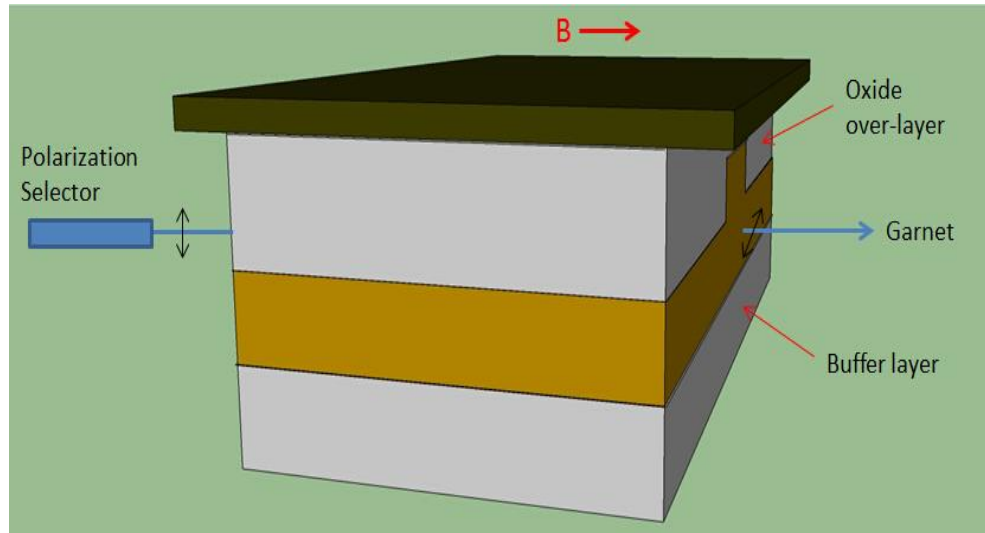
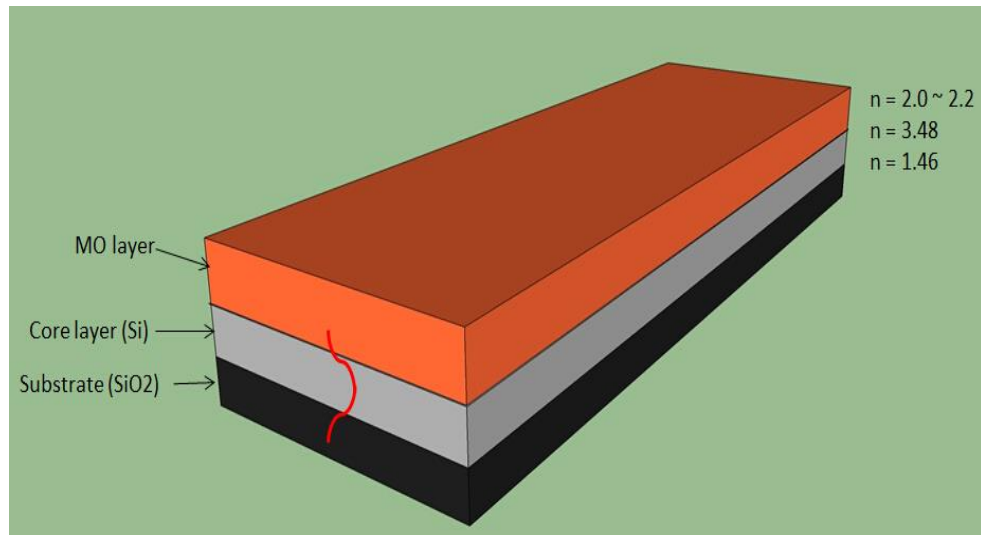


Figure 1-4. Structure of Waveguide Isolator.

A number of inherent obstacles arise when integrating bulk isolators to planar waveguides. First of all, Yttrium Iron garnet (YIG), with its large Faraday rotation index (Verdet Constant, 200 deg/cm) has been widely used thanks to its magneto-optic effect [46]. Later it was found that doping (substitution) can improve the magneto-optic effect, and Ce substituted-YIG aroused much more attention because of their larger Faraday rotation index [47] and Faraday rotation coefficient of  $-4500^\circ/\text{cm}$  at  $1.55 \mu\text{m}$  [48]. It therefore makes sense to use Ce-YIG as the core layer of the waveguide on a lattice-matched GGG (Gadolinium Gallium Garnet,  $\text{Gd}_3\text{Ga}_5\text{O}_{12}$ ) substrate with refractive index of 1.936 at 1550 nm. Such a choice derives from  $n_{\text{garnet}} > n_{\text{GGG}}$ , which is a traditional layer structure in a waveguide isolator, as seen in Figure 1-4. However, when SOI ( $n_{\text{Si}} > n_{\text{garnet}}$ ) is used as the substrate, based on the theory of mode guiding, the index of refraction of the core layer should be larger than that of both the substrate and the cladding layer. Therefore, Ce-YIG cannot be used as the core layer here. A solution is provided in [48][49] in which Ce-YIG was used as the upper cladding layer to take advantage of its magneto-optic effect through an interaction of the guided modes evanescent tail (see Figure 1-5).



**Figure 1-5.** Layer structure of waveguide-type isolator with Si as the core layer and the magneto-optical garnet as the upper cladding layer. All the refractive index of the material is given at 1.55  $\mu\text{m}$  wavelength.

Once a magneto-optic material has been chosen, birefringence needs to be dealt with. Birefringence is observed when light, not polarised along the optical axes of the material, is incident upon anisotropic material. There are primarily four kinds of birefringence: stress-induced birefringence due to lattice mismatch between film and substrate; growth-induced birefringence; geometrical/shape birefringence; and finally photo-elastic birefringence [50]-[52].

Research shows that we can reduce shape-induced birefringence by growing multilayer films. The growth-induced effect can instead be reduced by annealing at high temperature and choosing the proper waveguide width, whereas the photo-elastic effect is reduced by growing compressively strained films. Additionally, by growing the top layer too thick and then thinning it, or by growing the top layer too thin and adding a dielectric layer of suitable thickness and refractive index, we can eliminate the remaining birefringence[51][53]. In[54], R.Wolfe et al. overcome the inherent birefringence by using laser annealing to get the sub-lattice magnetisation (i.e. the sign of the Faraday effect) reversed. In order to realise phase-matching, we can sometimes choose the proper size of the core[55], the temperature of the waveguide[56], apply stress and use periodic structures[57]-[59].

In this project to achieve the NR-PMC we adopted a quasi-phase matching (QPM) technique to overcome the shape-induced birefringence of the waveguide

device, where the propagation constants of the two orthogonal modes are different and there is phase mismatching between the two modes. The QPM technique allows for a phase mismatch over a coherence distance (half beat-length), but then reverses or disrupts the nonlinear interaction at positions of coherence distance, in order to prevent the conversion to take place in the wrong direction and to avoid the polarisation rotation going back to 0. By utilising an upper cladding that alternates between MO material and non-MO material periodically (Figure 1-6) [58], we can achieve QPM in waveguide structure.

Periodical structures have been long used to exploit QPM for polarisation rotation [58] [60]–[62]. S.C.C. Tseng and A.R. Reisinger [60] used a periodic Permalloy structure to achieve periodic reversals of magnetisation and at  $1.15\ \mu\text{m}$  to get an optimum dc conversion efficiency of  $80\pm 2\%$  on  $\text{Gd}_{0.5}\text{Ga}_1$  garnet film. Y. Shani and R. Alferness [61] made asymmetric periodic loaded rib waveguides on InP to get polarisation rotation of 80%.

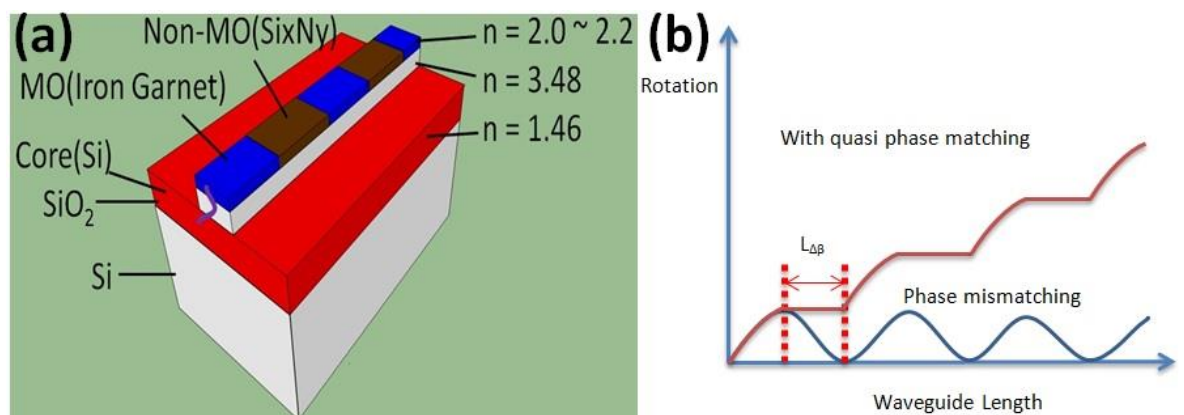


**Figure 1-6.** (a) The periodic loading structure of NR-PMC with alternating half beat-length long ( $L_{\Delta\beta}$ ) MO segments and Non-MO segments; (b) The difference in rotation between QPM and Phase Mismatching.

Finally, the polarisation orientation of light through the integrated waveguide isolator should either be in plane or normal to the plane, to facilitate following manipulations such as polarising, mode splitting and polarisation rotation in integrated optical systems. A reciprocal polarisation mode converter (R-PMC) is incorporated with the NR-PMC part to achieve light guiding in the forward direction and isolation when backwards [63].

The NR-PMC section of my project is to implement the isolator function in SOI, as part of the EPSRC (Engineering and Physical Sciences Research Council) project ‘Materials World Network: Complex oxides for heterogeneous optoelectronic integration’, in collaboration with Professor Bethanie Stadler’s

group from University of Minnesota. Professor Bethanie Stadler’s group will mainly use radio-frequency sputtering technique to provide the high-quality MO film deposited on the pre-patterned samples that we send to them. They will deposit the MO layer of different thicknesses and doping (substitution) on the sample surfaces. After the sample is deposited with MO layer in the US, we use lift-off techniques to create a patterned media, and then anneal to get the most appropriate and optimised Garnet phase MO layer, without unwanted crystal phases occurring, and fabricate samples with markers ready for patterning and etching of actual waveguide based devices.

In summary, the role of the collaborator is to deposit the high-quality garnet material on the pre-patterned samples I provide. The collaborators also provide most of the garnet material characterisation. These activities had to be outsourced as Glasgow does not have the facilities to carry them out. My role in this project includes all aspects of device design (i.e. simulation and layout) followed by nanofabrication and optical characterisation of the devices. The contribution of each party in this project is described in table 1-1.

NR-PMC Section	My Contribution	Device Design	
		Simulation	
		Nanofabrication	
		Device Characterisation	Optical
		Result Analysis	
	Collaborators’ Contribution	MO Garnet Deposition	MO Garnet Material Characterisation
R-PMC Section	Independent Work Carried Out by Me		

Table 1-1. Contribution of each party in this project.

## 1.4 Literature Review about Current Research conducted on SOI substrate

Integrated isolators currently developed are based on the destructive and constructive interference between two  $45^\circ$  rotations in the forward and backward direction, respectively. The two rotations are realised either by implementing a nonreciprocal phase shift through structures like MZI (Mach-Zehnder Interferometers) and rings, or by nonreciprocal mode conversion through the combination of a  $45^\circ$  Nonreciprocal Rotation ( $45^\circ$  Faraday Rotator) with a  $+45^\circ$  Reciprocal Rotation. Both the phenomenon of nonreciprocal phase shift and nonreciprocal mode conversion can be found in magneto-optic garnets in the presence of an applied external magnetic field.

Nowadays, waveguide isolators on Si platforms integrated with the magneto-optic garnet take advantage of either nonreciprocal phase shift or nonreciprocal mode conversion in different structures like rings[64]-[68], MZI[29][31][32][69]-[76] and periodic loading on top of normal waveguide[77]-[79] to achieve isolation. Due to lattice mismatch between garnet and Si surface, three approaches are usually employed to integrate magneto-optic garnet: they are deposition[64][67][77], adhesive bonding[31][72][73] and direct bonding[29][65][69]-[71]. The structure, fabrication method and characteristics of the devices are summarised in Table 1-2.

Researchers	Mode Working on	Structure	Fabrication Method	Isolation	Device Length	Wavelength Working	Year
T.Mizumoto 's group: Y.Shoji etc.[74]	TM	MZI	Direct Bonding	>21 dB	NA	1530-1565 nm	2007
T.Mizumoto 's group: Y.Shoji etc.[71]	TM	MZI	Direct Bonding	21 dB	4 mm	1559 nm	2008
T.Mizumoto 's group: Y.Shoji etc.[80]	TM	MZI	Direct Bonding	18 dB	>1.5x1.5 mm <sup>2</sup>	1322 nm	2012
T.Mizumoto 's group: Y.Shirato and Y.Shoji[75]	TM	MZI	Direct Bonding	28 dB	>1.5x1.5 mm <sup>2</sup>	1552 nm	2013
T.Mizumoto 's group: Y.Shoji etc.[76]	TM	MZI	Direct Bonding	>20 dB	>1.5x1.5 mm <sup>2</sup>	1550nm±4 nm	2014

T.Mizumoto 's group: Y.Shoji etc.[32]	TE	MZI	Direct Bonding	26.7 dB	>1.5x1.5 mm <sup>2</sup>	1553nm	2016 (to be published)
John E.Bowers' group: Ming-Chun Tien etc.[65]	TM	Ring	Direct Bonding	9 dB	Diameter: 1.8 mm	1550nm	2011
John E.Bowers' group: D. Huang, P.Pintus and etc.[68]	TM	Ring	Direct Bonding	32 dB	NA	1555 nm	2016 (to be published)
Caroline A. Ross's Group: L. Bi etc.[64]	TM	Ring	Deposition	19.5 dB	290 $\mu$ m	1550 nm	2011
Caroline A. Ross's Group: X. Sun etc.[67]	TM	Ring	Deposition	13 $\pm$ 2.2 dB	NA	1564.4 nm	2015
Roel Baets' group: S.Ghosh etc.[72]	TM	MZI	Adhesive Bonding	25 dB	3.46x0.46 mm	1495.2 nm	2012
Roel Baets' group: S.Ghosh etc.[73]	TM	MZI	Adhesive Bonding	11 dB	1.5 mmx4 $\mu$ m	1512.6 nm	2012
Roel Baets' group: S.Ghosh etc.[31]	TE	MZI	Adhesive Bonding	32 dB	6 mmx0.2 mm	1540.5 nm	2013

**Table 1-2.SOI-based Magneto-optical Isolator**

In our project we adopt the nonreciprocal mode conversion method by applying an external magnetic field along the direction of propagation of the light (along the z axis), so that both the TE and TM mode will be affected. The mode conversion requires phase matching while the non-reciprocal phase shift (NPS) method (based on MZI) does not. As such, it can be assumed that the latter may be easier to achieve. However, the NPS can be only applied for TM modes whilst the mode conversion method can be used for both. Also the vast majority of lasers emit TE polarized light [81]-[83] from the heavy-hole transition and since the TE

light becomes TM after the mode conversion, and the TE emitting devices are essentially transparent to TM, the reflected light will not have any effect on the system.

As shown in Table.1-1, currently all reported isolator designs on SOI substrates are based on nonreciprocal phase shift (NPS) where devices only work with either TM or TE mode. TM-mode isolators based on NPS are easier to fabricate, however they do not have many applications as most semiconductor sources have a TE-polarised output. To date the only TE polarised light optical isolator was realised by Ghosh etc.[31] and Shoji etc.[32], where MO garnet material was adhesively bonded on top of the waveguide and the NPS approach, together with complicated optical serpentine circuit and complicated design of asymmetric coupled waveguides for TE-TM mode conversion, were employed. Despite this approach used to achieve TE isolation, it does not work on TM modes and has quite a large footprint even designed in serpentine shape, where the total size is 6 mmx0.2 mm with a 4x2.86 mm long nonreciprocal phase shifter section. Additionally, the adhesive bonding method is also not ideal, being sensitive to any thermal expansion and not suitable for mass production.

In the following we use the device with MZI structure that works for the TM mode as an example to explain the process of isolation based on constructive/destructive interference [76]. Figure 1-7 shows the schematic of the device, composed of 3 dB couplers, nonreciprocal phase shifter, reciprocal phase shifter and Ce-YIG garnet bonded on top. An anti-parallel magnetic field is applied for the nonreciprocal phase shifter to provide a phase difference of  $-\pi/2$  in the forward direction and  $+\pi/2$  in the backward direction. The reciprocal phase shifter provides  $+\pi/2$  phase difference in both directions resulted from the asymmetric path length of the MZI arm.

In the forward directions, when the TM-polarised light is injected in, it is split into two waves with equal amplitude and phase. After transmitting through the nonreciprocal phase shifter and the reciprocal phase shifter, the phase difference between the two waves adds up,  $(-\pi/2) + (+\pi/2)$ , to be 0. At the output, the two waves have the same phase and they interfere with each other constructively to make a wave with the same amplitude as that of the input wave. In the backward direction, the phase difference between the two waves adds up,  $(+\pi/2) + (+\pi/2)$ , to be  $\pi$ . At the output, the two waves have a  $\pi$  phase difference and they escape from the side waveguide and no light comes out from the central

waveguide, so that isolation of the reflected light is achieved. The whole process of constructive interference and destructive interference in the forward direction and the backward direction respectively is depicted in figure 1-8.

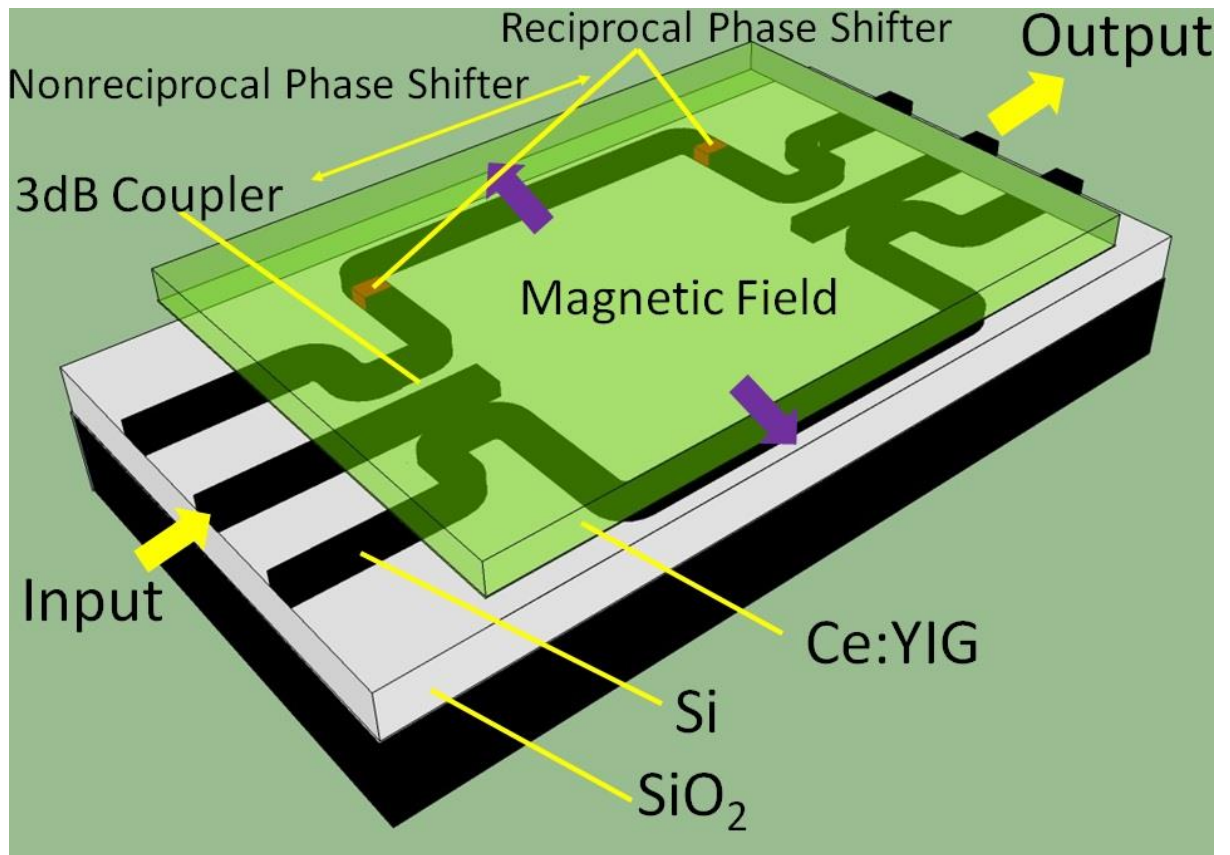


Figure 1-7. Schematic of a typical isolator with MZI structure based on nonreciprocal phase shift.

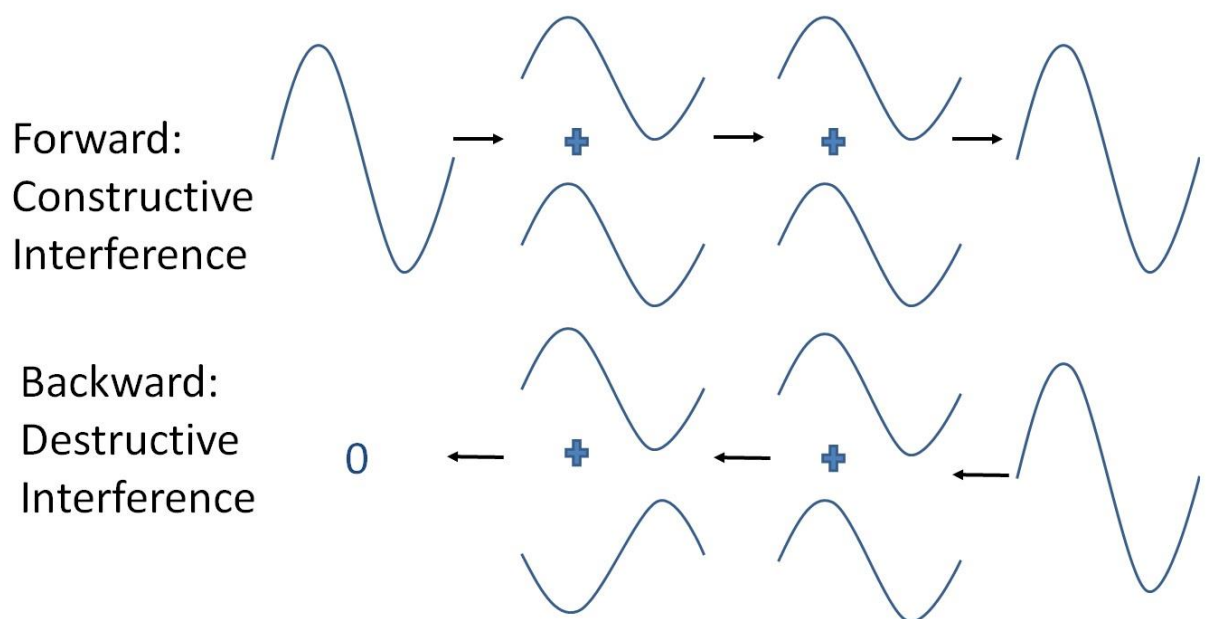


Figure 1-8. The constructive and destructive interference in the forward and backward direction of the isolator system described in figure 1-7.

John E. Bowers [84] has proposed a novel design of TE isolator based on nonreciprocal phase shift. According to its proposal the internal wall of an ultra-low loss[85]  $\text{Si}_3\text{N}_4$  arrayed ring waveguide, buried in a silica media, is coated with Ce-YIG garnet under a vertical magnetic field so that part of the TE mode is confined in the Ce-YIG garnet part. A great difference thus arises between the resonance wavelength of the rings in forward and backward directions in the presence of a vertical magnetic field. A top view and cross-section view of the rings with sidewall coated with Ce-YIG is depicted in Figure 1-9. Theoretical analysis on this device's loss, isolation has been carried out but no actual devices have been made yet, as there are significant fabrication challenges. Therefore, there has not been a TE/TM isolator realised on SOI substrate yet.

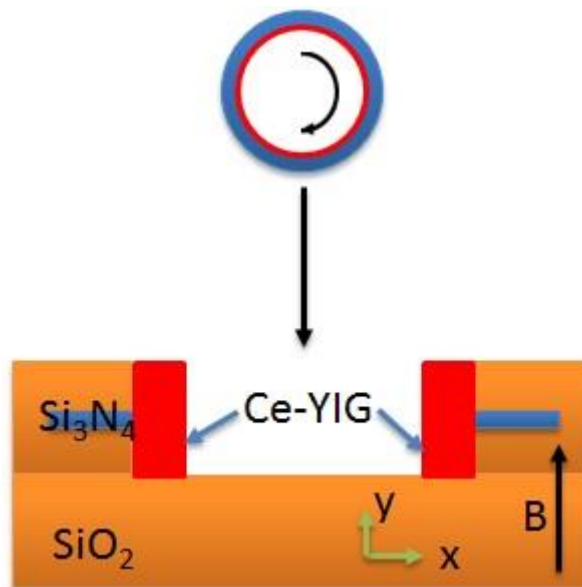


Figure 1-9. Top view and cross-section view of the  $\text{Si}_3\text{N}_4$  rings with sidewall coated with Ce-YIG[84].

## 1.5 Approach adopted in this project

### 1.5.1 NR-PMC (Non-Reciprocal Polarisation Mode Converter)

The project is titled Integrated Waveguide Optical Isolators. My role in the project is to fabricate integrated isolators that can modulate arbitrary polarisation states through the use of NR-PMCs and R-PMCs in the SOI material platform. These NR-PMCs are based upon the theory of Faraday rotation, and the

R-PMCs are based upon mode beating polarization conversion [86]. When hybrid polarised light (i.e. not at 0 or 90 degrees) propagates along in a planar waveguide, the TE and TM components propagate at different speeds (due to the different propagation constants resulting from structural birefringence in planar systems) which leads to a different polarisation at the waveguide output. The resultant of the two fundamental polarised modes can be linearly polarised, elliptically polarised, circularly polarised, elliptically, or linearly polarised periodically (Figure 1-10) depending on the phase difference  $\psi$  between the TE and TM components.

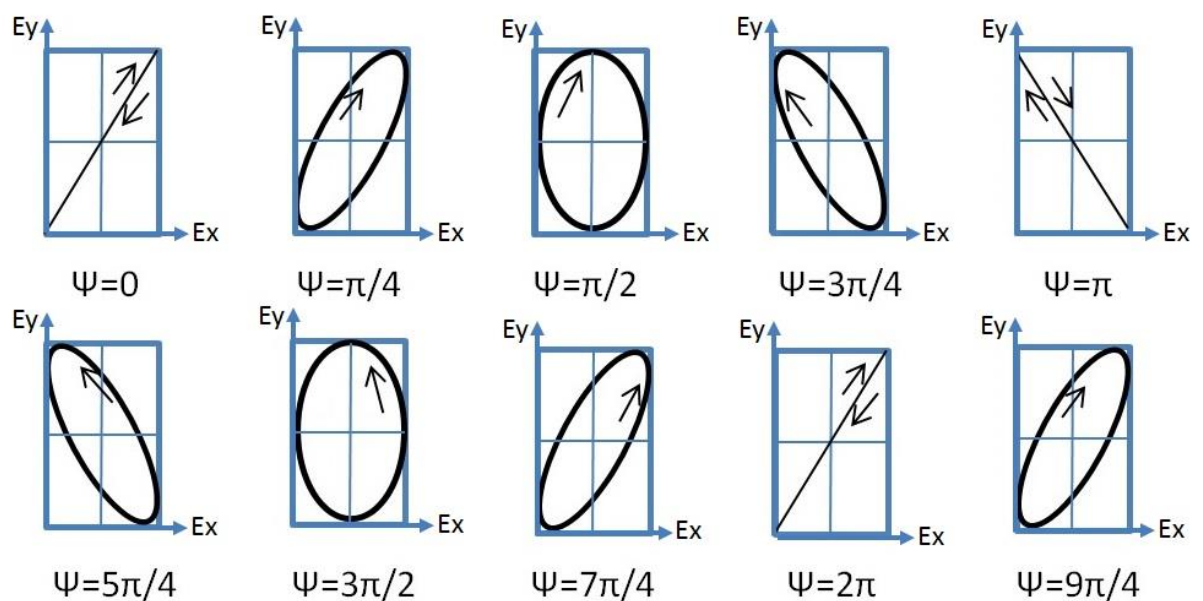


**Figure 1-10.** Changes in resultant polarisation from two modes propagating in anisotropic media, where  $\psi$  is the phase difference between the TE and TM components.

There are two approaches [70][87][88] commonly used to achieve non-reciprocal, magneto-optical isolation in waveguide formats: longitudinal field and transverse field. As previously discussed (see section 1.3), for the NR-PMC part, a periodic loading structure was adopted [77][79][86][89] in this thesis. Mode conversion is realised through the Faraday rotation effect resulting from the evanescent tail of the mode interacting with the magneto-optical garnet cladding, so that the first - longitudinal field approach - is employed. The relationship between dielectric tensor and Faraday rotation effect will be explained in more detail in Chapter 2. The simulation, fabrication and optical measurements of the NR-PMC part will be discussed in Chapter 3, Chapter 4 and Chapter 5 respectively.

## 1.5.2 R-PMC (Reciprocal Polarisation Mode Converter)

In order to obtain reciprocal polarisation mode conversion, we use an L-shape structure which is similar to the trench structure shown in Figure 1-11, that effectively will rotate the optical axis and excite the two TE and TM components from the incident pure TE mode which enables beating of the polarised light and achieves mode-conversion. Previously, slanted angled structures have been adopted, which are based on the same principle[90]-[93]. This solution is free of longitudinally periodic structures. However, although much effort has been put into fabricating the slanted structures, exploiting various techniques including wet etching[94] and dry etching at an angle[95], it still is a difficult technique. Comparatively, the trench structure can be realised relatively easily by using Electron Beam Lithography (EBL) and exploiting the Reactive Ion Etching (RIE) lag effect[96]. But since the RIE effect is not so obvious in Si, as it will be explained in Chapter 6, a similar structure, the L-shape, is adopted to achieve reciprocal polarisation mode conversion.

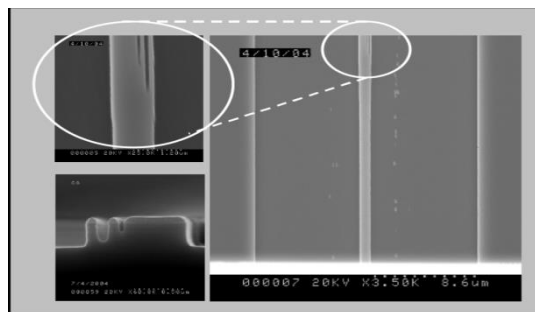


**Figure 1-11.** Trench structure realised by Electrical Beam Lithography (EBL) and Reactive Ion Etching (RIE) lag effect [96]. Got permission from Dr. Barry Holmes to reprint.

## 1.5.3 Integrated Waveguide Optical Isolator

An integrated waveguide optical isolator that works at a wavelength of 1550nm can be developed by integrating the 45° NR-PMC and the 45° R-PMC. The device proposed in this thesis is described in Figure 1-12. The rotation caused by the NR-PMC part is independent of the light propagation direction, while that caused by the R-PMC is dependent on the light propagation direction. In the forward direction, the TE-polarised light emitted from the laser source and

injected in the device will experience a  $+\pi/4$  rotation after the NR-PMC part, followed by a  $-\pi/4$  rotation after the R-PMC part. It thus turns back to TE-polarised light at the output. In the backward direction, when the TE-polarised light is reflected back into the device, it will experience a  $+\pi/4$  rotation after the R-PMC part then a  $+\pi/4$  rotation after the NR-PMC part. It turns into TM-polarised light, which is essentially transparent to the laser source, thus achieving isolation of the optical system.

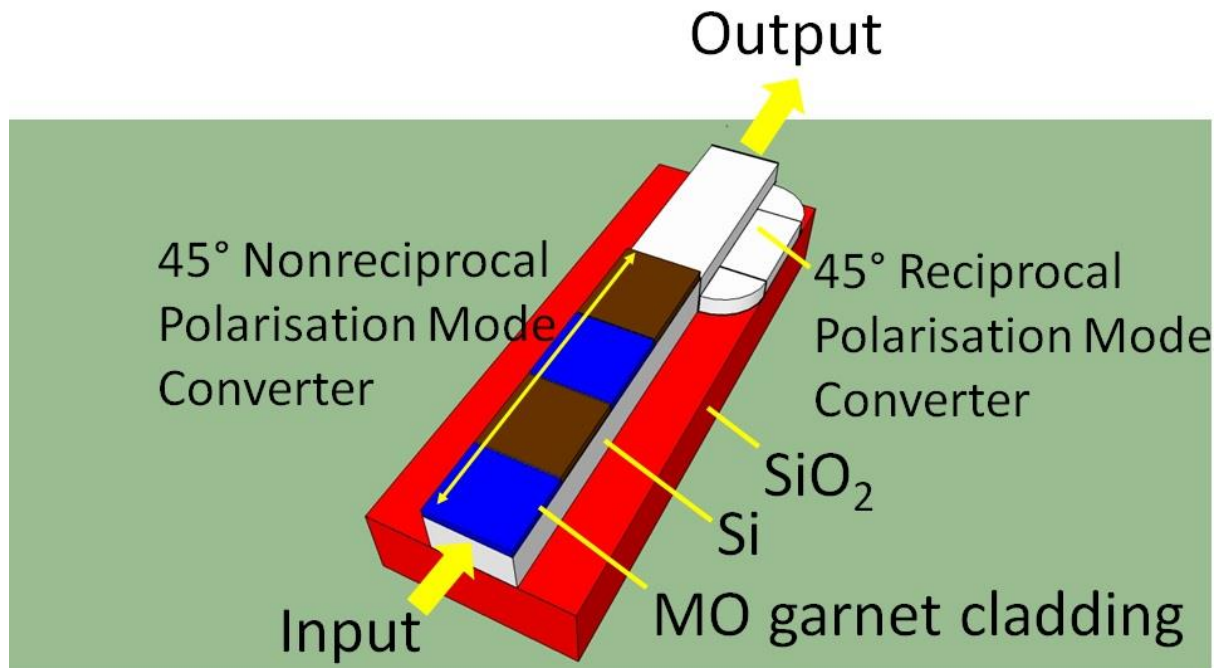


Figure 1-12. The schematic of the integrated waveguide optical isolator device proposed in this thesis.

## 2 Chapter 2 – Magneto-optic Effects

### 2.1 Magneto-optic Effects

The term Magneto-optic effect (MOE) refers to the phenomenon in which an electromagnetic wave propagates differently through a magnetic medium depending on the presence or absence of a magnetic field, which alters the electromagnetic (EM) properties of the magnetic medium. Magneto-optic (MO) materials are also called gyromagnetic, and they give rise to two of the best known magneto-optic effects, the Faraday and the Cotton-Mouton (CM) Effect (also called the Voigt Effect for gas media) where the light changes when transmitted through the MO material. The Magneto-Optic Kerr Effect (MOKE), in which the light changes when reflected from the surface of the MO medium, is also well-known. In materials with magnetic moments, either from atoms or ions, the type of MOE encountered reflects the corresponding kind of magnetism: ferromagnetism, ferrimagnetism, para-magnetism, anti-ferromagnetism and diamagnetism. In materials without magnetic moments, Larmor precession of the internal electron orbitals under an applied magnetic field can also change the interaction with an electromagnetic wave.

We consider the case of light waves transmitted in optical waveguides or fibres, applicable to, for example, optical communication systems. Thus, the propagation properties of the transmitted light can be affected by the Faraday Effect and the Cotton-Mouton Effect. Generally, application of MO effects is limited by two factors, the specific MO coefficients  $\theta$ , Faraday rotation coefficient  $\theta_F$  or linear birefringence, and the absorption coefficient  $\alpha$ . The ratio of the two factors is defined as the Figure of Merit (FOM) of the material[97]:

$$\text{F. O. M} \left[ \frac{\text{deg}}{\text{dB}} \right] = \frac{\theta[\text{deg/cm}]}{\alpha[\text{dB/cm}]} \quad (2-1)$$

The Faraday Effect is observed when an applied external magnetic field is parallel to the direction in which the transmitted light propagates, and the field induces a nonreciprocal magnetic circular birefringence (MCB). MCB causes the phase velocity, or the index of refraction of left-rotating circularly polarised light ( $n_-$ ), to be different from that of right-rotating circularly polarised light ( $n_+$ ). The difference in refractive index is proportional to the longitudinal component of the applied magnetic field. The Faraday Effect is a first-order effect.

The Cotton-Mouton Effect is observed when the applied external magnetic field is perpendicular to the direction of propagation, and it induces a reciprocal magnetic linear birefringence (MLB). Due to MLB the propagation velocity, or the index of refraction of the light polarised along the parallel direction to the magnetic field ( $n_{//}$ ) is different from that of the light polarised perpendicularly to the magnetic field ( $n_{\perp}$ ). In the MLB case, the difference in refractive index is proportional to the square of the applied transverse magnetic field. Differently from the Faraday Effect, the Cotton-Mouton one is a second-order effect.

When light waves are transmitted in optical waveguides, the propagation and coupling properties of the optical modes is determined by the permittivities of the cladding layer, core layer and substrate[98]. Since the Faraday Effect is nonreciprocal and Cotton-Mouton Effect is reciprocal, the combination of the two effects can be used to make an isolator[99][100]. However, implementing a design with two orthogonal magnetisation directions on a single chip presents great technical challenges[101]. For the magneto-optical media used in this project, rare-earth doped garnets, over the 1 to 3  $\mu\text{m}$  wavelength range the Cotton-Mouton Effect is very small compared to the Faraday Effect. The Cotton-Mouton Effect is thus usually neglected[98][102][103], and the Faraday Effect is the predominant influence factor for the permittivity.

In the case of thin films waveguides, the fundamental modes of the waveguide are conventionally called ‘transverse electric (TE)’, and ‘transverse magnetic (TM)’. The TE modes are polarised in the plane of the wafer, whereas TM modes are polarised perpendicularly to the plane of the wafer. This description is an approximation, as normally some hybridisation of both modes exists, and the quasi-TE and quasi-TM denomination is often used instead. However, in each dimension, one of the two components is predominant and typically much larger

than the other one, so it is common practice to still refer to them as TE and TM polarisations [104].

The off-diagonal elements of the permittivity tensor represent the Faraday Effect contribution from an external magnetic field, as derived from the perturbation theory developed by Yamamoto and Makimoto [105]. As shown in Figure 2-1, the propagation direction of the light wave is along the z axis. According to perturbation theory, an external magnetic field applied in the direction of any of the three axes causes a corresponding perturbation to the waveguide system. The applied magnetic field will affect the components of the electric field which are perpendicular to the magnetic field, but will not affect the parallel electric field components. When an external magnetic field is applied along the z axis, as seen in Figure 2-1(a), the perturbed system is Longitudinal (L) and induces the  $i\varepsilon_{xy}$  and  $-i\varepsilon_{xy}$  off-diagonal elements; when an external magnetic field is applied along the y axis, as seen in Figure 2-1(b), the perturbed system is Equatorial (E) and induces the  $i\varepsilon_{xz}$  and  $-i\varepsilon_{xz}$  off-diagonal elements; finally, when an external magnetic field is applied along the x axis, as seen in Figure 2-1(c), the perturbed system is Polar (P) and induces the  $i\varepsilon_{yz}$  and  $-i\varepsilon_{yz}$  off-diagonal elements. The Equatorial and Polar perturbed systems can be regarded together as the Transverse system. Equation 2-2 describes the perturbation involving all three axes:

$$\varepsilon = \begin{bmatrix} \varepsilon_{xx} & i\varepsilon_{xy} & i\varepsilon_{xz} \\ -i\varepsilon_{xy} & \varepsilon_{yy} & i\varepsilon_{yz} \\ -i\varepsilon_{xz} & -i\varepsilon_{yz} & \varepsilon_{zz} \end{bmatrix} \quad (2-2)$$

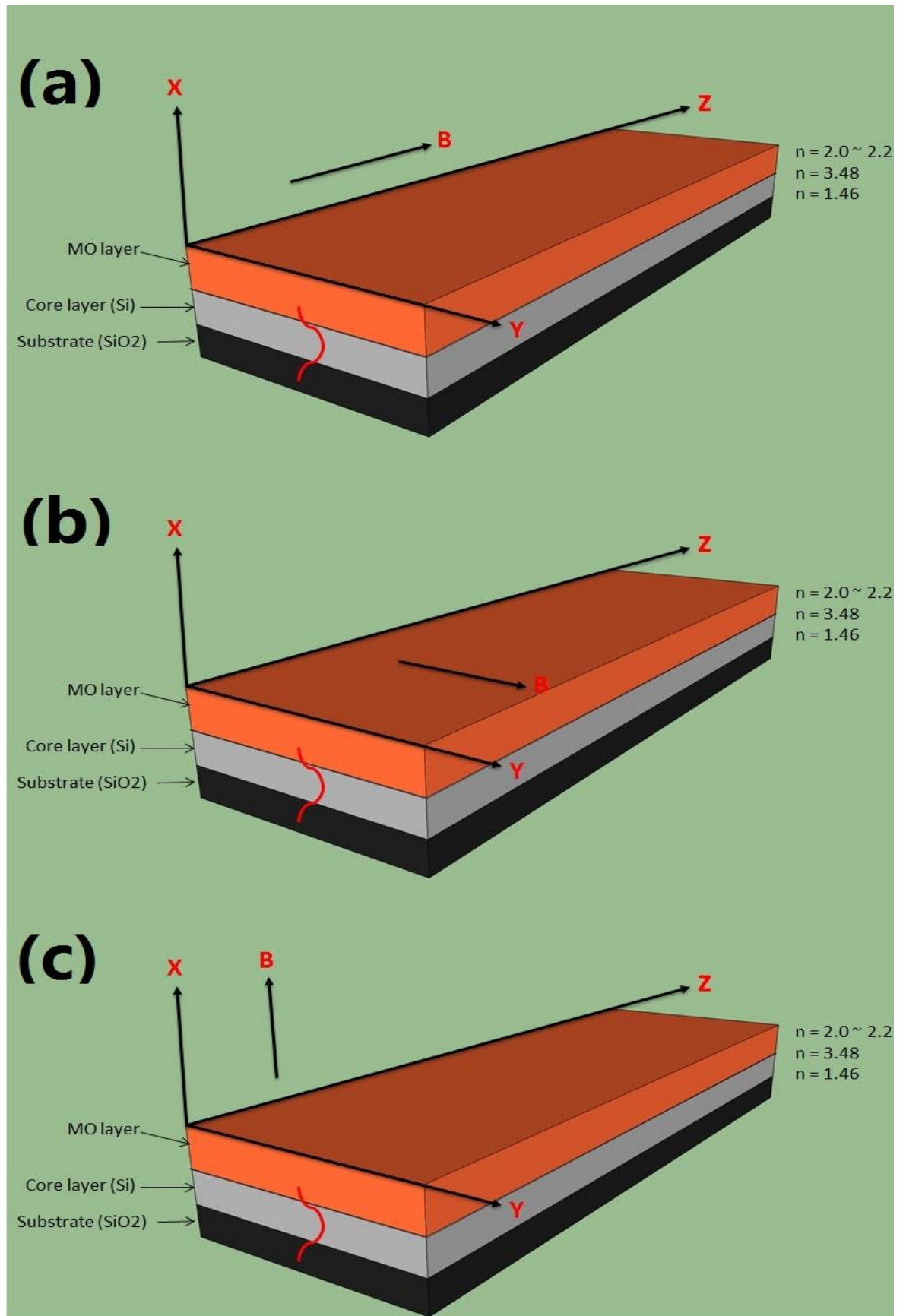
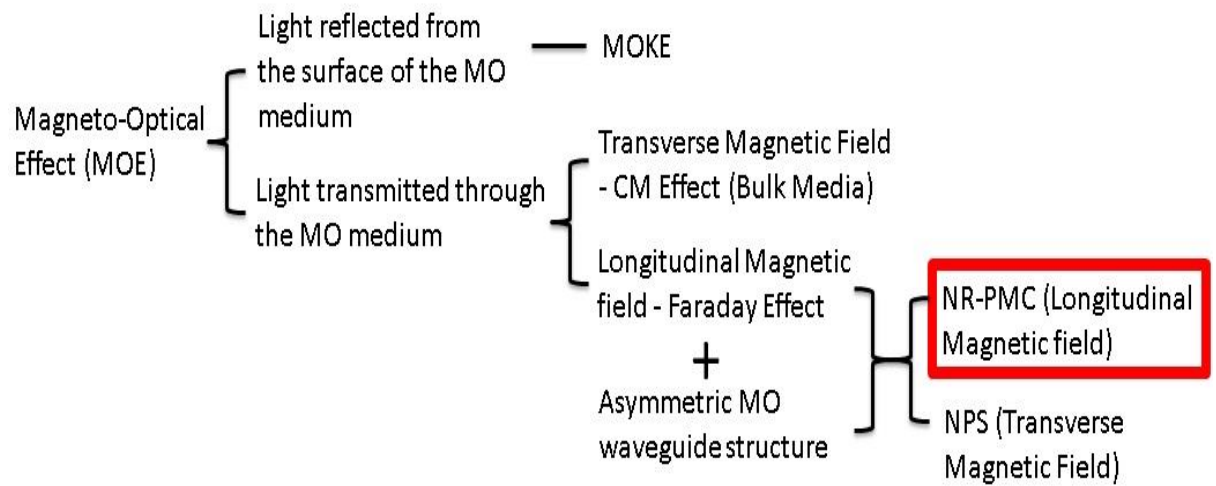


Figure 2-1. Illustration of possible magnetisation direction. Light propagation is along the z axis and (a) (b) (c) describe the external magnetic field along z axis, y axis and x axis respectively.

In a longitudinally perturbed system, the electric field components in both the x and y directions are involved and there is coupling between TE and TM modes, thus mode conversion between TE and TM modes takes place, and this phenomenon is nonreciprocal. In a transversely perturbed system, only one component of the electric field is affected by the perturbation, either the TE or TM mode. A phase difference is therefore induced between the forward and backward traveling waves, when the propagation direction is parallel or anti-parallel to the external magnetic field. This phenomenon is also a nonreciprocal effect. When the external magnetic field is in the plane of the waveguide, along the y axis, a phase shift is induced on the TM mode. When the external magnetic field is normal to the plane of the waveguide instead, i.e. along the x axis, there is a phase shift for the TE mode. By combining the phase shifts between forward and backward directions with special structures, like 3dB splitters, constructive and destructive interference takes place, and can be exploited to achieve devices such as Mach-Zehnder Interferometers (MZIs). MZIs can be used as isolators and structures have been proposed and designed to induce the right phase shift for both modes[106]-[110].

Therefore, both the nonreciprocal polarisation mode conversion (NR-PMC) in the longitudinal approach, and the nonreciprocal phase shift (NPS) in the transverse approach result from the perturbation to the waveguide system caused by the Faraday Effect. It is important to differentiate between the NPS and the Cotton-Mutun Effect. As previously mentioned, the latter takes place when an external magnetic field is perpendicular to the direction of light propagation, and it might seem confusing. NPS, however, is a transverse expression of the Faraday Effect, while the Cotton-Mutun Effect is a reciprocal effect. NPS does not exist when light travels in bulk materials, while the Cotton-Mutun Effect does. Discontinuities of the waveguide structure and the Faraday effect are required for NPS[110]. It is safe to say that the Cotton-Mutun Effect is a bulk transverse magnetisation phenomenon while NPS is inherently a waveguide phenomenon[111]. The relationship between different kinds of magneto-optical effects is summarised in Figure 2-2. The NR-PMC effect has been highlighted with a red frame, since it has been employed in this thesis.



**Figure 2-2. Summary of the relationship between different kinds of magneto-optical effects. The NR-PMC effect has been highlighted as it has been employed in this thesis.**

### 2.1.1 Nonreciprocal Polarisation Mode Conversion (NR-PMC) - Longitudinal approach of Faraday Rotation Effect

Despite Nonreciprocal Polarisation Mode Conversion (NR-PMC) being just the longitudinal expression of the Faraday Effect, conventionally Faraday Rotation Effect is used to refer to NR-PMC, whereas Nonreciprocal Phase Shift (NPS) is preferred when referring to the transverse expression of the Faraday effect. The Faraday Rotation Effect is a type of magnetic circular birefringence, where a rotation of the wave polarisation plane results from the left-rotating circularly polarised (LCP) light and the right-rotating circularly polarised (RCP) light propagating at different speeds. Such birefringence is due to the splitting of the ground or excited-state energy levels when an external magnetic field is applied in the direction parallel to that of light propagation. The direction of the rotation depends on the direction of magnetisation of the material from the external magnetic field, but not on the propagation direction of the light, meaning the Faraday rotation is non-reciprocal. The non-reciprocity is very useful in applications like Faraday rotators, isolators and circulators. Rare earth iron

garnets (REIG)  $R_3Fe_5O_{12}$  are a typical and popular ferrimagnetic Faraday rotation material due to their transparency in the infrared window from 1.5 to 5  $\mu\text{m}$ , coupled with high Faraday rotation coefficient [112]. Ferrimagnetism is somewhat similar to antiferromagnetism, but within antiferromagnetic materials equal and opposite magnetic moments are present and they will cancel each other so that the total magnetization is zero; in ferrimagnetic materials instead, the opposite magnetic moments are not equal and give rise to a net remaining magnetisation.

Faraday rotation in a ferrimagnetic garnet is the response of the ferrimagnetism to the applied external magnetic field and is related to both the electric dipole transitions and the ferromagnetic resonance (FMR). The Zeeman splitting of the energy eigenvalues in the ferromagnetic material at the presence of a static internal magnetic field  $H_i$  [112] determines the resonance frequency, where  $\hbar\omega = g\mu_B H_i$ , with  $\hbar = \frac{h}{2\pi}$ ,  $h$  is the Planck constant,  $g$  is gyromagnetic or Lande factor,  $\omega = 2\pi\nu$  is the resonance frequency, and  $\mu_B$  is the Bohr magneton, therefore  $h\nu = g\mu_B H_i$ . The resonance splitting process is depicted in Figure 2-3. The Zeeman splitting occurs at the resonance peak and the original state is split into two quantum states of magnetic quantum number  $m = +\frac{1}{2}g\mu_B H_i$  and  $m = -\frac{1}{2}g\mu_B H_i$ , respectively. Summarising, the Faraday rotation results from electric dipole transitions, while FMR from the whole sub-lattices responding to the external magnetic field.

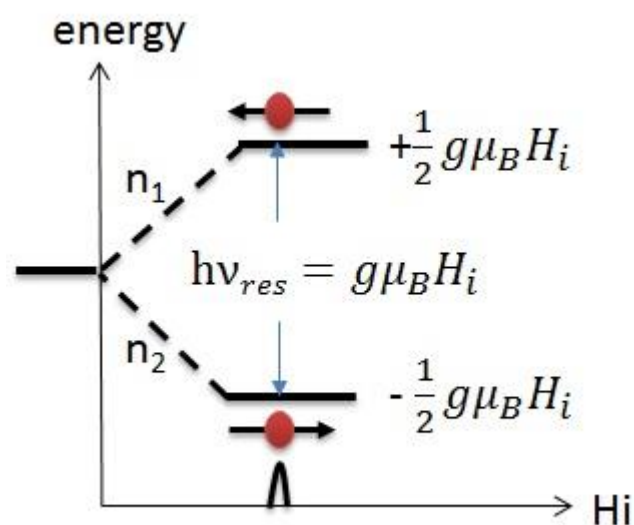
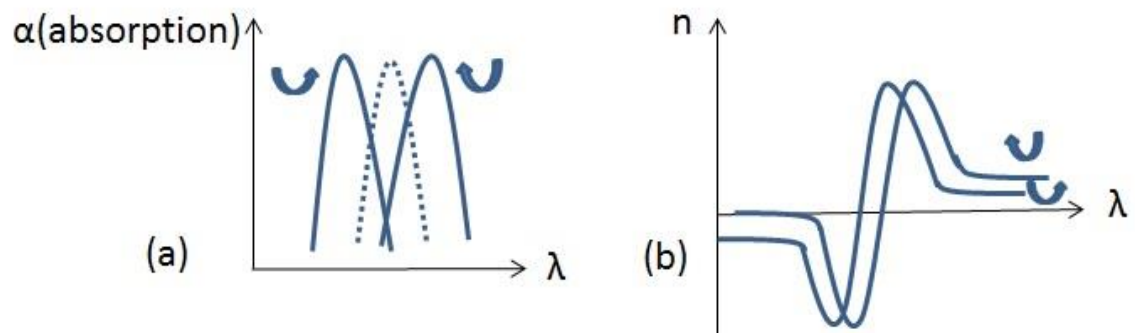


Figure 2-3. Illustration of the ferromagnetic resonance splitting process in presence of a static internal magnetic field  $H_i$ .

A TEM wave subject to a magnetic field splits into two counter-rotating circularly polarised waves as a consequence of the splitting from Zeeman Effect[113] (see Figure 2-4 (a)). The combination of the two counter-rotating circularly polarised waves could result in a linear, elliptical, or circular polarisation [114]. Two equal-amplitude counter-rotating circularly polarised waves combine into a linearly polarised wave, while two unequal-amplitude ones with no phase difference will give rise to an elliptically polarised wave. A circularly polarised wave outcome is a sub-case of elliptical polarisation, and it will depend on the difference in amplitude between the two waves. The two initial counter-rotating circularly polarised waves are called right-hand circular polarisation (RHCP) and left-hand circular polarisation (LHCP), rotating clockwise and counter-clockwise, respectively. In this work + and - will stand for RHCP and LHCP, respectively. By using the Kramers-Krönig relations[115], the refractive indices will also be modified, as Figure 2-4 (b) shows.



**Figure 2-4.(a)** Under magnetic field, because of the Zeeman Effect, the wave splits into two circularly polarised waves, right-hand polarised and left-hand polarised. **(b)** By the Kramers-Krönig relations the corresponding refractive indices are modified.

When the difference between the phase of LHCP and RHCP is  $90^\circ$ , the wave travels a distance of half beat length,

$$L_{\frac{1}{2}} = \frac{\lambda}{2|n_L - n_R|} = \frac{\lambda}{2|\Delta n|} \quad (2-3)$$

If there's no external magnetic field, the propagation constants of the two circularly polarised waves are equal, i.e.  $\beta_+ = \beta_-$ . Under the influence of an external magnetic field, the propagation constants are different ( $\beta_+ \neq \beta_-$ ) and the permittivity  $\epsilon$  changes:

$$\varepsilon = \begin{bmatrix} \varepsilon_{xx} & i\varepsilon_{xy} & 0 \\ -i\varepsilon_{xy} & \varepsilon_{yy} & 0 \\ 0 & 0 & \varepsilon_{zz} \end{bmatrix} \quad (2-4)$$

And correspondingly the refractive index:

$$n_{\pm} = \sqrt{\mu\varepsilon} \quad (2-5)$$

Here  $\mu = 1$ , so:

$$n_{\pm} = \sqrt{\varepsilon} \quad (2-6)$$

Setting the eigenvalue of permittivity  $\varepsilon$  as  $\Phi$ , one gets the following equation:

$$\begin{vmatrix} \varepsilon_{xx} - \Phi & i\varepsilon_{xy} & 0 \\ -i\varepsilon_{xy} & \varepsilon_{yy} - \Phi & 0 \\ 0 & 0 & \varepsilon_{zz} - \Phi \end{vmatrix} = 0 \quad (2-7)$$

The formula for the determinant of a 3x3 matrix yields:

$$(\varepsilon_{zz} - \Phi)[(\varepsilon_{xx} - \Phi)(\varepsilon_{yy} - \Phi) - \varepsilon_{xy}^2] = 0 \quad (2-8)$$

For uniaxial crystals  $\varepsilon_{xx} = \varepsilon_{yy}$ , thus substituting one obtains:

$$(\varepsilon_{xx} - \Phi)^2 - \varepsilon_{xy}^2 = 0 \quad (2-9)$$

Solving for the permittivity,  $\Phi = \varepsilon_{xx} \pm \varepsilon_{xy}$ , therefore the refractive index is given by:

$$n_{\pm} = \sqrt{\varepsilon} = \sqrt{\Phi} = \sqrt{\varepsilon_{xx} \pm \varepsilon_{xy}} \simeq \sqrt{\varepsilon_{xx}} \left(1 \pm \frac{1}{2} \frac{\varepsilon_{xy}}{\varepsilon_{xx}}\right) \quad (2-10)$$

$$\Delta n = \frac{\varepsilon_{xy}}{\sqrt{\varepsilon_{xx}}} = \frac{\varepsilon_{xy}}{n_0} \quad (2-11)$$

And from (2-3), through the half-beat length  $L_{\frac{1}{2}} \equiv 90^\circ$ , one can get the Faraday rotation angle at a distance of  $x$ .

$$\theta = \frac{90^\circ}{L_1} \cdot x = \frac{2\Delta n}{\lambda} 90^\circ \cdot x = \frac{2}{\lambda} \frac{\varepsilon_{xy}}{n_0} 90^\circ \cdot x \quad (2-12)$$

If  $\varepsilon_{xy}$  is known, the Faraday rotation coefficient  $\theta_F$  can be derived:  $\varepsilon_{xy} = 2\theta_F n_0 / k_0$  [30], where  $n_0$  is the refractive index, and  $k_0$  is the vacuum wavenumber. The Faraday rotation coefficient  $\theta_F$  is dependent on the temperature and wavelength of operation, but independent of the amplitude of the external magnetic field, thus  $\varepsilon_{xy}$  will also share this feature.  $\theta_F$  can be obtained experimentally or can be derived analytically as it will be shown later in the chapter. Given all other parameters in the equation are known, the rotation angle as after propagation along a distance  $x$  can be expressed as:

$$\theta = \frac{4}{\lambda} \frac{\theta_F}{k_0} 90^\circ \cdot x \quad (2-13)$$

### 2.1.2 Nonreciprocal Phase Shift (NPS) - Transverse approach of Faraday Rotation Effect

The Nonreciprocal Phase shift is the transverse expression of the Faraday Effect, and can be achieved by properly adjusting the spatial variation of the Faraday rotation. In order to demonstrate the nonreciprocity of the phase shift in a waveguide cladded with a thin film of MO garnet, T. Mizumoto *et. al.* [116]-[118] derived the eigenvalue equation for both TE and TM modes considering the boundary conditions of a three-layer asymmetric slab waveguide. As seen in Figure 2-5, when light propagates along the  $z$  direction and the magnetic field is applied along the  $y$  axis, the permittivity tensor  $\tilde{\varepsilon}_1$  shows off-diagonal tensor components  $\gamma(\varepsilon_{xz})$ :

$$\tilde{\varepsilon}_1 = \begin{pmatrix} \varepsilon_1 & 0 & j\gamma \\ 0 & \varepsilon_1 & 0 \\ -j\gamma & 0 & \varepsilon_1 \end{pmatrix} \quad (2-14)$$

The eigenvalue equation for the TM mode can be obtained by considering the boundary conditions[116], [118],

$$\tan(qd) = \frac{\frac{q}{\varepsilon_2} \left( \frac{p_1}{\varepsilon'_1} + \frac{p_3}{\varepsilon_3} + \frac{\gamma}{\varepsilon_1 \varepsilon'_1} \beta \right)}{\left( \frac{q}{\varepsilon_2} \right)^2 - \frac{p_1 p_3}{\varepsilon'_1 \varepsilon_3} - \frac{p_3 \gamma}{\varepsilon_1 \varepsilon'_1 \varepsilon_3} \beta} \quad (2-15)[118]$$

where

$$\varepsilon'_1 = \frac{\varepsilon_1^2 - \gamma^2}{\varepsilon_1}$$

$$\beta^2 = p_1^2 + \varepsilon_1 k_0^2 = p_3^2 + \varepsilon_3 k_0^2 \quad (k_0^2 = \omega^2 \varepsilon_0 \mu_0)$$

And  $k_0$  is the wavenumber in vacuum. The quantity  $q$  is the transverse propagation constant in the guiding layer;  $p_i (i = 1,3)$  indicates the decay constants along the x direction in respective regions; finally,  $\beta$  is the propagation constant along the z axis.

From equation 2-15, a nonzero linear term in  $\beta$  can be observe, indicating that  $\beta$  depends on the direction of propagation. The sign in the linear term of  $\beta$  changes for opposite directions of propagation, thus leading to different propagation constants between forward ( $\beta_{fw}$ ) and backward ( $\beta_{bw}$ ) modes.

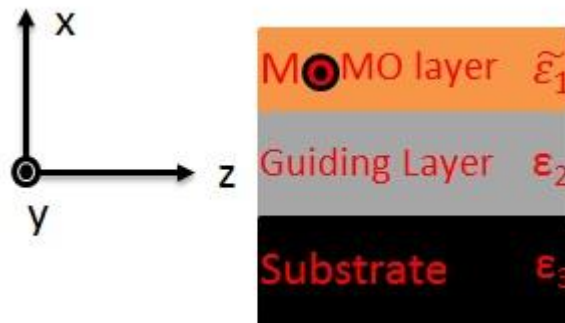


Figure 2-5. Schematic of a three-layer slab waveguide with MO garnet as cladding layer. The light wave propagates along the z axis, while the external magnetic field is applied along the y axis.

The difference between the forward (and the backward propagation constant  $\Delta\beta = \beta_{fw} - \beta_{bw}$ ) is the nonreciprocal phase shift. In order to get constructive or destructive interference, a  $0^\circ/360^\circ$  or  $180^\circ$  phase difference is required, respectively. The lengths needed for  $360^\circ(L_1)$  or  $180^\circ(L_2)$  phase differences are:

$$L_1 = \frac{2\pi}{\beta_{fw} - \beta_{bw}} = \frac{2\pi}{\Delta\beta} \quad (2-16)$$

$$L_2 = \frac{\pi}{\beta_{fw} - \beta_{bw}} = \frac{\pi}{\Delta\beta} \quad (2-17)$$

In order to calculate  $\Delta\beta$ , O. Zhuromskyy *et al.* [108] have derived the phase shifts for TE modes in media with magnetic field applied along the x axis, and TM modes in media with magnetic field applied along the y axis. If the external magnetic field is perpendicular to the direction of light propagation (i.e. along the x or y axis), then the permittivity  $\varepsilon$  becomes:

$$\varepsilon = \begin{bmatrix} \varepsilon_{xx} & 0 & i\varepsilon_{xz} \\ 0 & \varepsilon_{yy} & i\varepsilon_{yz} \\ -i\varepsilon_{xz} & -i\varepsilon_{yz} & \varepsilon_{zz} \end{bmatrix} \quad (2-18)$$

The TE and TM modes of the waveguide, as presented in Figure 2-1, are represented by their electric and magnetic fields, respectively[107]:

$$\text{TE: } \mathbf{E} = [0, E_y(x), 0] \exp[i(\omega t - \beta_{TE}z)] \quad (2-19)[107]$$

And

$$\text{TM: } \mathbf{H} = [0, H_y(x), 0] \exp[i(\omega t - \beta_{TM}z)] \quad (2-20)[107]$$

Where  $\omega$  denotes the angular frequency and  $\beta$  denotes the mode propagation constant.

The shift  $\delta\beta$  in one direction due to gyrotropy can be expressed as[108]:

$$\delta\beta = \omega\varepsilon_0 \frac{\iint \vec{E}^* \Delta\varepsilon \vec{E} dx dy}{\iint [\vec{E} \times \vec{H}^* + \vec{E}^* \times \vec{H}]_z dx dy} \quad (2-21)[108]$$

where  $\varepsilon_0$  is the permittivity in absence of perturbation,  $\Delta\varepsilon$  indicates the part of the permittivity tensor representing gyrotropy, and the difference between forward and backward propagation constants is given by  $\Delta\beta = 2\delta\beta$ . The light propagating in opposite directions can be modelled by opposite signs of off-diagonal elements  $\varepsilon_{xz}$ ,  $\varepsilon_{yz}$  and  $\varepsilon_{xy}$ .

The applied magnetic field affects those components of the electric field which are perpendicular to the magnetic field, but will not affect the components of the electric field which are parallel to the magnetic field. TE modes have an electric field component along the y axis and TM modes have an electric field component along the x axis, since we are considering light propagation along the z axis, see Fig. 2.1. Thus, when the magnetisation is along the x axis, only TE modes are affected and their phase shift is:

$$\delta\beta_{TE} = \frac{\omega\varepsilon_0}{\beta_{TEN}} \iint \varepsilon_{yz} E_y \partial_y E_y dx dy \quad (2-22)[108]$$

where  $N = \frac{1}{2} \iint [\vec{E} \times \vec{H}^* + \vec{E}^* \times \vec{H}]_z dx dy$ ,  $\varepsilon_{yz} = 2\theta_F n_0 / k_0$

Whereas when the magnetization is along the y axis, only TM modes are affected and the corresponding phase shift is given by:

$$\delta\beta_{TM} = -\frac{\beta_{TM}}{\omega\varepsilon_0 N} \iint \frac{\varepsilon_{xz}}{n_0^4} H_y \partial_x H_y dx dy \quad (2-23)[108]$$

where  $N = \frac{1}{2} \iint [\vec{E} \times \vec{H}^* + \vec{E}^* \times \vec{H}]_z dx dy$ ,  $\varepsilon_{xz} = \frac{2\theta_F n_0}{k_0}$ ,  $n_0^2 = \varepsilon_{xx} = \varepsilon_{yy} = \varepsilon_{zz}$ .

Combining equations 2-22 and 2-23 with the fact that  $\Delta\beta = 2\delta\beta$ , and also exploiting equations 2-16 and 2-17, the lengths  $L_1$  and  $L_2$  needed for constructive or destructive interference ( $360^\circ$  or  $180^\circ$  phase difference) can be derived.

## 2.2 Magneto-optic Materials

Since the discovery of Magneto-Optics and of the various Magneto-optic Effects (Faraday Effect, Magneto-Optic Kerr Effect, Cotton-Mouton Effect, Zeeman Effect to list but a few) in the nineteenth century, various MO materials

have been researched and developed. Magneto-optics finds application most prominently for optical isolators and Magneto-optical memories, where the binary information is stored/erased in the magnetic domains taking advantage of MOKE and of the difference in magnetisation and coercivity below and above their Curie temperature. Generally, magneto-optical materials have been divided into three categories: (a) Magneto-optical storage materials; (b) Magneto-optical semiconductors; (c) Antiferromagnets[119].

Magneto-optical storage materials are used for magneto-optical recording. Initially, MnBi was the material of choice, given its large MOKE signal. Its polycrystalline structure, however, meant high media noise. Later, the amorphous RE-TM (rare earth - transition metal, RE = Tb, Gd and TM = Fe, Co) alloys replaced MnBi as magneto-optical memory materials due to their large MOKE signal together with extremely low media noise; examples of RE-TM alloys are TbFeCo films[119].

Magneto-optical semiconductors have been classified under three categories: (a) ‘magnetic insulators’; (b) semimagnetic semiconductors (SMS, or diluted magnetic semiconductors, DMS) and (c) ferromagnetic semiconductors. The denomination ‘magnetic insulators’ denotes ‘large gap magnetic semiconductors’, and it includes all magnetic ionic crystals that can be applied in optical isolators.

Among all the ‘magnetic insulators’, cubic garnets stand out for two reasons: their large Faraday rotation coefficient (and related Verdet constants), and their low loss in the infrared window[97][112][119][120]. Remaining magnetic insulating materials include magneto-optical glasses (oxides and fluorides such as FeF<sub>2</sub> and MnO, that contain large concentrations of ions like Ce<sup>3+</sup>, Pr<sup>3+</sup>, Eu<sup>2+</sup>, Tb<sup>3+</sup>, etc. [121]).

The semimagnetic semiconductors (SMS) are II-VI semiconductors where nearly half of the host semiconductor material has been substituted by transition ions of magnetic semiconductors. Usually they have strong field-induced magnetism and large Verdet constants, and MOKE rotation has been observed at UV wavelengths. Finally, a III-V ferromagnetic semiconductor, Ga<sub>1-x</sub>Mn<sub>x</sub>As, has attracted research attention for its picosecond spin dynamics of photoinduced spin polarisation, which can be employed in ultrafast magnetic devices [119]. For the antiferromagnets (oxides, fluorides and chlorides of the transition metals like NiO, FeF<sub>2</sub>, NiCl<sub>2</sub>, Fe<sub>1-x</sub>Zn<sub>x</sub>F<sub>2</sub>), magnetic linear birefringence (MLB) has found applications in spin electronics, magnetoelectric and multiferroic systems. Furthermore, MLB

is excellent in determining the specific heat  $c_m$  of optically transparent materials[119].

## 2.3 Magneto-optical Garnets

Rare earth iron garnets (REIG), an elemental unit of which has chemical formula  $\text{Re}_3\text{Fe}_5\text{O}_{12}$ , are typical and popular ferrimagnetic Faraday rotation materials for their transparency in the infrared window (from 1.5 to 5  $\mu\text{m}$ ) which is coupled with a high Faraday rotation coefficient [97][112][120][121]. The figure of merit (FOM) for garnet films is the ratio of Faraday rotation per unit attenuation, i.e. degrees/decibel (dB)[122]. The FOM of YIG was found to be 800 deg/dB with  $\theta_F$  of 240 deg/cm and  $\alpha$  of approximately 0.3 dB/cm at a wavelength of 1200 nm, with doped YIG yielding even higher FOM [97]. Other MO materials with large Faraday rotation coefficient also have high light absorption at the wavelengths of interest, e.g. ferromagnetic metals and alloys. Fe thin films and Fe-Ni permalloys have FOMs of less than 1 deg/dB[97] or they have much lower Faraday rotation coefficient[97][121].

REIG  $\text{Re}_3\text{Fe}_5\text{O}_{12}$  gets the name from natural garnet  $(\text{M}^{2+})_3(\text{M}^{3+})_2(\text{Si}^{4+})_3\text{O}_{12}$ , where  $\text{M}^{2+}$  can be Ca and  $\text{M}^{3+}$  can be Al, as they two share the same complex crystal structure. The rare earth ion  $\text{Re}^{3+}$  can be a non-magnetic ions (like  $\text{Y}^{3+}$ ) or a magnetic ion (like  $\text{Bi}^{3+}$ ,  $\text{Ce}^{3+}$ [120], and  $\text{Tb}^{3+}$  [123] ). Moreover, the  $\text{Fe}^{3+}$  ion can be partially substituted, which enables REIGs to accommodate elements from half of the periodic table. The key parameters used to characterise garnet films include optical absorption, temperature and wavelength dependence of Faraday rotation coefficient, refractive index, optical birefringence and lattice constants[120]. Different doping and substitutions will change the properties of the garnet film. By properly tailoring the composition of the garnet film, films with the desired properties can be grown by various techniques, like Liquid Phase Epitaxy (LPE), sputtering, chemical vapour deposition, sol gel and Pulsed laser deposition (PLD) [112]. The composition of the film can be changed to match the lattice constant of the garnet films to that of the substrate surfaces, in order to reduce strain.

### 2.3.1 Basics of Magneto-optic Garnets

The crystal structure of a garnet is a twisted form of the body centred cubic crystal structure, and results from the distortion of the dodecahedron cube [124] inside the structure frame. The chemical formula of garnets is  $3\text{Re}_2\text{O}_3 \cdot 5\text{Fe}_2\text{O}_3$ . There are 8 units of  $\text{Re}_3\text{Fe}_5\text{O}_{12}$  composing each unit cell. Re stands for the trivalent rare earth such as non-magnetic yttrium or a magnetic rare earth such as lanthanum through ytterbium [125]. All rare earth cations in garnets are trivalent, which means there will not be any divalent ion of iron in garnets, and all iron will be trivalent. There are in total 160 ions in each unit cell, arranged by 24  $\text{Fe}^{3+}$  taking the position of an octahedral site (a  $\text{Fe}^{3+}$  ion surrounded by six  $\text{O}^{2-}$  ions), 16  $\text{Fe}^{3+}$  taking the position of a tetrahedral site (with the  $\text{Fe}^{3+}$  ion surrounded by 4  $\text{O}^{2-}$  ions), 24  $\text{Re}^{3+}$  taking the position of a 12-sided polyhedral-dodecahedral site (with  $\text{Fe}^{3+}$  surrounded by 8  $\text{O}^{2-}$ ), and finally 96  $\text{O}^{2-}$ .

Figure 2-6 displays two possible presentations of a unit cell [30]. The top right section of the figure shows the location of all cation ions within the cubic structure, while the bottom left highlights their connections with the  $\text{O}^{2-}$  ions. The lattice constant of the garnet unit is 12-13 Å, while that of Si is approximately 5 Å, meaning there is a strong mismatch between the two materials. Post-deposition rapid thermal annealing (RTA) is thus needed in order to achieve crystallisation whilst overcoming lattice mismatch.

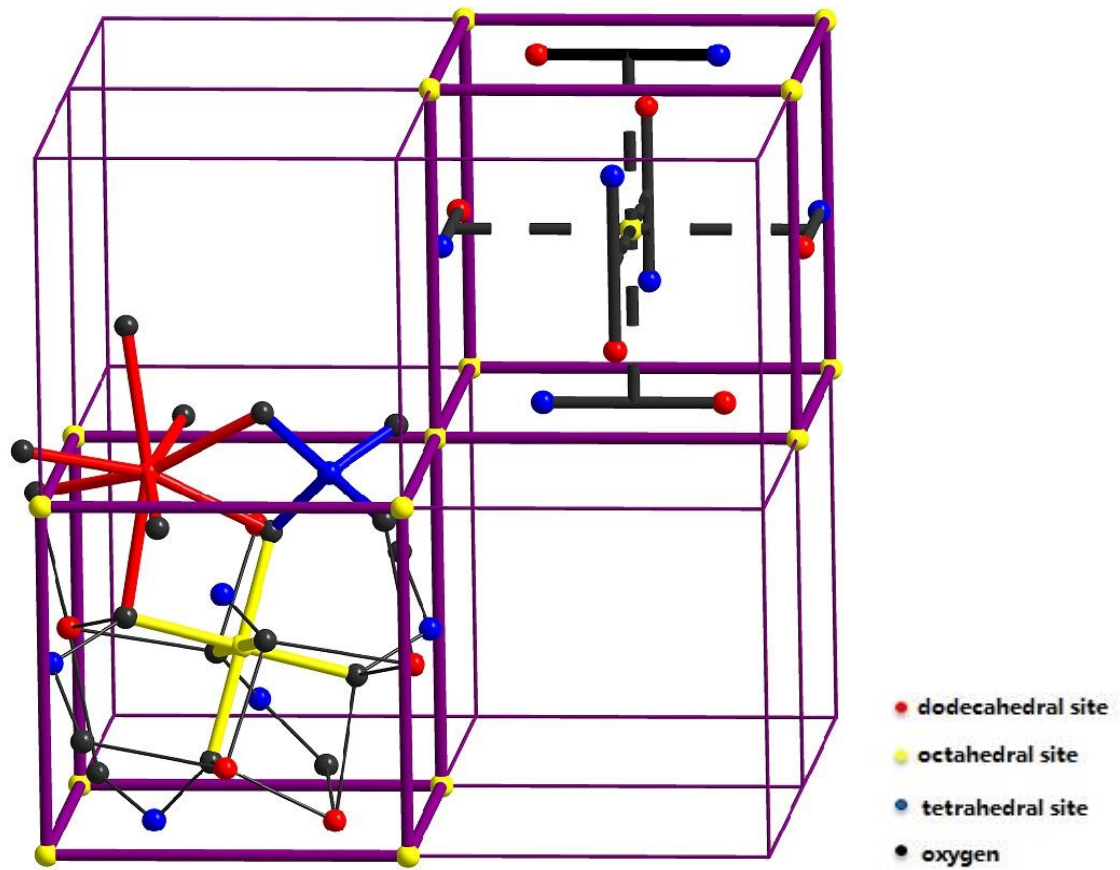


Figure 2-6. Two possible presentations of a unit cell, showing both the location of all the cations within the cubic structure (top right), and their bonds with O<sup>2-</sup> ions (bottom left).

The octahedral sites Fe<sup>3+</sup> and the tetrahedral sites Fe<sup>3+</sup> have an anti-parallel magnetic coupling, with a net magnetic moment of one Fe<sup>3+</sup> ion from octahedral sites. The direction of the dodecahedral site Re<sup>3+</sup> can be either way, depending on the specific ion. So the net magnetisation  $M_s(T)$  of the garnet can be given by[120]:

$$M_s(T) = |M_d(T) - M_a(T) \pm M_c(T)| \quad (2-24)$$

Where  $M_d(T)$ ,  $M_a(T)$ , and  $M_c(T)$  are the temperature-dependent sub-lattice magnetisations of the tetrahedral, octahedral and dodecahedral sub-lattices, respectively.

Conventionally, the magnetisation of the material is thought of as being only positive, so the absolute value is used. The saturated magnetisation of the material is  $4\pi M_s$  (Gauss). A particular temperature called Compensation Point ( $T_c$ ) exists, for which the sum of the sub-lattice magnetisations is zero. The reason is the temperature dependency of the sub-lattice magnetisations of the three sites,

together with the fact that under the same applied field the sub-lattice magnetisation switches direction below and above the compensation point.

However, the net magnetisation/saturation magnetisation remains in the same direction as that of the external magnetic field while the Faraday rotation changes sign below and above the compensation point. The process of how the sub-lattice magnetisation switches direction below and above the compensation temperature is shown in Figure 2-7.

The Faraday rotation coefficient  $\theta_F(T, \lambda)$  can be calculated by [120]:

$$\theta_F(T, \lambda) = C(\lambda)M_c(T) + A(\lambda)M_a(T) + D(\lambda)M_d(T) \quad (2-25)$$

$\theta_F(T, \lambda)$  is the sum of the Faraday rotation coefficient of each site and is a function of wavelength and temperature, while it can be clearly seen that it is independent of the size of the magnetic field. Attention needs to be paid to the fact that the compensation point represents the temperature at which the Faraday rotation changes its sign from negative to positive (for increasing temperature), but it does not mean that the Faraday rotation will be zero (only the magnetisation will be) [30].

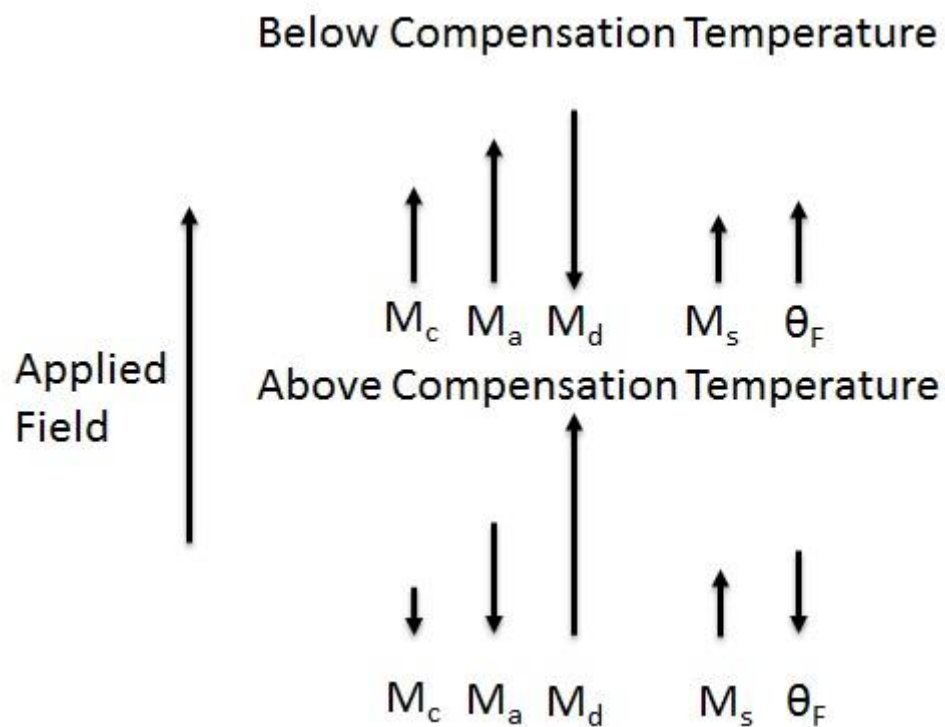


**Figure 2-7. Schematic illustrating the change of direction in the sub-lattice magnetisation below and above compensation temperature.**

### 2.3.2 Radio Frequency Sputtering Deposition

Various techniques, including Liquid Phase Epitaxy (LPE), sputtering, chemical vapour deposition, sol gel, and Pulsed laser deposition (PLD) [112] can be used to grow garnet films. Traditionally, garnet films are grown on lattice-matched GGG (Gadolinium gallium garnet,  $\text{Gd}_3\text{Ga}_5\text{O}_{12}$ ) substrate by the LPE method. This process requires the use of lead (Pb) which then ends up in the film as an impurity and leads to an increase in the optical absorption of the film [126].

In this project, our collaborators, Prof. Bethanie Stadler's group from University of Minnesota, adopted a Pb-free RF (radio-frequency) multi-target sputtering method to prepare garnet thin films of various compositions on a semiconductor platform [127]. As targets made of different materials can be used for deposition of different garnet films while the sputtering condition is kept constant, RF sputtering has an improved deposition rate and offers accurate control of the stoichiometry of the film, thus helping to produce garnet thin films of very good quality.

After extensive research, our collaborators have succeeded in producing different substitutions of high quality garnet films with large Faraday rotation coefficients. All the MO films used in this project were provided by the University of Minnesota, that deposited the films and carried out initial characterisation. The garnets used for this work include Ce-YIG (Cerium Yttrium Iron Garnet,  $n=2.22$  at 1550 nm) films on YIG (Yttrium Iron Garnet,  $+200^\circ/\text{cm}$  at room temperature,  $n=2.1$  at 1550 nm [127]) seedlayers showing a Faraday rotation of  $-3700^\circ/\text{cm}$ , Bi-YIG (Bismuth Yttrium Iron Garnet) films [128] on YIG (Yttrium Iron Garnet) seedlayers showing a Faraday rotation of  $-1700^\circ/\text{cm}$ , Ce-YIG (Cerium Yttrium Iron Garnet) films on MgO (Magnesium oxide) buffer layer [129], Ce-TIG (Cerium Terbium Iron Garnet,  $n=2.3$  at 1550 nm) film with  $-2600^\circ/\text{cm}$ , TIG (Terbium Iron Garnet,  $n=2.3$  at 1550 nm) films with  $+500^\circ/\text{cm}$  and Bi-TIG (Bismuth Terbium Iron Garnet,  $n=2.3$  at 1550 nm) with  $-500^\circ/\text{cm}$  [123].

The sputtering deposition of TIG (Terbium Iron Garnet) film will be used as an example to explain the deposition process, but obviously the numerical quantities will vary depending on the specific garnet material and composition.

The garnets were deposited in Minnesota on pre-masked samples prepared in Glasgow JWNC, using RF sputtering with an argon plasma and 20.4 sccm Ar flow. The Fe target was sputtered at 220 w of RF power and the Y and Tb (or Re) targets were sputtered at 120 w. A 2.0 standard cubic centimeters (sccm) oxygen flow was also performed during deposition, and the chamber pressure was kept at 6.0 mTorr. During the process, the  $\text{Ar}^+$  ions bombard the Fe/Re targets ejecting  $\text{Fe}^{3+}/\text{Re}^{3+}$  from the targets, with the ejected ions then travelling to the sample substrate, building up a thin film. The structure of the deposition chamber and the process is shown in Figure 2-7.

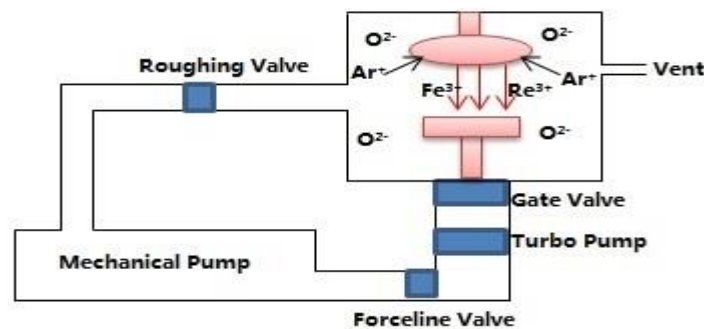


Figure 2-8. Schematic showing the structure of the deposition chamber and the deposition process.

### 2.3.3 Characterisation of the garnet thin film

All deposition, sputtering optimisation, and characterisation of the garnet film itself were carried out by our collaborators, Professor Bethanie Stadler's group from University of Minnesota, so all the deposition parameters and characterisation results discussed in this chapter have been gently provided by them. The properties of the iron garnet film that matter for the application sought are the chemical stoichiometry, crystallinity, refractive index, magnetic properties (e.g. saturation magnetisation and saturation magnetic field), and the Faraday rotation coefficient. Targeted measurement methods were adopted for each individual property[38].

The chemical stoichiometry is related to optical absorption and crystallinity. A lack of stoichiometry in the garnet is the main cause of optical

absorption within the 1310 nm and 1550 nm telecommunication bands[120]. The correct stoichiometry should have  $\text{Fe}^{3+}$  in the garnet, while  $\text{Fe}^{4+}$  and  $\text{Fe}^{2+}$  ions cause strong absorption in both the visible and the infrared wavelength range. Also, only garnets films with the right stoichiometry can exhibit perfect crystallinity, and this in turn explains why amorphous non-crystallised garnet films have larger optical propagation losses than crystallised films.

A scanning electron microscope (SEM) equipped with energy dispersive X-ray spectroscopy analysis is normally used to obtain the chemical composition of the garnet films, while information on crystal structure and crystallinity are obtained through standard  $\theta$ - $2\theta$  X-ray diffraction (XRD) methods. XRD, however, lacks the spatial resolution needed for accurate analysis of the morphology of the film, and also it requires the film under test to be densely packed with a smooth flat surface. Moreover, the size of garnet film also needs to be in the order of few hundred of microns, as the smallest beam spot size of a standard commercially available XRD tool is 100  $\mu\text{m}$ .

The XRD method is therefore mainly used on wafer-scale specimens with smooth surface. Our collaborators use XRD during a trial sputtering run on an unpatterned wafer, to check the crystallinity of the thin film deposited before the actual deposition on a patterned sample. XRD can also be used on samples with dense patterns: the data will in this case be provided by the so-called polycrystalline powder diffraction, rather than by single-crystal diffraction.

Another measuring method is the Electron Backscattered Diffraction (EBSD) system, which can be added as an accessory in a SEM and has a lateral spatial resolution from 0.1 to 0.01  $\mu\text{m}$ , which is two orders of magnitude higher than that of the XRD methods[130]. EBSD methods are used for smaller patterns and precise phase examination, such as crystal orientation, crystallinity percentage, and phase boundary.

In order to get the refractive index at a wavelength of 1550 nm (relevant to our application) a visible/near infrared spectrometer is used to measure the optical transmission spectra of the film. Magnetic properties, like saturation magnetisation and saturation magnetic field, are measured using a vibrating sample magnetometer (VSM) and the Faraday rotation coefficient is obtained using a dedicated measurement rig which detects a net signal difference resulting from the Faraday rotation in presence of a magnetic field.

In this work an SEM equipped with different detector systems is used to analyse both chemical composition and crystallography. Based on the differences in interaction depth between the electron beam and the specimen, and on the energy carried by the excited signal, the detected elements usually employed in the analysis are: Auger electrons, Secondary electrons (SE), Backscattered electrons (BSE), Characteristic x-rays and X-ray continuum (see Figure 2-9)[131].

Auger electrons usually occur at a few nm depth, SEs usually occur at 1-10nm depth, while BSEs occur at 10 nm-1000 nm depth[132]. Auger electrons, SEs and BSEs all result from elastic scattering, where there is only a change in trajectory between the scattered electron and the incident electron, with nearly no energy loss. Characteristic X-rays and X-ray continuum instead derives from inelastic interactions with energy transfer taking place from the incident electrons to the atoms of the sample.

Therefore, the electrons emitted from just beneath the surface can be used to get the topography of the surface, while the electrons excited from deeper, and carrying a characteristic energy of the atoms of the film, can be used for chemical composition analysis. In our application, SEs and BSEs can be used for normal SEM imaging; BSEs can be used together with the EBSD system for crystallographic analysis, and Characteristic X-ray can be used in energy dispersive X-ray diffraction (EDX) analysis to provide the chemical composition information.

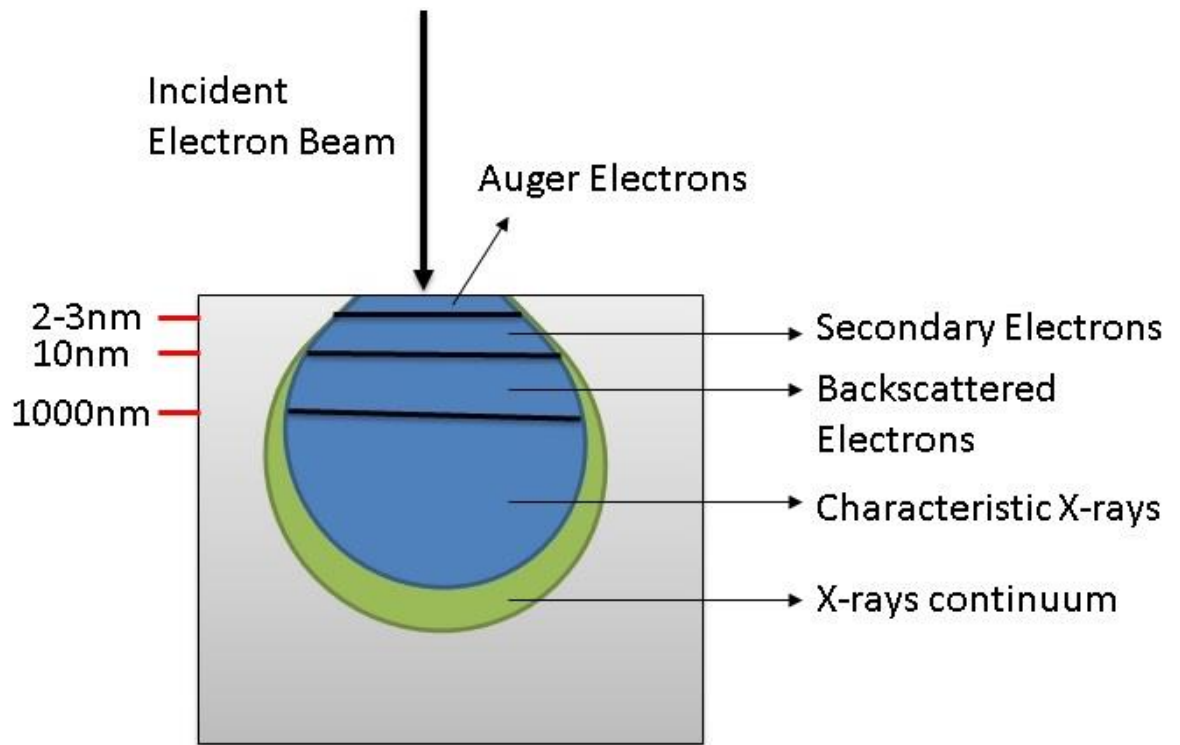


**Figure 2-9.** Describes that in the SEM chamber different forms of signals are emitted based on the differences in interaction depth between the electron beam and the specimen and the energy the excited signal carries.

### 2.3.3.1 Crystallographic analysis - XRD and EBSD

Through XRD ( $\theta$ - $2\theta$  X-ray diffraction) and EBSD (Electron Backscattered Diffraction), the two important crystallographic research tools, one can identify the atomic/molecular structure, the mean positions of the atoms and their chemical bonds, their disorder, crystallography, crystallographic orientation, crystal systems, orientation mapping, defect studies, phase identification, and grain boundary. In this work, only the crystallinity and the crystalline percentage of the garnet film are the properties of primary concern. Nowadays, all commercial XRD and EBSD tools are highly automated, so that they can collect the information from the specimen and automatically analyse the collected data by comparing them with a database to work out all the crystallographic information about the specimen.

Both methods are based on Bragg's diffraction law (see Figure 2-10), stating that the difference between the distances travelled by two beams that interfere constructively is an integer multiple of the wavelength:

$$2d \sin \theta = n\lambda \quad (2-26)$$

where a beam of X-ray radiation (in the XRD case) or electrons (in the EBSD case) is incident on a periodic crystal structure and the emitted signals satisfy the Bragg condition to produce a constructive interference. At last, the total effect of all constructive interferences will contribute to the XRD spectra, that will have peaks of different intensities in preferred lattice planes.

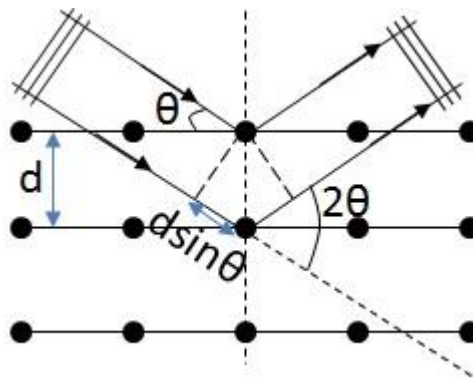
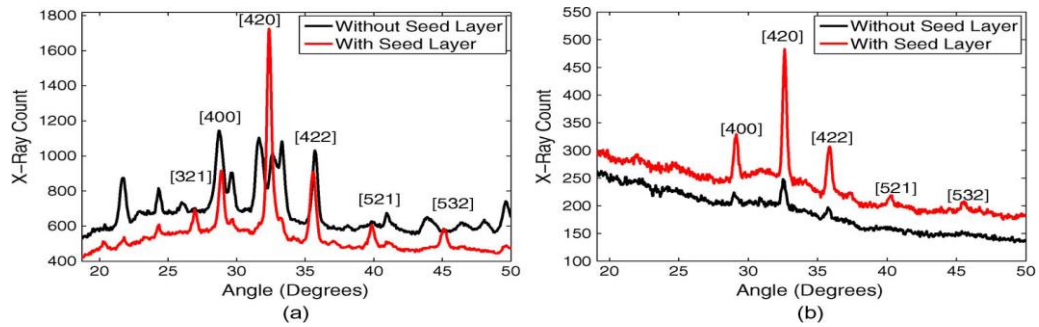


Figure 2-10. Illustration of Bragg's condition, where the difference between the distances travelled by two beams that interfere constructively is an integer multiple of the wavelength,  $2d \sin \theta = n\lambda$ .

As previously discussed, there are limitations to the spatial resolution of XRD, and XRD is used in research for garnet thin films deposited on a whole wafer. Since XRD is a relatively simple-operation tool, it's useful to quickly check the crystallinity of the garnet thin film during the sputtering optimisation and development process. The XRD spectra of Bi:YIG and Ce:YIG layers grown with or without a seed layer is shown in Figure 2-11 (a) and (b), respectively[128]. The figures show the polycrystalline garnet crystal phase having three major peaks at orientations (400), (420), (422) and two minor peaks oriented in plane (521) and (532), agreeing with the XRD spectrum of garnet in database.



**Figure 2-11. XRD spectra of: (a) Bi:YIG layers grown with or without seed layer; (b) Ce:YIG layers grown with or without seed layer[35].**

As the garnet film on top of the samples used in this work is patterned in  $\mu\text{m}$ -scale segments and is also polycrystalline, XRD is less useful. As such, EBSD (Electron Backscattered Diffraction) with its much higher resolution is used to check the crystallographic orientation and also the crystal orientation mapping, necessary to work out the crystalline percentage. Differently from standard SEM imaging where the incident beam is perpendicular to the surface of the specimen, the stage carrying the specimen is tilted by approximately  $70^\circ$ [132], so that the angle between the incident electron beam and the surface of the specimen is approximately  $20^\circ$  in order to increase the intensity of the backscattered electron signal (see Figure 2-11)[133][134]. When the specimen is tilted, the incident beam approaches the surface at a small angle, increasing the chance of electrons escaping from the surface and thus maximising the intensity of the EBSD pattern, which is depicted in Figure 2-12[134].

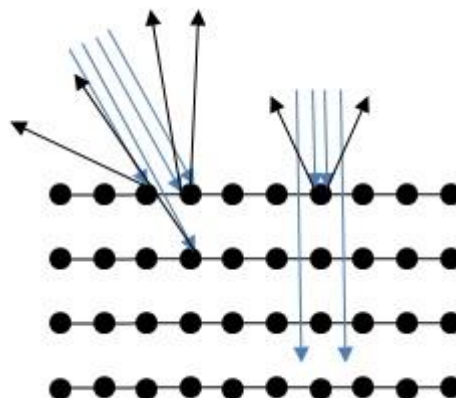


**Figure 2-12. Schematic showing how the chance of electrons escaping from the surface increases by tilting the specimen.**

The biggest characteristic of the EBSD pattern is the Kikuchi bands. When the electron beam enters the tilted specimen, it is first diffused underneath the surface and then inelastically scattered in all directions, including the ones satisfying Bragg's condition which can escape the surface. As the diffraction is in all directions, the electrons that satisfy Bragg's condition are emitted out of the surface at the Bragg angle  $\theta_B$  in all directions, which makes the locus of the diffracted trace the surface of a cone with its normal to the reflecting atomic planes with half-apex angle as  $90 - \theta_B$ . A typical Bragg angle of approximately  $0.5^\circ$ [133] is obtained by substituting typical values of electron wavelength and lattice inter-planar spacing in Bragg's law equation, which makes the cone almost flat. The diffraction occurs at both the front and the back of the atomic planes, so that two cones are observed from each atomic plane. When the two cones extend to intercept the phosphor screen of the EBSD detector, a pair of nearly straight lines with an angular width of  $2\theta_B$  is imaged, called Kikuchi lines or bands.

Knowing the angular width of the Kikuchi lines, the inter-planar spacing can be calculated. Each lattice plane has a pair of corresponding Kikuchi lines with specific orientation and angular width imaged on the screen. Some of the Kikuchi bands intersect, where the intersection corresponds to a zone axis of the garnet structure. Thus, the EBSD Kikuchi pattern reflects both the inter-planar and inter-zonal information. When an EBSD Kikuchi pattern is gained from the specimen, an automated indexing is performed by the software and the specific material and structure can be identified by comparing the collected EBSD pattern with thousands in the database.

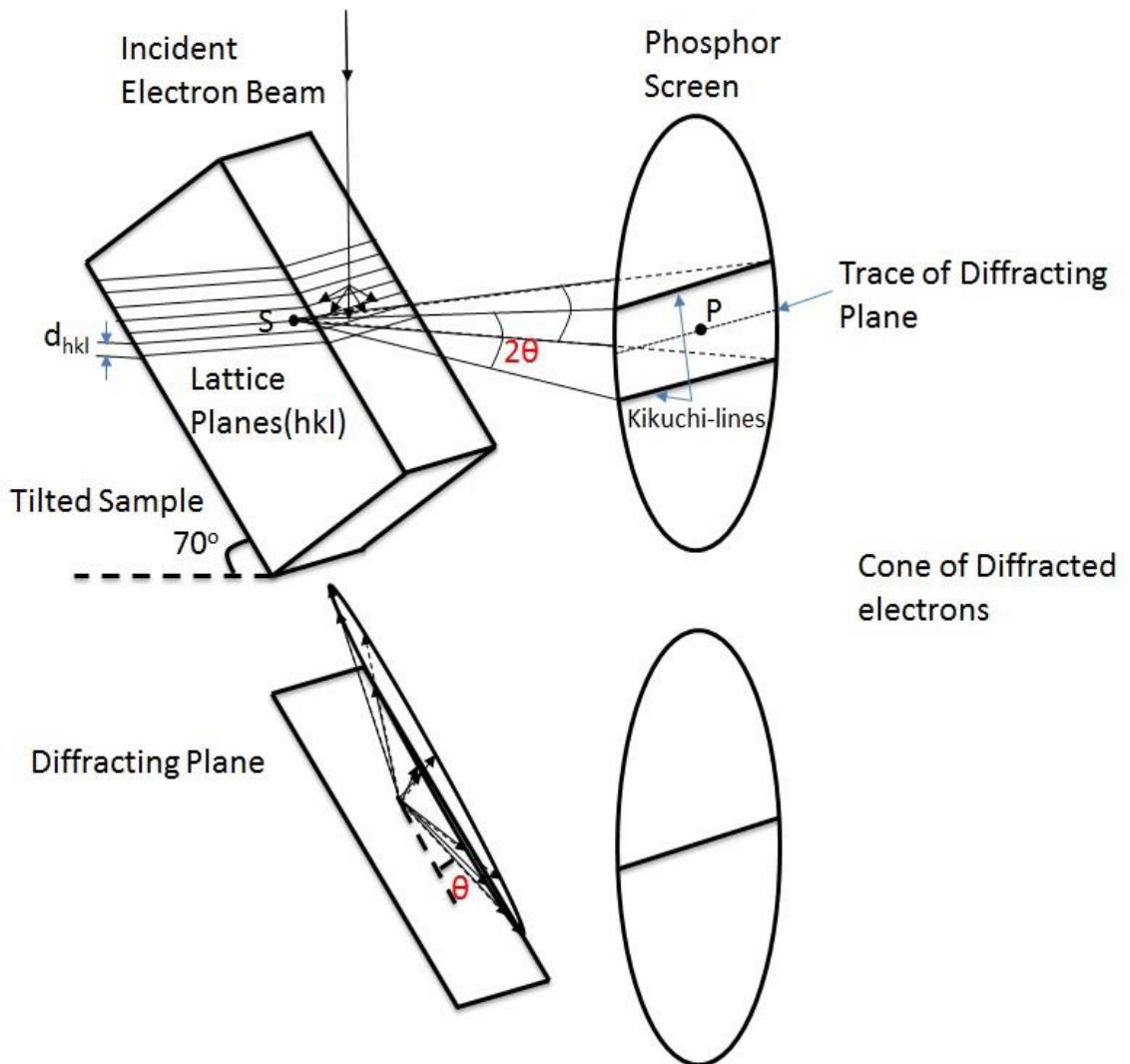
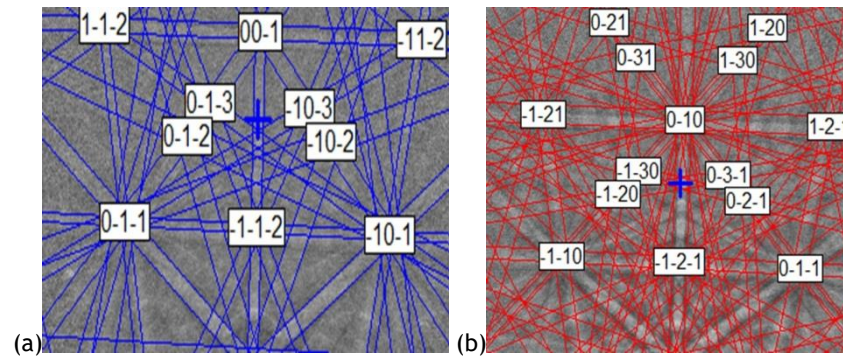


Figure 2-13. Illustration of the EBSD Kikuchi pattern formation.

Figure 2-13 shows the indexed and matched EBSD Kikuchi pattern of Ce-YIG on 5 nm MgO annealed at 750 DegC in 120 mBar O<sub>2</sub> atmosphere. Figure 2-13(a) shows a good match with the EBSD pattern of garnet saved in the database, while Figure 2-13(b) shows the EBSD pattern from silicon. Also by carrying out a crystallography mapping, the garnet turns out to be partially crystallised.



**Figure 2-14. EBSD patterns of: (a) garnet, with the blue lines outlining the crystalline structure which agrees with that in the database; (b) Si, with the red lines outlining the crystalline structure which agrees with that in the database**

### 2.3.3.2 Hysteresis Curve and Faraday rotation Coefficient Measurement

The magnetic properties of the garnet film are measured using the traditional Vibrating Sample Magnetometre (VSM), where the sample is placed inside a strong uniform magnetic field and vibrated up and down and the magnetic moment of the garnet film is measured using “pick-up” coils placed above the vibrating sample and orientated perpendicular to the applied field. The field from the sample is then detected and converted to an electrical signal to be collected in a lock-in amplifier and then analysed and converted back to corresponding magnetic expressions. By varying the magnitude and direction of applied magnetic field, a characteristic hysteresis curve of the material can be obtained.

Figure 2-14 shows the VSM hysteresis curves (normalised) of Ce-TIG [123], where the saturation magnetisation ( $m_s$ ), remnant magnetisation ( $m_{rs}$ ), coercivity ( $h_c$ ), and magnetic field needed to saturate the film ( $h_s$ ) are visibly presented. Here, coercivity ( $h_c$ ) is the intensity of the magnetic field required to reduce the magnetization of that material to zero after the magnetic saturation of the sample. Therefore, when the sample needs to be magnetized in the opposite direction, the magnetic field needs to be larger than  $h_c$ . In our optical characterisation process, samples are saturated in opposite directions and measured separately. In order to get the sample with Ce-TIG on top, the magnetic field needs to be larger than  $h_s$ , around 3000 Oe. Here we use a permanent magnet, which can provide around 1200 Oe, to magnetize the sample. After being magnetized in one direction, the sample is taken away from the permanent

magnet for measurement, so that remnant magnetization ( $m_{rs}$ ) is used in the measurement process.

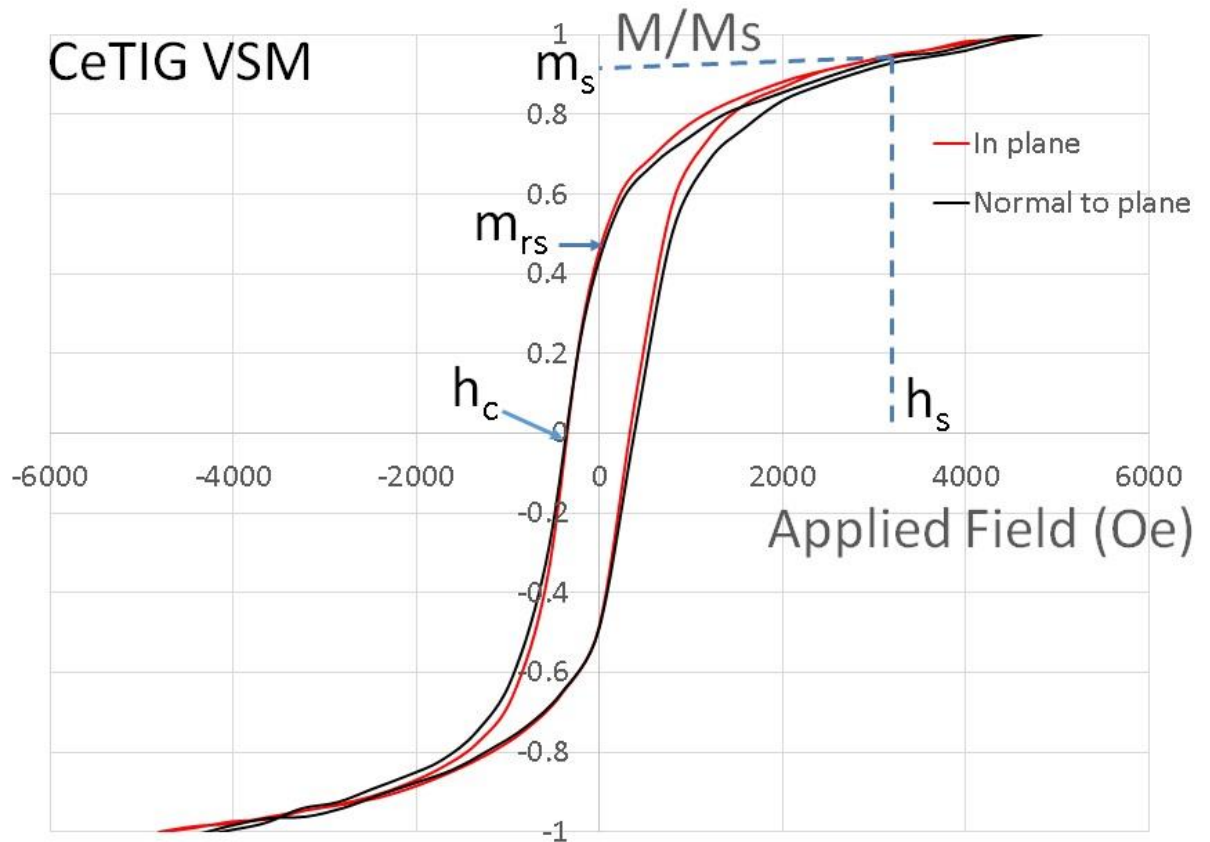


**Figure 2-15. VSM hysteresis curve of Ce-TIG. A 1.5k Oe-2k Oe magnetic field is needed to saturate all these garnets.**

The Faraday rotation coefficient is measured by using the measurement rig shown in Figure 2-15 [38]. First, a linearly polarized and collimated beam from the laser source passes through a halfwave plate, rotating at  $45^\circ$ , where the amplitude of the TE and TM modes (conventionally, p and s orthogonally polarised beams in free space) are the same, and the beam is then modulated to reference frequency by the chopper. Then, it passes through the sample and is split into TE and TM modes using a polarizing beamsplitter. A pair of magnets are set at the sides of the sample where an external magnetic field parallel to the light propagation direction can be applied. When there is no magnetic field, no Faraday rotation occurs when light passes through the unmagnetised sample, and there is no difference in the signal strength between the TE and TM modes, unless there is remnant magnetisation present. Therefore, a net signal difference resulting

from the Faraday rotation is detected when the sample is in the presence of a magnetic field, from which the Faraday rotation can be calculated.

The Faraday rotation coefficient of the material adopted in this project, measured at a working wavelength of 1550 nm at room temperature, is YIG (200 deg/cm,  $n=2.1$  [127]), Bi-TIG (-500 deg/cm,  $n=2.3$  [123]), TIG (500 deg/cm,  $n=2.3$  [123]), Ce-YIG on YIG (-3700 deg/cm,  $n=2.22$  [128]), Ce-TIG (-2600 deg/cm,  $n=2.3$  [123]).

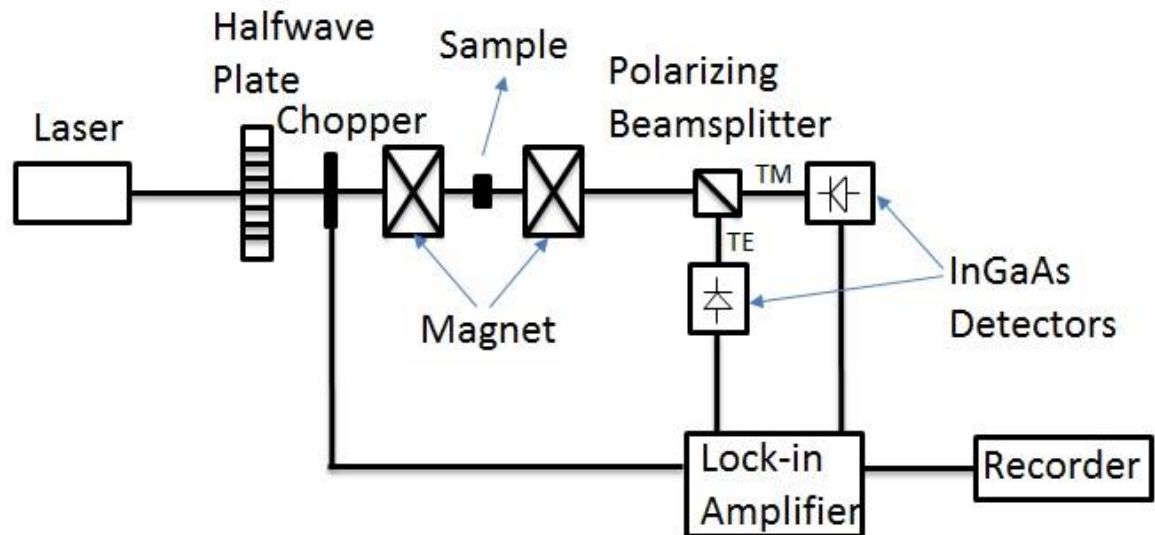


Figure 2-16. Faraday rotation coefficient measurement rig.

## 3 Chapter 3—Simulation and Design of Nonreciprocal Polarisation Mode Converter

### 3.1 Introduction

In order to avoid the mis-match in thermal expansion between the MO (magneto-optical garnet ( $10.4 \text{ ppm}/^\circ\text{C}$ , ppm means parts-per-million,  $10^{-6}$ ) and Si ( $2.33 \text{ ppm}/^\circ\text{C}$ ) [135] substrate during the annealing process that is necessary to crystalize garnet, small micron-scale widths of garnet island segments are used [136]. For garnet-segmented cladding on Si waveguides, there are two ways leading to it: one is to deposit whole garnet layers on Si and then getting it re-masked by spinning HSQ, PMMA, or photoresist and patterned through e-beam lithography or photolithography, and then to use phosphoric acid to etch down to get garnet islands. The other is to use the lift-off process to get the garnet islands mask, and then deposit garnet on the sample; after lift-off, no etch process is needed, and we can get garnet islands.

Dr. Barry Holmes initially tried the first method on III-V (GaAs) (however, the GaAs etched quicker than the garnet), and Sang-Yeob Sung et al. [135] tried wet etching on a Si substrate, which led to non-vertical sidewalls and rough edges. Therefore, Dr. Holmes pioneered the second method on III-V wafers - the lift-off process - which was adopted here to obtain garnet segments on SOI [89].

Simulation of both the NR-PMC part and R-PMC part is run in MATLAB<sup>®</sup>. The simulation of the NR-PMC section is conducted in WGMODES<sup>®</sup>, which is a MATLAB<sup>®</sup>-based full-vector finite difference discretization mode-solver package, and is used to calculate the electromagnetic modes of optical waveguides with transverse, non-diagonal, anisotropy based on transverse magnetic field components developed by Thomas E. Murphy from the University of Maryland [137]. Meanwhile, the simulation of the R-PMC part was also carried out in a MATLAB<sup>®</sup> program.

The incorporation of the xy off-diagonal elements in the permittivity tensor allows us to model the magneto-optical Faraday effect when applying a longitudinal magnetic field. Magneto-optical Faraday Rotation in MO cladding

modifies the guided modes in waveguides that are related to the off-diagonal elements of the permittivity tensor, which was discussed in detail in Chapter 2, and results in a significant Stokes parameter  $S_3$  component. The bigger the Faraday coefficient, the bigger the absolute value of the  $S_3$  Stokes parameter, the shorter the device required for the same rotation degree [138].

### 3.1.1 Stokes Parameters and Poincare Sphere

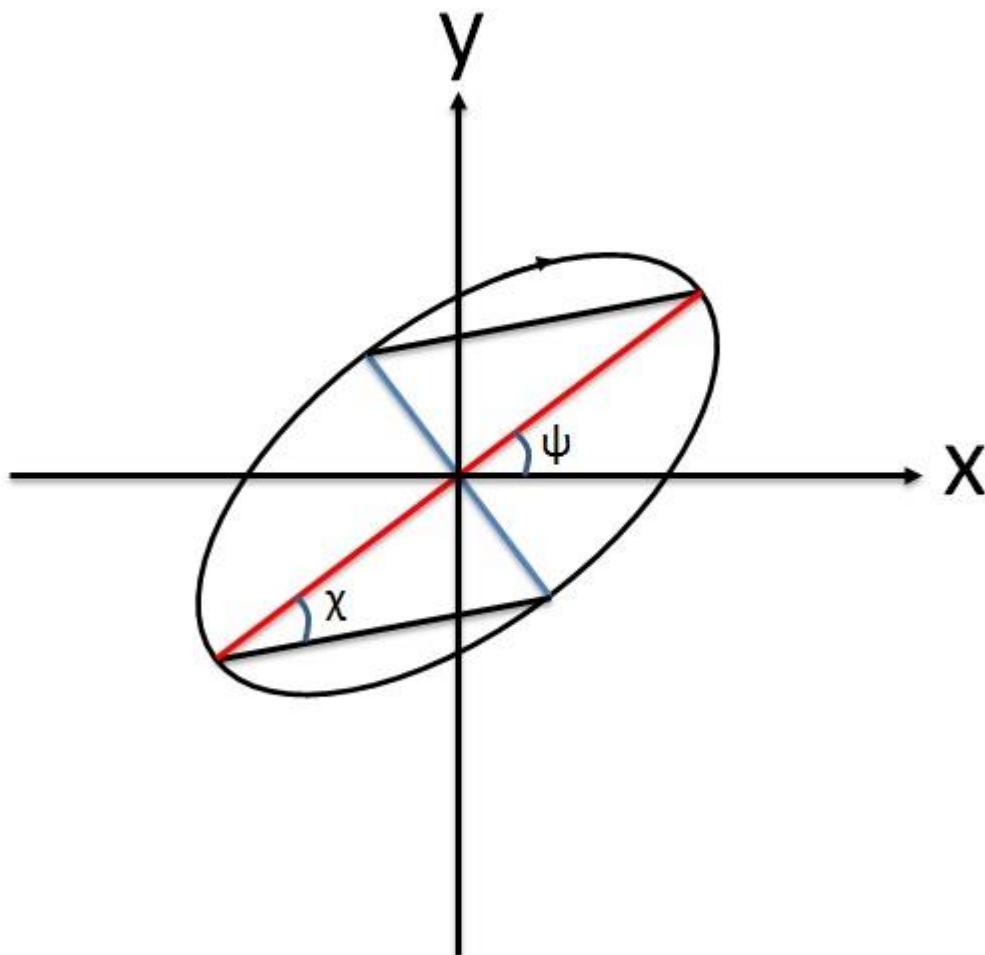


Figure 3-1. The rotation degree/azimuth ( $\psi$ ) and the ellipticity angle ( $\chi$ ) of a normal elliptically polarized lightwave in an x-y coordinate system.

Stokes parameters ( $S_0, S_1, S_2, S_3$ ) [139]-[141] are a set of values used to describe the polarization state of electromagnetic waves. They can reflect the

total intensity ( $I$ ), the rotation degree/azimuth ( $\psi$ ), and the ellipticity angle ( $\chi$ ) of a normal elliptically polarized lightwave, as seen in Figure 3-1. The relationship of the four Stokes parameters is shown in the equations below:

$$S_0 = I \quad (3-1)$$

$$S_1 = Ip \cos 2\psi \cos 2\chi \quad (3-2)$$

$$S_2 = Ip \sin 2\psi \cos 2\chi \quad (3-3)$$

$$S_3 = Ip \sin 2\chi \quad (3-4)$$

$S_0$  describes the total intensity of the optical beam, which is usually normalized as unit 1. As shown in Figure 3-2,  $S_1$  describes the preponderance of LHP (linearly horizontal polarized) light, of which the Stokes parameters are (1, 0, 0) over LVP (linearly vertical polarized) light, of which the Stokes parameters are (-1, 0, 0).  $S_2$  describes the preponderance of L+45°P (+45° linearly polarized) light, of which the Stokes parameters are (0,1,0) over L-45°P (-45° linearly polarized) light, of which the Stokes parameters are (0, -1, 0).  $S_3$  describes the preponderance of RCP (right circularly polarized) light, of which the Stokes parameters are (0, 0, 1) over LCP (left circularly polarized) light, of which the Stokes parameters are (0, 0, -1). Thus, the  $S_3$  parameter is an indication of the gyromagnetic effect. The Faraday rotation effect is a kind of gyromagnetic effect. The absolute value of the  $S_3$  parameter is used in the simulation in this chapter as an indication of the magnitude of magneto-optical Faraday rotation. The bigger the Faraday coefficient of the magneto-optical garnet material, the bigger the absolute value of the  $S_3$  Stokes parameter, the shorter the device required for the same rotation degree [138].

The Poincaré sphere [142] (Figure 3-2) is a sphere used to visualise ( $S_1, S_2, S_3$ ). Then, for polarised light with a given power  $I$ , there is:

$$I = S_0 \quad (3-5)$$

$$p = \frac{\sqrt{S_1^2 + S_2^2 + S_3^2}}{S_0} \quad (3-6)$$

$$2\psi = \tan^{-1} \frac{S_2}{S_1} \quad (0 \leq \psi \leq \pi) \quad (3-7)$$

$$2\chi = \tan^{-1} \frac{S_3}{\sqrt{S_1^2 + S_2^2}} \quad \left(-\frac{\pi}{4} \leq \chi \leq \frac{\pi}{4}\right) \quad (3-8)$$

Where  $p$  denotes the degree of polarisation of the lightwave.

Each point on the Poincaré sphere represents a specific polarisation state. Points on the equator stand for all orientations of linearly-polarized light; the north and south poles stand for right and left circular polarization, respectively. All other points on the sphere represent elliptically polarised states, with ellipticity increasing with the distance from the equator. Two diametrically opposite points on the Poincare sphere represent two orthogonal modes, such as the TE mode and TM, shown in Figure 3-2, with the axis through them corresponding to the optic axis [138]. The Stokes vector angle of the two orthogonal modes is  $\pi$ . The Stokes Vector  $(S_1, S_2, S_3)$  angle between opposite directions of magnetization is used to indicate the magnitude of Faraday rotation of the device in the optical characterisation process, detailed in Chapter 5. An angle of  $\pi$  indicates that the two modes are orthogonal to each other while magnetized in opposite directions, and total isolation can be achieved combined with appropriate waveplate and polarisers.

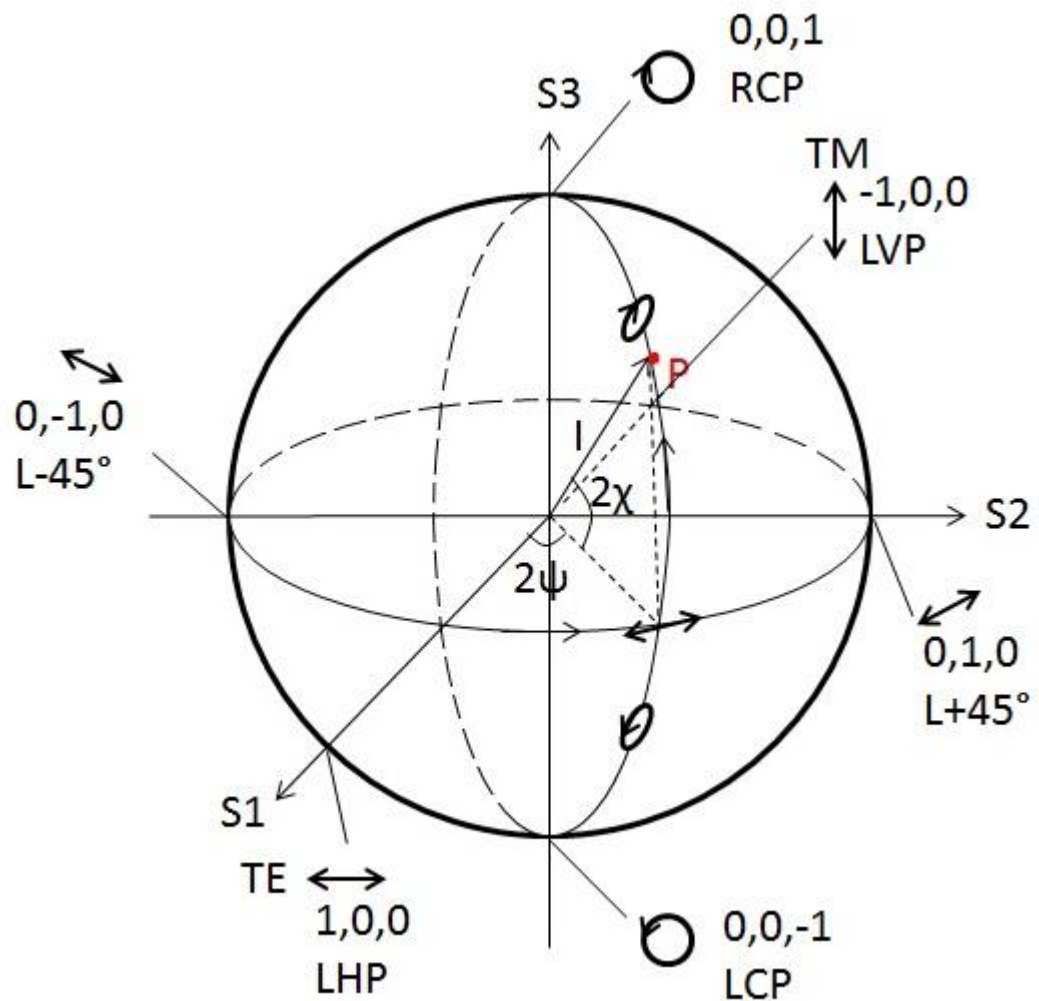


Figure 3-2. The Poincaré sphere is a sphere used to visualise  $(S_1, S_2, S_3)$ . Points on the equator stand for all orientations of linearly polarized light; the north and south poles stand for right and left circular polarization, respectively. All other points on the sphere represent elliptically polarised states, with ellipticity increasing with the distance from the equator.

As an excellent way to visualize the polarised light, and also to describe the trace of the change of the polarisation of the light, the Poincaré sphere has been widely used [138][143][144] to show the changes in the state of polarised light.

### 3.1.2 Simulation Methods

In order to compute the electromagnetic modes of waveguides, finite element methods, mode-matching techniques, the Eigen-mode expansion (EME) method, mode-solving techniques, the beam propagation method (BPM), the

method of lines, the finite-difference time domain (FDTD) method, and finite difference methods are commonly used [145]. Among them, the Eigen-mode expansion method/mode-solving techniques, the beam propagation method, and the finite-difference time domain method are the most popularly integrated and commercialized in software like Rsoft™ BeamPROP™ (BPM), FullWAVE™ (FDTD), ModePROP™ (EME), Lumerical® FDTD, and Lumerical® ModeSolutions (EME, FDTD).

Since the beam propagation method relies on the slowly varying envelope approximation, it is not accurate for devices with high refractive-index contrast, like silicon photonics (Si:3.48, SiO<sub>2</sub>:1.44 at  $\lambda=1550$  nm) [146]. To use FDTD, however, the entire computational domain must be gridded sufficiently, and very large computational domains can be developed, requiring large PC storage and extremely long computational hours [145]. For other methods, they either ignore the material's anisotropy, or they require the off-diagonal elements to be very small compared to the diagonal elements.

WGMODES® is a full-vector finite difference discretization mode-solver package based in MATLAB®, and is used to calculate the electromagnetic modes of optical waveguides with transverse, non-diagonal, anisotropy based on the transverse magnetic field components developed by Thomas E. Murphy from the University of Maryland [137].

Here, in our case, in order to calculate the basic modes properties (modes guiding, effective refractive index, half-beat length), as well as incorporate the off-diagonal elements in the permittivity tensor to model the Faraday effect in the longitudinal approach in an asymmetric magneto-optical waveguide, the WGMODES® package [137] run in MATLAB® turns out to be the simplest and quickest method. Each simulation only takes around 1-2 minutes, even on a computer with an Intel® core™ i3 processor.

Through simulation, the range of the half-beat lengths and the optimum width of the waveguides were obtained. Based upon the results from the simulation, a lift-off mask for e-beam lithography was designed and optimised. Here, all simulations were done at a wavelength of 1550 nm, at which the fibres have the lowest attenuation over all wavelengths, so the device we designed is also intended to work at 1550 nm.

### 3.2 Faraday Rotation Effect Simulation

A software package called WGMODES<sup>®</sup>, written as MATLAB<sup>®</sup> scripts by the University of Maryland run in MATLAB<sup>®</sup>, was utilized for the simulation to get the optimum range of the half-beat length, the width of the waveguides, and also the effect of different thicknesses of seed/buffer layers on  $S_3$  Stokes parameters (the Faraday rotation effect). In order to mitigate the asymmetry in the waveguide (where any slight misalignment of the garnet islands creates an anisotropic waveguide cross section - leading to reciprocal rotation effects), a layer of  $Si_xN_y$ , with a similar refractive index to garnet, is coated on the sample before applying HSQ on top to make waveguides (Figure 3-3). Therefore, there are two layer structures:  $Si_xN_y$ -Garnet-SOI and  $Si_xN_y$ -SOI (Figure 3-4). The model we used is based on the SOI wafer we are going to use in fabrication: a 500 nm-thick Si layer on a 3  $\mu m$ -thick  $SiO_2$  lower cladding layer on an Si substrate. When making waveguides in the 500 nm Si core layer, all 500 nm Si is etched down to the  $SiO_2$  layer.

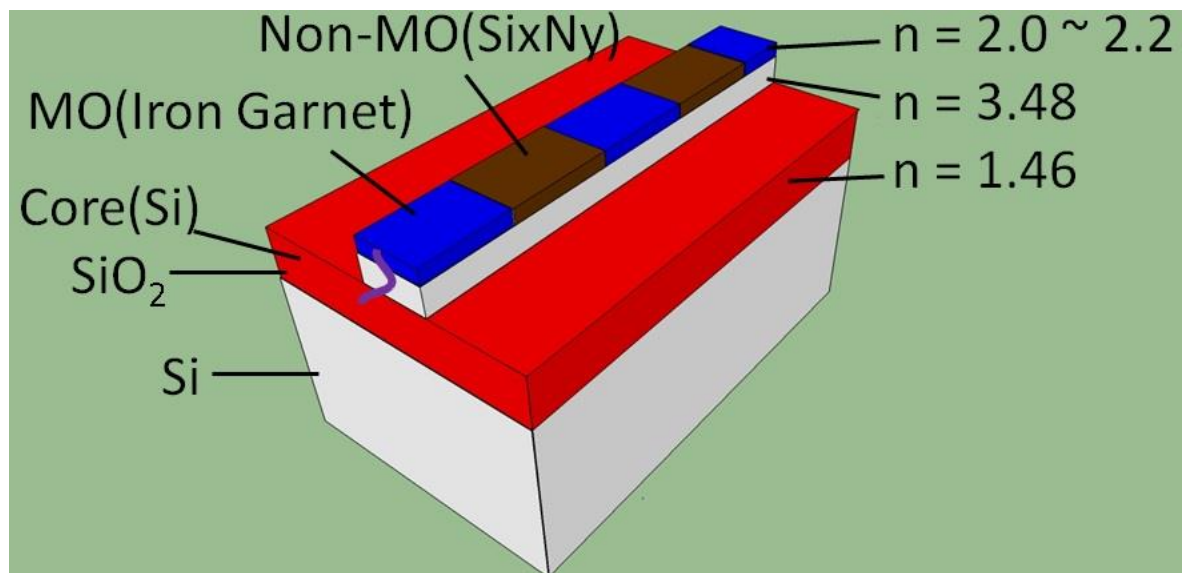


Figure 3-3. The Si core is cladded by garnet segments alternating with  $Si_xN_y$  segments.

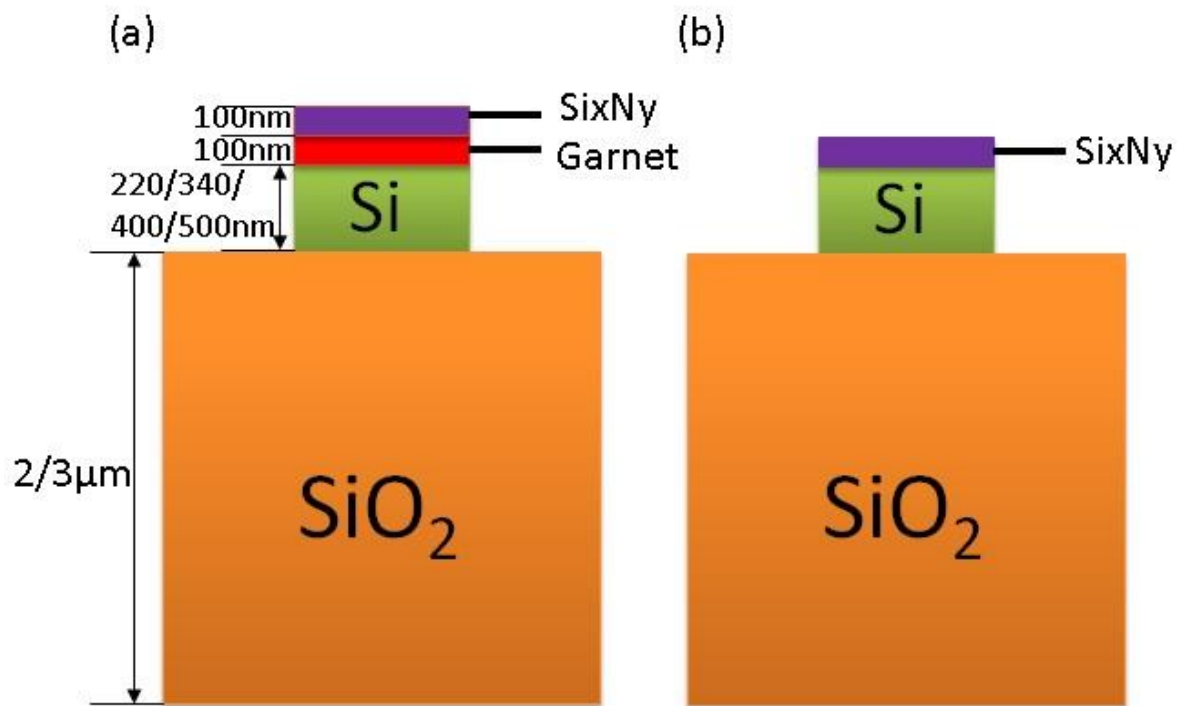


Figure 3-4. a) A cross-sectional profile of the Si Waveguide on SiO<sub>2</sub> with garnet segment claddings capped in SixNy; b) A cross-sectional profile of the Si Waveguide on SiO<sub>2</sub> with SixNy capped on top.

Although various magneto-optical materials were researched throughout the project: TIG (Terbium Iron garnet), Bi-TIG (Bismuth Terbium Iron garnet), Ce-YIG (Cerium Yttrium Iron garnet) on MgO (Magnesium Oxide), and Ce-TIG (Cerium Terbium Iron garnet), the refractive index of the four are much alike at 1550 nm ( $n(\text{Ce-YIG})=2.22$ ,  $n(\text{YIG})=2.2$ ,  $n(\text{TIG})=2.1$ ), and there is nearly no difference in the results of the simulations done to obtain the half-beat lengths of the materials. Hence, a refractive index of 2.2 is used in all simulations (for a wavelength of 1.55 μm).

Of all the garnets, Ce-TIG is very promising since it has a very large Faraday coefficient and, more importantly, does not need any seed layer or buffer layer [123], unlike Ce-YIG - the only other garnet with such a comparatively large magneto-optical effect at 1550 nm. Multi-mode waveguides result in a conversion between the TE-polarised component and TM-polarised component of different orders. Consequently, here, only the fundamental modes were considered and studied, where mode conversion only happens between the two fundamental modes, which, thus, simplifies both the research and analysis process. Therefore, single mode waveguides were required. Conditions for cut-off and multi-mode behaviour were first obtained by judging from the effective refractive index of

the mode. Only those with the effective refractive index  $n$  ranging between 1.44 ( $\text{SiO}_2$ ) and 3.48 (Si) were guided.

Based on previous measurement experience of garnet-clad waveguides on a 500 nm-thick SOI platform, waveguides with a width less than 500 nm will not be able to guide any light at a working wavelength of 1550 nm as a result of high propagation loss, even though the simulation results show that all fundamental, 1<sup>st</sup> order, and 2<sup>nd</sup> order modes are guided in 500 nm wide waveguides. This is believed to be due to stress induced from both the deposited  $\text{Si}_x\text{N}_y$  layer and the garnet layer, or the large scattering loss resulting from the rough interface between the garnet layer and the Si substrate layer, or the absorption loss from the non-crystallized MO garnet material that is partially crystallized [79].

The reason that a thick core of SOI (340 nm, 400 nm, 500 nm) was used here, in spite of the unavoidable multi-mode behaviour, is that the higher order modes are more lossy than the fundamental modes, and also need thick cores to realise either the L-shaped design or RIE trench design to achieve reciprocal mode conversion sections. As such, it was decided to continue using a thick core SOI, even whilst being multi-moded, in order to prove the concept of the Faraday Rotation Effect from the garnet-cladding layer. Widths ranging from 500 nm-1000 nm were chosen to get the half-beat length of garnet on SOI for the reason mentioned above, and confirmed using a mode-solver in MATLAB<sup>®</sup>.

Later, a 220 nm core SOI was also used to test the effect of the thickness of the core on the interaction between the evanescent guided wave and the garnet layer, thus testing the effect on the Faraday rotation. For both the  $\text{Si}_x\text{N}_y$ -Garnet-SOI model and the  $\text{Si}_x\text{N}_y$ -SOI model, where the thickness of the Si core layer is 500 nm, it turns out that even the 500 nm wide waveguides are multi-moded: fundamental, 1<sup>st</sup> order, and 2<sup>nd</sup> order of both the TE-polarised component and TM-polarised component were obtained.

Table 3-1 shows the effective refractive index of all the guided modes (fundamental modes, 1<sup>st</sup> order modes, and 2<sup>nd</sup> order modes) in 500 nm-wide waveguides on a 500 nm SOI platform for the  $\text{Si}_x\text{N}_y$ -Garnet-SOI model and the  $\text{Si}_x\text{N}_y$ -SOI model, respectively. For waveguides wider than 500 nm (600 nm-1000 nm), more modes are supported.

	Effective Refractive Index	Effective Refractive Index
Modes	Si <sub>x</sub> N <sub>y</sub> -Garnet-SOI Model	Si <sub>x</sub> N <sub>y</sub> -SOI Model
Fundamental modes	2.955301, 2.934846	2.946493, 2.923915
1 <sup>st</sup> order modes	2.321610, 2.060357	2.280050, 2.014293
2 <sup>nd</sup> order modes	2.009915, 1.614194	1.917639, 1.537461

**Table 3-1.** The effective refractive index of all the guided modes (fundamental modes, 1<sup>st</sup> order modes, and 2<sup>nd</sup> order modes) in 500 nm-wide waveguides on a 500 nm SOI platform for the Si<sub>x</sub>N<sub>y</sub>-Garnet-SOI model and the Si<sub>x</sub>N<sub>y</sub>-SOI model, respectively.

In mode solver - MATLAB<sup>®</sup>, a mode solver was utilized and modified to our needs in order to calculate how many modes are guided within the waveguide, as well as to obtain the half-beat length. When the hybrid light traverses a half-beat length  $L\pi$ , the major axis of the resultant polarisation vector effectively rotates  $\pi/2$ ,

$$L\pi = \frac{\pi}{|\beta_{TE} - \beta_{TM}|} \quad (3-14)$$

Or

$$L\pi = \frac{\lambda}{2|n_{eff,TE} - n_{eff,TM}|} \quad (3-15)$$

Where  $\beta_{TE}$  and  $\beta_{TM}$  are the propagation constants of the two fundamental modes and  $\Delta\beta = \beta_{TE} - \beta_{TM}$  is the difference of the propagation constant between the two fundamental (single-lobed) modes that propagate in the asymmetric waveguides [77]. The effective refractive index of TE- and TM-polarised components will change with the shape asymmetry (height and width) of the designed waveguide. Here, the height of the waveguide is fixed, so the width would be the only factor that is affected.

Figure 3-5 shows how the effective refractive index of the two single-lobed fundamental modes changes with width for the Si<sub>x</sub>N<sub>y</sub>-Garnet-SOI model and the Si<sub>x</sub>N<sub>y</sub>-SOI model at a working wavelength of 1550 nm, while the relationship between  $L\pi$  and the width for both of the two models is indicated in Figure 3-6. It is obvious that the two models have much the same changing trend, and that the half-beat length decreases with the increase of the width and equivalent length.

It agrees with what is shown in Figure 3-5, where the difference in  $n_{\text{eff}}$  between the two fundamental modes increases with the increase of width.

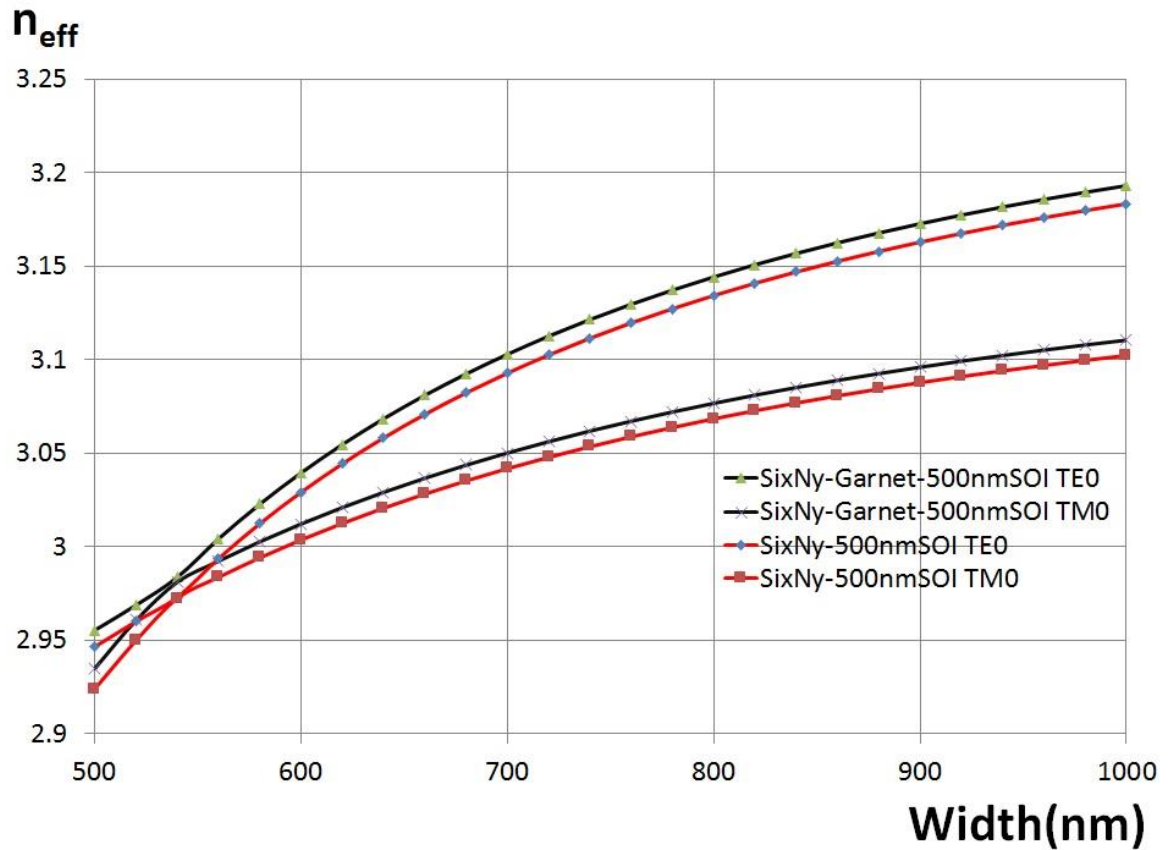
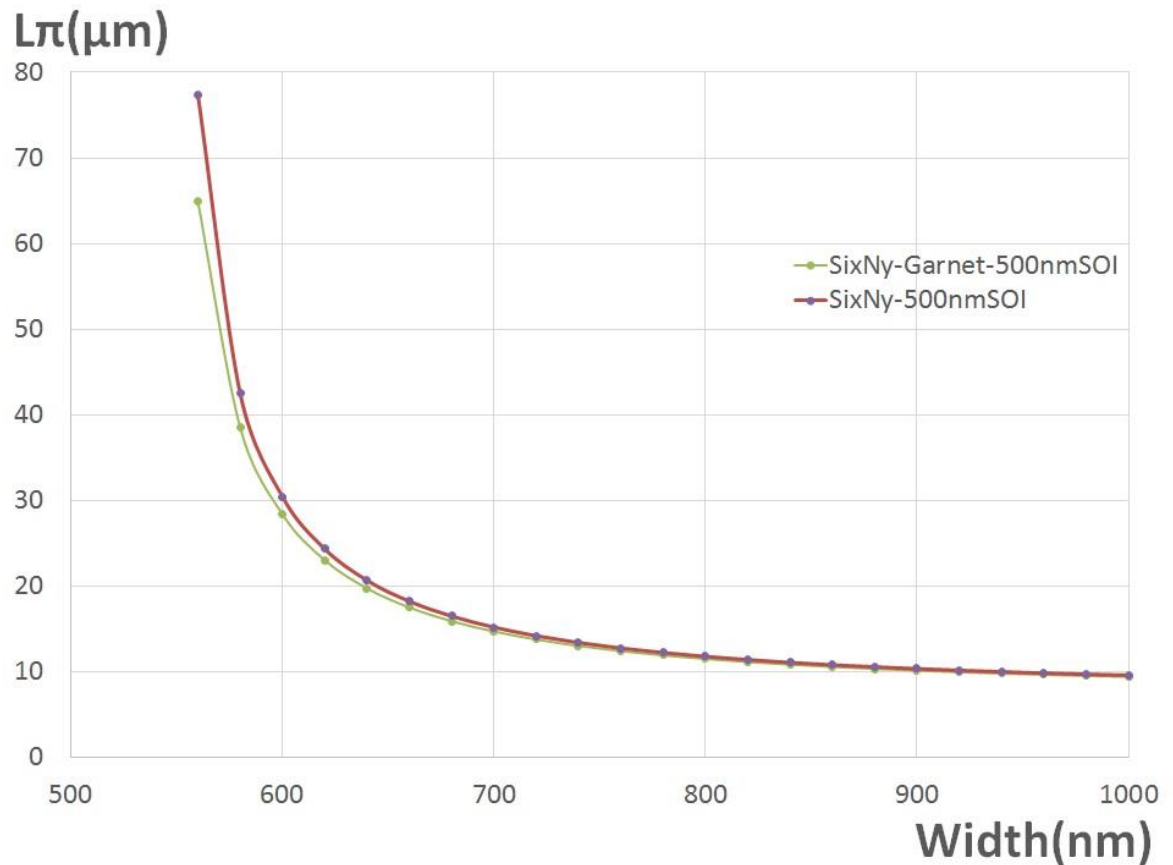


Figure 3-5. How the effective refractive index of the two single-lobed fundamental modes changes with width for the SixNy-Garnet-SOI model and the SixNy-SOI model, respectively, at a working wavelength of 1550 nm.



**Figure 3-6.** The relationship between  $L\pi$  and the width for both of the two models for the 500nm SOI platform at a working wavelength of 1550 nm.

Therefore, by defining the correct beat length using equation (3-14) for the MO-cladding segments, quasi-phase matching (QPM) can be achieved in the MO-cladded waveguides. Later on, by carrying out the corresponding optical measurements, the Faraday rotation degree per cm length can be obtained for the actual device. From this, the total length of the QPM waveguides and the number of periods required for a polarisation state change necessary for an integrated isolator,  $45^\circ$  nonreciprocal rotation, or any other arbitrary angles of polarisation can be decided.

All fabrication errors, simulation errors, and the influence of garnet on light guiding are considered, for both  $\text{Si}_x\text{N}_y$ -Garnet-SOI and  $\text{Si}_x\text{N}_y$ -SOI (as shown in Figure 3-4). The width range of 600 nm-1100 nm is chosen for the Si core layer of the waveguide. The width of the garnet-cladding segments needs to be 100 nm-200 nm less than that of the Si waveguides to be sure that all garnets are situated on top of the Si waveguides; otherwise, part of the garnet cladding may fall out and act as a dry etch mask in the following process. This would both affect the

evanescent interaction, as the majority of interaction occurs in the middle of the guide, and also increase propagation loss, resulting from the rougher edge of the waveguide with garnet masking in the dry etch process. Thus, the widths of garnet islands were chosen as 500 nm-900 nm.

The designed half-beat length of garnet-covered areas (length of the garnet islands) ranged from 10  $\mu\text{m}$ -15  $\mu\text{m}$ , with an increment of 0.5 $\mu\text{m}$ , and different ranges of gaps, starting from 10  $\mu\text{m}$ , were chosen according to the length of the half-beat length for the non-garnet-covered areas. This takes account of the different refractive index of the garnet-clad areas to the non-garnet-clad areas. (This is not an issue when over-coating with  $\text{Si}_x\text{N}_y$ ). As a result, different duty cycles of waveguides were designed to test the Faraday rotation that resulted from the garnet islands on top. For example, for the half-beat length of 12  $\mu\text{m}$ , gaps vary from 10  $\mu\text{m}$ -12  $\mu\text{m}$  with an increment of 0.5  $\mu\text{m}$ ; therefore, duty cycles start from 22  $\mu\text{m}$  and end at 24  $\mu\text{m}$  when the half-beat length is 12  $\mu\text{m}$ , which applies to all widths. Based on what we learned from the results of the simulation, a suitable mask for fabrication can be constructed using L-edit<sup>®</sup>.

The same simulation method applies to 400 nm SOI, 340 nm SOI, and 220 nm SOI platforms. Similarly, we can get the relationship between  $L_\pi$  and the width for both of the two models for these three platforms, which is indicated in Figure 3-7. The same parameters selection rules applied as for 500 nm SOI and 600 nm-1000 nm are chosen for the width range. For the 400 nm SOI platform, the designed half-beat length of garnet-covered areas (length of the garnet islands) ranged from 5  $\mu\text{m}$ -14  $\mu\text{m}$ , with an increment of 0.5  $\mu\text{m}$ . Different ranges of gaps starting from 5  $\mu\text{m}$  were chosen according to the length of the half-beat length for the non-garnet-covered areas. For the 340 nm SOI platform, the length of the garnet islands ranged from 3  $\mu\text{m}$ -5.5  $\mu\text{m}$ , with an increment of 0.5  $\mu\text{m}$ , and different ranges of gaps, starting from 3  $\mu\text{m}$ , were chosen for the non-garnet-covered areas. For the 220 nm SOI platform, the length of the garnet islands ranged from 1.1  $\mu\text{m}$ -2.4  $\mu\text{m}$ , with an increment of 0.1  $\mu\text{m}$ , and different ranges of gaps, starting from 1.1  $\mu\text{m}$ , were chosen for the non-garnet-covered areas.

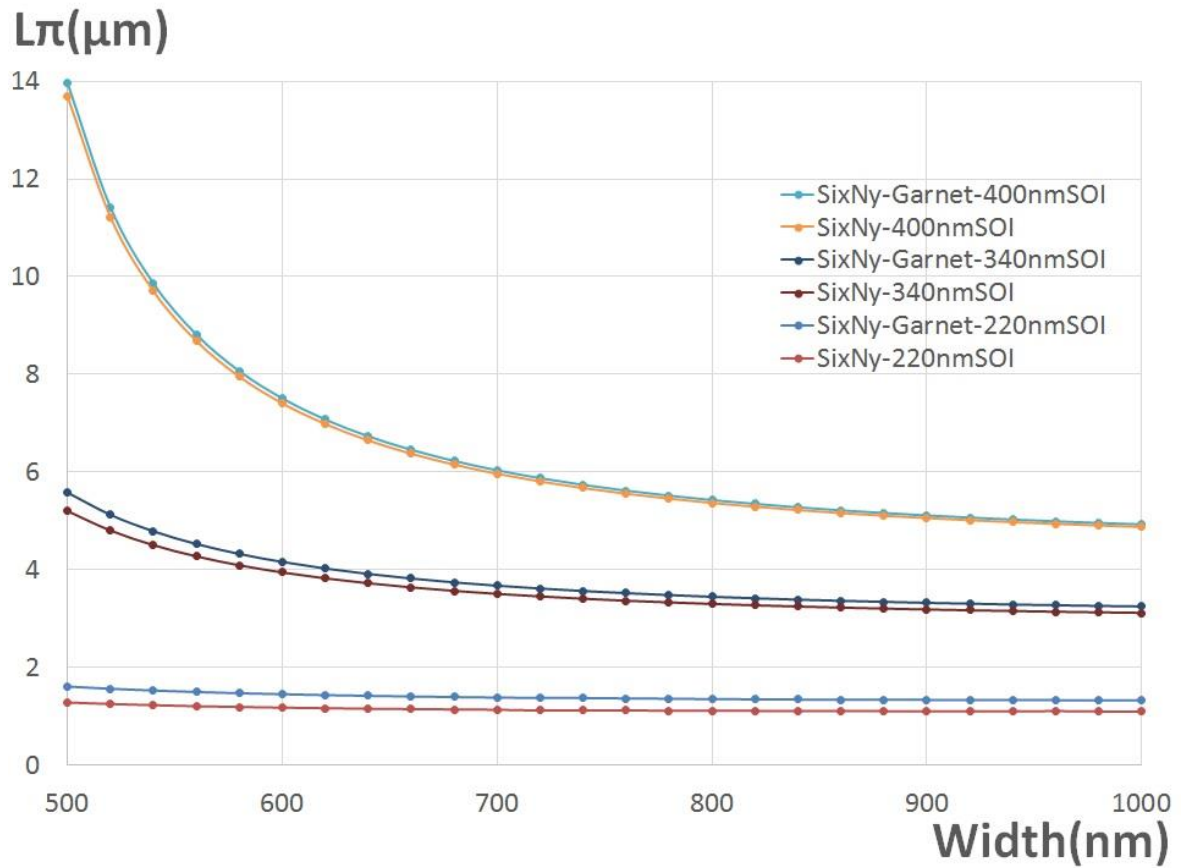


Figure 3-7. The relationship between  $L\pi$  and the width for both the SixNy-Garnet-SOI and SixNy-SOI models on 400 nm SOI, 340 nm SOI, and 220 nm SOI platforms, respectively.

### 3.3 Effect of Seed/Buffer Layer of Different Thicknesses on the Faraday Rotation

Here, all of the simulation was done on a 500 nm SOI platform with a working wavelength of 1550 nm. The various kinds of magneto-optical garnet materials (YIG (Yttrium Iron Garnet), TIG (Terbium Iron garnet), Bi-TIG (Bismuth Terbium Iron garnet), Ce-YIG (Cerium Yttrium Iron garnet) on MgO, and Ce-TIG (Cerium Terbium Iron garnet)) researched had different Faraday Rotation Coefficients. It leads to the difference in the off-diagonal elements in equation (3-12), where  $\varepsilon_{xy} = 2\theta_F n_0 / k_0$  and  $\varepsilon_{xx} = n_0^2$  and  $\theta_F$  is the amount of the Faraday rotation. YIG has the smallest Faraday rotation coefficient of  $200^\circ/\text{cm}$ . TIG and Bi-TIG have the same amount of  $500^\circ/\text{cm}$  but with the opposite sign, which,

however, can be used to advantage in the MO(+)/MO(-) alternating design (Figure 3-8) to enhance the Faraday rotation [79] over a given length. Ce-YIG is reported to have the biggest coefficient, reaching  $-4500^\circ/\text{cm}$  [72] or  $-3700^\circ/\text{cm}$  [128]. However, in our application, as the garnet layer acts as a cladding layer and only the evanescent tail of the guided mode interacts with it, the garnet is patterned in segments instead of a full thin film, which was researched by our collaborators. Therefore, the quality of the garnet is uncertain, and a relatively smaller Faraday coefficient was used here,  $-2000^\circ/\text{cm}$ .

Knowing the Faraday rotation coefficient, we can get  $\varepsilon_{xy}$  used in the modesolver<sup>®</sup>, and use the simulation to find out the optimal thickness needed to achieve the best performance. All of the characteristics are shown in Table 3-2. The first column shows the Faraday rotation coefficients of the garnet material, which was obtained from the Faraday rotation measurement obtained by our collaborators. The second column is the off-diagonal parameter  $\varepsilon_{xy}$ , calculated using equation  $\varepsilon_{xy} = 2\theta_F n_0/k_0$  and  $\varepsilon_{xx} = n_0^2$  and  $\theta_F$  is the amount of the Faraday rotation coefficient displayed in the first column. The third column is the optimal thickness needed as the upper-cladding layer for each garnet material obtained from the simulation result shown in Figure 3-9.

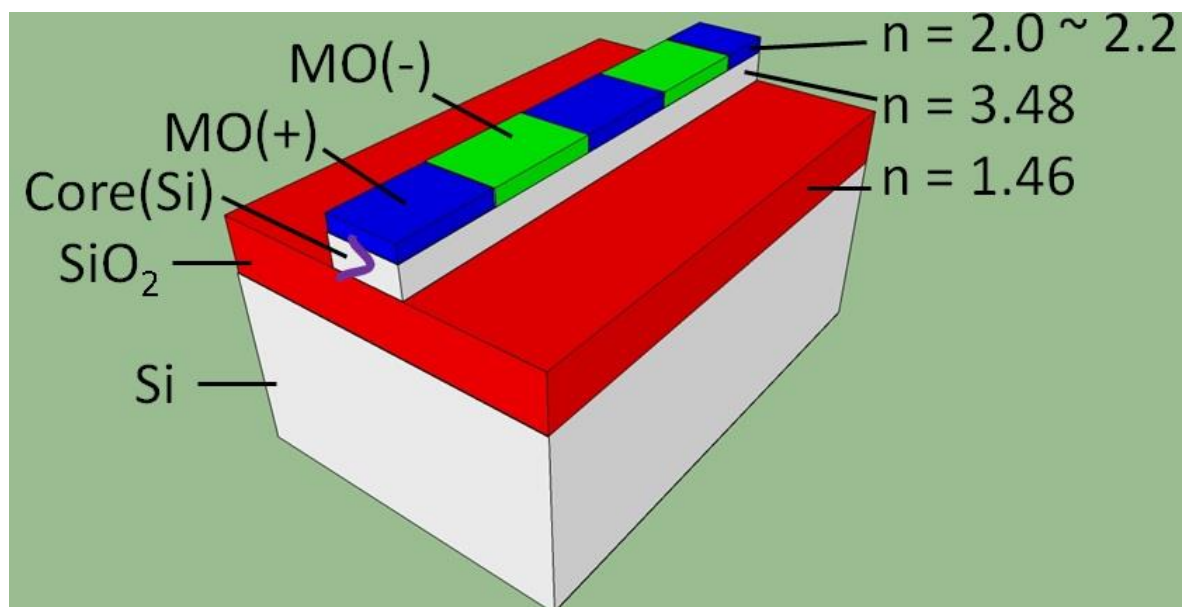


Figure 3-8. The Si core is cladded by garnet segments MO(+) alternating with MO(-) segments.

	Faraday Rotation Coefficient (° /cm)	$\varepsilon_{xy}$ ( $\times 10^{-4}$ )	Thickness for optimal performance (nm) (Figure 3-9)
YIG	200	4	110
TIG	500	10	150
Bi-TIG	-500	-10	150
Ce-TIG	-2000	-40	200
Ce-YIG	-2000	-40	200

**Table 3-2.** The Faraday rotation coefficient,  $\varepsilon_{xy}$ , and thickness for optimal performance of different garnet layers.

Figure 3-9 shows how different thickness of the garnet layer affect the Average  $S_3$  parameters of the quasi-TE and quasi-TM mode. Here, the  $S_3$  component is taken as a characteristic to show the Faraday rotation in the magneto-optical cladding [86]. From the  $S_3$  component, the length of device needed for a certain degree of rotation ( $\theta$ ) can be calculated as:  $L = N \times (L\pi_{garnet} + L\pi_{SixNy})$ ,  $N = \frac{\theta}{2\bar{S}_3}$ . Here, we suppose  $2 \sin^{-1} \bar{S}_3 \approx 2\bar{S}_3$ ,  $N$  is the period needed, and  $\theta$  is the degree rotated [86]. As the absolute value of the Faraday coefficient of TIG and Bi-TIG is the same, they are present together; the same applies to Ce-TIG and Ce-YIG. It is clear that the garnet layer of the bigger Faraday rotation coefficient gets bigger absolute Average  $S_3$  parameters, and it increases with the increase of the thickness of the garnet layer until it reaches an optimal thickness and goes steady.

The garnet material is employed as upper cladding in our structure. The evanescent tail of the mode extends into a limited thickness of the upper cladding layer. Thus, after a certain thickness, the absolute Average  $S_3$  parameters stop increasing with the increase of the upper cladding thickness. The optimal

thickness for the YIG layer is 110 nm, for TIG/Bi-TIG it is 150 nm, and for Ce-TIG/Ce-YIG it is 200 nm.

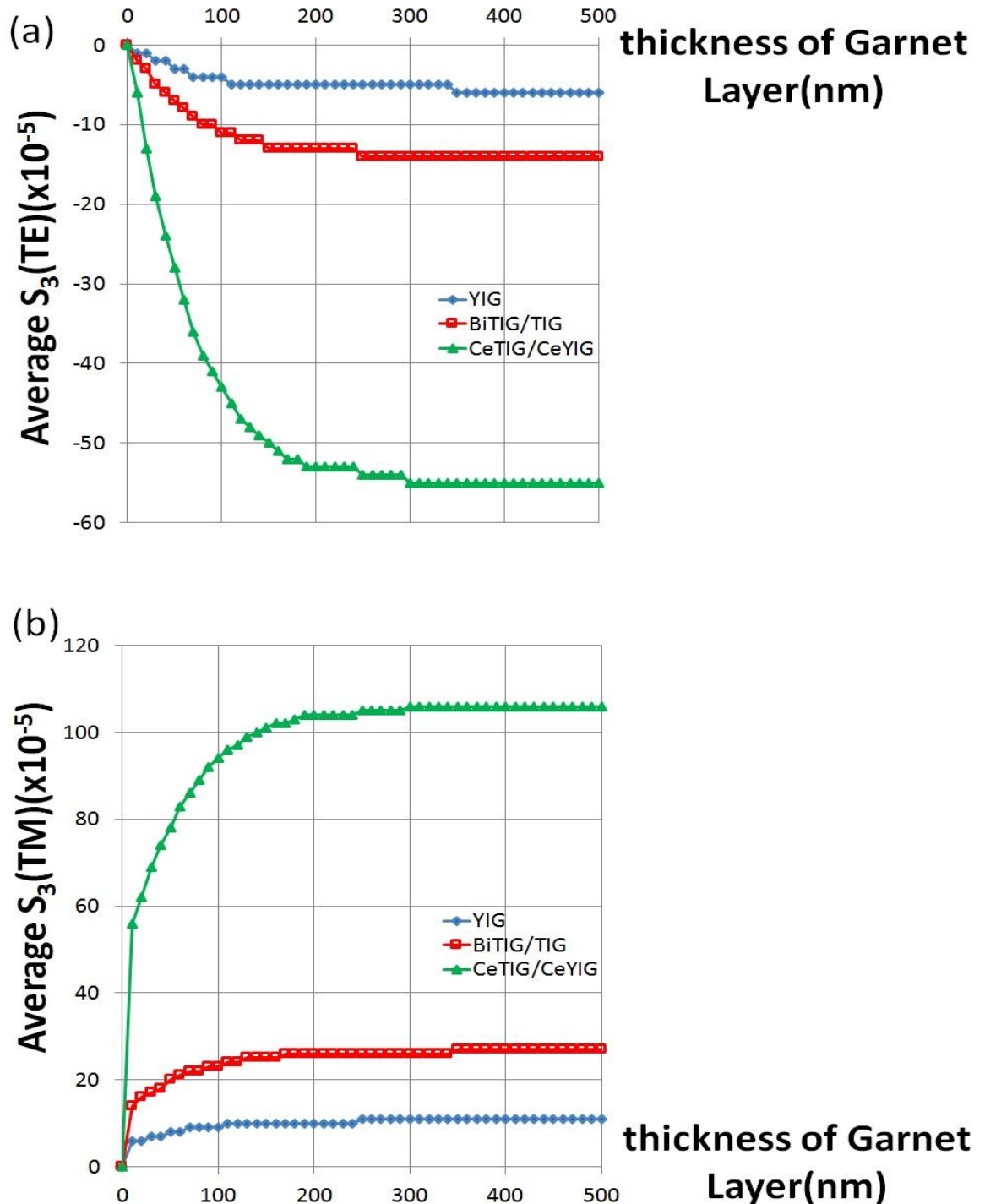


Figure 3-9. How different thickness of the garnet layer affect the Average  $S_3$  parameters of the quasi-TE and quasi-TM mode. As the absolute value of the Faraday coefficient of TIG and Bi-TIG is the same, they are presented together; the same applies to Ce-TIG and Ce-YIG. It is clear that the garnet layer of the bigger Faraday rotation coefficient gets bigger absolute Average  $S_3$  parameters, and it increases with the increase of the thickness of the garnet layer until it reaches an optimal thickness and goes steady. The optimal thickness for the YIG layer is 110 nm, for TIG/Bi-TIG it is 150 nm, and for Ce-TIG/Ce-YIG it is 200 nm.

Of all the garnet materials, terbium-based novel garnet is the most promising material as it does not require any seed/buffer layer, usually using YIG/MgO to achieve the crystallised phase [123]. This is a very important advantage when integrated into an integrated system as the adoption of a seed/buffer layer weakens the magneto-optical performance of the garnet layer [77]. However, in the early stage of research into terbium-based garnets, samples with/without an MgO buffer layer had to be checked to discover whether terbium-based garnets needed a seed/buffer layer to get crystallized or not (discussed more fully in Chapter 4).

Simulation of the existence and different thickness of MgO buffer layers on the performance of all the garnets were carried out and are displayed in Figure 3-10. Here, the optimal thickness of the garnet layer is used, YIG (110 nm), Bi-TIG/TIG (150 nm), and Ce-TIG/TIG (200 nm). It is demonstrated that the MgO buffer does severely decrease the Average  $S_3$  parameters. Compared to the quasi-TE mode, the quasi-TM mode is more sensitive to the MgO layer. Only 10 nm of the MgO layer will weaken the  $S_3$  component by more than half of its original value. Also, the  $S_3$  component completely vanishes when the MgO layer reaches 100nm. In actual fabrication, as the Tb (Terbium) family of garnets, like Bi-TIG, TIG, and Ce-TIG, do not require a buffer/seed layer to get crystallized [123], the  $S_3$  component will stay at its maximum value and not decrease at all.

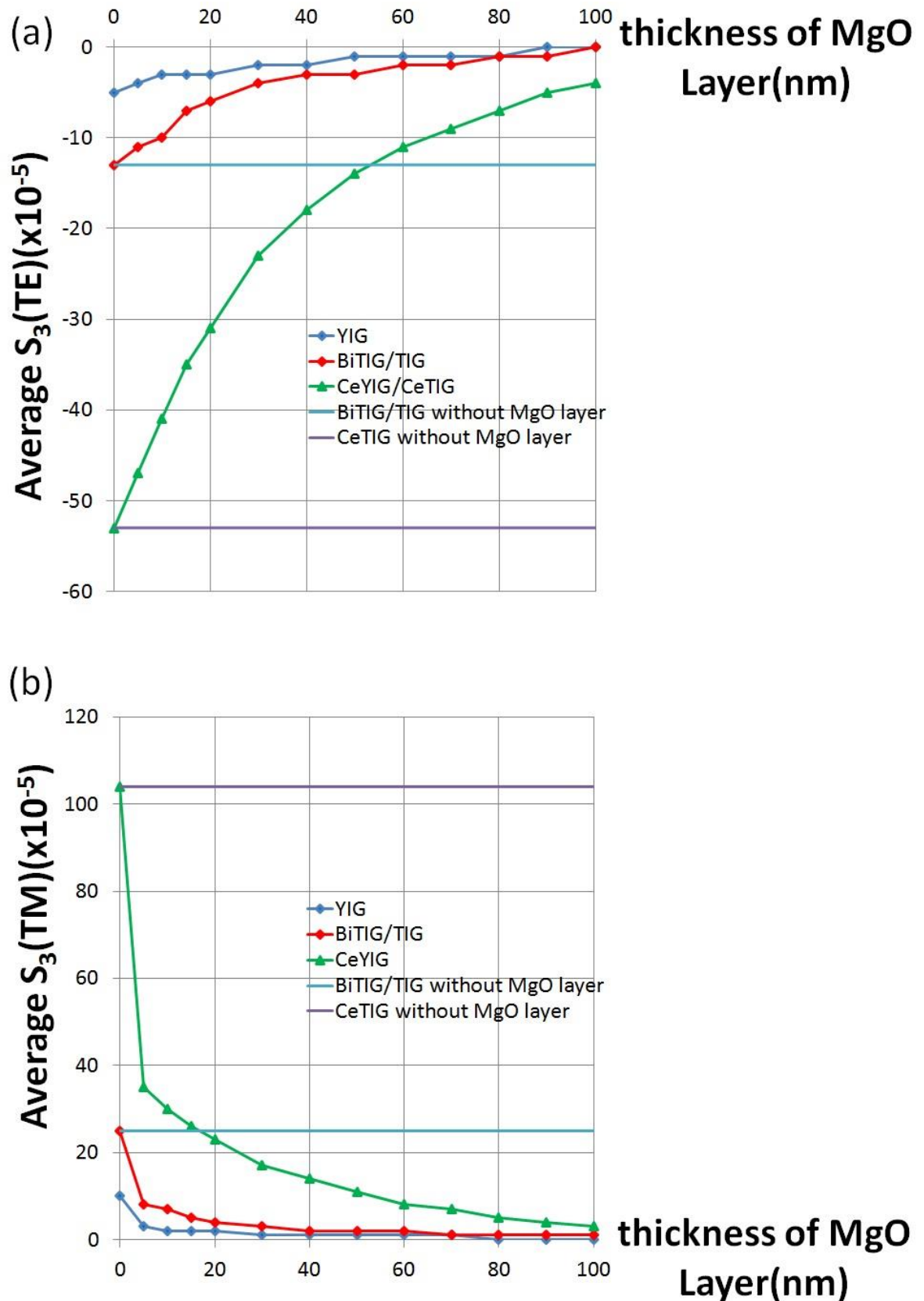


Figure 3-10. The existence and different thickness of the MgO buffer layer on the performance of all the garnets. It is demonstrated that the MgO does severely decrease the Average  $S_3$  parameters. Compared to the quasi-TE mode, the quasi-TM mode is more sensitive to the MgO layer. Only 10nm of the MgO layer will weaken the  $S_3$  component by more than half of the original value. Also, the  $S_3$  component completely vanishes when the MgO layer reaches 100 nm.

From Figure 3-10 we can see that, among the terbium-based garnets, Ce-TIG has the same level quantity of Faraday coefficient as Ce-YIG, and can get crystallized without any buffer/seed layer and, thus, becomes the best material. Comparatively, in order to crystallize Ce-YIG, a seed layer (YIG) or buffer layer (MgO) is required as a precursor before the deposition of Ce-YIG, or else the Cerium oxide phase forms instead of the Ce-YIG garnet phase. Our collaborators, Professor Bethanie Stadler's group from the University of Minnesota, have made enormous endeavors and produced some of the best quality Ce-YIG film [129] [136] to date. A seed/buffer layer of MgO/YIG will be deposited before the Ce-YIG; the MgO layer acts as the block layer for the interaction between GaAs and Ce-YIG [147][148]; the YIG layer can act as a virtual substrate to enhance Ce-YIG's crystallization [149] at a lower temperature.

The effect of the MgO buffer layer on the magneto-optical performance of Ce-YIG is shown in Figure 3-10. Alternatively, the YIG seed layer can also be used to help in the garnet-phase-forming process. As predicted, the presence of a YIG seed layer underneath the Ce-YIG layer does even more harm to the performance (Figure 3-11) than an MgO layer (Figure 3-10), as YIG (+200 deg/cm for thin film) has the opposite Faraday rotation coefficient to Ce-YIG (-3700 deg/cm for thin film). Meanwhile, MgO behaves neutrally and, what is worse, in order to use YIG as a seed layer, the fabrication process becomes much more complicated and troublesome compared to the single deposition process using an MgO buffer layer. The YIG layer needs to be deposited, lifted-off, and annealed first, and then a new lift-off mask needs to be prepared for the deposition of Ce-YIG.

Block *et al.* [128] reported that 15 nm of a YIG layer is needed to get the Ce-YIG layer 86.1% crystallised, and 45 nm is needed for nearly 100% crystallised. From Figure 3-11, we know that if we want 100% crystallised Ce-YIG film with a 45 nm seed layer, the Faraday rotation effect is substantially decreased; while, if we want a bigger magneto-effect with a 15 nm thick seed layer, then the Ce-YIG film is only partially crystallised. There is always a compromise between the magneto-optical performance and the garnet quality.

However, recently, an MIT group [67] have come up with a single-step deposition using the YIG layer as a cap layer deposited on top of the Ce-YIG layer,

which gets the Ce-YIG crystallised as well as avoids hindering the magneto-optical performance and strengthens and broadens the usage of Ce-YIG in the future.

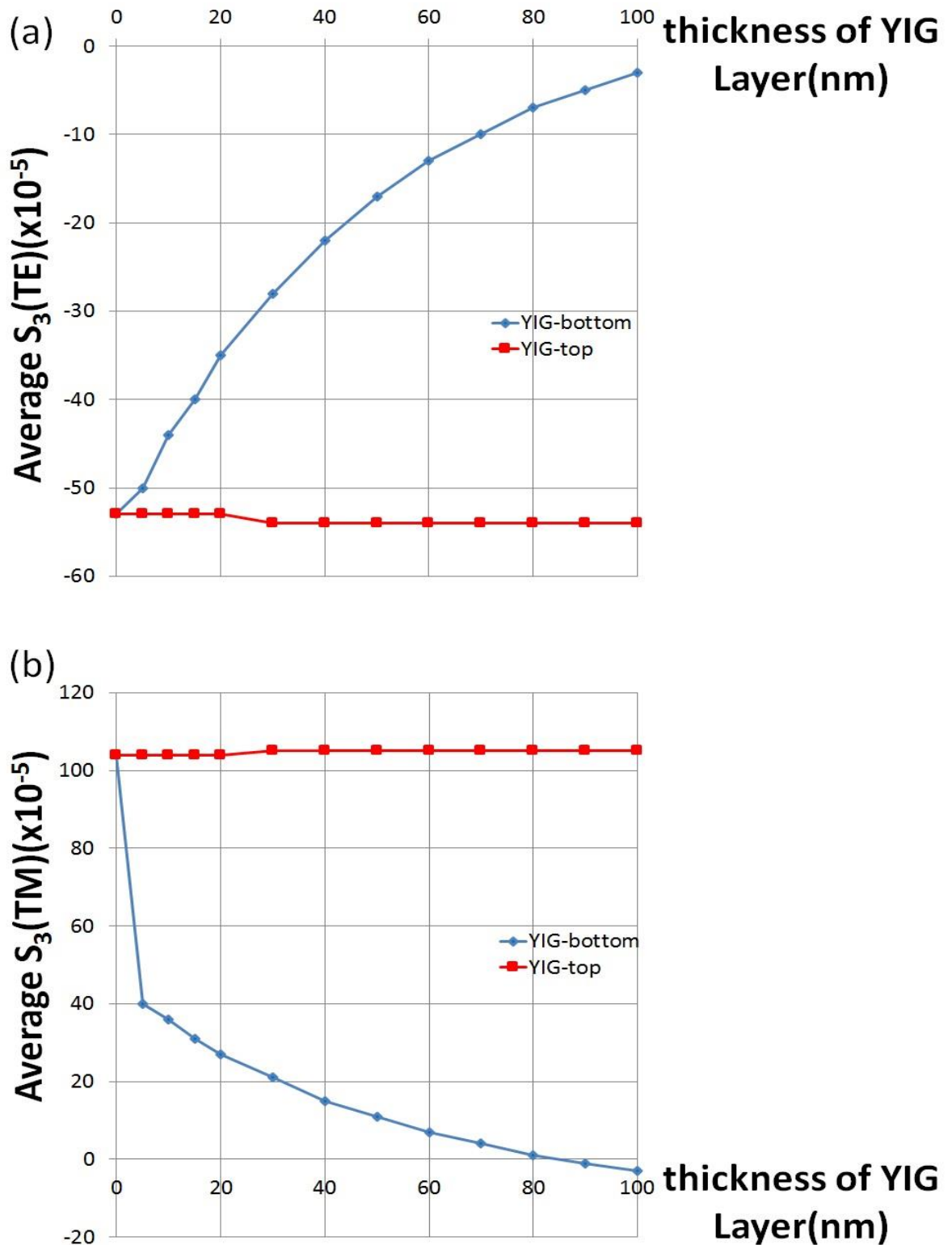
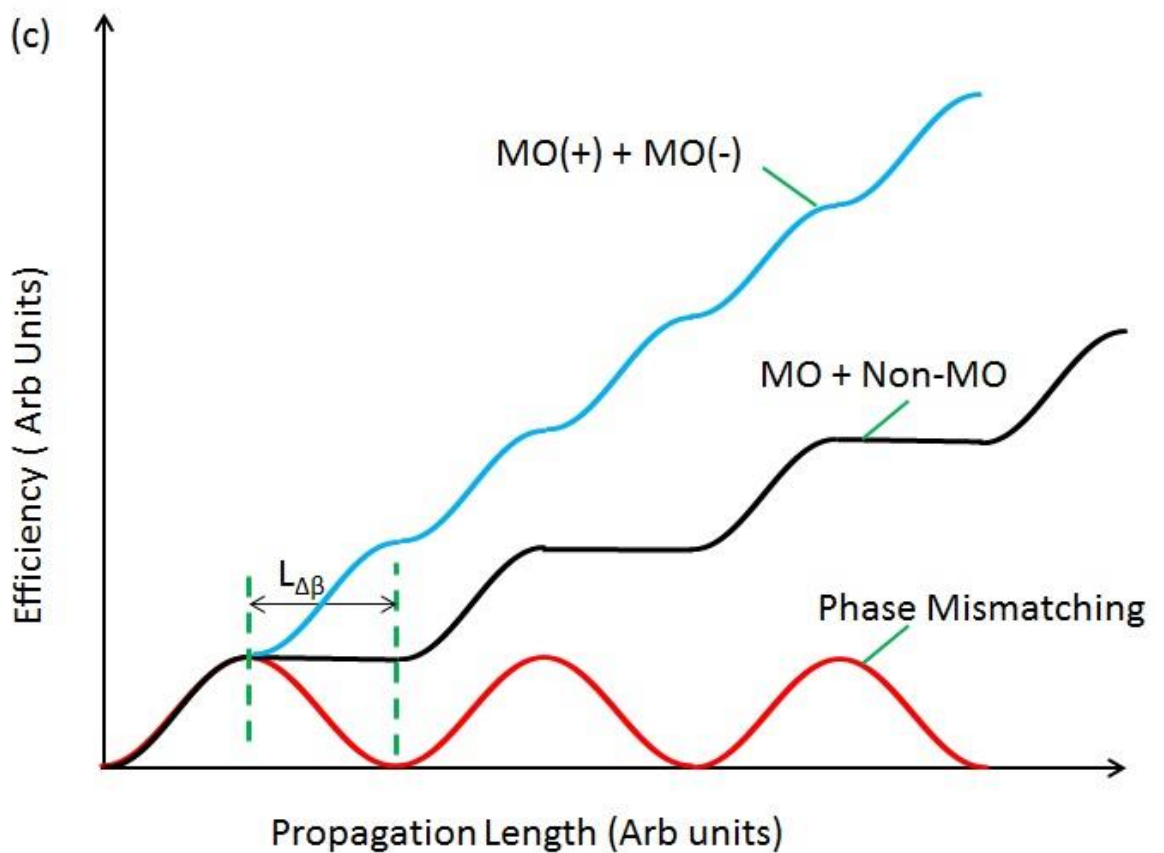
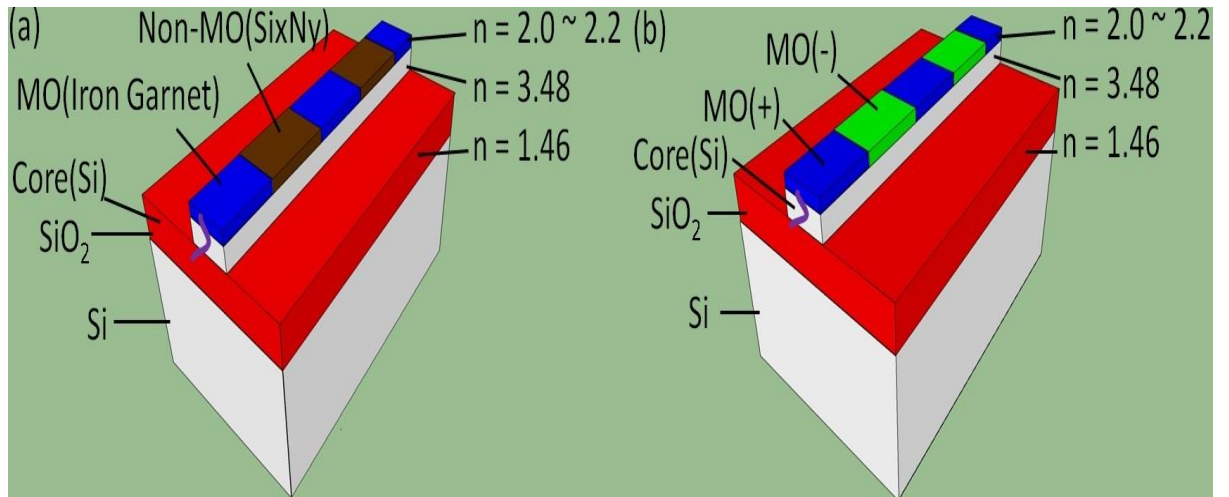


Figure 3-11. The presence and different thicknesses of the YIG layer underneath the Ce-YIG layer, and on top of the Ce-YIG layer on the performance of Ce-YIG. It is seen that it will not affect the magneto-optical effect of the Ce-YIG layer when the YIG layer acts as a cap layer put on top of it.

## 4 Chapter 4 - Fabrication of Nonreciprocal Polarisation Mode Converter

### 4.1 Introduction

A solution is provided in papers[48][49], where we can use garnet as the cladding layer to take advantage of its magneto-optical effect, through an interaction of the guided modes' evanescent tail (see Figures 4-1 (a) and 4-1 (b)). To use the garnet as cladding, people have used deposition [64], adhesive bonding [31][72], and direct bonding [71][80] techniques, combined with non-reciprocal phase shift sections to achieve isolation. In our application, the garnet material is deposited on a SOI platform using RF (radio frequency) sputtering. Additionally, we adopted a quasi-phase matching technique to overcome the inherent birefringence effects from planar waveguides, by utilising an upper cladding that alternates between magneto-optical (MO) material and non-magneto-optical (Non-MO) material, or, between MO(+) segments and MO(-) periodically, like Bi-TIG ( $-500^\circ/\text{cm}$ ) and TIG ( $500^\circ/\text{cm}$ ), respectively (Figures 4-1 (a) and 4-1 (b)). Figures 4-1 (a) and (b) show the two structures of alternating segments, and Figure 4-1 (c) indicates the difference in conversion efficiency between the QPM design and designs that are not phase matched.



Figures 4-1 (a) and (b). The layer structure of a waveguide-type isolator with Si as the core layer and the magneto-optical garnet as the upper cladding layer indicates the structures of NR-PMC alternating between MO segments and Non-MO segments, and between MO(+) and MO(-), respectively, All of the refractive index of the material is given at a  $1.55\mu\text{m}$  wavelength. (c) demonstrates the difference in rotation efficiency between QPM (MO+ Non-MO structure and MO(+) + MO(-) structure) and Phase Mismatching.

## 4.2 Whole Fabrication Process

### 4.2.1 Electron-Beam Resist: PMMA (Polymethyl Methacrylate) and HSQ (Hydrogen silsesquioxane)

An electron-beam resist was used in the fabrication process to help define the structure features. There are two types (tones) of e-beam resist: positive tone resist and negative tone resist. The exposed areas of the positive tone resist clear out after development in appropriate chemical solvents, while that of the negative tone resist stays and the non-exposed areas are removed. The relation is described in Figure 4-2.

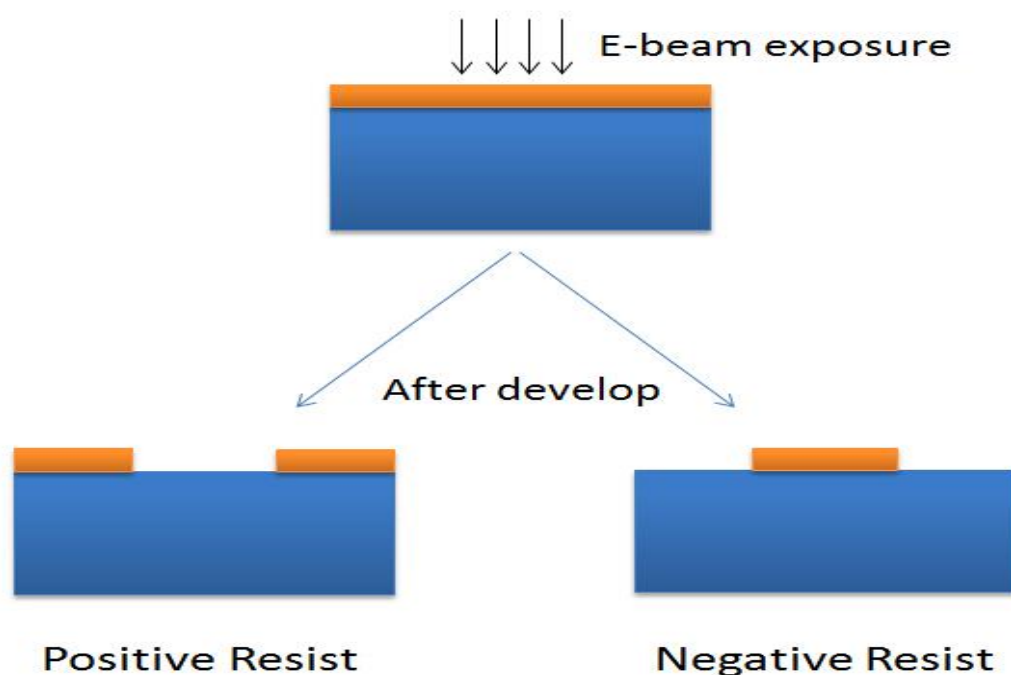
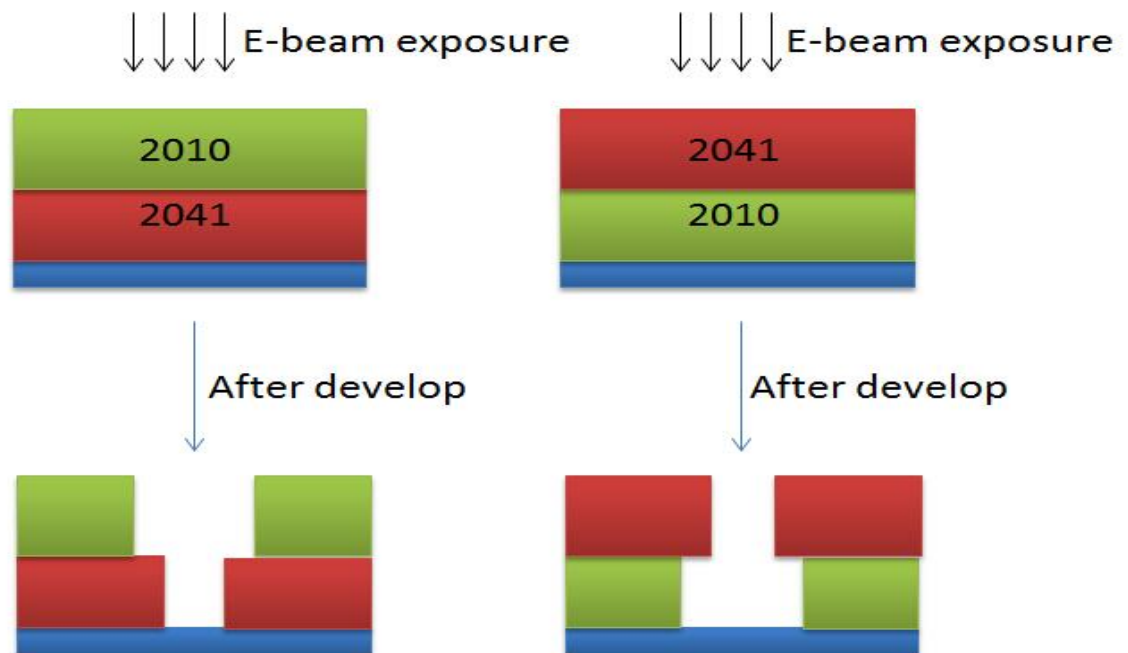


Figure 4-2. Two kinds of electron-beam resist are used in the fabrication process: PMMA (Polymethyl Methacrylate, positive-tone resist) and HSQ (Hydrogen silsesquioxane, negative tone resist).

Two kinds of electron-beam resist were used in the fabrication process: PMMA (Polymethyl Methacrylate, positive-tone resist) and HSQ (Hydrogen silsesquioxane, negative tone resist). As an EBL resist, PMMA has been used for decades, and is still very popular for excellent definition of ultra-high resolution patterns, and multiple layers of any combination of molecular weights can be used to minimise pinholes in the resist or provide improved undercut profiles for lift-off.

The two most common molecular weights used are the PMMA 2010 series with an average molecular weight of 150,000 g/mol, and the PMMA 2041 series with an average molecular weight of 500,000 g/mol. The one with the heavier molecular weight is less sensitive to the electron beam, based on which bilayers of these two molecular weights can create various different resist profiles for different purposes. Figure 4-3 shows two examples of bilayer structures. The left can be used as the mask for T-gate devices while the right structure is very useful in the lift-off process. However, the PMMA resist has very poor dry etch resistance when acting as the dry etch mask in many types of plasma.



**Figure 4-3.** The two kinds of bilayer structures.

Comparatively, the HSQ resist has very high dry-etch selectivity, and can also provide ultra-high resolution features. The HSQ has negative resist. After e-beam exposure, the Si-H bonds in the net structure are broken and cross-linking occurs. After development, the cross-linked structures form a porous silicon dioxide [150], as shown in Figure 4-4 [151]. HSQ can be adopted to achieve clear sub 10 nm resolution features [152].

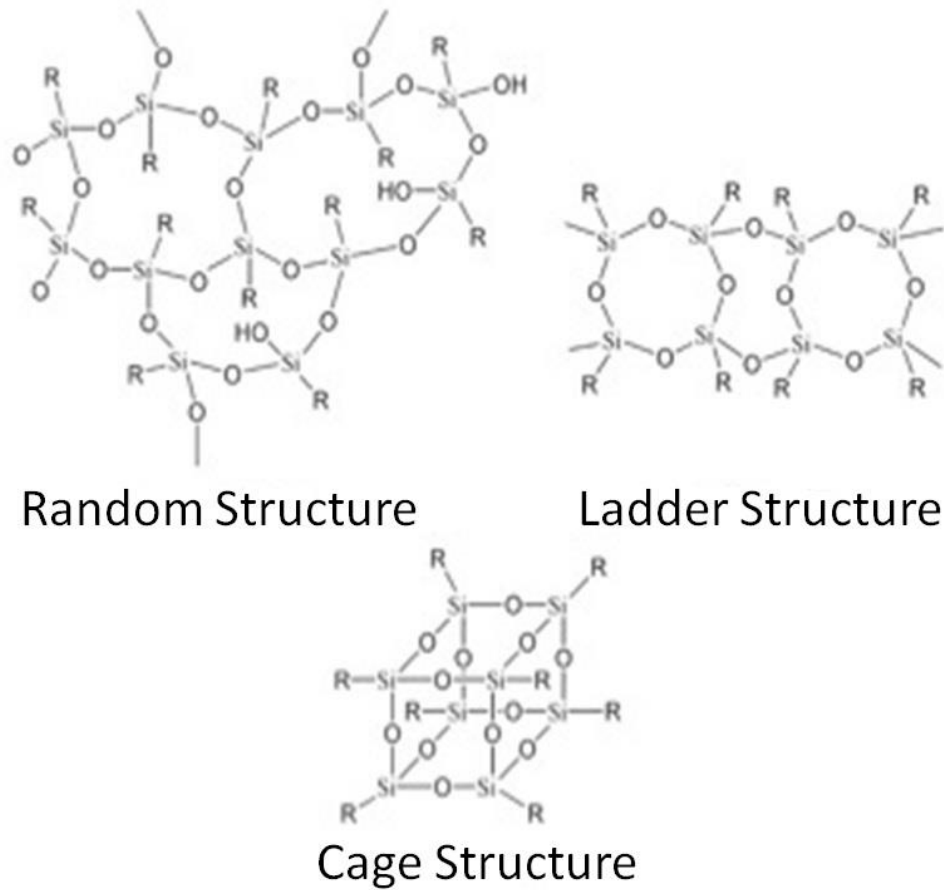


Figure 4-4. The network structures and Cage structures before and after exposure [14].

#### 4.2.2 Whole Fabrication Process

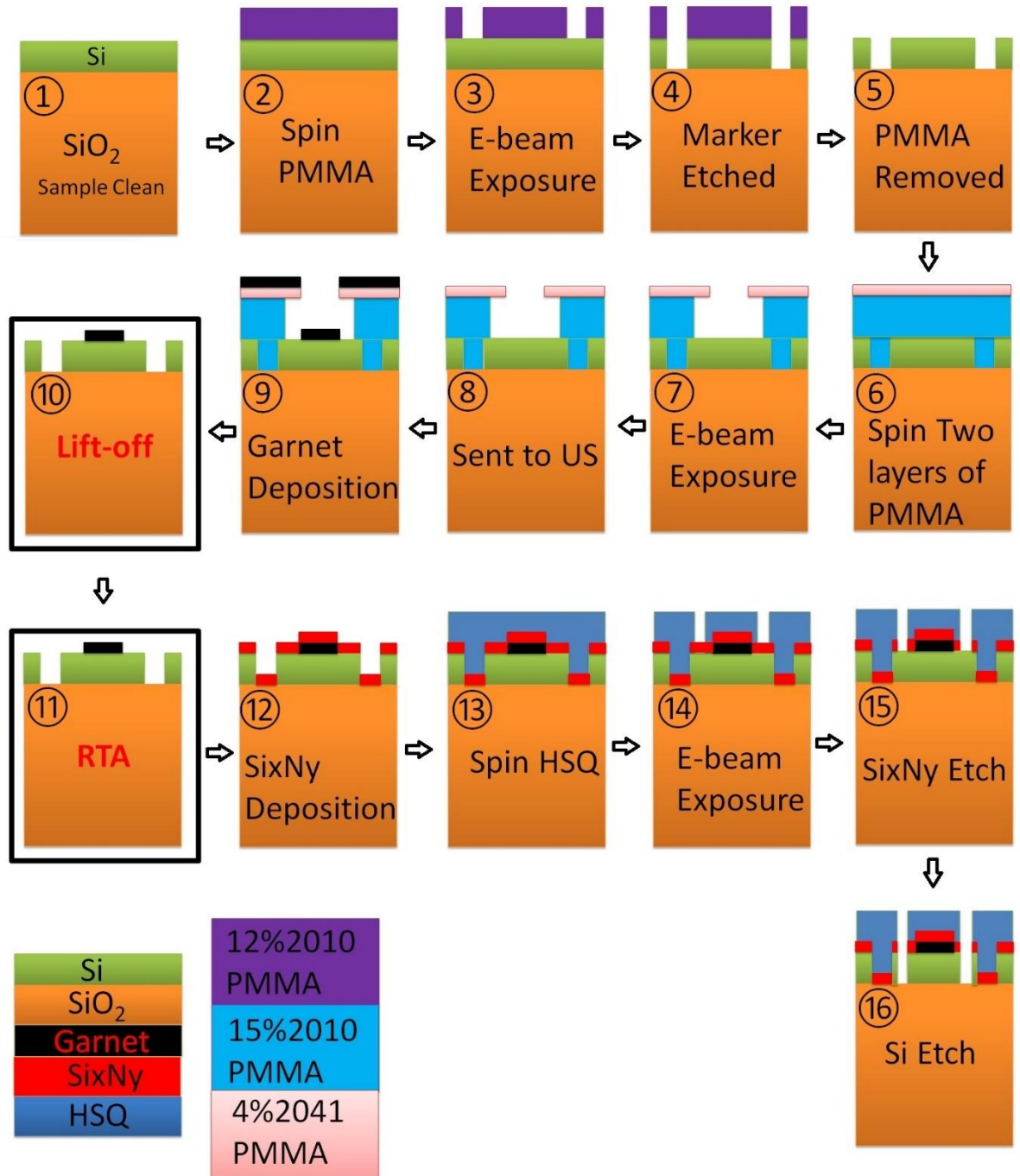


Figure 4-5. The whole device fabrication process: Sample clean — Spin PMMA on — E-beam exposure — Development — Etch markers down — PMMA removed — Spin bi-layer PMMA for lift off — E-beam exposure — Sent to US — Garnet deposition — Lift-off — RTA — SixNy coating — Spin HSQ on to — E-beam exposure — Si<sub>x</sub>N<sub>y</sub> etch — Si etch.

The whole fabrication process is described in Figure 4-5. At step ①, a sample clean process was carried out. The SOI (Silicon on Insulator) wafers are usually 6-inch or 8-inch depending on different manufacturers. The larger wafers need to be cut into small pieces, usually 15x15 mm square pieces, for different purposes of processing. In order to protect the sample surface and prevent more

pollutants (like particles from the scribed line) being introduced during the cleaving step, a layer of PMMA resist is applied beforehand to the whole wafer. Then, a solvent cleaning process was used to clean the SOI sample pieces - opticlear, Acetone ( $(\text{CH}_3)_2\text{CO}$ ), Methanol/IPA (Isopropyl alcohol,  $\text{C}_3\text{H}_8\text{O}$  or  $\text{C}_3\text{H}_7\text{OH}$  or  $\text{CH}_3\text{CHOHCH}_3$ ) in an ultrasonic bath, each for 5 mins. Finally, the substrate was rinsed under the running tap of RO (Deionized) water and was dried with a nitrogen blow dryer. The whole process for sample cleave and clean steps is presented in Figure 4-6. If the substrate surface is not clean enough, contamination will act as an etch mask in the following pattern-transfer process, and 'grass' will form all over the sample surface (Figure 4-7), which will lead to poor device performance like high optical loss.

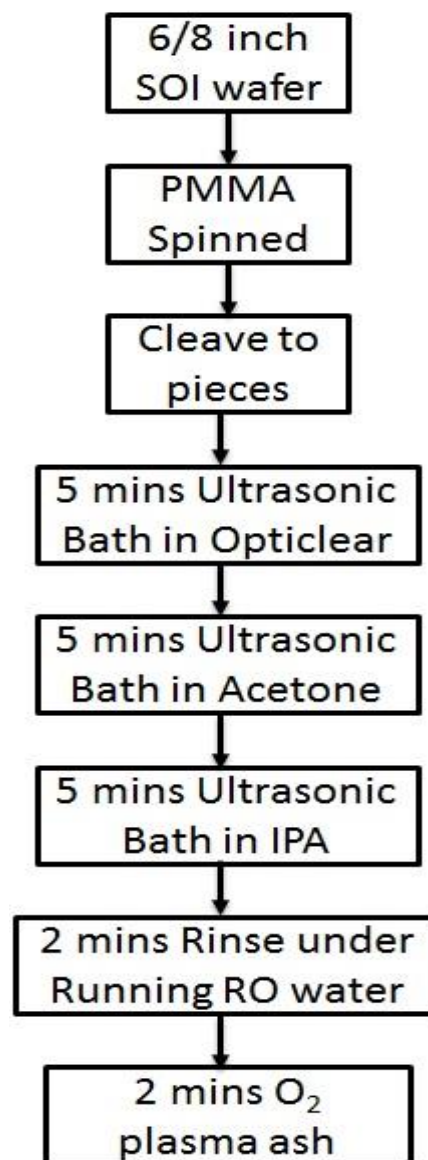
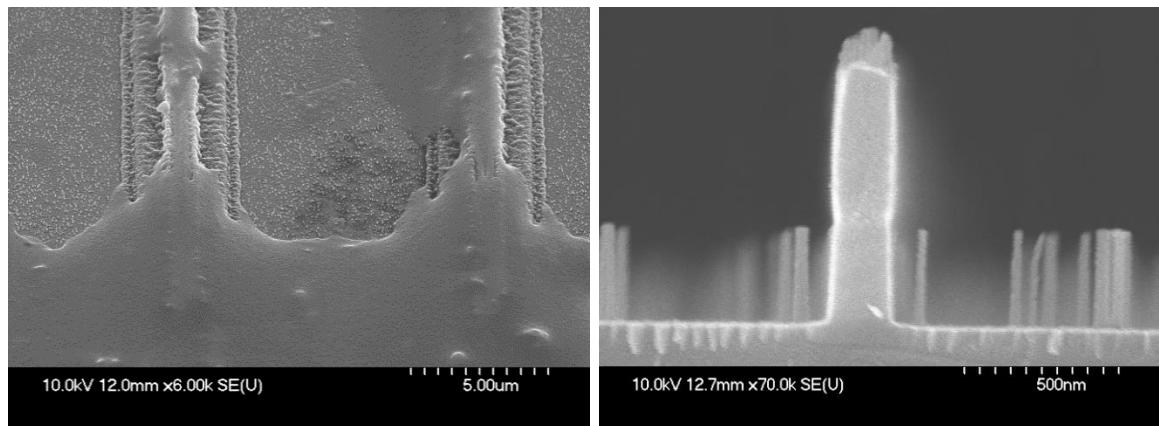


Figure 4-6. Sample cleave and clean process.



**Figure 4-7. Contaminated surface and ‘grass’ after etch.**

For step ②, before getting the PMMA lift-off mask, etched markers used for alignment between layers were prepared in e-beam lithography (Au is not used due to the high anneal temperatures in subsequent steps). Two layers of 12% 2010 PMMA were used as the etch resist mask and written at a dose of  $650 \mu\text{C}/\text{cm}^2$  with a 64 nA e-beam current along with a VRU (variable resolution unit) of 16 under 100 kV at step ③. The sample was developed in 2.5:1 IPA: MIBK for 140 s followed by 45 s IPA at 23.5 Degrees. At step ④, an Si etch tool was used to etch the markers down into the Si layer on the  $\text{SiO}_2$ , which was confirmed using the end point detector to get the interferometer trace. Therefore, all of these markers are 500 nm deep, the same thickness as that of the Si core layer. At step ⑤, overnight, hot acetone (50 Deg C) and then 2 mins Oxygen Plasma ash were adopted to remove the remnant PMMA resist.

At step ⑥, a lift-off mask was patterned on the SOI samples for MO garnet material deposition. Two layers of 15% 2010 PMMA and 4% 2041 PMMA were applied on the sample. After spinning the 15% 2010 PMMA, 10 mins on the hotplate at 180 Degrees, and 1.5 hours in a 180 Degree oven were conducted for thermal curing. At step ⑦, the lift-off mask was written at a dose of  $1000 \mu\text{C}/\text{cm}^2$  with a 64 nA e-beam current along with a VRU of 16 under 100 kV. Then, the lift-off mask was developed in 2.5:1 IPA: MIBK for 65 s followed by 45 s in IPA at 23.5 Degrees. At step ⑧ and ⑨, samples were carefully packed and sent to the US for magneto-optical garnets deposition by our collaborators, Andrew Block (involved in the project in the first year), then Prabesh Dulal (main collaborator throughout the project) in Professor Bethanie Stadler’s group at the University of Minnesota.

According to the simulation results in Chapter 3, the optimal thickness for the YIG layer it is 110 nm, for TIG/Bi-TIG it is 150 nm, and for Ce-TIG/Ce-YIG it is 200 nm. As there is atomic trajectory restriction in the RF deposition process, thicker garnet, 300 nm, was deposited.

Once returned, a lift-off process was carried out at step ⑩. Four hours in hot acetone would lift-off the bi-layer PMMA mask and 5 mins in acetone and 5 mins in IPA in an ultra-sonic bath were used to give thorough PMMA lift-off and a good clean of the whole sample. Then, it was annealed in an RTA (rapid thermal annealing) tool in an oxygen atmosphere at 900° for 2 mins to achieve crystallisation at step ⑪. Afterwards, the crystallisation phase was analysed in an XRD (X-ray diffractometer) and with an EBSD (electron backscatter diffraction) by our collaborators.

Hereafter, at step ⑫, a 100 nm thick  $\text{Si}_x\text{N}_y$  of the same refractive index as the garnet material, around 2.1 at a wavelength of 1550nm, was coated all over the sample surface to exclude the observed periodic loading effect that arose from slight offsets of the garnet segments on top of the Si waveguides. The slight offsets led to a reciprocal mode conversion from the periodic garnet segments (as the offset led to asymmetric profiled guides, in turn leading to mode conversion). The  $\text{Si}_x\text{N}_y$  film was deposited in an ICP-CVD (Inductively Coupled Plasma Chemical Vapor Deposition) tool. The standard recipe for  $\text{Si}_x\text{N}_y$  deposition is with  $\text{SiH}_4/\text{N}_2=7/6$  sccm, ICP/Platen=100/0 w at a pressure of 4 mTorr at 25 °C.

Then, at step ⑬ and step ⑭, HSQ (Hydrogen silsesquioxane)-negative resist was spun at 2000 rpm and baked on a hotplate for 15 mins and written at a dose of 650  $\mu\text{C}/\text{cm}^2$  with an 8 nA e-beam current along with a VRU of 8 under 100 kV. Afterwards, the mask was developed in neat TMAH for 30 s, followed by 30 s in RO (de-ionised) water, 30 s in RO (de-ionised) water, and 45 s in IPA.

Then, at step ⑮, the pattern was transferred to the  $\text{Si}_x\text{N}_y$  layer by etching into the  $\text{Si}_x\text{N}_y$  layer with the 80 PLUS RIE tool. Gas  $\text{CHF}_3/\text{O}_2 = 50/5$  sccm was used to get vertical features at room temperature while setting the platen power to 150 w and the pressure at 55 mTorr.

Afterwards, at step ⑯, the STS-ICP dry etch tool was usually used to etch Si to obtain the Si waveguide. Gas  $\text{SF}_6/\text{C}_4\text{F}_8$  at 30/90 sccm was demonstrated to get a straight sidewall for Si. The recipe was run at the pressure of 10 mTorr with the platen at 12 w and the coil power 600 w at room temperature. The He/Cool rate was 7/4, and the DC-bias voltage was 152 V. The etch rate was measured at

150nm/min with the selectivity to HSQ of 3:1. Meanwhile, an ICP 180 dry etch tool can be also used for this sample if the STS-ICP is not available. In this tool, gas  $\text{Cl}_2/\text{BCl}_3$  at 18/2 sccm is used to etch Si (Temp=20 Deg, ICP Power=1000 w, Platen=60 w, Pressure=20, Back cooling=10 Torr). It took 3 mins and 40 s to etch down 500 nm Si. The HSQ remaining on top was taken as an  $\text{SiO}_2$  cap rather than removed after the dry etch.

The whole fabrication process was then finished. Waveguides with alternating magneto-optical garnet-HSQ upper cladding segments were completed and ready to cleave. The two sides of the sample were cleaved to form a Fabry-Perot cavity in order to adopt the Fabry-Perot loss measurement method. Before cleaving, the sample was coated with PMMA resist for protection against particle pollution from the cleaving process. After cleaving, the cleaved piece was soaked in Acetone and IPA for 5 mins to remove the resist and any other introduced particles or organics in the cleaving process.

All fabrication processes were carried out in the James Watt Nanofabrication Centre (JWNC) based at the University of Glasgow. Finally, the cleaved central piece was used for all optical measurements and the two cleaved side pieces were used to check the thickness and profile of each layer, the sidewall roughness, and the cross-section profile under a scanning electron microscope (SEM).

Below, Figure 4-8 (a) displays the cross section of a waveguide on the completed sample with Bi-TIG as upper cladding. From top to bottom, HSQ,  $\text{Si}_x\text{N}_y$ , Bi-TIG, and Si are clearly shown. Figures 4-8 (b), (c), and (d) show the octant and the cross section of the structure with  $\text{Si}_x\text{N}_y$  removed by HF.

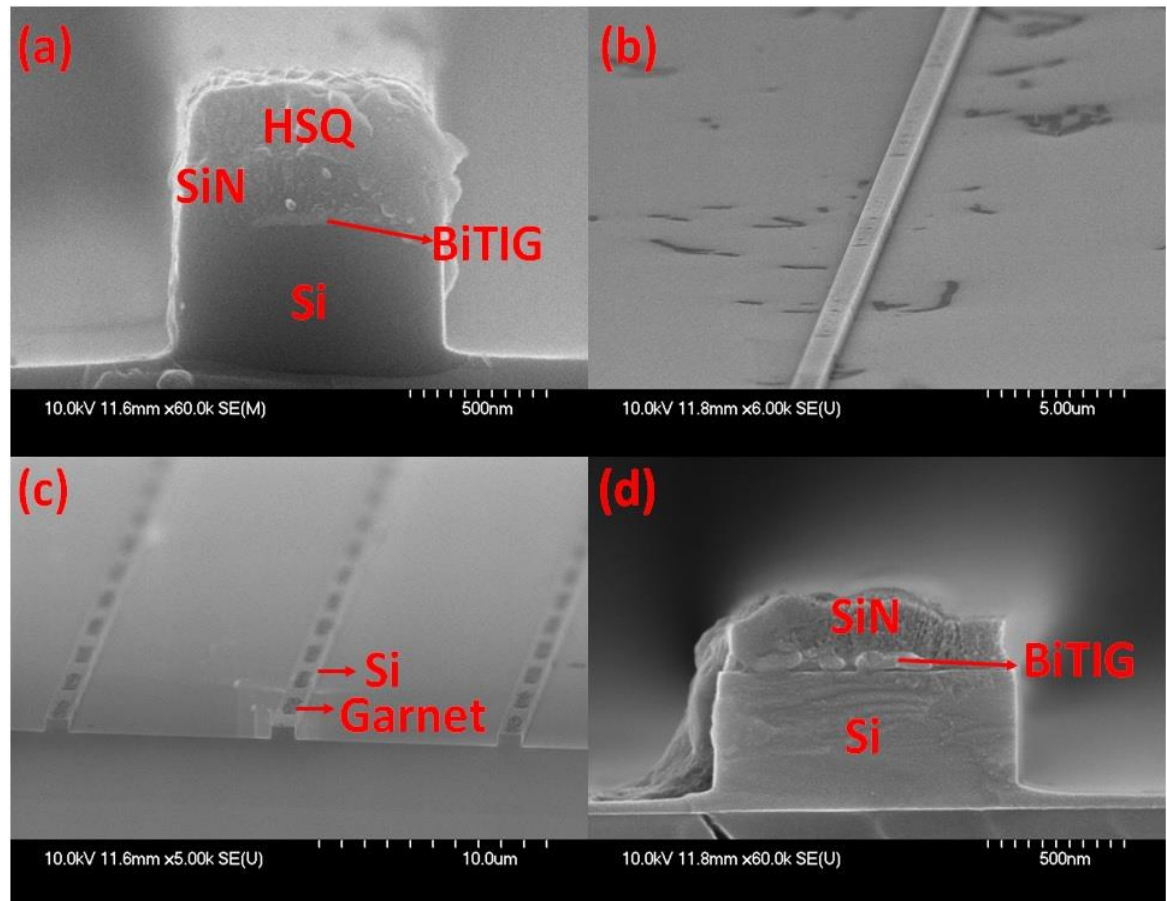


Figure 4-8 (a). The cross section of a waveguide on the Bi-TIG sample. From top to bottom, HSQ, SixNy, Bi-TIG, and Si are clearly shown in the micrograph. Figures 4-8 (b), (c), and (d) show the octant and the cross section of the structure with SixNy removed by HF.

Among all the fabrication steps, great effort was spent on the optimization of the lift-off process (including the preparation of the lift-off mask, MO garnet deposition, lift-off) and the RTA process.

### 4.2.3 Lift-off

As discussed above, the bilayer structure of PMMA with different sensitivities results from the different molecular weights of the resist. After development, a decent undercut profile can be created (the right bilayer structure of Figure 4-3). Using the heavier resist on top of the lighter resist, it is very useful for the lift-off process. The ideal lift-off mask for our application is the one that, after lift-off, has no ‘buttresses’ or edges on the garnet segments [77]. They will lead to an increase of optical propagation loss in finished devices, mainly through scattering loss. A nice undercut profile for garnet deposition is shown in Figure 4-

9 [77]. The two layers of PMMA resist is a layer of 15% 2010 series underneath and a layer of 4% 2041 series on top. The optimised e-beam mask writing and development parameters are confirmed to be: the lift-off mask was written at a dose of  $1000 \mu\text{C}/\text{cm}^2$  with a 64 nA e-beam current along with a VRU of 16 under 100 kV. Also, the lift-off mask was developed in 2.5:1 IPA: MIBK for 65 s, followed by 45 s in IPA at 23.5 Degrees. The garnet segments after lift-off under optical microscope and SEM are shown in Figure 4-10.

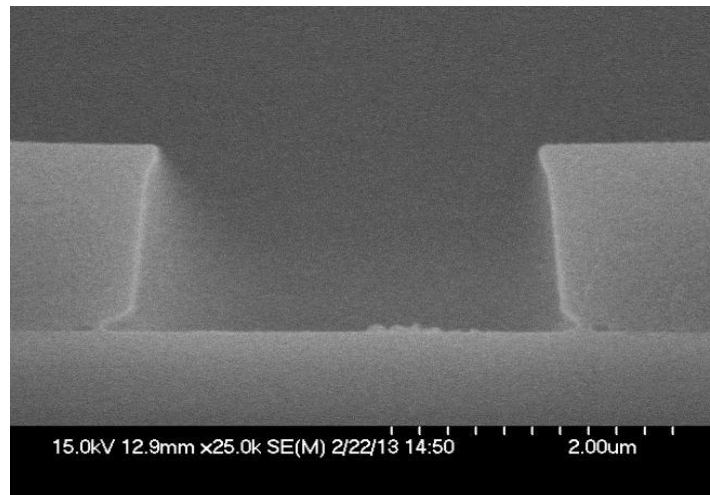


Figure 4-9. Cross section undercut profile of two layers of PMMA for the garnet lift-off.

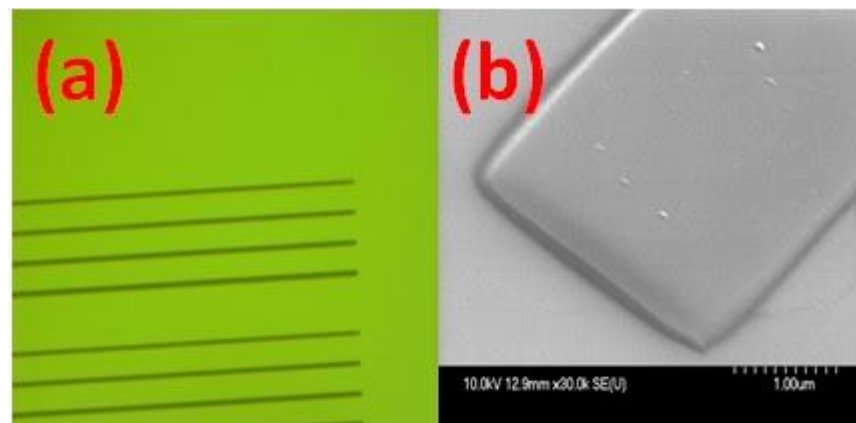


Figure 4-10. Left a) is the optical micrograph for the garnet islands after lift-off, and right b) is the  $2.2 \mu\text{m}$ -wide garnet islands under SEM when written with the dose of  $976 \mu\text{C}/\text{cm}^2$ .

The lift-off profile is especially sensitive to the parameters in the development step. The development temperature, time, and the concentration of the developer solvent (the ratio of MIBK and IPA, MIBK - Methyl isobutyl ketone, the chemical formula is  $(\text{CH}_3)_2\text{CHCH}_2\text{C}(\text{O})\text{CH}_3$ ) heavily affect the resist profile. The

higher the temperature of the developer or the longer the development process is, the further along the continuum of solubility the dissolution will extend [153], causing the feature width to widen, and the undercut profile to resolve. The concentration of the developer solvent plays a vital role in the formation of the feature. Table 4-1 [154] lists the sensitivity of different concentrations of developer and how they affect the resolution of the pattern features. The more concentrated the developer solvent is, such as neat MIBK and 1:1 MIBK/IPA, the more sensitive it is; in particular, the development time and temperature. By contrast, the more dilute the developer solvent is, such as 1:3 MIBK/IPA, the better the resolution that can be provided. Depending on applications, the proper combination of these parameters can be employed.

Developer Composition	Resolution	Sensitivity/Throughput
1:1 MIBK to IPA	High	High
1:2 MIBK to IPA	Higher	Medium
1:3 MIBK to IPA	Very high	Low
MIBK	Low	High

**Table 4-1. [23] The characteristics of different ratios of developers.**

At the first stage, the sample was developed 1:2 MIBK/IPA developer at 22°C for 75 s, followed by 45 s in RO water, and finished with 15 s in IPA. Here, a rinse in RO water after the 75 s in the developer helps to neutralise the developer and prevent further reaction by the remaining developer on the surface of the sample. However, buttresses were found at the corner of the segments after lift-off (Figure 4-11), which might result from the 1:2 developer solvent being aggressive to the features. Subsequently, a 1:2.5 MIBK/IPA developer solvent was adopted. The pattern was developed at 23.5°C for 35 s then directly in an IPA solvent for 45 s. Here, the RO rinse step was omitted so that the reaction kept going, but very slowly and mildly in the rinse step in the IPA solvent. It turned out that some of the resist was not cleared out totally. There were 30 s more development in the 1:2.5 MIBK/IPA developer carried out, and also finished with a 45 s rinse in the IPA solvent. This time, edges instead of buttresses were found around the islands (Figure 4-12). Based on this process, the final development process was taking shape. This time, the sample was developed at 23.5°C for 65

s, then directly in the IPA solvent for 45 s, from which lift-off segments without buttresses or edges were obtained (Figure 4-10).

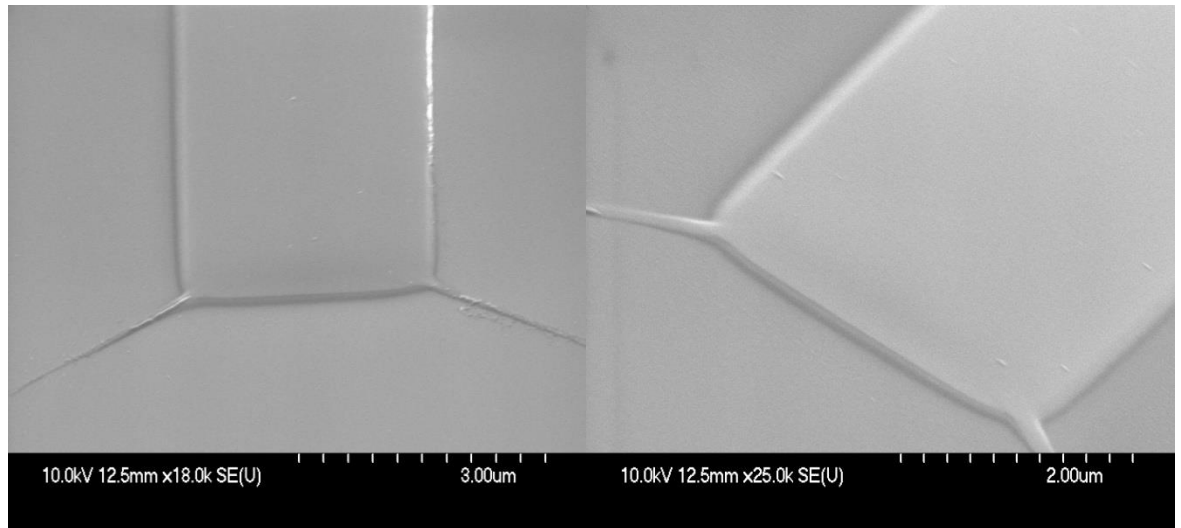


Figure 4-11. Buttresses are found at the corners of the segments after lift-off.

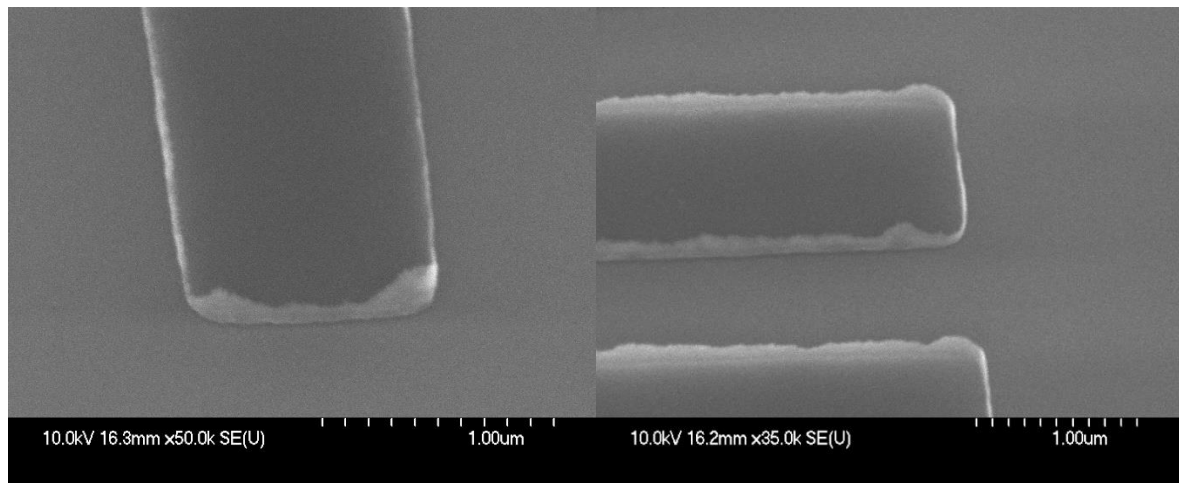
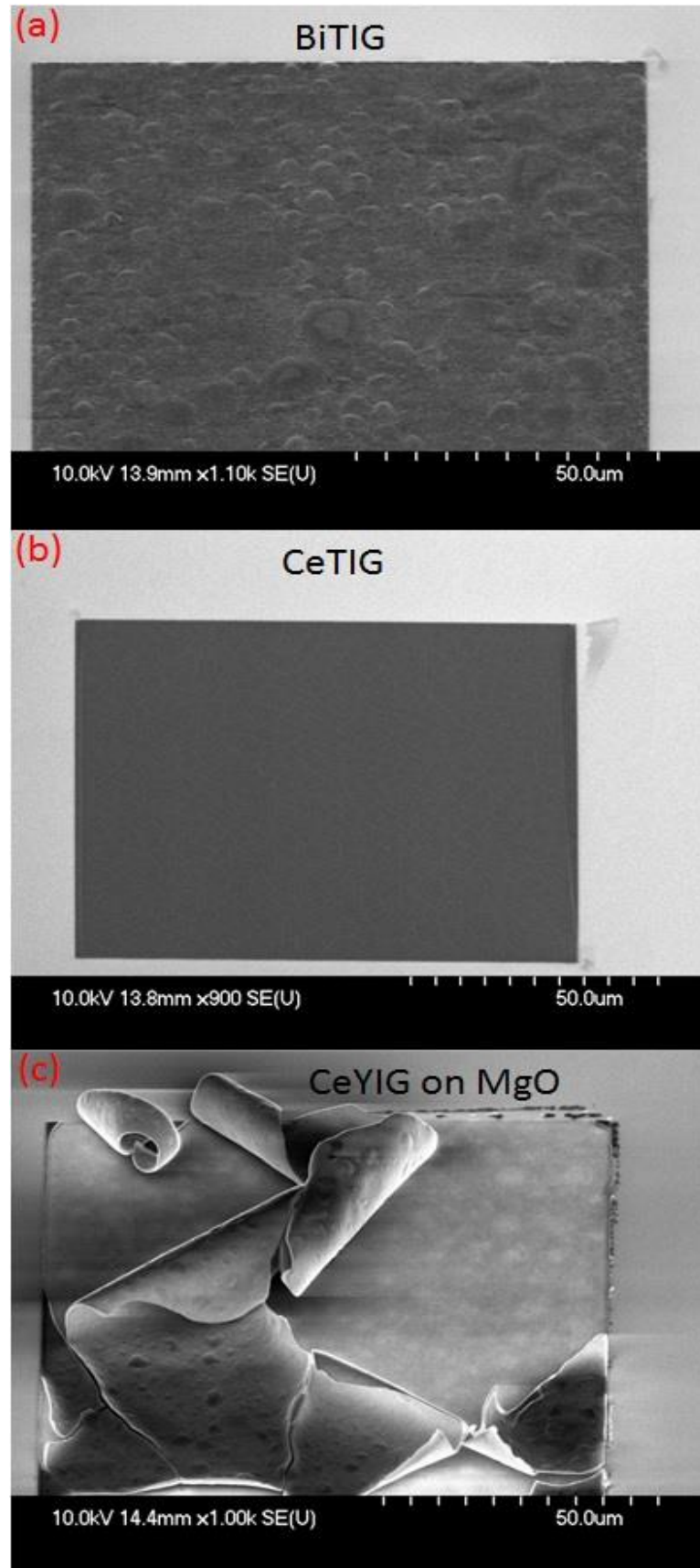


Figure 4-12. Edges instead of buttresses are found around the islands.

#### 4.2.4 RTA (Rapid Thermal Annealing)

Rapid Thermal Annealing (RTA) after lift-off was carried out to get the deposited magneto-optical layer crystallized. Here, the RTA process helped reduce the thermal budget of crystallization. It also offered the optimized crystalline conditions during the process where reactions between the deposited cladding layer and under-layer are decreased. Research carried out by our collaborators, Professor Bethanie Stadler's group from the University of Minnesota, shows that samples with YIG/TIG films on top should be annealed at no more than 800°C, and those with Ce-YIG films should be annealed at no more than 750°C, as higher temperature annealing will lead to cracks in the garnet film [136]. Figures 4-13 (a), (b), and (c) describe 100x100 µm square of Bi-TIG, Ce-TIG, and Ce-YIG on MgO material after annealing at 900°C for 2 mins. Cracks existed in all of the three patterns, and the square of Ce-YIG on MgO even started to peel off, which means that the stress was beyond the limit that part could bear.

This also explains why the rapid thermal annealing process needs to happen before the coating of the porous Si<sub>x</sub>N<sub>y</sub> layer, which also attributes a certain amount of stress to the substrate surface and waveguide structure, or else the stress from the Si<sub>x</sub>N<sub>y</sub> layer will be enlarged and the interaction and tension between the layers can lead to cracks during the thermal process. This gives damage to the waveguide structure and, therefore, gives such substantial propagation loss that no light is guided through.



Figures 4-13 (a), (b), and (c). 100x100 $\mu\text{m}$  square of Bi-TIG, Ce-TIG, and Ce-YIG on MgO material after annealing at 900 $^{\circ}\text{C}$  for 2 mins. Cracks exist in all of the three patterns and the square of Ce-YIG on MgO even starts to peel off, which means that the stress is beyond the limit.

Here in our application, periodic segments instead of wafer-scale whole thin film were deposited. Patterning the garnet material in small segments prior to the crystallisation process under rapid thermal annealing (RTA) helps to increase the stress tolerance and compensate the mis-match in thermal expansion between the garnet material and the substrate [136], thus avoiding any cracks in the garnet material after annealing. It turns out that all kinds of magneto-optical cladding layers can be annealed at or over 900°C, which also helps improve the crystallization percentage of the segments.

Before the actual annealing step, a 10 s Oxygen inlet and 10 s gas purge process was repeatedly performed (three times) to give a nice clean chamber, and also prepare the chamber for an O<sub>2</sub> atmosphere. Afterwards, O<sub>2</sub> process gas was inlet into the process chamber without pumping out until the pressure reached 80mBar. This ensures that the pressure was around 120~130mBar when the temperature rose over 900°C.

Then, the temperature was first raised to 350°C in 20 s at a ramp rate of 17.5°C/s, and stayed the same for 20 s, after which it was increased to the desired temperature (like 900/950°C) in 20 s and stayed for 120 s/2 mins. At the end of this step, it entered the cooling step. The default cooling process of the system lasted for 180 s with N<sub>2</sub> filling in the process chamber and cooling water circulating in the metal chamber walls. The simulated process and the actual annealing process for 900°C and 950°C is shown in Figure 4-14 and Figure 4-15, respectively.

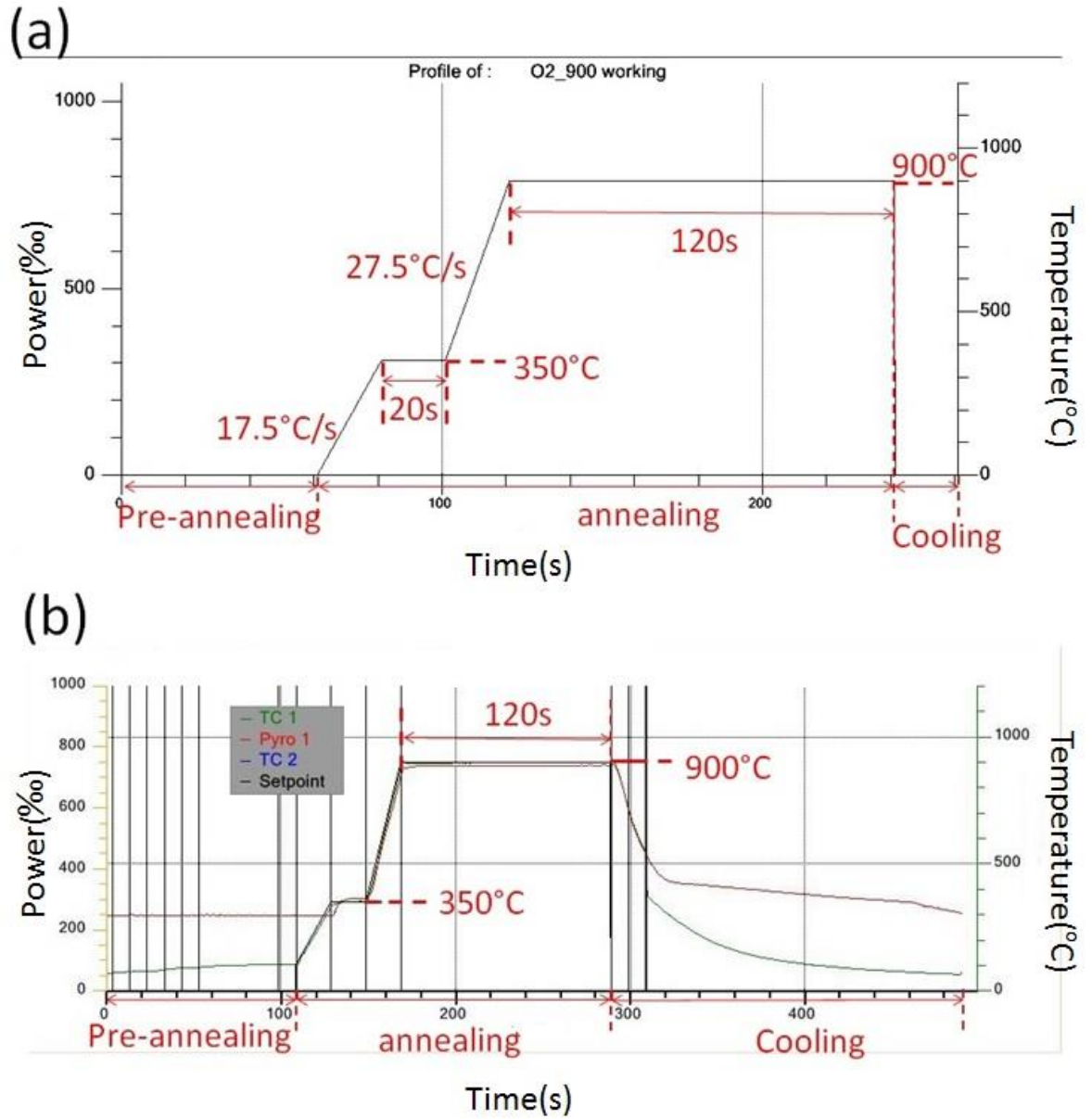


Figure 4-14. The simulated process (a) and the actual annealing process (b) for 900°C, respectively.

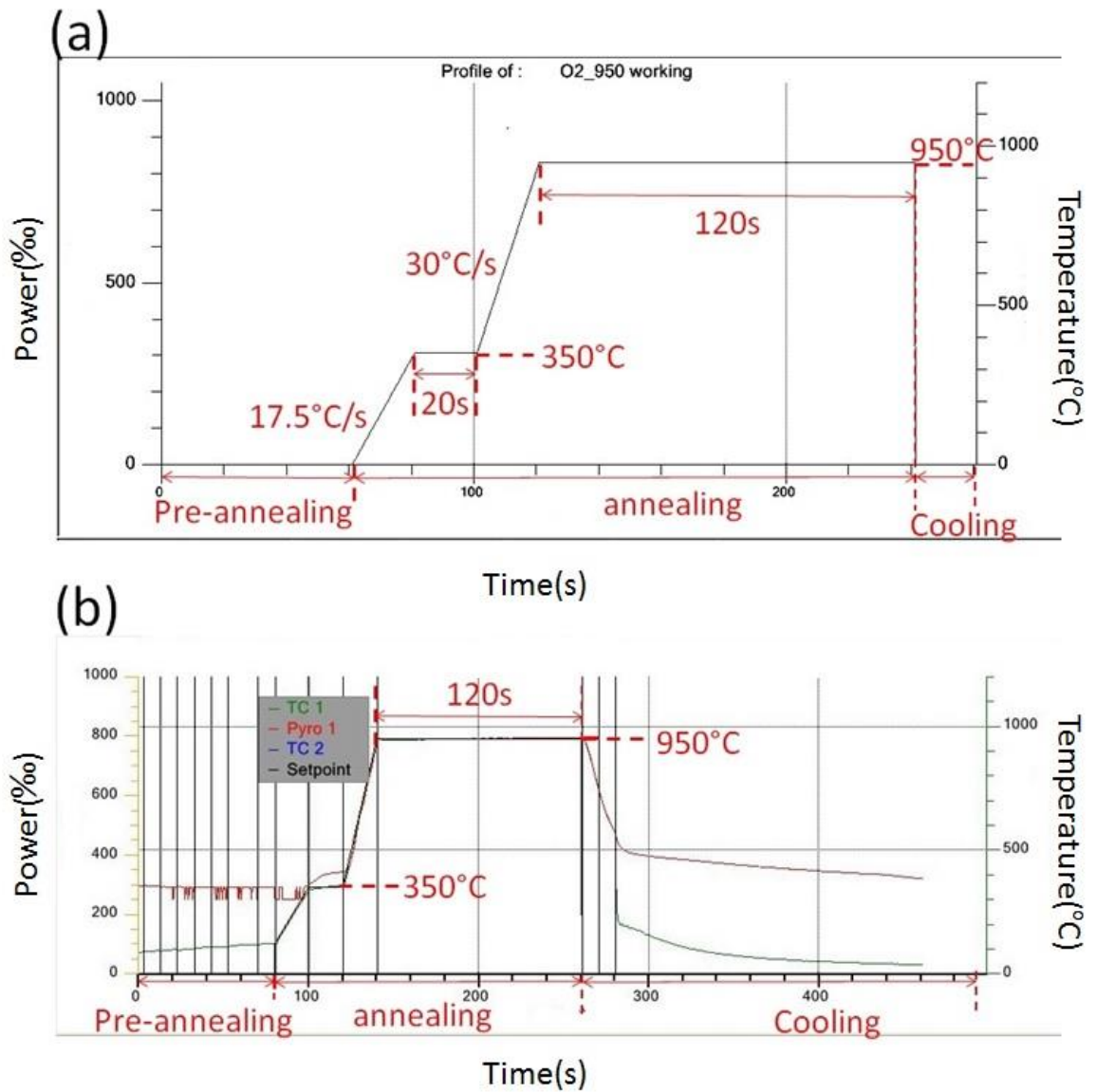
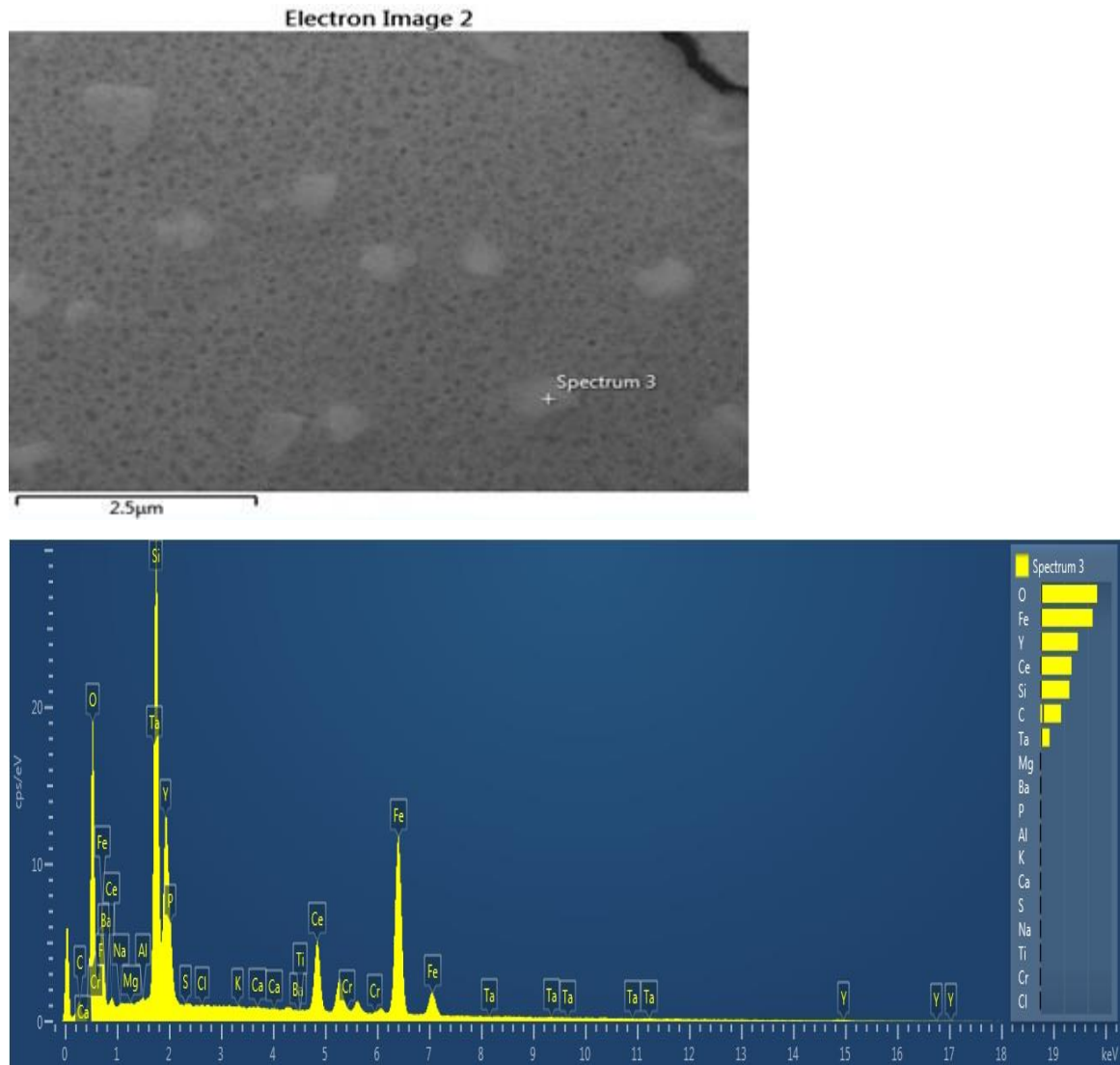


Figure 4-15. The simulated process (a) and the actual annealing process (b) for 950°C, respectively.

#### 4.2.5 Garnet Material Characterisation

Figure 4-16 displays the X-ray emission spectrum on the bright spot where the crystalline phase of Ce-YIG was found, from which we can confirm the existence of O, Fe, Y, Ce, and also an Si signal from the substrate surface on which the Ce-YIG islands sit. The ratio of all the elements can help work out the stoichiometry of the Ce-YIG garnet.



**Figure 4-16.** The X-ray emission spectrum on the bright spot where the crystalline phase of Ce-YIG was found, from which we can confirm the existence of O, Fe, Y, Ce, and also an Si signal from the substrate surface on which the Ce-YIG islands sit. The ratio of all the elements can help work out the stoichiometry of the Ce-YIG garnet. (Courtesy to Mr. Peter Chung in ISAAC from the School of Geographical and Earth Sciences, University of Glasgow, for the pics).

The Ce-TIG and Bi-TIG material is used to demonstrate how the characterisation for garnet material is carried out in SEM with different detector systems, including the topography (both the top-down view and the cross-section view) and the crystallographic structure.

There was 300nm Ce-TIG/Bi-TIG deposited in the multi-target radio-frequency (RF) sputtering tool in an oxygen atmosphere in various ranges of length, from 10-15 μm long segments, at a step of 0.5 μm to accommodate the substantive thermal expansion mis-match between garnets and semiconductor substrates, (in the University of Minnesota) before annealing. Because of atomic restriction where narrower deposition space restricts the angular trajectory of the ions, around 100nm-thick Ce-TIG/Bi-TIG material was deposited in the segments

area after lift-off[77]-[79]. Afterwards, the magneto-optical material was partially crystallised by rapid thermal annealing three times, at 900 Degrees, at 120 mbar in an oxygen atmosphere for 2 mins.

Figure 4-17 and Figure 4-19 show the Ce-TIG and Bi-TIG before and after annealing under a scanning electron microscope (SEM), respectively. The clear crystalline garnet phase can be easily seen from the micrographs of Bi-TIG after annealing. The three micrographs in Figure 4-18, taken in a 3-in-1 Multi-beam (gallium, neon, and helium ion beams) Ion Microscope, indicate the crystallisation of Ce-TIG in thicker segments; the white spots are crystallised while the grey areas are not. It can also be seen that the garnet has grown in different directions, making it poly-crystalline with the grain size ranging from 20-50 nm.

Some Electron Backscattered Scanning Diffraction results of Bi-TIG are displayed in Figure 4-20. (a) shows the EBSD diffraction pattern for both the Si substrate and the Garnet segments pattern; (b) shows the EBSD mapping results in the grating pattern in (a); coloured spots are crystallised. It is clearly seen that it is poly-crystalline and partially crystallised. Later, in order to remove the periodic loading effect of the garnet segmented islands, 100 nm  $\text{Si}_x\text{N}_y$  with the same refractive index of 2.1 with garnets was coated all over the sample in an ICP deposition tool. Therefore, the garnet segments of different lengths were alternating with  $\text{Si}_x\text{N}_y$  of different lengths in the gap, corresponding to the calculated half-beat length/coherence length between the fundamental quasi-TE and quasi-TM modes [86]. Silica waveguide masks aligned to the garnet segments were written by electron-beam lithography of spun HSQ, with widths from 600 to 1100 nm. Silicon-core waveguides were formed with fluorine-based plasma processes to etch through the  $\text{Si}_x\text{N}_y$  layer and Si layer in an 80+ RIE tool and an STS ICP etcher. Here, all the waveguides were etched down 500 nm to the  $\text{SiO}_2$  layer (Figure 4-21).

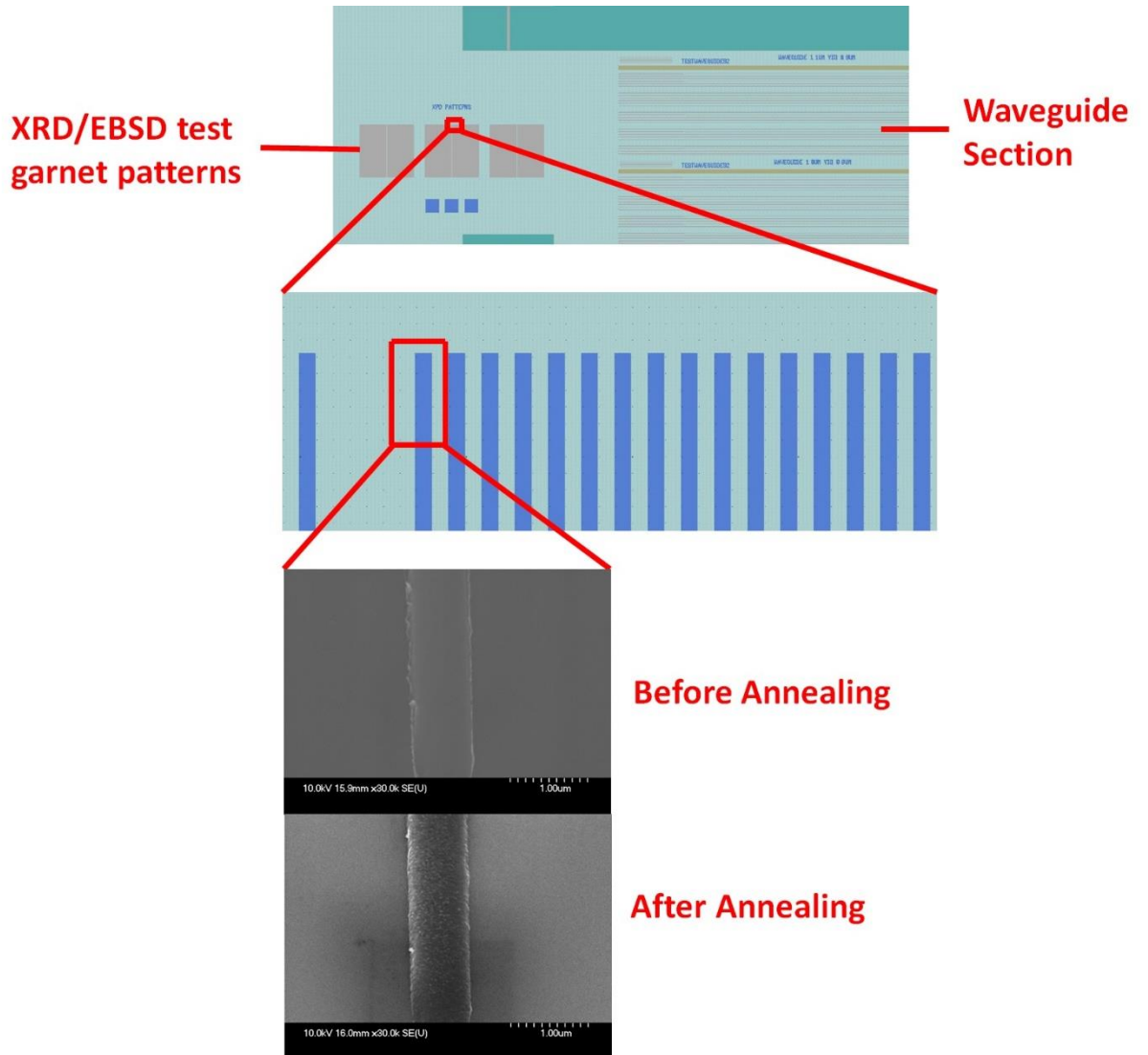
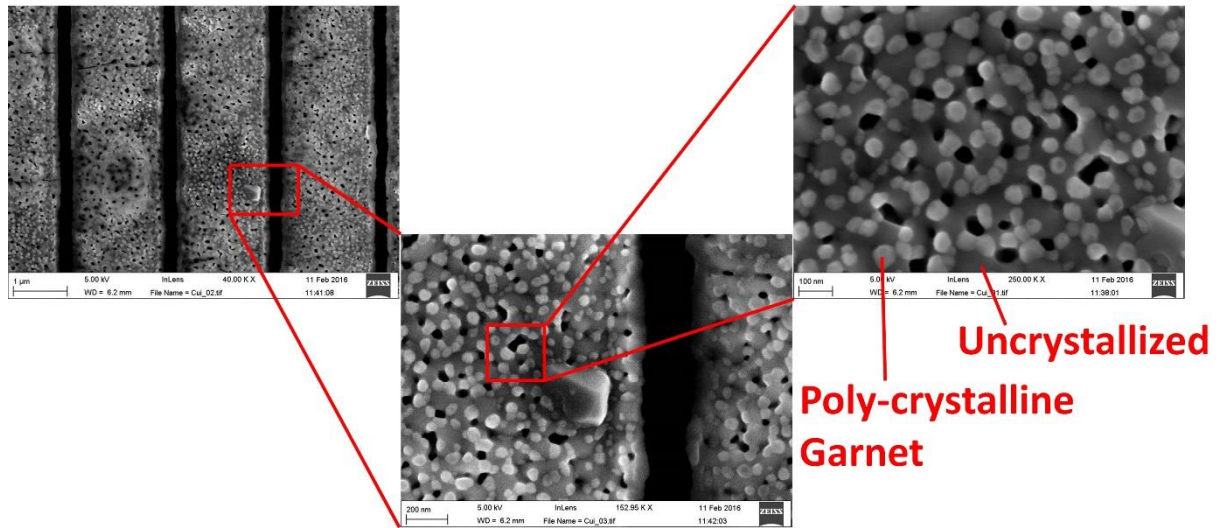
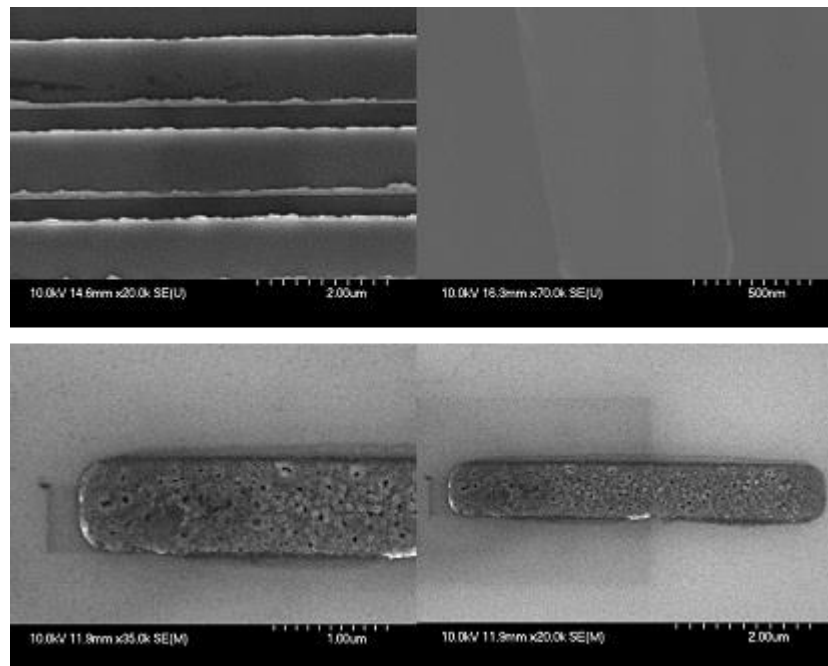


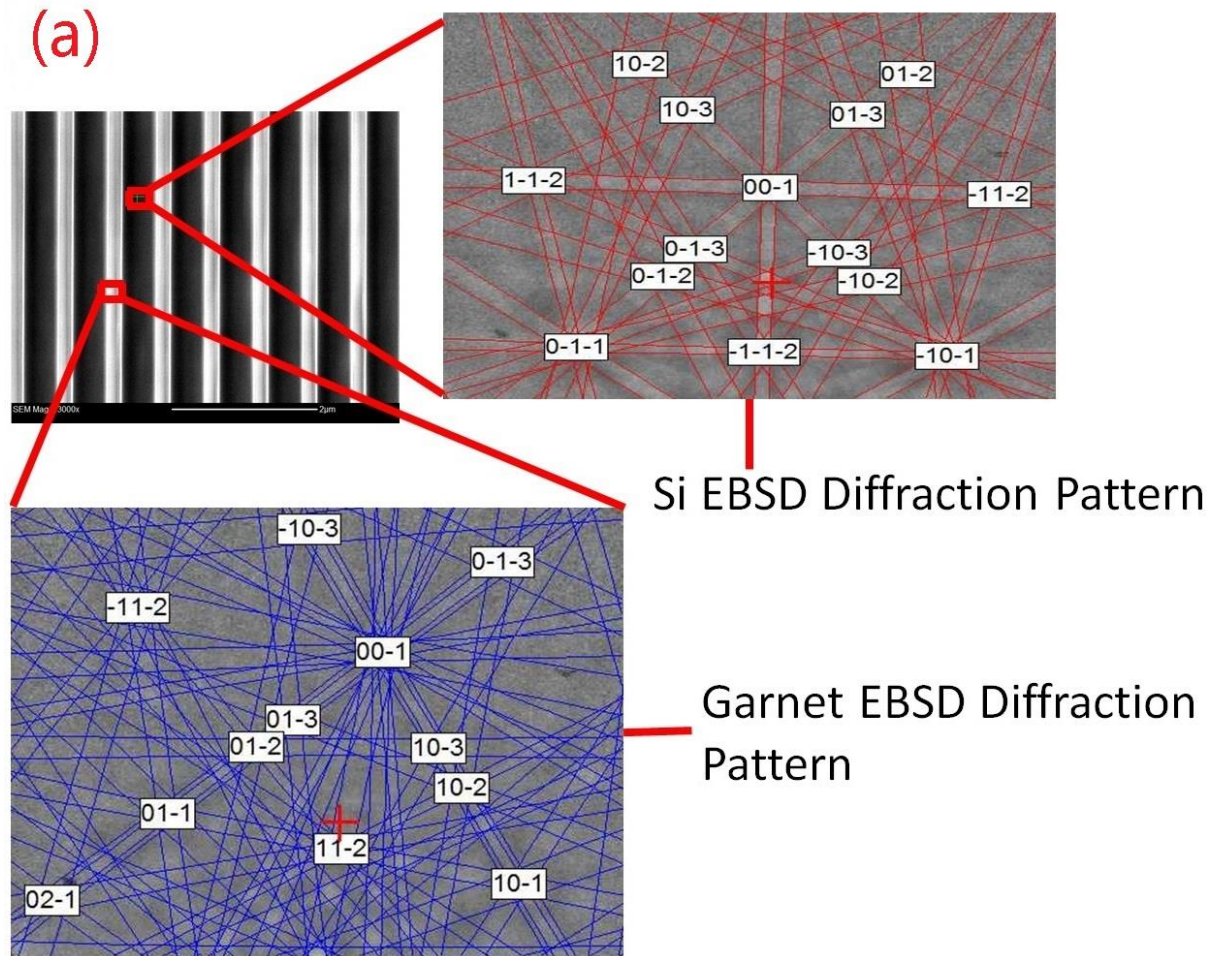
Figure 4-17. The upper two pics show the position of the segment in an e-beam mask taken under SEM. The upper SEM micrograph is the Ce-TIG segments after lift-off. The lower SEM micrograph is the Ce-TIG segments after annealing three times at 900 deg at 120 mbar in an oxygen atmosphere for 2 mins.



**Figure 4-18.** The three micrographs taken in a 3-in-1 Multi-beam (gallium, neon, and helium ion beams) Ion Microscope indicate the crystallisation of Ce-TIG in thicker segments; the white spots are crystallised while the grey areas are not. It can also be seen that the garnet has grown in different directions, making it poly-crystalline with the grain size ranging from 20-50 nm. (Courtesy to Mr. Peter Chung in ISAAC from the School of Geographical and Earth Sciences, University of Glasgow for the micrographs).



**Figure 4-19.** The upper two micrographs are the Bi-TIG segments after lift-off. The lower two micrographs are the Bi-TIG segments after annealing three times at 900 deg at 120 mbar in an oxygen atmosphere for 2 mins. The clear crystalline garnet phase can be easily seen from the micrographs after annealing.



(b)  
EBSD mapping over the segments

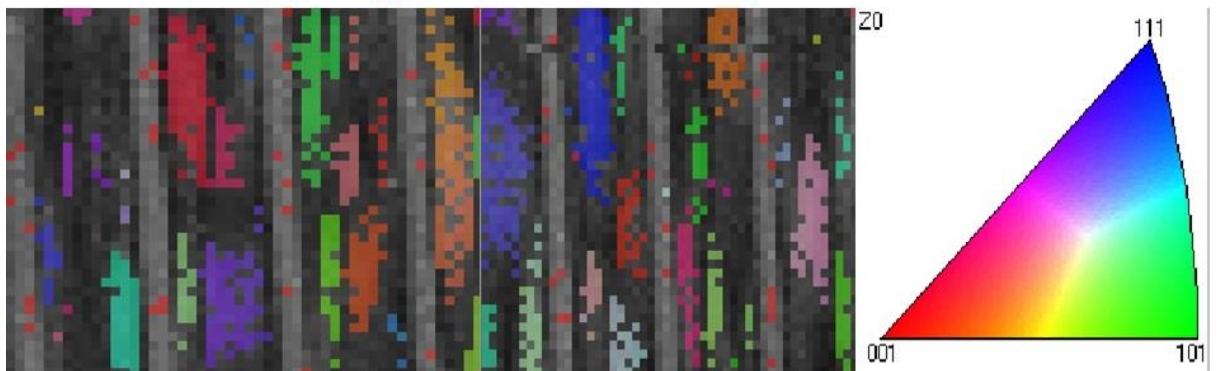
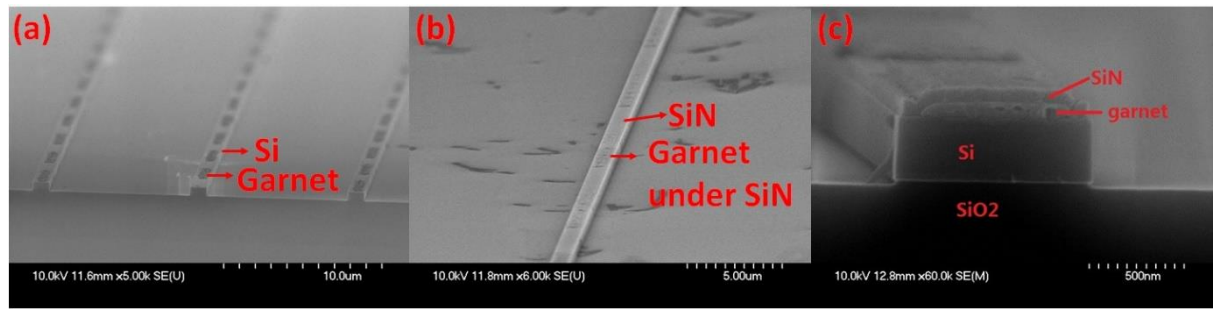


Figure 4-20. EBSD results of annealed Bi-TIG: (a) shows the EBSD diffraction pattern for both the Si substrate and the Garnet segments pattern; (b) shows the EBSD mapping results in the grating pattern in (a); the coloured spots are crystallised. It is clearly seen that it is polycrystalline and partially crystallised.



**Figure 4-21.** The micrographs (a) and (b) show the periodic alternating garnet segments with bare Si or Si<sub>3</sub>N<sub>4</sub>; micrograph (c) shows the cross-section profile of all the layers: Si core layer, garnet cladding layer, and Si<sub>3</sub>N<sub>4</sub> layer.

#### 4.2.6 Effect of MgO Buffer Layer on the Crystallisation of the Magneto-optical Garnets

Rapid Thermal Annealing (RTA) tests after lift-off were carried out to find whether a buffer layer, MgO, or a seed layer, YIG, is needed for different garnet materials to crystallize. Even using the RTA process, the problem for optimal crystallization of Ce-doped YIG with rather high Faraday rotation quality (giving about 3700 deg/cm) still remains. Our collaborators, Professor Bethanie Stadler's group from the University of Minnesota, have conducted extensive trials and made some of the best quality Ce-YIG film [129] [136] to date. A seed/buffer layer of MgO/YIG will be deposited before the Ce-YIG; the YIG layer can act as a virtual substrate to enhance Ce-YIG's crystallization [149] at lower temperatures.

However, though our collaborators have developed mature skills to produce garnet films of high quality, as it is garnet segments and not a whole thin film that is used in this project, research needed to be carried out by ourselves to confirm whether garnet material patterned in segments of a much smaller scale before annealing hold the same material properties as the whole thin film.

For the first set of samples, YIG was tried with or without the MgO buffer layer annealed at several different temperatures: pure YIG were annealed at 800°C (Figure 4-22 (1a) and (1b)); YIG on the MgO seed layer were annealed at 800°C (Figure 4-22 (2a) and (2b)); YIG on the MgO seed layer were annealed at 825°C (Figure 4-22( 3a) and (3b)); and YIG on the MgO seed layer were annealed at 900°C (Figure 4-22 (4a) and (4b)).

Figure 4-22 presents the four situations in both optical pictures (top) and scanning electron micrographs (bottom). All annealing processes were performed in about 150 mB oxygen for 120 s. Some erosion of the YIG segment was observed for the YIG alone on SOI annealed at 800°C, while, for the other three tests, no erosion was seen. However, for the YIG on the MgO seed layer that were annealed at 825°C and 900°C, there were some obvious and visible changes to the segment morphology under both optical microscope and SEM, which is more obvious for the one annealed at 900°C. It seems that there is some unclear phase within the grains at a comparable size to the segment width. Judging from the micrographs taken in a 3-in-1 Multi-beam (gallium, neon, and helium ion beams) Ion Microscope (Figure 4-18), which clearly shows the poly-crystalline phase with the grain size ranging from 20-50 nm in the segments after annealing, it can be inferred that higher temperatures help the crystallisation of YIG on MgO. While YIG can get crystallized without an MgO buffer layer, the MgO buffer layer seems to increase YIG's tolerance for higher temperature annealing. From the EBSD analysis provided by our partners, all samples here were partially crystallized.

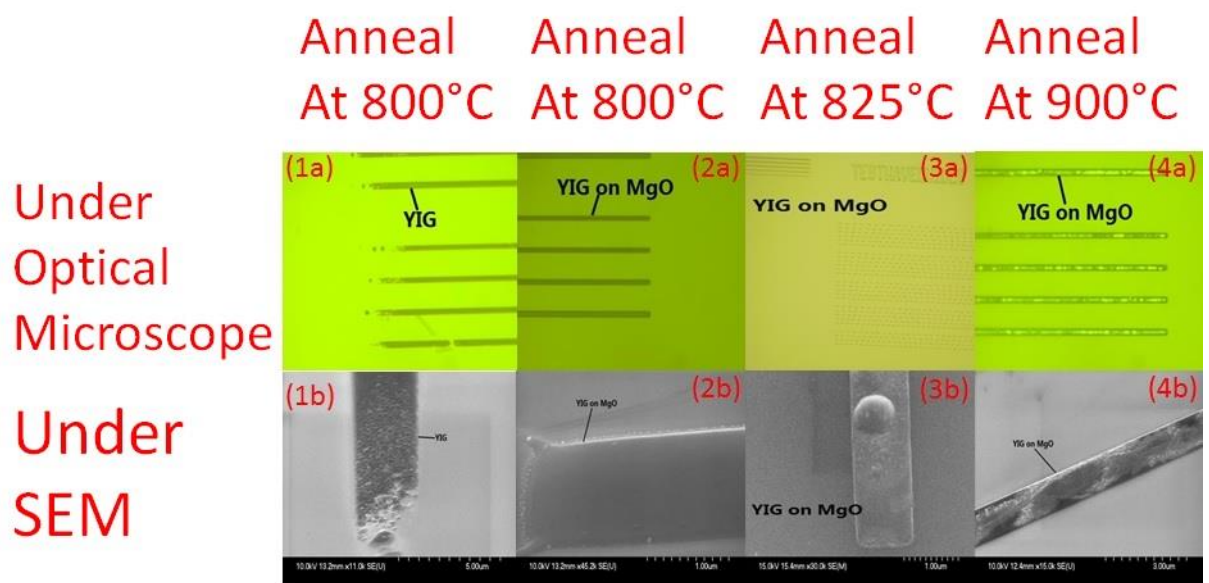
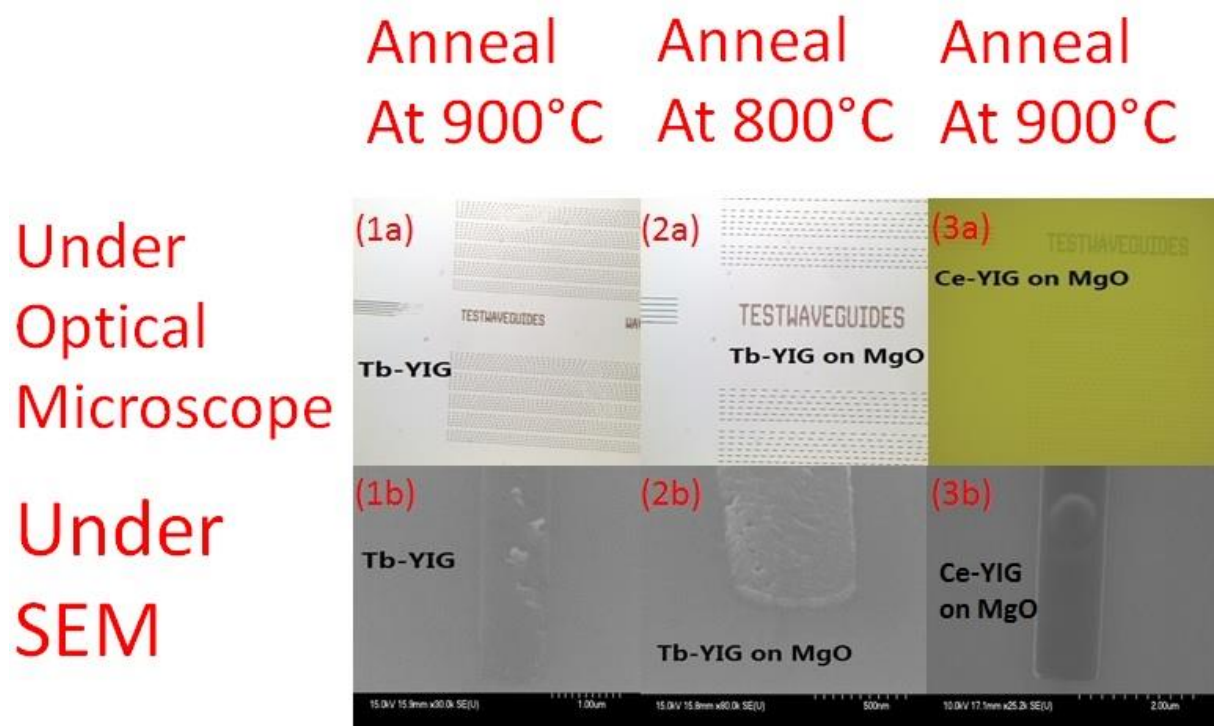


Figure 4-22. 1a) and 1b): the Optical microscope and SEM micrograph for YIG were annealed at 800°C; 2a) and 2b): the Optical microscope and SEM micrograph for YIG on the MgO seed layer were annealed at 800°C; 3a) and 3b): the Optical microscope and SEM micrograph for YIG on the MgO seed layer were annealed at 825°C; and 4a) and 4b): the Optical microscope and SEM micrograph for YIG on the MgO seed layer were annealed at 900°C.

In addition to YIG, other magneto-optical materials were also researched, including Ce-YIG and TIG, which demonstrate a larger and opposite sign for the saturated magneto-optic Faraday rotation effect at room temperature when compared to YIG. This time, we tried Tb-YIG alone annealed at 800°C, Tb-YIG on MgO (120 nm/5 nm) annealed at 900°C, and Ce-YIG on MgO annealed at 900°C. All annealing processes were performed in about 150 mB oxygen for 120 s. From the EBSD analysis provided by our partners, all samples here were partially crystallized. Both optical and SEM micrographs are shown in Figure 4-23.



**Figure 4-23.** 1a) and 1b): the Optical microscope and SEM micrograph for Tb-YIG on MgO (120nm/5nm) annealed at 900°C; 2a) and 2b): the Optical microscope and SEM micrograph for Tb-YIG alone annealed at 800°C; and 3a) and 3b): the Optical microscope and SEM micrograph for Ce-YIG on MgO annealed at 900°C.

Our partner group provided the analysis for the crystallisation of garnets using electron backscatter diffraction (EBSD). The research result on the effect of the buffer/seed layer (MgO/YIG) on the crystallisation of various garnets is summarized in Table 4-2. It uncovers that YIG, TIG, Bi-TIG, and Ce-TIG do not require a buffer/seed layer to get crystallized, while Ce-YIG needs either a buffer layer/MgO or seed layer/YIG to prevent it from getting oxidised first, and to enable it to achieve the garnet phase upon annealing.

As discussed in Chapter 3, compared to YIG, MgO is a better candidate as a buffer layer. MgO is a non-magnetic material, while YIG is of the opposite Faraday rotation coefficient to that of Ce-YIG. Placed under a Ce-YIG layer, YIG will weaken the MO effect of Ce-YIG. However, better controllability has been achieved in the crystalline process of Ce-YIG on YIG. Thus, both Ce-YIG on YIG and Ce-YIG on MgO have been chosen in this research. From the simulation in Chapter 3 and also in paper [77], we know that just a 10nm seed/buffer layer will make a big difference and substantially decrease the interaction between the garnet layer and the guided evanescent tail. Ce-TIG becomes the optimal material. It has a comparative level quantity of Faraday coefficient of about  $-2600^\circ/\text{cm}$  to Ce-YIG, and gets crystallized without the need of a buffer/seed layer. Thus, the range of promising material used in this project was chosen as TIG ( $\theta_F(\text{TIG})=500 \text{ deg/cm}$  at 1550 nm), Bi-TIG ( $\theta_F(\text{Bi-TIG})=-500 \text{ deg/cm}$ ), Ce-YIG on MgO ( $\theta_F(\text{Ce-YIG})=-3700 \text{ deg/cm}$ ), Ce-YIG on YIG ( $\theta_F(\text{Ce-YIG})=-3700 \text{ deg/cm}$ ), and Ce-TIG ( $\theta_F(\text{Ce-TIG})=-2600 \text{ deg/cm}$ ).

Considering that high temperature annealing ( $900^\circ\text{C}$ ) will not provide any obvious harm to the garnets in our application, later on, the garnet segments used in actual devices were all annealed at  $900^\circ\text{C}$ , or even higher at  $950^\circ\text{C}$ .

	Material	Thickness(nm)	Thickness of MgO/YIG(nm)	Annealing Temp( $^\circ\text{C}$ )	EBSD Result
No Buffer/Seed Layer	YIG	120	0	800	Partially Crystallized
	TIG	120	0	800	Partially Crystallized
	Bi-TIG	200	0	900	Partially Crystallized
	Ce-TIG	200	0	900	Partially Crystallized
With Buffer/Seed Layer	Ce-YIG	200	20nm YIG	800/900	Partially Crystallized
	Ce-YIG	200	12nm MgO	900	Partially Crystallized

**Table 4-2.**The effect of a seed layer (MgO/YIG) on the crystallisation of various garnets.

Besides, the garnet islands are well aligned so as to act as the magneto-optic alternating upper cladding on top of the Si waveguides (Figure 4-24). We can see from the picture that a set of waveguides with different widths have been

designed, 600 nm-1100 nm. The width of the garnet is about 100-200 nm less than that of the waveguide in order to increase the misalignment tolerance. In each waveguide set of fixed width, there are five sets of waveguides of different lengths of garnet segments and gaps. Here, as shown in the bottom graph of Figure 4-24, the width of the waveguide is fixed at 600 nm and the width of the garnet segments is 500 nm. The length of the garnet segments ranged from 9  $\mu\text{m}$ -11  $\mu\text{m}$  with an increment of 0.5  $\mu\text{m}$ . From bottom to top, the length of the garnet islands were 9  $\mu\text{m}$ , 9.5  $\mu\text{m}$ , 10  $\mu\text{m}$ , 10.5  $\mu\text{m}$ , and 11  $\mu\text{m}$ , respectively. Within each sub-set, different gaps are considered to get different duty cycles. For the length of 9  $\mu\text{m}$ , the gap starts from 6  $\mu\text{m}$  and ends at 9  $\mu\text{m}$  with an increment of 1  $\mu\text{m}$ , making the duty cycles 15  $\mu\text{m}$ -18  $\mu\text{m}$ .

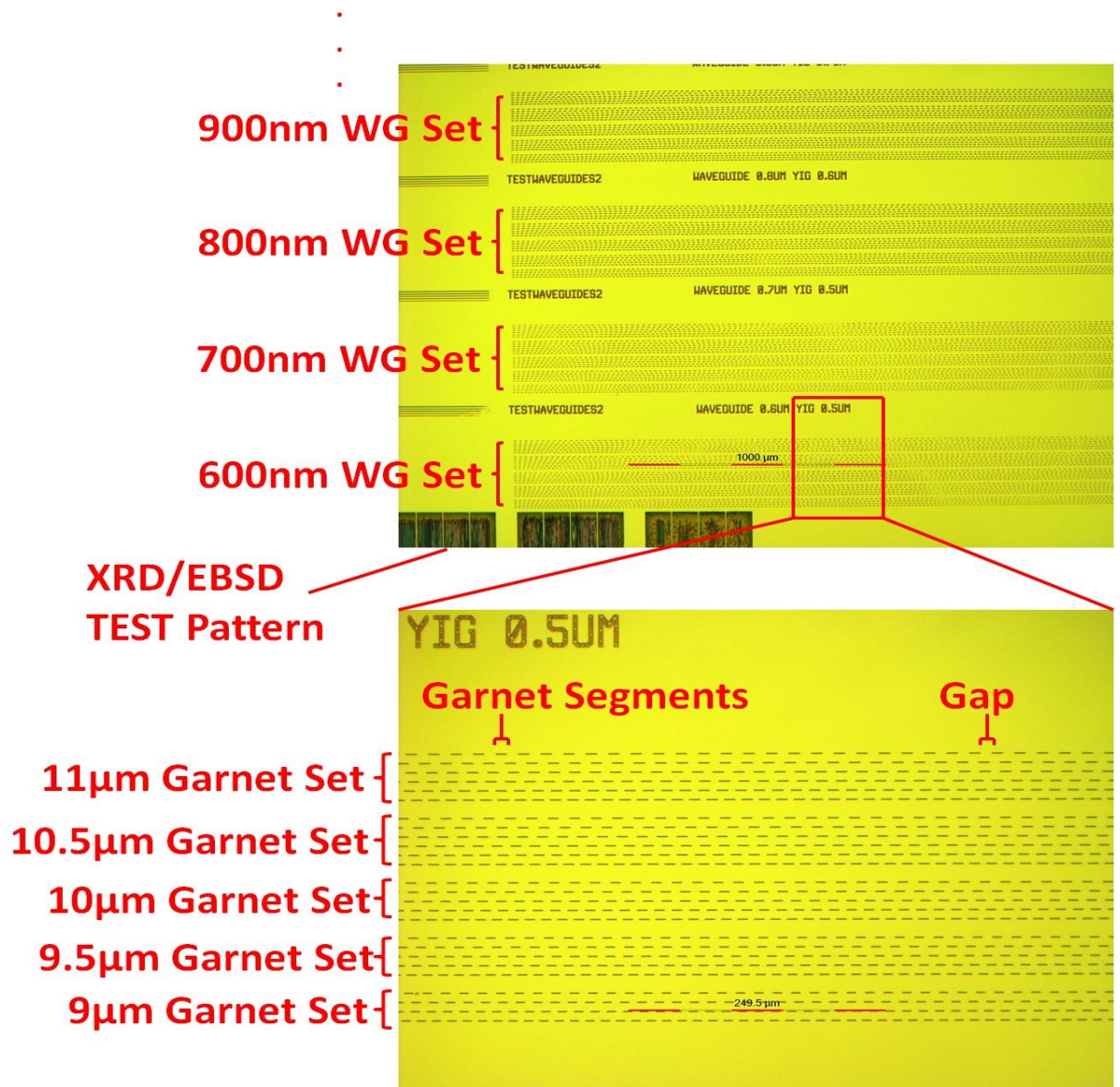


Figure 4-24. General map of well-aligned garnet islands segments on substrate.

## **5 Chapter 5 — Optical Measurement for Nonreciprocal Polarisation Mode Converter**

When characterising waveguides, the key characteristics include: layer thickness, refractive index, optical coupling, optical losses, and non-linear properties [155]. The layer thickness can be inspected by checking the cross-section profile under a scanning electron microscope (SEM) or by using a DEKTAK stylus surface profiler after patterning and etching down the layers of the waveguides. The refractive index can be confirmed using an ellipsometer for multi-layer thin films. Usually this step is omitted as the wafer manufacturers will provide the tested parameters. Here, for my application, the end coupling method was adopted to couple the laser beam into the waveguides. Using this technique, the propagation loss and Faraday rotation magneto-optical effect were checked.

Initially, a lensed-fiber was used to couple TE-polarised light emitted from a 1550 nm Tunable laser into the waveguide. Later, a free space (Lens) coupling technique was adopted for increased stability. Generally speaking, the free space coupling technique is used to couple TE-polarised light by converting the TM-polarised light emitted from a 1550 nm tunable laser into the waveguide using an in-line polariser and a TE-TM in-line converter. Additionally, a polarising beam-splitting cube is placed before the input lens, which couples this light out from the laser into the sample in a pure TE-polarised plane. Moreover, a second polarising beam-splitting cube is placed at the end of the output, before the detector, to separate the TE component from the TM component for the purpose of measurement. In the measurement process, TE-polarised light is injected and the TM component is measured. Thus, any substantial TM power measured at the output is from the polarisation conversion process based on the Faraday rotation effect introduced by the periodic upper magneto-optical garnet cladding at the presence of an external magnetic field.

In all measurements in this work, TE-polarised light is used as the input as the majority of semiconductor lasers used in integrated optical systems are TE-polarised as a result of the quantum mechanical selection rule. Here we have

successfully demonstrated the achievement of an integrated Faraday rotator by integrating periodic magneto-optic garnet as cladding on top of the waveguide, which acts as the nonreciprocal part of the designed isolator device.

In the future, the same optical characterisation methodology can be applied for TM-input or circularly-input to further confirm the feasibility of the integrated Faraday rotation device and support the claim that it can work for light with arbitrary polarisation.

## **5.1 Introduction**

### **5.1.1 Coupling Method**

In order to couple the laser beam into the waveguides, four methods can be used: prism coupling, end-fire coupling, tapered/non-tapered launch coupling, and grating coupling. Among them, prism coupling and end-fire coupling are the most popular methods for their high coupling efficiency and relatively easier realisation [155]. Prism coupling was discarded in our application for the complex setup and high accuracy requirement of the gap between the prism and the waveguide surface. End-fire coupling was implemented in all of our optical measurements, which requires the coupling-in/out end facet to be flat and defect-less when preparing it by cleaving. Also, strict alignment accuracy is needed in order to get good coupling.

### **5.1.2 Propagation Loss Measurement – The Fabry-Perot Measurement Method**

There is attenuation or loss of the lightwave signal while it propagates through an optical waveguide. There are mainly five aspects that can contribute to propagation loss [155], which are depicted in Table 5-1. When the refractive index of the core layer film is close to that of the substrate, or the thickness of the core layer film is close to cut-off thickness, the mode will be radiated into the

substrate and/or the cladding layer/air. When there is mode conversion from an excited mode to other guided modes, the optical energy can also be lost, especially in a device where a guided mode performs a function. There can be inherent absorption or induced absorption arising from the fabrication process of the waveguide itself, mainly consisting of inter-band absorption, impurity absorption, and carrier absorption. The inherent or induced imperfections, like surface roughness, rough sidewalls, porosity, cracks, pores, grain boundaries, etc., can also lead to diffusion/scattering losses.

Apart from the tunnelling losses, the four other kinds of losses exist in our waveguide. First of all, the thickness of the core layer is 500 nm, which is not thick enough to confine all the light. Part of the light will radiate in the upper cladding layer and finally radiate away while propagating along. Our device also involves TE-TM mode conversion sections, which induce mode conversion loss. Interactions between layers, the porous  $\text{Si}_x\text{N}_y$  cladding layer, the rough garnet layer, and the rough sidewall, etc., can give substantially large scattering losses. Also, the grain size of the garnet is 20-50 nm, while a nano-crystal structure larger than 10-15 nm will increase the propagation losses dramatically [155].

Type of Loss	Origin of the Loss
Radiation losses	The refractive index of the core layer is close to that of the substrate, or the thickness is close to cut-off thickness
Mode conversion losses	Conversion from the excited mode to other guided modes
Absorption losses	Light absorption in the waveguide materials
Diffusion losses/Scattering losses	Imperfection of the waveguide structure
Tunnelling losses	Only in barrier optical waveguide caused by Ion modification

**Table 5-1. Different types of losses and the origin of them.**

There are essentially four ways to measure the propagation losses: the Cutback Method, Sliding-Prism Method, Fabry-Perot Resonances Method, and

Scattered Light Measurement Method [155]. As discussed above, end-coupling is used in the measurement. Therefore, only the Cutback Method and Fabry-Perot Resonances Method are suitable, since the Sliding-Prism Method needs prism coupling and the Scattered Light Measurement uses optical fibres to collect the scattered light.

For the Cutback Method, the device needs to be cut short after the first measurement, which makes a change to our device and will affect the function as it changes the periods of the garnet, and most probably will change the rotation degree. Besides, there is a higher requirement for the coupling-in/out facets to produce repeated measurements, and it is also much harder to cleave the sample the second time (as they get smaller each time). Additionally, the Fabry-Perot Resonances Method is more stable, repeatable, and more accurate than the Cutback Method, thus it is adopted in this thesis.

After cleaving the two sides of the sample, the waveguides on top form a Fabry-Perot cavity with the two cleaving facets acting as two semi-mirrors. The ratio of the output and the input powers can be expressed by:

$$\frac{P_{out}}{P_{in}} = \frac{(1-R)^2 e^{-\alpha L}}{(1-Re^{-\alpha L})^2 + 4Re^{-\alpha L} \sin^2(\emptyset/2)} \quad (5-3) [155]$$

Where R stands for the facet reflectivity, and can be expressed as:

$$R = \frac{(n-1)^2}{(n+1)^2} \quad (5-4)$$

While  $\emptyset = 2nkL \cos \theta + \varphi_r$  is the phase difference related to the optical path difference of the resonator, and  $\theta \approx 0$  is the incident angle.

If the ratio of the maximum intensity to the minimum intensity of the Fabry-Perot resonances fringes can be expressed as:

$$\xi = \frac{I_{max}}{I_{min}} = \frac{(1+Re^{-\alpha L})^2}{(1-Re^{-\alpha L})^2} \quad (5-5) [155]$$

Then the propagation loss  $\alpha$  can be depicted as:

$$\alpha = -\frac{1}{L} \ln\left(\frac{1\sqrt{\xi}-1}{R\sqrt{\xi}+1}\right) \quad (5-6) [155]$$

Here,  $n = 3.45$  (Si at  $\lambda = 1550$  nm),  $R = \frac{(3.45-1)^2}{(3.45+1)^2} = 0.3031$ . So, once we get the Fabry-Perot resonances fringes from the measurement,  $\xi = \frac{I_{max}}{I_{min}}$  can be easily obtained from the traces and  $L$  is the device length, which can be easily measured. The propagation loss can be calculated from equation (5-6). As in the third graph of Figure 5-1 (a),  $I_{max}$  reads as around 55 while  $I_{min}$  reads as 43.5. So  $\xi = \frac{I_{max}}{I_{min}} = \frac{55}{43.5}$ . The length of the device is measured at 6.2 mm and  $R = 0.3031$ . According to equation 5-6, we can get the propagation loss  $\alpha = 11.2$  dB/cm.

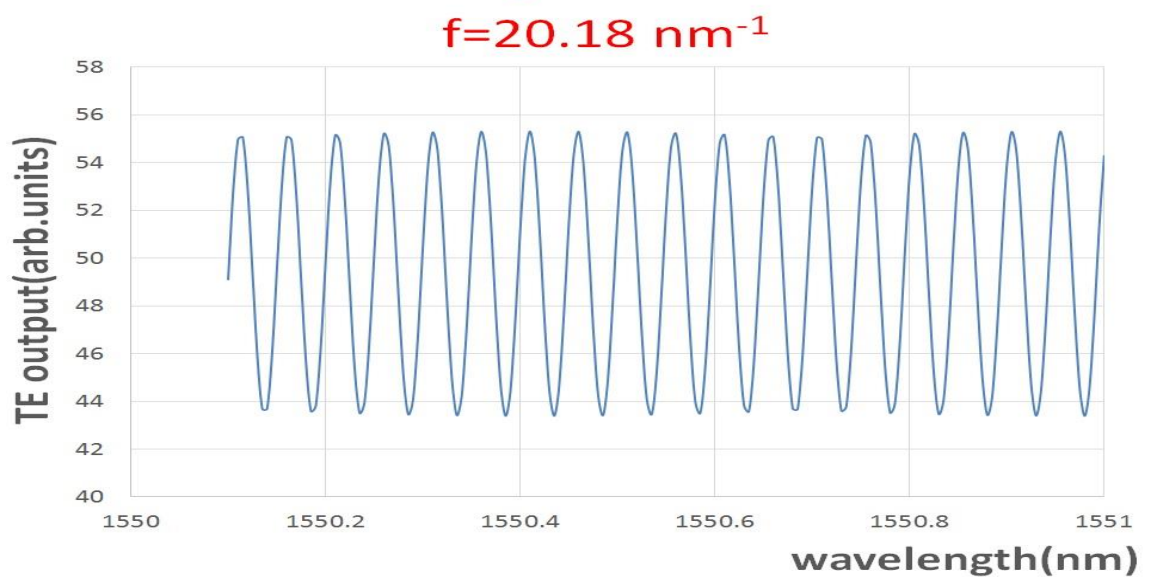
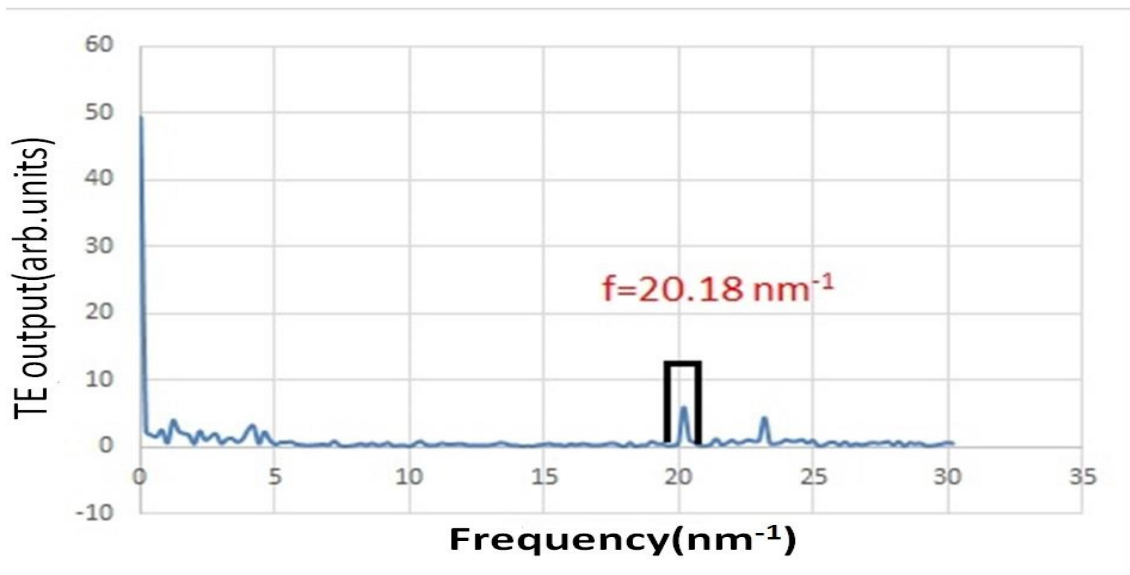
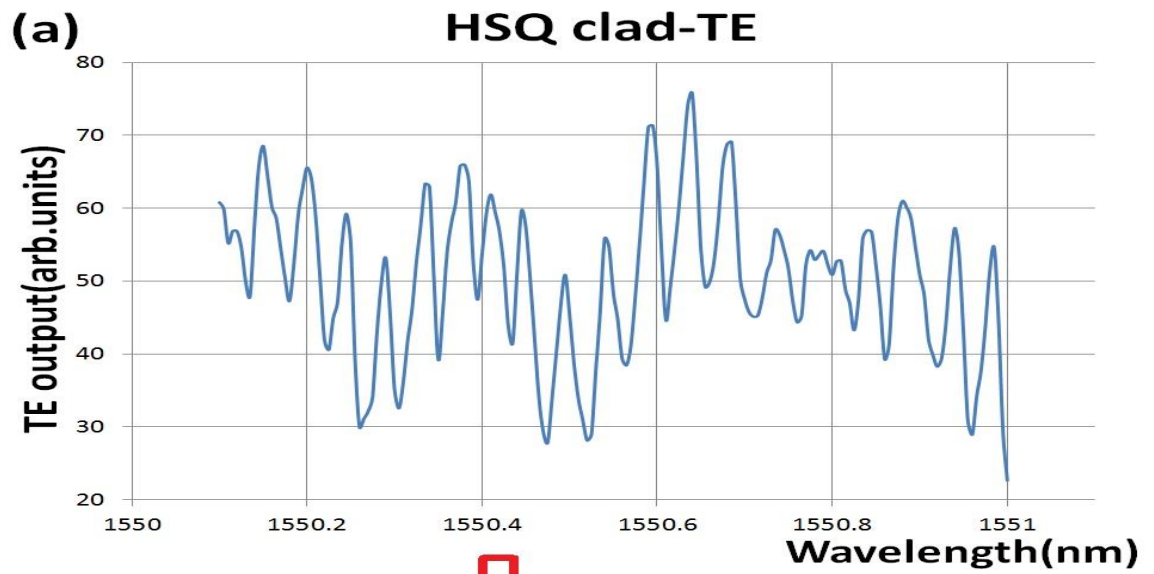
During the measurement process, FP fringes were obtained by putting a beamsplitting cube at the output to measure only the TE or TM polarised components at 1550 nm when scanned at a step of 0.005 nm over the 1nm wavelength range from 1550 nm-1551 nm. The choice of the wavelength range needs to be near 1550 nm, and is fairly flat on the response, which also indicates that it should be away from the quasi-phase matching/peak wavelength. However, proper FP fringes can only be obtained from the waveguides with just HSQ or YIG on top as cladding along the whole waveguides, but not from the waveguides with periodic garnet cladding, which probably resulted from the periodicity of the cladding layer.

Figure 5-1 shows the transmission spectra, associated FFTs, and FFT-filtered spectra of (a) the TE mode and (b) the TM mode of HSQ-cladded waveguides, respectively. We can see that in the second graph of (a), a peak is shown at a frequency of  $20.18 \text{ nm}^{-1}$ , which corresponds to the spatial frequency of the TE mode in a 6.2mm-long SOI waveguide at a wavelength around 1550 nm, and can be calculated by  $f = \frac{2n_{eff}L}{\lambda_0^2}$ , where  $n_{eff}$  is the effective refractive index of the corresponding mode,  $L$  is the length of the Fabry-Perot cavity/device, and  $\lambda_0$  is the central transmission wavelength. In the second graph (b), a peak is shown at a frequency of  $20.98 \text{ nm}^{-1}$ , which corresponds to the spatial frequency of the TM mode in a 6.2 mm-long SOI waveguide at a wavelength around 1550 nm. Based on equation 5-6, knowing the readings of the maximum and minimum output from the third graph of Figure 5-1 (a) and (b), we will be able to get the propagation loss for the TE mode, 11.2 dB/cm, and the TM mode, 14.7 dB/cm. Also, the  $\Delta\lambda=0.04\text{nm}$  from the received FP modulation agrees well with the theoretical

calculated results from  $\Delta\lambda = \frac{\lambda^2}{2nL}$ , which suggests that the FP fringes loss pattern is correct (Figure 5-1).

Figure 5-2 shows the transmission spectra and associated FFTs of (a) the TE mode and (b) the TM mode of YIG cladded waveguides, respectively. We can see that in the second graph of Figures 5-2 (a) and (b), a peak is shown at the same frequency of  $7.79 \text{ nm}^{-1}$  for both the TE and TM modes, while no peak is shown at the frequency around  $20 \text{ nm}^{-1}$ , which corresponds to the spatial frequency of the TE mode in a 6.2 mm-long SOI waveguide at a wavelength around 1550 nm. Also, the value of  $\Delta\lambda$  does not match the theoretical value, which makes it a potentially false result (Figure 5-2), and probably resulted from other cavities in the setup, like the cavity between the lens to the sample facet, the cavity between the couple-in and couple-out lenses, etc., or resulted from the polarisation modulation of the laser itself. Therefore, FP fringes cannot always be used to measure the propagation loss of the waveguides with garnet cladding on top because they are too lossy.

Lei Bi et al. [156] reported that the losses of YIG,  $\text{Bi}_{0.8}\text{YIG}$ , and Ce-YIG films of nearly fully polycrystalline garnet films were around 50 dB/cm, 150 dB/cm, and 40 dB/cm, respectively. The more amorphous the garnet film is, the higher the optical loss will be. For our example, the garnet cladding is partially polycrystalline, which leads to a larger optical loss. Another option to measure optical loss is the Cutback Method. Because of the destructive nature of this method, it is not suitable for our application for now. In the future, spare samples will be prepared in order to measure the propagation loss through the Cutback Method.



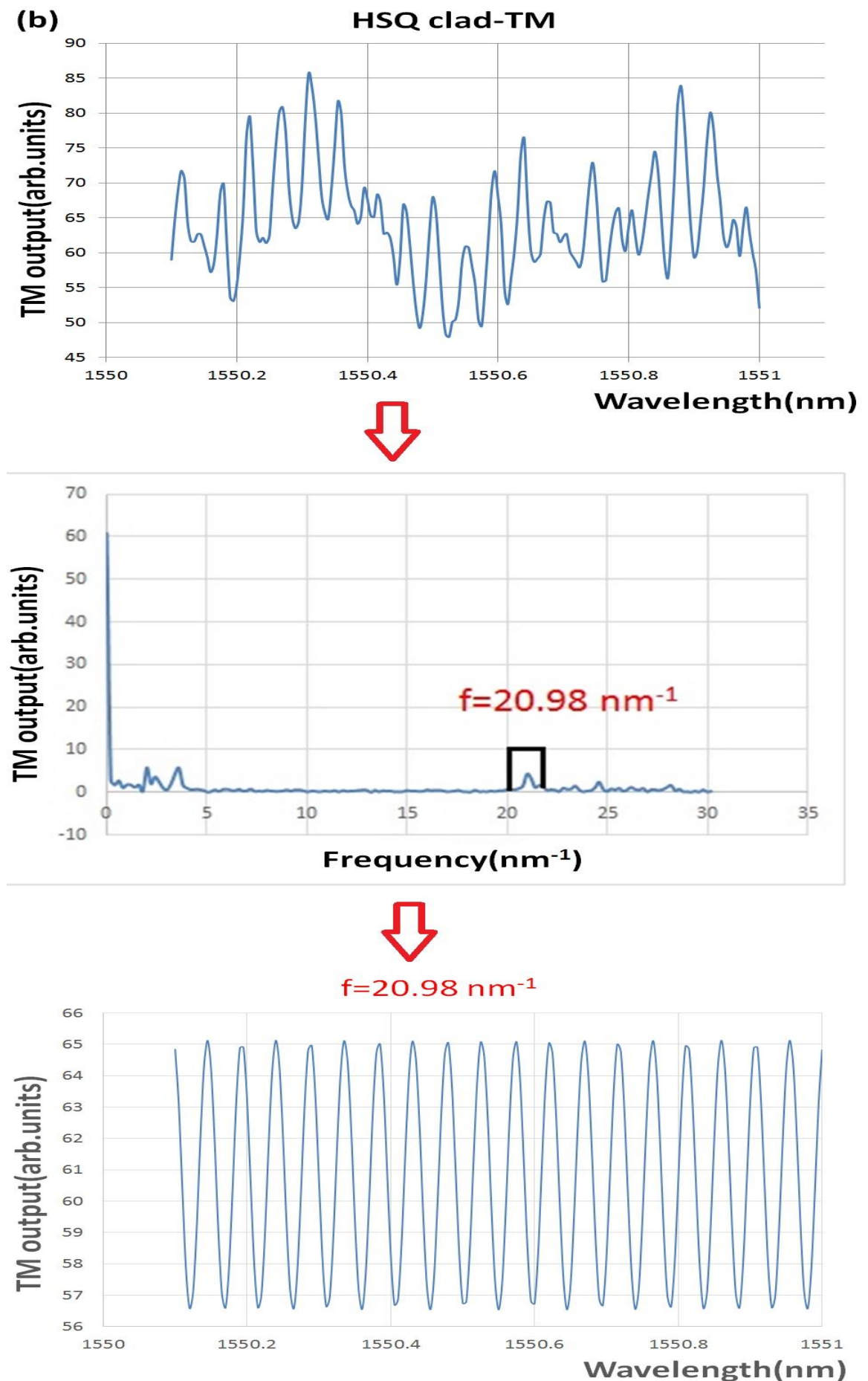
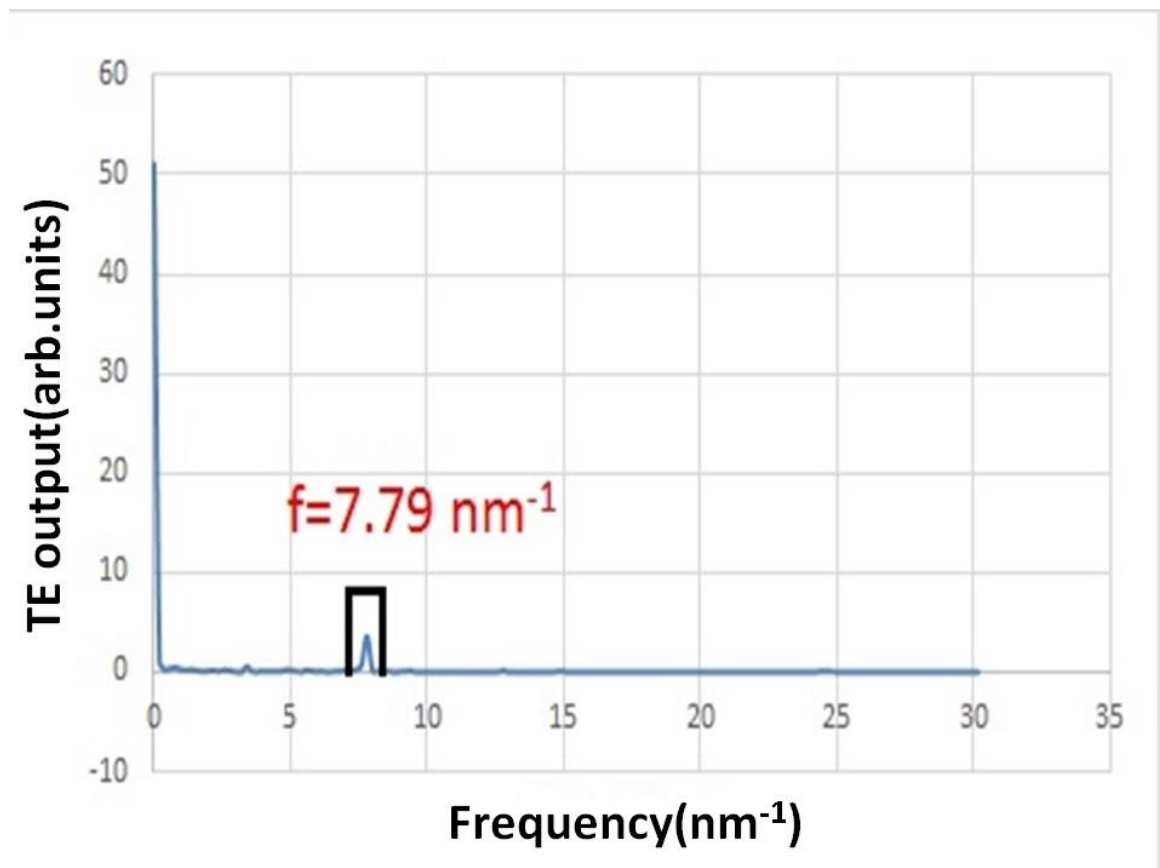
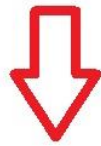
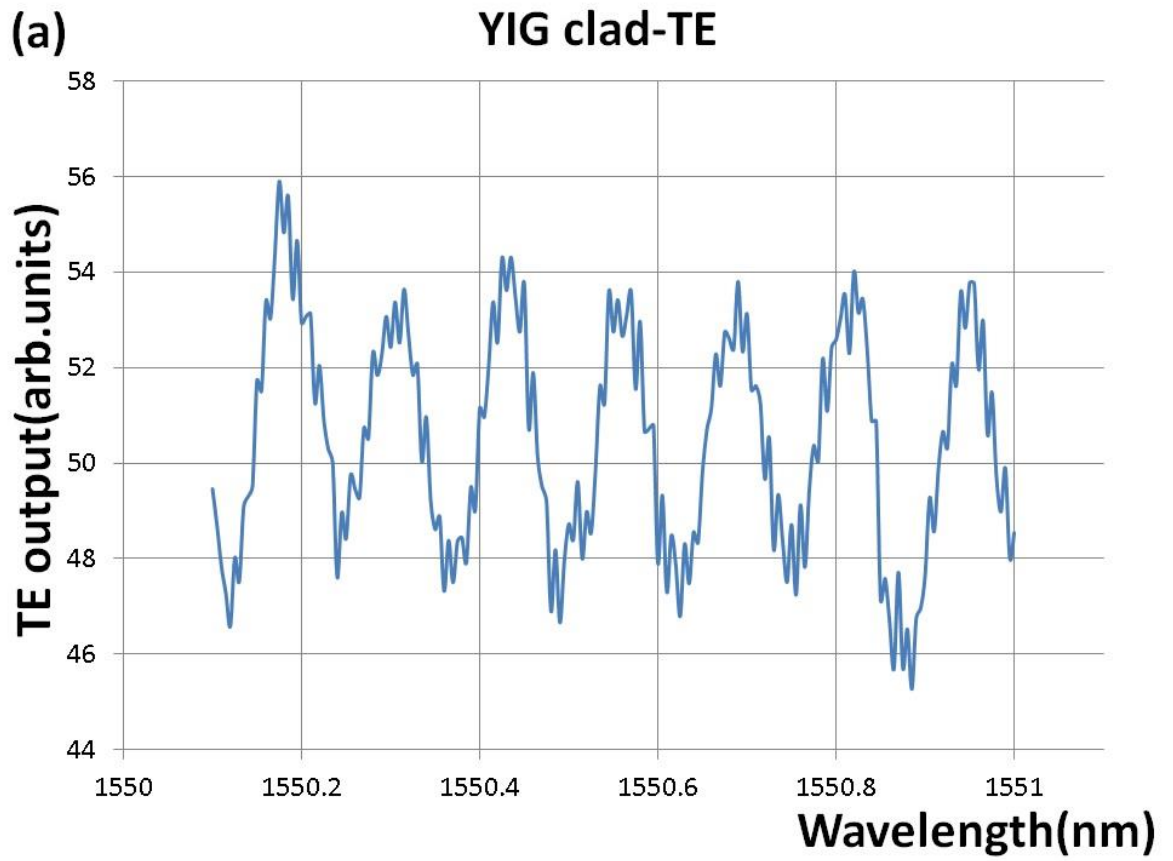


Figure 5-1. The transmission spectra, associated FFTs, and FFT-filtered spectra of (a) the TE mode and (b) the TM mode of HSQ-clad waveguides, respectively.



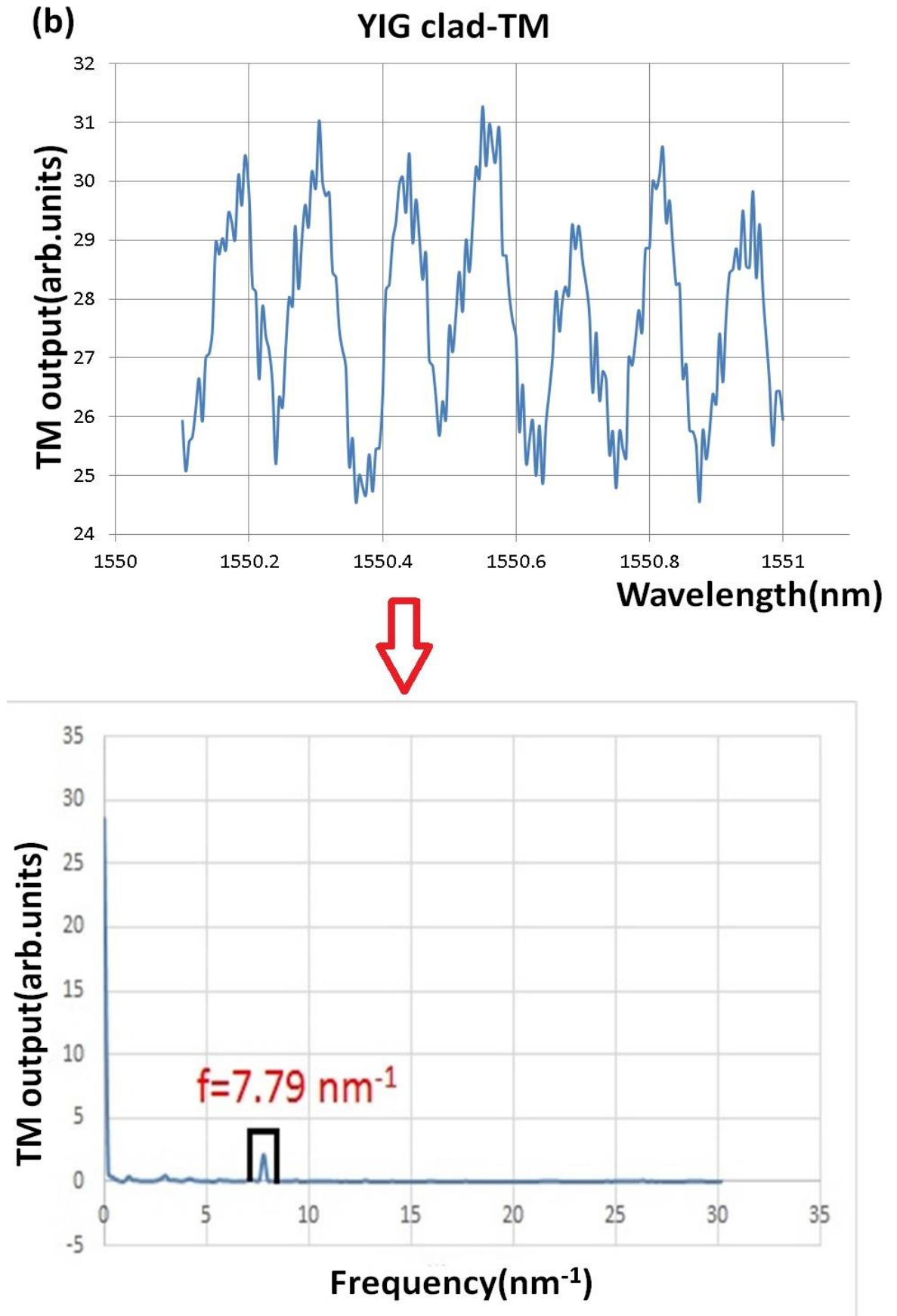


Figure 5-2. The transmission spectra and associated FFTs of (a) TE mode and (b) TM mode of YIG-clad waveguides, respectively.

## 5.2 Measurements with Permanent Magnets

### 5.2.1 Setup of the Whole Measurement Rig

In experimentation, both lensed fibre and optical microscope objective lenses of different magnifications can be used to couple the laser beam with the waveguides. Compared to the optical lens, lensed fibre is getting more attention for its simplicity of alignment and better coupling efficiency. However, the lensed fibre is less stable, and the slightest vibration of the lensed tip can be a potentially serious problem for delicate measurement, especially when the output signal is relatively small. Thus, in our experiment, only the optical lens was used in order to get better stability and to separate the TE and TM components of the input beam.

In the early stage of measurement, a periodic longitudinal magnetic field provided by a pair of Helmholtz coils (one on either side of the sample) driven by a waveform amplifier with the periodic signal coming from the wave function generator was used to magnetize the sample. However, there is a problem using the Helmholtz coils as a source of magnetic field. On one hand, the heat interaction of light and the magnetic field leads to a slight mechanical movement off/in the pinhole, which presents as a false signal of the periodic modulation of light. This inherent noise factor cannot be ruled out easily. On the other hand, at least a 1.5 kOe-2 kOe magnetic field is needed to saturate the MO garnet material, and over 0.4 kOe is needed to switch the direction of magnetization. The Helmholtz coils cannot provide such a high magnetic field. A maximum of 150 Oe (11936 A/m) can be achieved, and 300 Oe (23873 A/m) can be shortly achieved while starting to heat up and overload. Here, in our experiment, permanent magnets of around 1.2 kOe were used to saturate the samples with subsequent optical characterisation undertaken using the remnant magnetisation only.

The two sides of the sample were cleaved to form a Fabry-Perot cavity. The schematic of the whole measurement setup is shown in Figure 5-3. As the output of the tunable 1550 nm laser is TM-polarised, TE polarised radiation was coupled

with the guides using an in-line polariser followed by an in-line TM-TE converter together with a 20x optical lens, and the output passed through a polarising beam-splitting cube in order to separate the TE- and TM-polarised components (Figure 5-4, right). The in-line polariser is to only allow TM-polarised light through. Then, the in-line TM-TE converts TM-polarised light to TE-polarised light. Next, the polarising beam-splitting cube after the 20x lens is a double guarantee for a pure TE injection. Subsequently, a collimated 40x ( $f=4.5$  mm) objective lens was used to inject TE-polarised light into the millimetre scale long waveguides (Figure 5-4, left), while a second 40x optical lens was used to couple the light signal out from the waveguide. Here, all lenses and the sample were situated on 3-axis micro-positioning stages, of which all 3 axes can be adjusted to achieve the best alignment. A photodiode detector linked with a lock-in amplifier modulated by a mechanical chopper or a polarimeter was used to receive the signal out of the waveguides (see Figure 5-5). In the measurement process, TE-polarised light was injected and the TM component was measured. Thus, any substantial TM power measured at the output is from the polarisation conversion of the device.

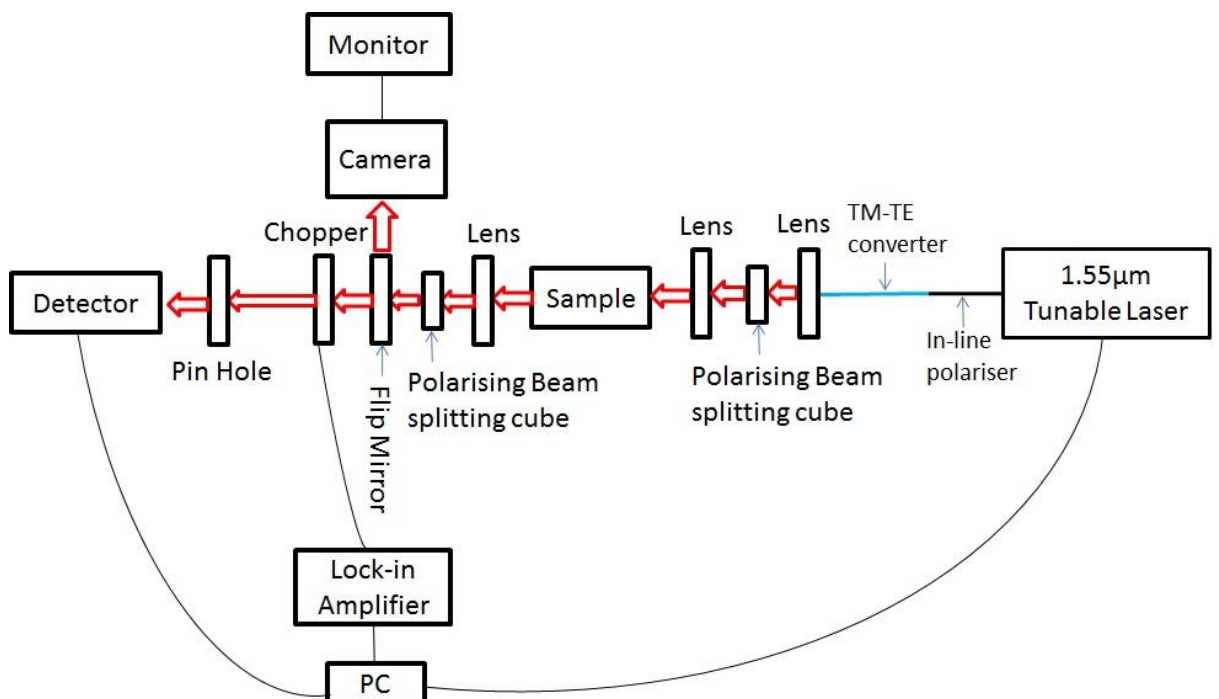


Figure 5-3. Measurements rig set-up using permanent magnets.

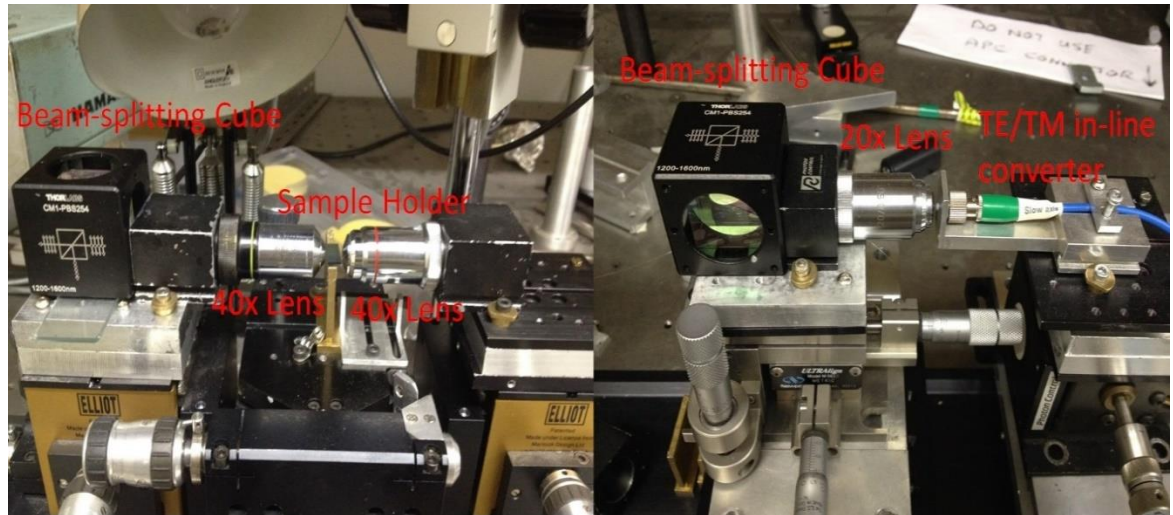


Figure 5-4. The right pic shows that TE-polarised radiation was coupled with the guides using an in-line polariser followed by an in-line TM-TE converter, and the output passed through a polarising beam-splitting cube in order to separate the TE- and TM-polarised components; the left pic shows that a collimated objective lens was used to inject TE-polarised light into the millimetre scale long waveguides.

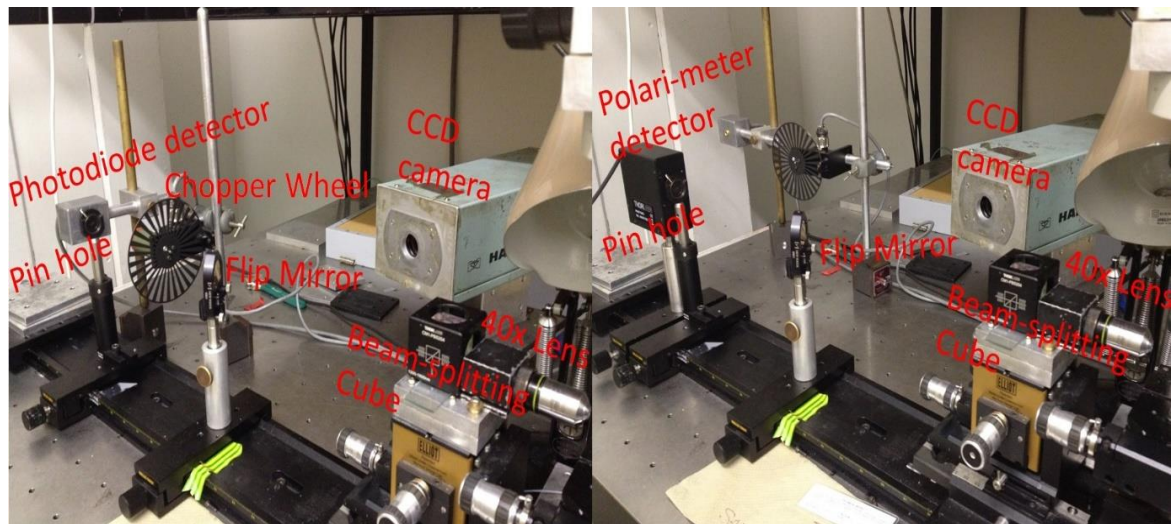


Figure 5-5. A photodiode detector linked with lock-in amplifier modulated by a mechanical chopper (left) or a polarimeter (right) was used to receive the signal out of the waveguides.

## 5.2.2 Measurement Process

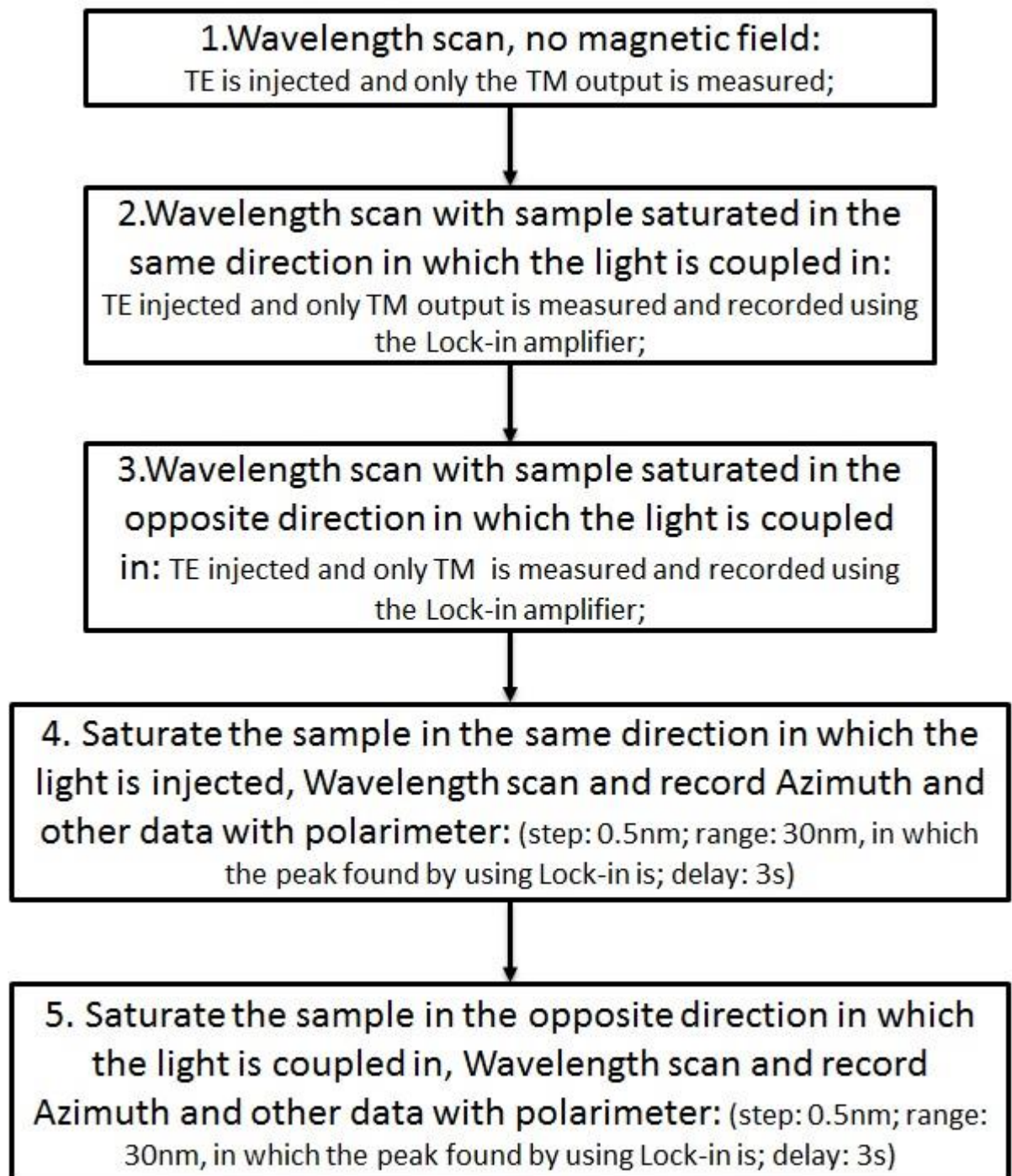


Figure 5-6. The steps for the whole measurement process.

The steps for this method of measurement are described in Figure 5-6. In the 1<sup>st</sup> step, a wavelength scan (1500 nm-1630 nm) is performed, while no magnetic field is applied, with the results recorded by a Lock-in amplifier. Here, any large rotations observed were actually due to a slight misalignment in the position of the MO garnet islands relative to the Si waveguides (slightly off-centre). This resulted in the waveguides being asymmetric in the cross-sectional profile, and, hence, led to the reciprocal mode conversion. In order to avoid this

problem in future, new samples were prepared with  $\text{Si}_x\text{N}_y$  overcladding (which has a much closer refractive index to garnet). Figure 5-7 and Figure 5-8 describe the optical characterisation results of samples on a 500 nm SOI platform with Ce-YIG on MgO and Ce-TIG as upper cladding, respectively. We can see that there is a small peak in Figure 5-7 (a) before saturation, most likely due to the small misalignment between lithography mask writings, and there is no peak confirmed at all in Figure 5-8 (a) before saturation, which means that there is no misalignment between the two mask writings.

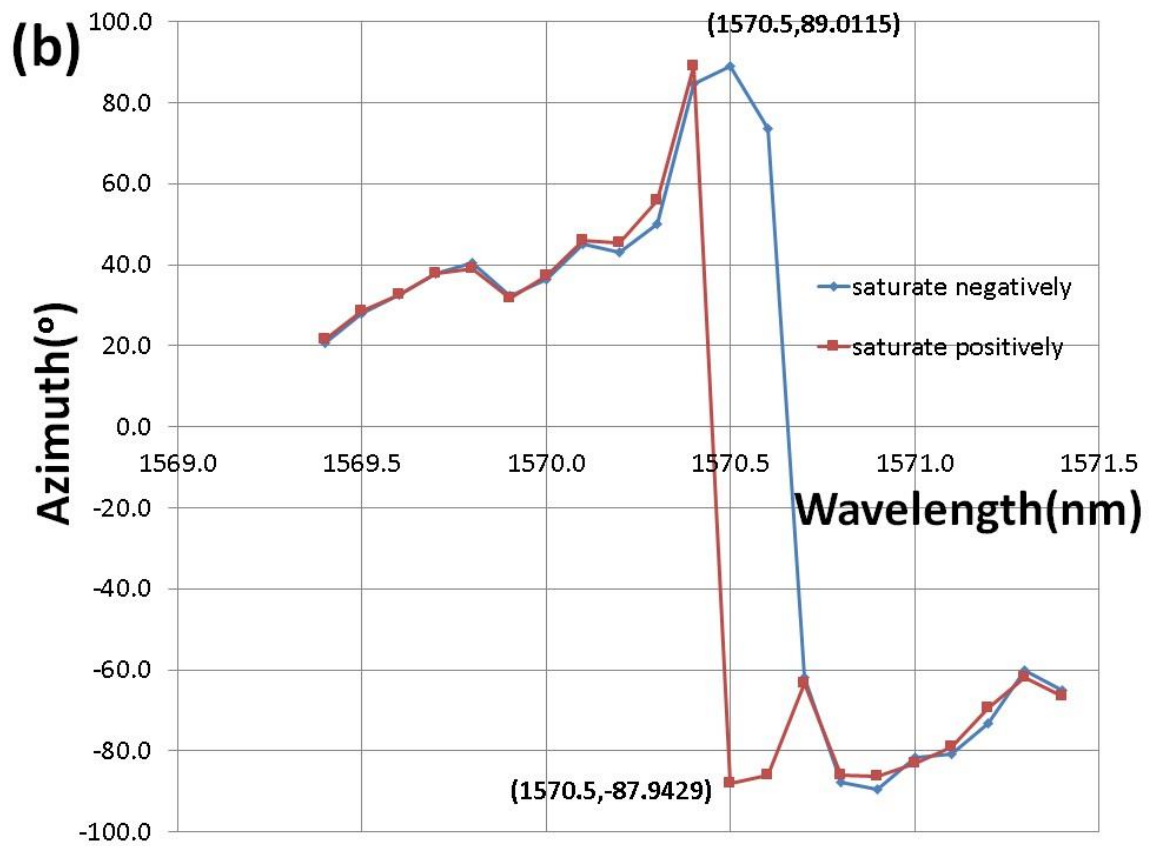
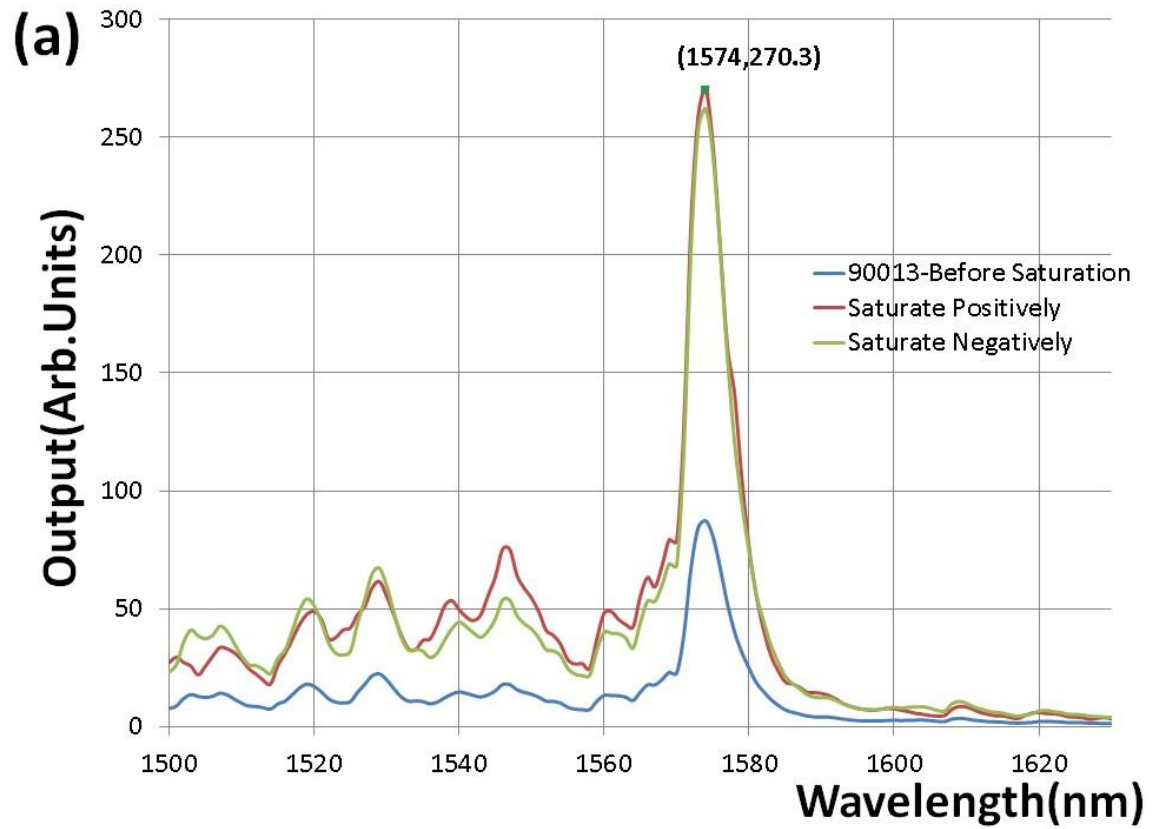
In the 2<sup>nd</sup> and 3<sup>rd</sup> steps, a wavelength scan was carried out when a longitudinal magnetic field ( $\geq 1$  kOe, around 1.2 kOe) was applied to saturate the samples with subsequent optical characterisation undertaken using the remnant magnetisation only, with the results recorded by a Lock-in amplifier. It was found that the polarisation mode conversion exhibits a peak when the phase-matching criterion is satisfied, and different quasi-phase matching periods lead to different wavelength peaks [89]. Peaks purely resulting from the magneto-optical Faraday rotation effect can be spotted, and peaks resulting from the combination of the reciprocal loading effect and MO Faraday rotation effect experienced an enhancement compared to the same peak obtained in the 1<sup>st</sup> step. As shown in both Figure 5-7 (a) and Figure 5-8 (a), substantially bigger peaks were found after saturating the sample both negatively and positively.

In the 4<sup>th</sup> and 5<sup>th</sup> steps, wavelength scans with a smaller range (30nm; even smaller for finer resolution scans) centred at the peak wavelength were done on the saturated sample, and the output signal was recorded by polarimeter, which analysed the signal and records  $S_1$ ,  $S_2$ ,  $S_3$ , azimuth, ellipticity, etc. When saturating the sample in opposite directions, the azimuth turns in opposite directions, as seen in Figure 5-7 (b) and Figure 5-8 (b), and the Stokes parameter of the traces should behave differently from each other at the same peak wavelengths.

A potential difficulty using azimuth and ellipticity to characterize polarisation states is that these are essentially periodic functions, and that small changes in the polarisation state can appear as large changes when they occur near the limits of the measurement range. For example, the azimuth could appear to switch randomly between + and - in the vicinity of  $\pm 90^\circ$ , as  $+90^\circ$  and  $-90^\circ$  are equivalent to each other on Poincare sphere. However, there can be just a small difference between the polarisation states as shown in the Poincare sphere.

Therefore, the opposite changes observed can potentially be interpreted as false signals. Further analysis was required on these opposite azimuths at the peak positions to exclude this possibility. Stokes parameters, on the other hand, are continuous functions bound by  $-S_0$ ,  $+S_0$  and, hence, Stokes vectors were chosen for the following analyses. Thus, the Stokes parameters were used to confirm that the signal is true when the azimuth turns in opposite directions at the same peak wavelengths when saturated in opposite directions.

Initially, a comparison of  $S_1$ ,  $S_2$ , and  $S_3$  of the two opposite directions of saturation was carried out, where the points of oppositely saturated directions determined by the three Stokes parameters should be situated in opposite sections on the Poincare sphere, while the points of the false signal resulting from the system should be the same in both saturated directions. Hence, the true non-reciprocal polarisation change resulting from a magneto-optical effect can be identified. As predicted, some of the results are false signals, as the traces of  $S_1$ - $S_3$  are exactly the same both ways, as seen in Figure 5-7 (c). Figure 5-8 (c) presents the true signals. It is observed that at  $\lambda=1511\text{nm}$  there is an opposite change in the sign of the  $S_2$  and  $S_3$  Stokes parameters of the two opposite saturation directions, which indicates that both the orientation of the major axis *and* the sense of the ellipse of the transmitted polarisation state have reversed with the reversal of the longitudinal magnetic saturation direction.



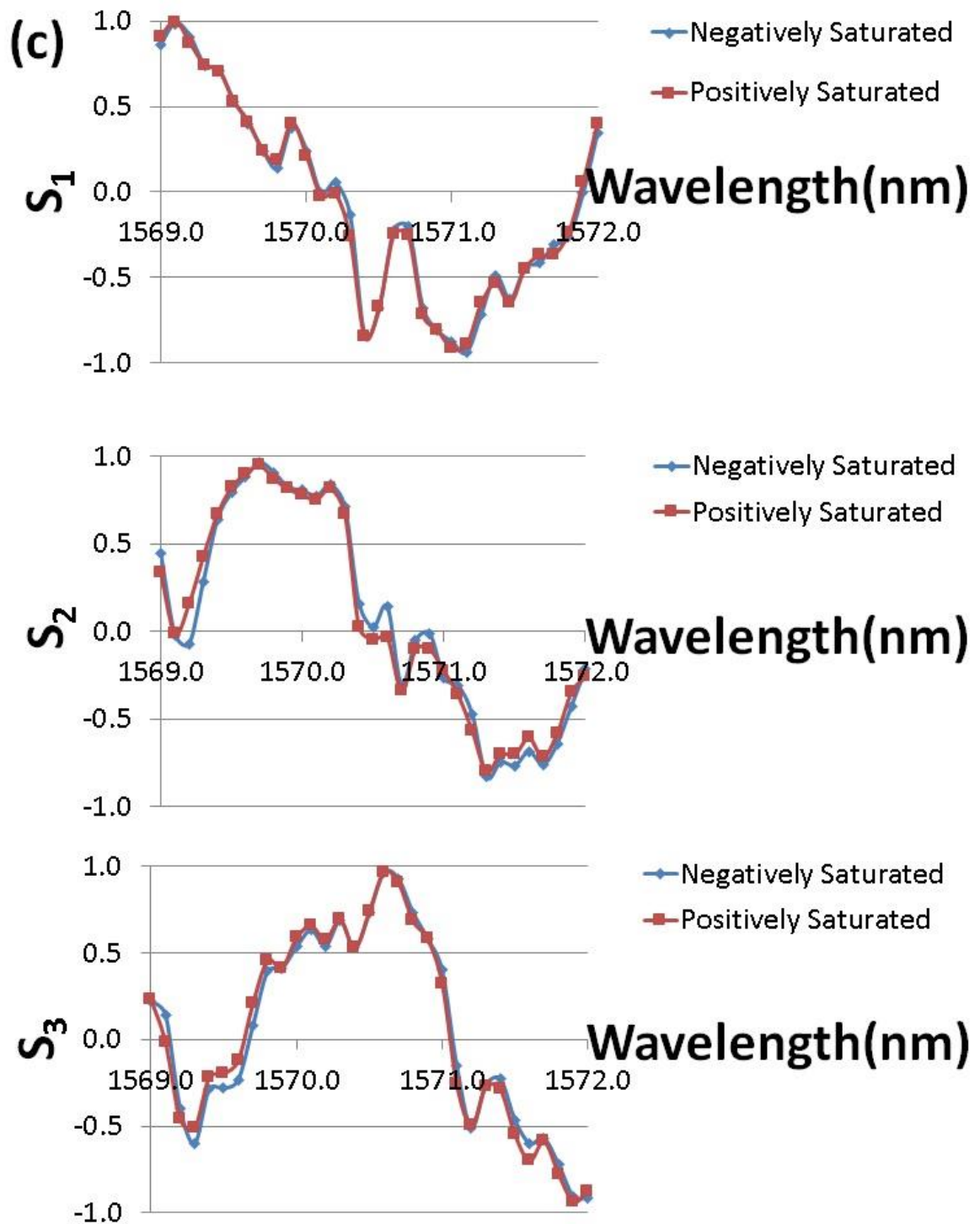
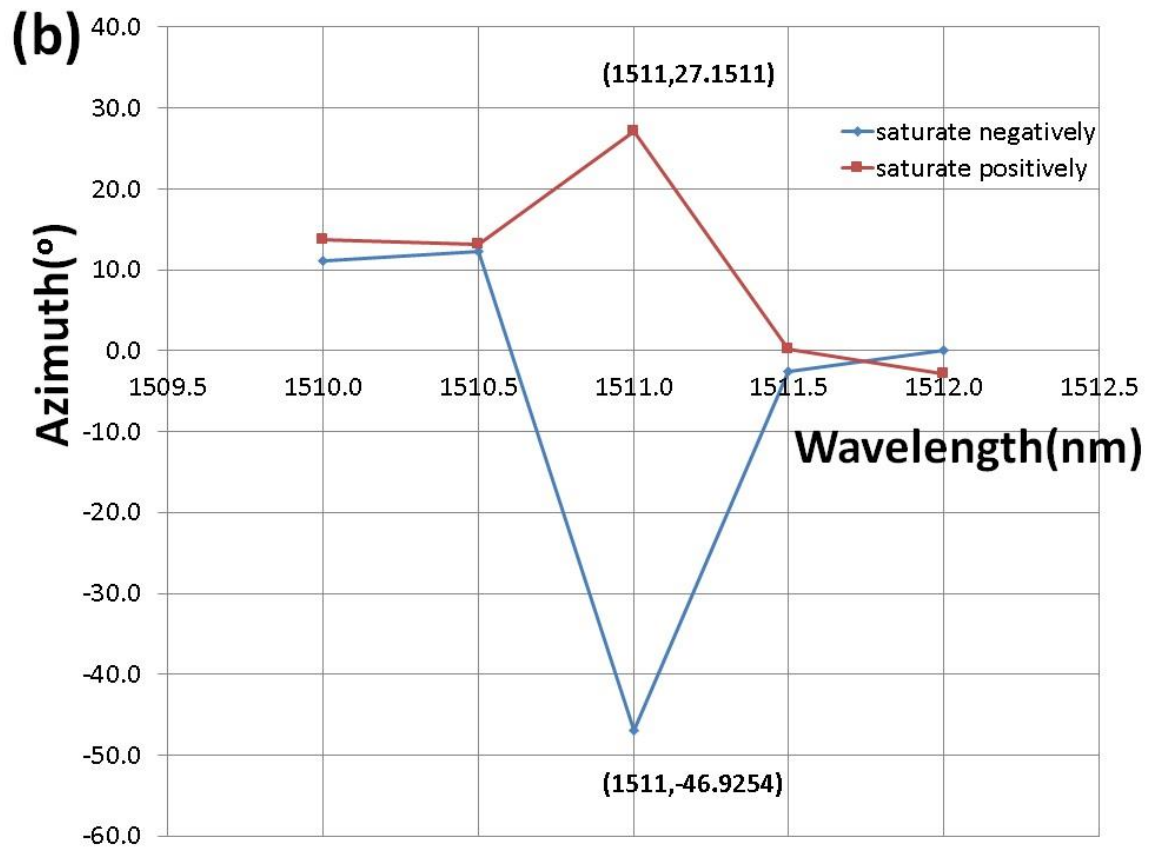
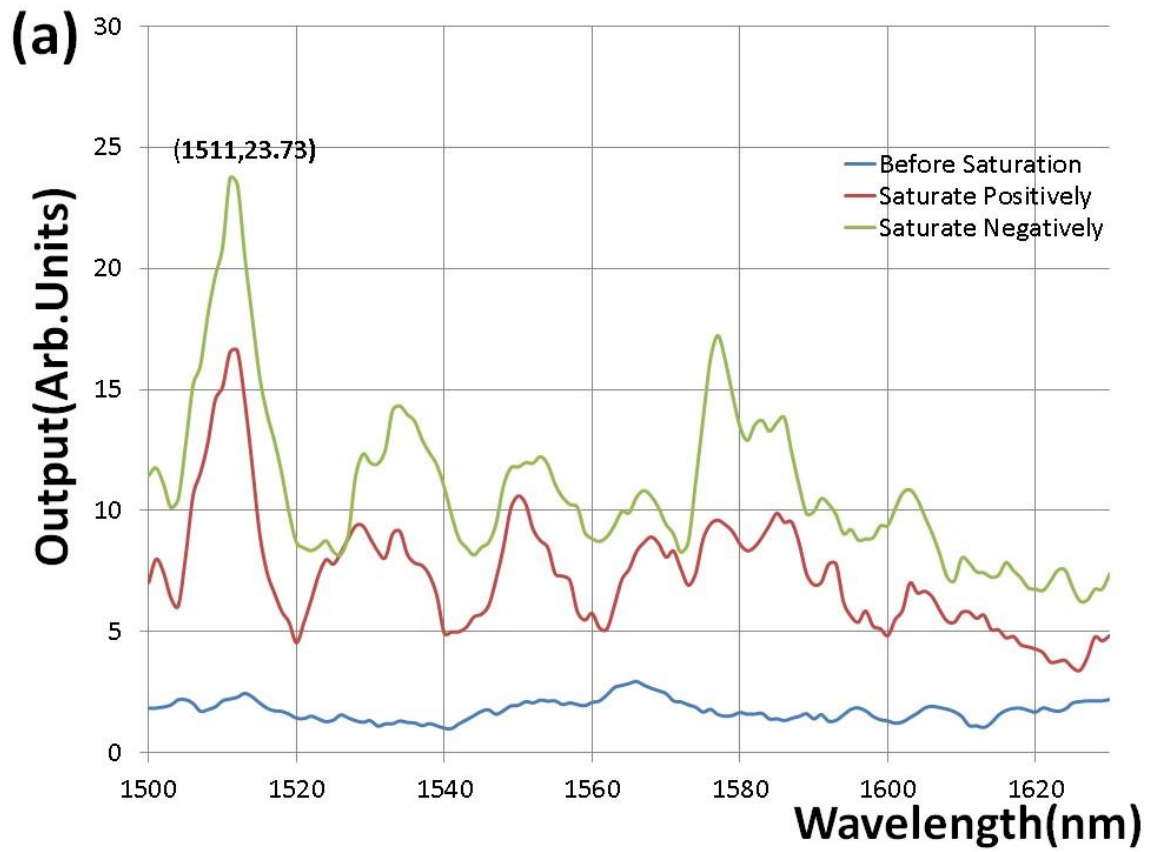


Figure 5-7. The optical characterisation results of Ce-YIG on the MgO sample. (a) displays that substantially bigger peaks occur after saturating the sample both negatively and positively, while there is a small peak before saturation, most likely due to the small misalignment between lithography mask writings. (b) shows that the azimuth of the light turns in the opposite direction when saturated in different directions at the same wavelength peak, as found in the upper graph. (c) shows traces of the  $S_1$ ,  $S_2$ , and  $S_3$  Stokes parameters of the two saturated directions. It is clearly seen that there is no difference in the Stokes parameters of two opposite directions of saturation.



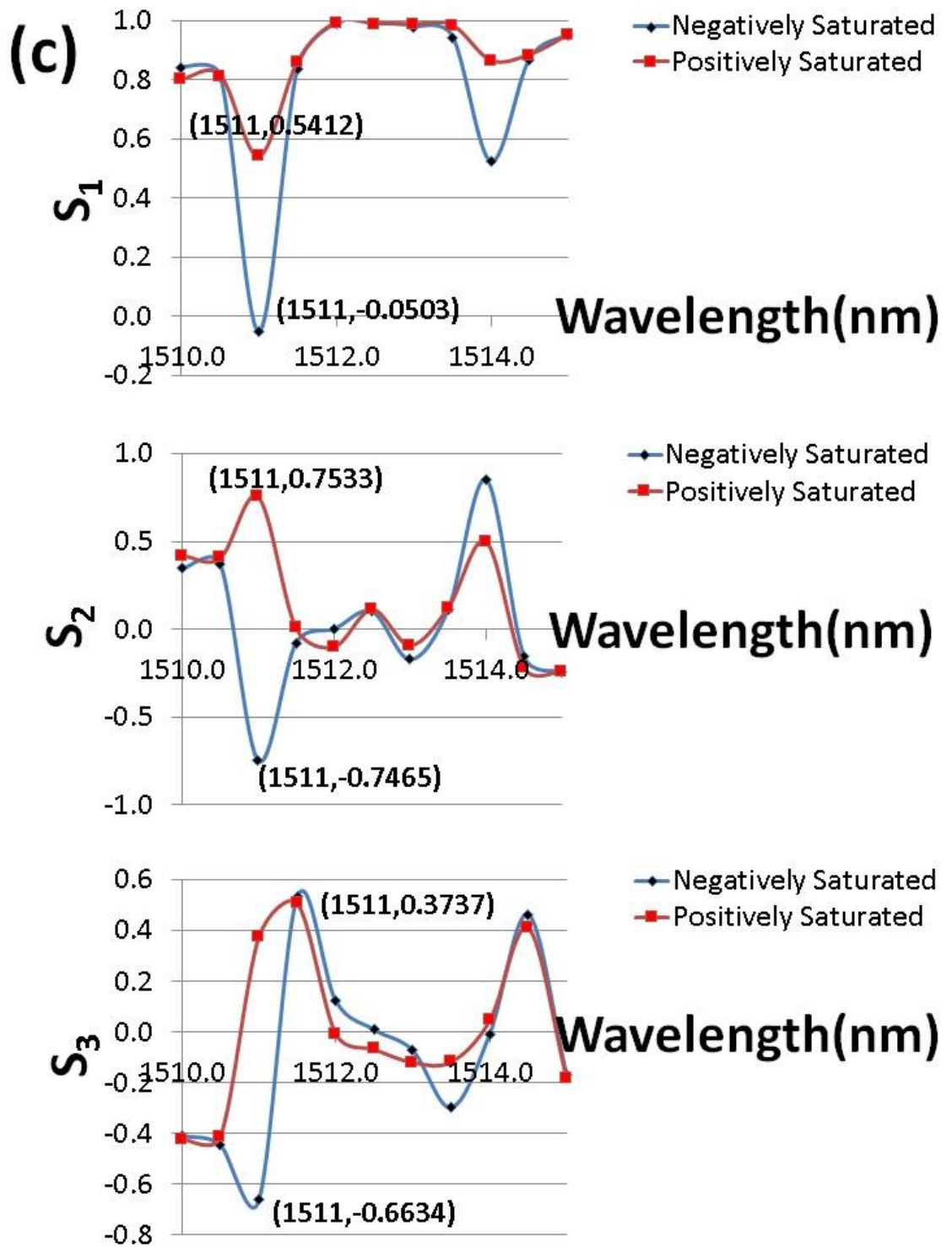


Figure 5-8. The optical characterisation results of the Ce-TIG sample. (a) displays that good peaks occur after saturating the sample both negatively and positively, while there is no peak at all before saturation. (b) shows that the azimuth of the light turns in the opposite direction when saturated in different directions at the same wavelength peak, as found in the left graph. The waveguide is with the beat length of Ce-TIG/HSQ=10.5/10.5  $\mu\text{m}$ . (c) shows traces of the  $S_1$ ,  $S_2$ , and  $S_3$  Stokes parameters of the two saturated directions. It is observed that at  $\lambda=1511$  nm there is an opposite change in the sign of the  $S_2$  and  $S_3$  Stokes parameters of the two opposite saturation directions, which indicates that both the orientation of the major axis *and* the sense of the ellipse of the transmitted polarisation state have reversed with the reversal of the longitudinal magnetic saturation direction.

### 5.2.3 Analysis of the Results – Poincare Sphere and Angle Between Two Stokes Vectors

In order to simplify the identification and quantify the nonreciprocal magneto-optic component of the quasi-phase-matched polarisation mode conversion of the two real results, the position of the points on the Poincare sphere corresponding to the Stokes parameters and the angle between the Stokes vectors were adopted. The positions of the Stokes vectors corresponding to the peak points were displayed in the Poincare sphere. Orthogonal polarisations states, as are required for an optical isolator, will appear as diametrically opposite points and an angle between the vectors of  $\pi$ .

Here, a Bi-TIG sample (Figure 5-9) and a Ce-TIG sample (Figure 5-10) on a 500 nm SOI platform are used to explain the analysis process. For the Bi-TIG sample in Figure 5-9, it was noticed that there was a 1-1.5 nm shift of peak wavelength while analysing by Polarimeter from that analysed by the Lock-in amplifier measurement system. Unfortunately, there is no way to automatically couple the two measurement systems together. Furthermore, it is time scans of a tuning laser instead of absolute wavelength scans in the Polarimeter measurement, so the wavelength difference can be simply caused by switching between absolute wavelength scans vs time using the Lock-in amplifier measurement system and time scans using the Polarimeter. There was also an estimate in time for the starting point of the scan.

The angle between the two Stokes vectors of scans of different directions of magnetic saturation was used to quantify the non-reciprocity and isolation extinction of the device. For devices with 100% isolation, the two vectors should rotate  $\pm 90^\circ$ , which makes the angle between the two vectors  $180^\circ$ . The third graph of Figure 5-9 (the Bi-TIG sample on the 500 nm SOI platform) and Figure 5-10 (the Ce-TIG sample on the 500 nm SOI platform) plots the angle between the two Stokes vectors vs wavelength. For Bi-TIG, it reached around  $55^\circ$  at  $\lambda=1531.5$  nm. For the Ce-TIG sample, the angle got to nearly  $180^\circ$ , which indicates that the number of quasi-phase matching periods on this device is near ideal for implementation in an isolator.

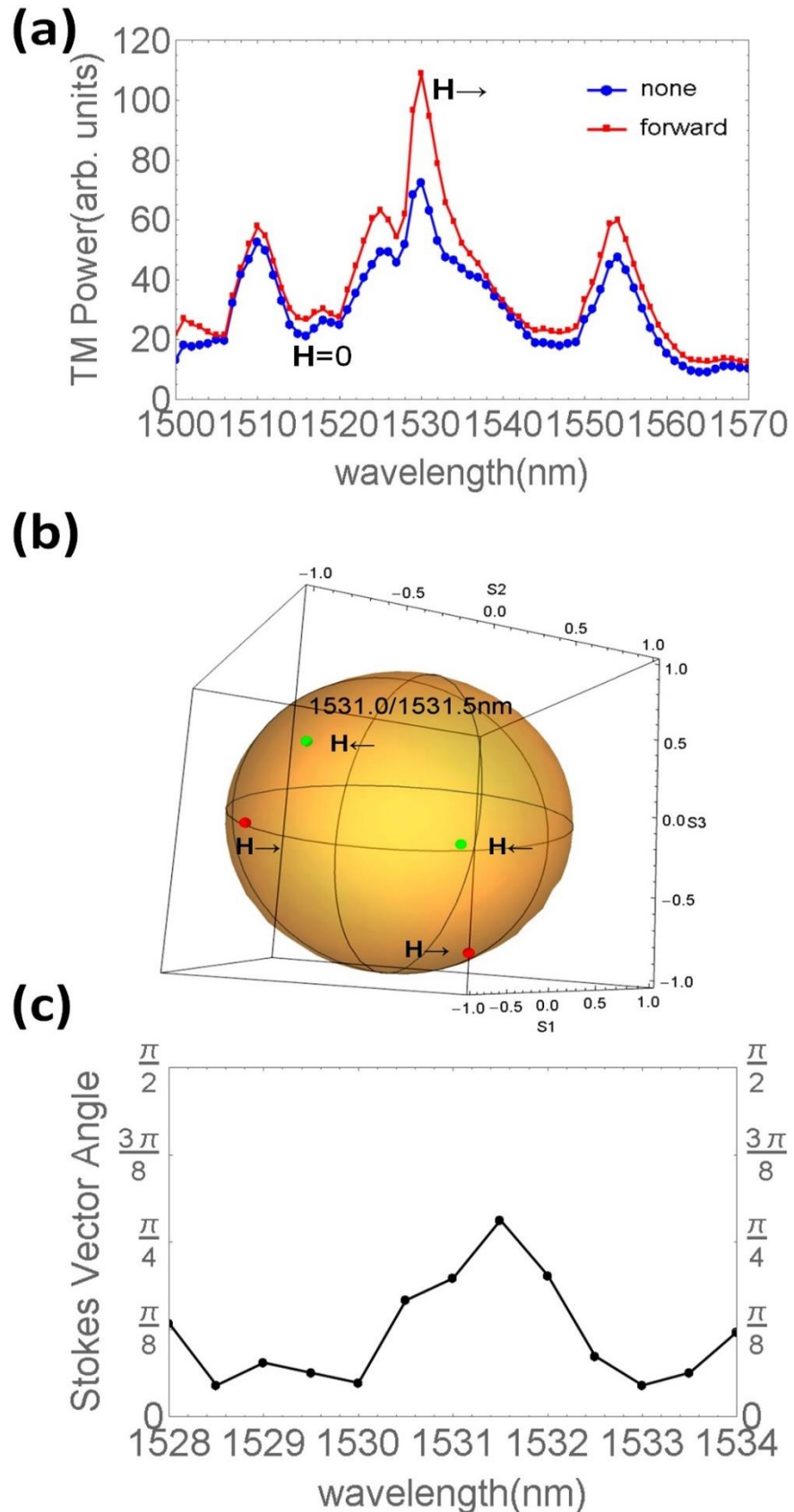


Figure 5-9. The optical characterisation result of the Bi-TIG device. The first plot shows the relative fraction of the TM-polarised output as a function of the input wavelength; a peak at  $\lambda=1530$  nm is observed. The second plot displays the position of the peak points on the Poincaré sphere. It is clearly seen that they are situated on different sections of the sphere while saturated in different directions. The third graph shows the angle between the two Stokes vectors in opposite directions of saturation. The maximum angle is around  $55^\circ$ .

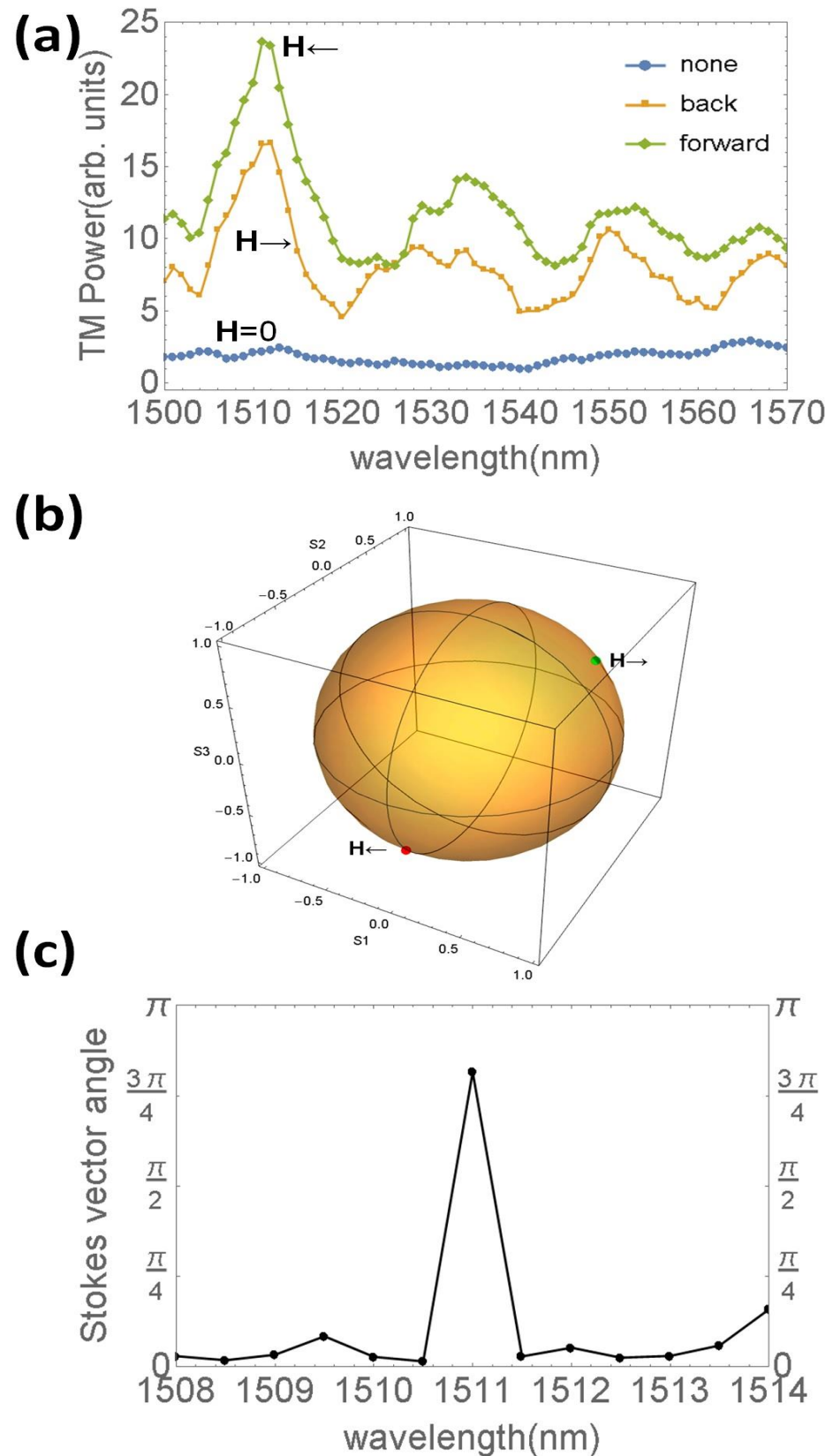


Figure 5-10. The optical characterisation result of the Ce-TIG device. The first plot shows the relative fraction of the TM-polarised output as a function of the input wavelength; a peak at  $\lambda=1511$  nm is observed. The second plot displays the position of the peak point on the Poincare sphere. It is clearly seen that they are situated on different spheres while saturated in different directions. The third graph shows the angle between the two Stokes vectors in opposite directions of saturation. The angle is nearly  $180^\circ$ , which indicates that the number of quasi-phase matching periods on this device is near the ideal for an optical isolator implementation.

In order to calculate the isolation ratio of the NR-PMC part according to the obtained Stokes vector angle, we suppose that in the forward direction the output light from the NR-PMC part first goes through an integrated quarter-wave plate, where the circularly polarized light is converted into linearly polarised light. It then goes through a polariser oriented at the same angle as the output linearly polarised light, which makes sure that 100% of the output light is getting through in the forward direction. We set the optical power of the output light as unit 1. In the backward direction, a similar integrated quarter-wave plate and polariser were placed at the output of the NR-PMC section, where the polariser was oriented orthogonally to the polariser in the forward propagating direction. We set the angle between the two Stokes vectors of opposite propagation directions as  $\theta$ ; thus, the angle between the azimuths of the output light of opposite propagation directions was  $\frac{\theta}{2}$ , as was the angle between the output light and the polariser in the backward direction. Therefore, the optical power of the output light that passes through the polariser and goes back to the laser source is  $\left(\cos\frac{\theta}{2}\right)^2$ . We know that isolation is defined as:

$$d = -10 \log \frac{P_{out}}{P_{in}} \quad (5-10)$$

Where  $P_{out}$  is the optical power of the output light and  $P_{in}$  is the optical power of the input light.

Therefore, the isolation ratio becomes:

$$d = -10 \log \left( \cos\frac{\theta}{2} \right)^2 \quad (5-11)$$

Where  $\theta = \cos^{-1} \left( \frac{\overline{S}_f \cdot \overline{S}_b}{|\overline{S}_f| |\overline{S}_b|} \right)$ ,  $\overline{S}_f$  is the Stokes vector of forward direction, while  $\overline{S}_b$  is the Stokes vector of backward direction. The Stokes vector angle for the Ce-TIG on the 500nm SOI platform in Figure 5-10 is  $0.8158 \pi$ , i.e., 2.563 rad, and the isolation ratio  $d = 10.9$  dB.

### 5.2.4 Observed Promising Results on Both 500 nm SOI and 340 nm SOI Platforms with Different Garnets on Top

As discussed in Chapter 4, for the fabrication of the NR-PMC part, different kinds of MO garnets, including Bi-TIG, TIG, Ce-TIG, and Ce-YIG on YIG/MgO were used as cladding layers on both 500 nm SOI and 340 nm SOI platforms, and corresponding devices were fabricated and measured. Though there was a misalignment problem in the fabrication process of the devices on 340 nm SOI platforms, there are still some devices that were well aligned, with the MO Faraday rotation effect observed on both the 340 nm SOI substrate and 500 nm SOI substrate. Depending on the quality of the garnet and the number of quasi-phase matching periods, the Faraday rotation degree and, thus, Stokes vector angle vary among these devices. All of the results presented below (on the 500 nm SOI platform) and in the Appendix (on the 340 nm SOI platform) indicate that, with proper optimisation of the quality of the garnet and the right device length, all of the garnets presented here can be used to achieve non-reciprocal mode conversion as part of the isolator device.

#### 5.2.4.1 500 nm SOI Platform with Bi-TIG, Ce-TIG, Ce-YIG on YIG, and Ce-YIG on MgO as a Cladding Layer

The measurement results of the devices with 300 nm Bi-TIG and 300 nm Ce-TIG as an MO cladding layer on a 500 nm SOI platform, the wavelength scan with the sample unsaturated and saturated positively and negatively, the peak wavelength point on the Poincare sphere, and the angle between Stokes vectors are presented in Figure 5-9 and Figure 5-10, respectively.

Figure 5-11 and Figure 5-12 display the measurement results of the device with Ce-YIG on YIG (330 nm/50 nm) as cladding. Figure 5-11 shows the relative fraction of the TM-polarised output as a function of input wavelength when the sample is not saturated, and saturated in a forward direction and back direction; a peak at  $\lambda=1612$  nm is observed.

Figure 5-12 presents the Stokes vector angle of opposite magnetic saturation at a resolution of 0.01 nm, where an angle of nearly  $3/4\pi$  is observed

and there is fringe-like noise. By calculating the frequency spacing  $\Delta\lambda$  in the free spectral range (FSR), it can be confirmed that the fringe-like noise came from the Fabry-Perot fringes, which can be avoided by applying an anti-reflection coating on the facets of the cleaved sample. Besides, quasi-phase matching (QPM) is found on 800 nm-wide and 900 nm-wide devices of different lengths of beat-length at different peak wavelengths (Figure 5-13). Compared to the simulation results, though there is a small difference in the QPM period length, there is good agreement in the general development trend, where devices with a shorter QPM period length tend to have a longer peak wavelength.

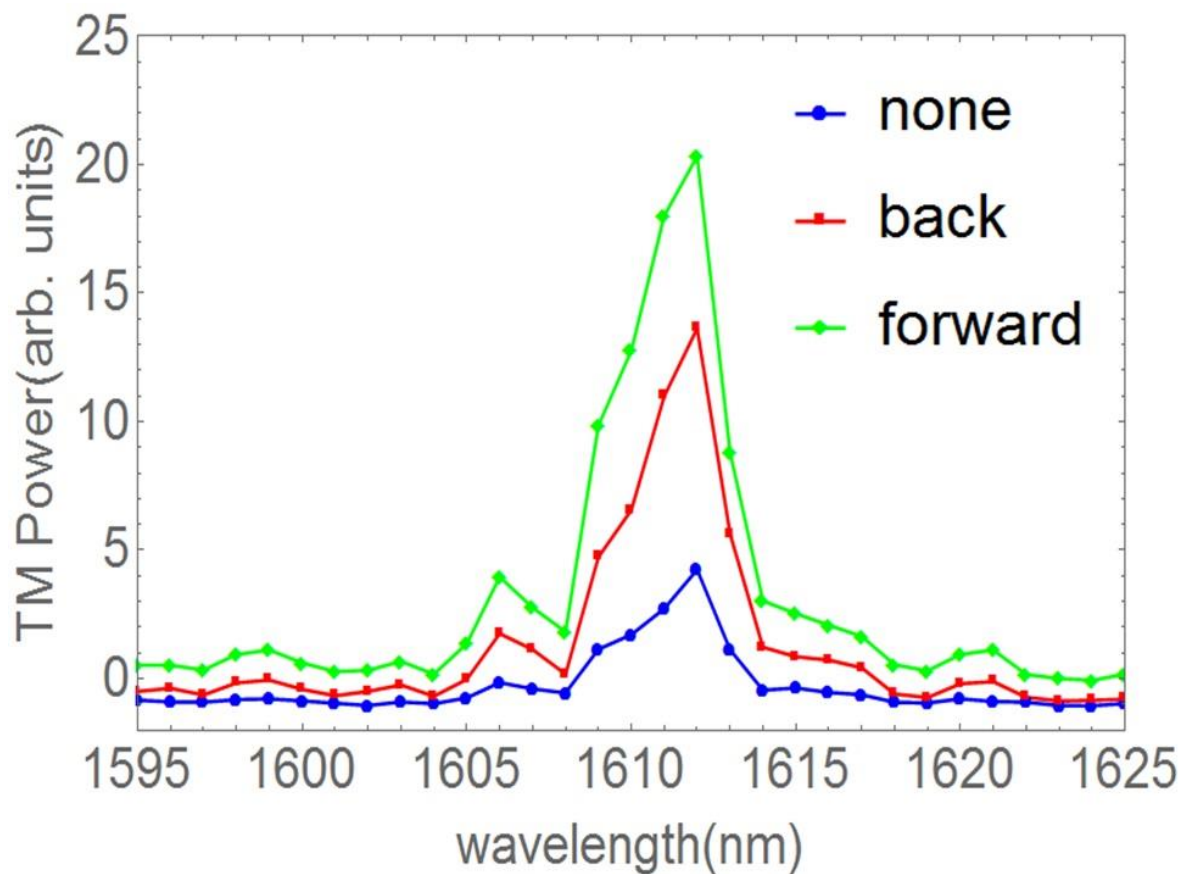


Figure 5-11. Device with Ce-YIG on YIG cladding on a 500nm SOI platform: the relative fraction of the TM-polarised output as a function of input wavelength when the sample is not saturated, and saturated in a forward direction and back direction; a peak at  $\lambda=1612$  nm is observed.

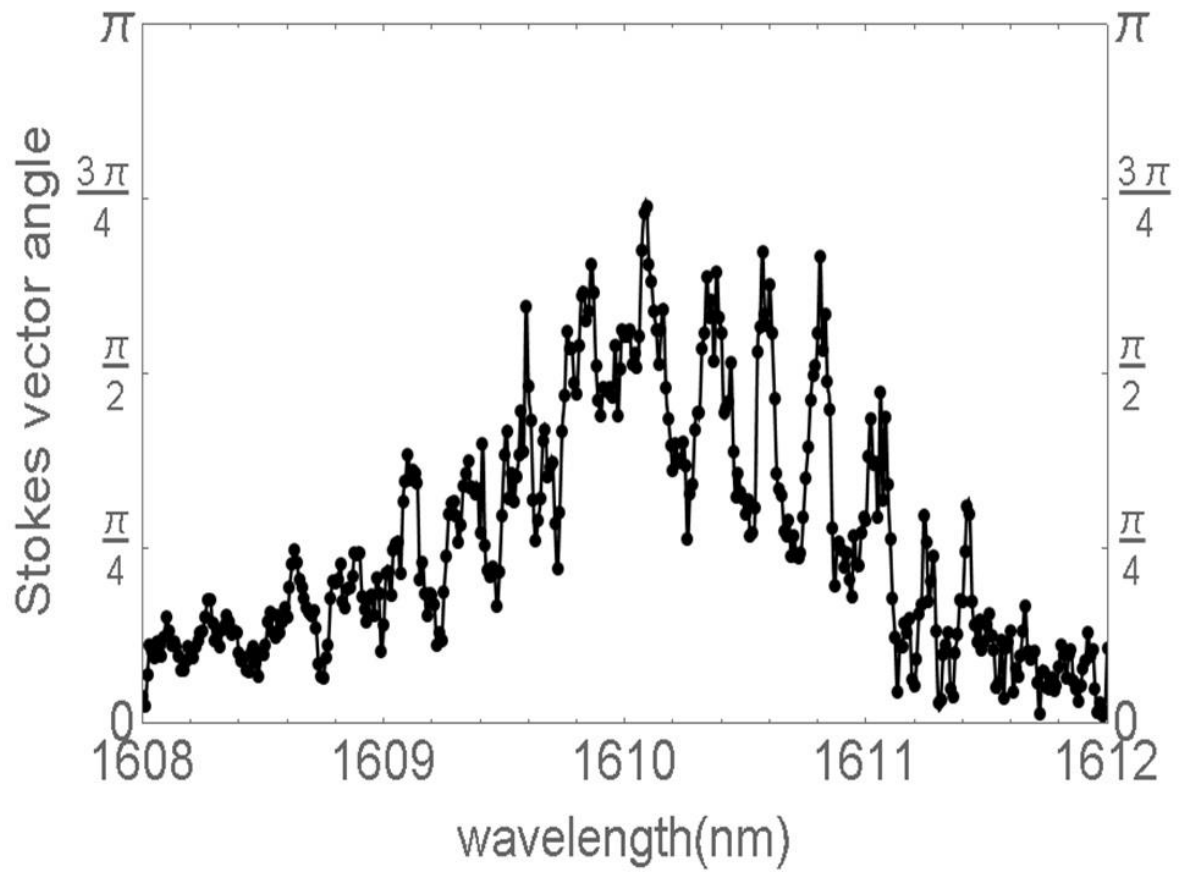


Figure 5-12. Device with Ce-YIG on YIG cladding on a 500 nm SOI platform: it presents the Stokes vector angle of opposite magnetic saturation at resolutions of 0.01 nm, where an angle of nearly  $\frac{3}{4}\pi$  is observed and there is fringe-like noise.

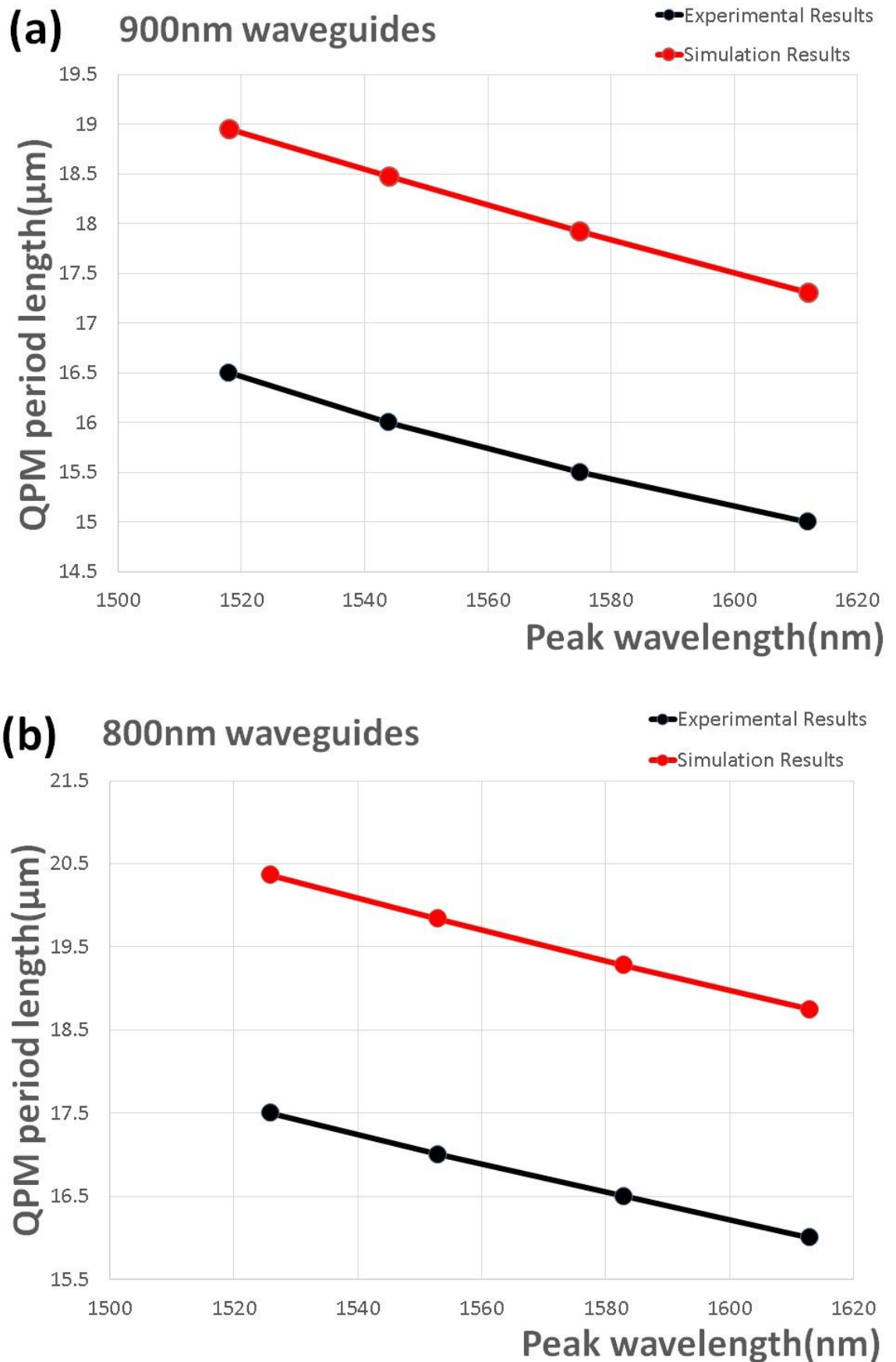


Figure 5-13. Device with Ce-YIG on YIG cladding on a 500nm SOI platform: (a) and (b) compare the experiment results of the QPM period length to the simulation results of QPM period length on 900 nm-wide devices and 800 nm-wide devices, respectively.

Figure 5-14 and Figure 5-15 display the measurement results of the device with Ce-YIG on MgO (300 nm/20 nm) as cladding. Figure 5-14 shows the relative fraction of the TM-polarised output as a function of input wavelength when the sample is not saturated, and saturated in a forward direction and back direction; a peak at  $\lambda=1614$  nm is observed. Figure 5-15 presents the Stokes vector angle of opposite magnetic saturation at 0.5 nm resolution, where an angle of about  $1/2\pi$  is observed.

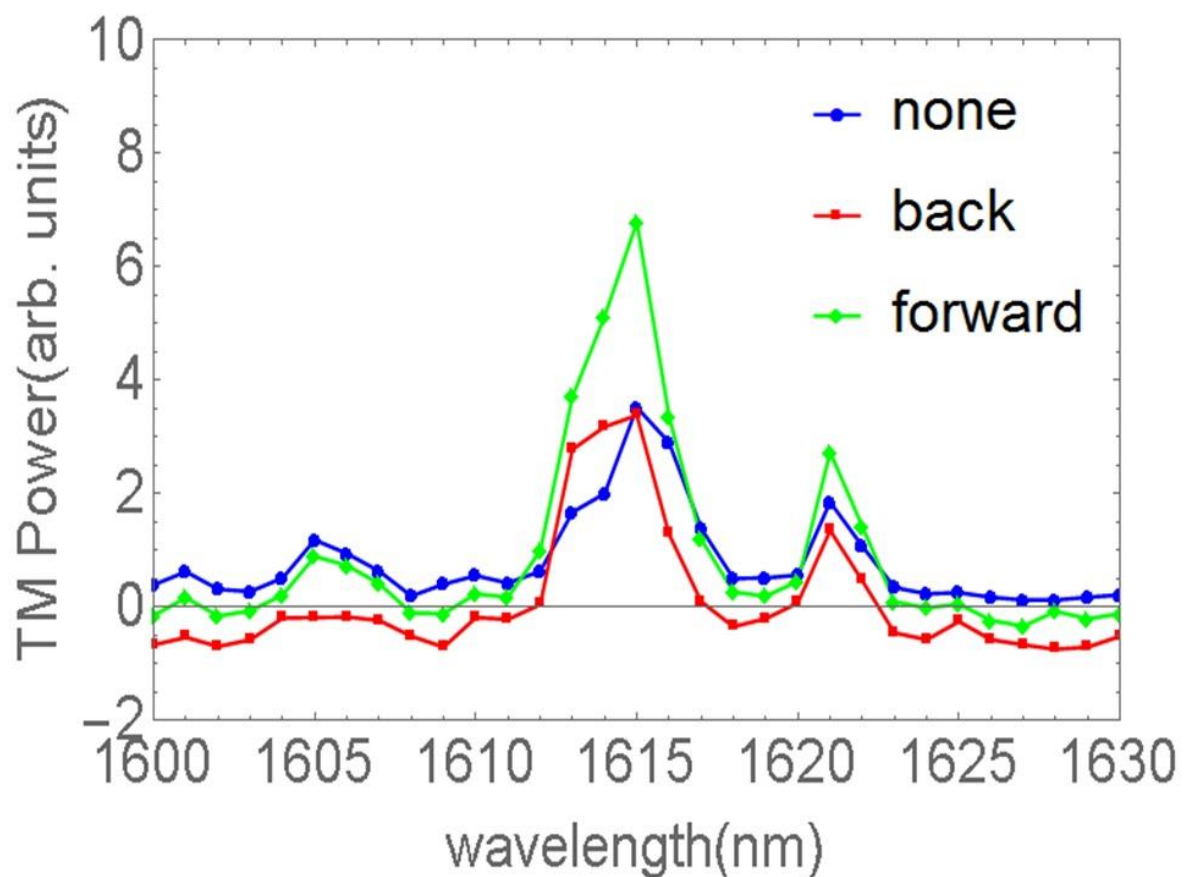


Figure 5-14. Device with Ce-YIG on MgO cladding on a 500 nm SOI platform: the relative fraction of the TM-polarised output as a function of input wavelength when the sample is not saturated, and saturated in a forward direction and back direction; a peak at  $\lambda=1612$  nm is observed.

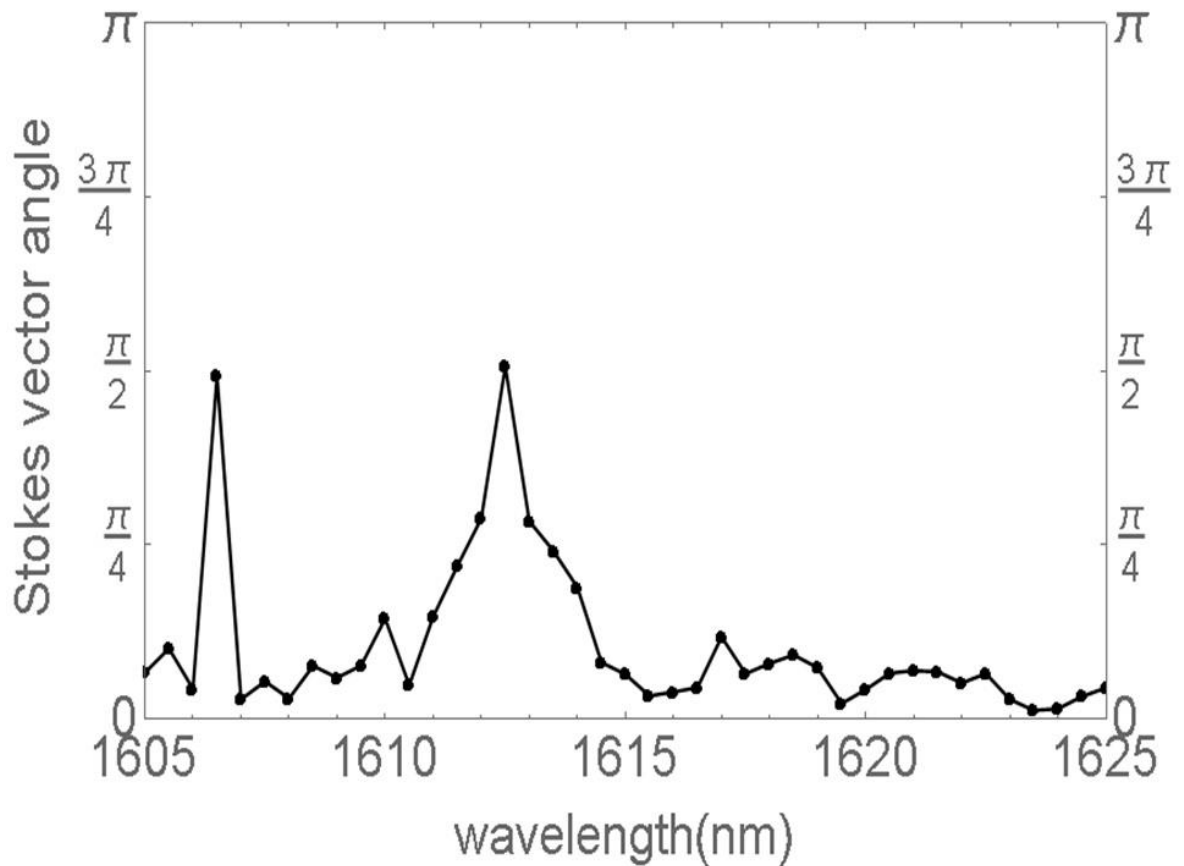


Figure 5-15. Device with Ce-YIG on MgO cladding on a 500 nm SOI platform: it presents the Stokes vector angle of opposite magnetic saturation at a 0.5 nm resolution, where an angle of about  $1/2\pi$  is observed.

### 5.2.5 Summary of the Observed Promising Results

Table 5-2 summarises the measurement results of all the NR-PMC devices fabricated on both 500 nm SOI and 340 nm SOI, which have been described above. The actual device lengths in measurement ( $L_m$ ), angle between Stokes vectors ( $\Theta$ ), and calculated Isolation ratio ( $d_c$ ) of the devices fabricated are presented. However, the isolation ratio we got here from the measurements is not the optimised performance that each device should have. Here, the isolation ratio depends on the number of QPM (Quasi-Phase Matching) periods on the device. Thus, the longer the device is, the more QPM periods there are. When the device is cleaved at the proper length, a Stokes vectors angle of  $\pi$  is expected, where the lightwaves of opposite propagation directions are orthogonal to each other and there is 100% isolation theoretically, and ideally more than 60 dB can be achieved, integrated with some other necessary components, like wave-plates and

polarisers, as discussed above. The lengths needed to achieve  $\pi$  between Stokes vectors ( $L_{\text{optimal}}$ ) for all devices are also calculated and presented in the table.

Among all the devices on 500 nm SOI platforms, the one with Ce-YIG/YIG claddings stands out to be the best, where  $0.74\pi$  has been obtained on a 4.07 mm-long device, and 5.5 mm will be needed to get total isolation. The second best is the one with Ce-TIG cladding, where  $0.816\pi$  has been obtained on a 6 mm-long device, and 7.35 mm will be needed to get total isolation. This, however, does not agree with what was discussed in Chapter 2, whereby devices with the Ce-TIG MO (magneto-optical) cladding should have the best performance with the smallest footprint. Besides, the performance of the device with Ce-YIG/YIG cladding outbids that of the device with Ce-YIG/MgO cladding, which, in theory, should be the other way around, as YIG has an opposite Faraday coefficient from that of Ce-YIG, which weakens the performance, while MgO has a neutral magneto-optical performance.

Among all of the devices on 340 nm SOI platforms, the one with Bi-TIG claddings stand out to be the best, where  $0.84\pi$  was obtained on a 3.4 mm-long device, and 4.1 mm will be needed to get total isolation. The second best is the one with Bi-TIG + TIG cladding, where  $0.81\pi$  was obtained on a 3.7 mm-long device, and 4.57 mm will be needed to get total isolation. This, also, does not agree with what was discussed in Chapter 2, whereby devices with the alternating MO cladding (MO+/MO-) should have the better performance with a much smaller footprint than the devices with just a single sign of MO cladding.

All of these contradictions between theory and application can most probably be attributed to the inconsistency of the quality of the partially crystallised garnet materials. Full crystallisation is a worldwide problem yet to be overcome. Recently, our collaborators have been using low temperature laser annealing to improve the crystallinity of the garnet materials. The results seem very promising and re-producible and are to be published. Therefore, in the future, devices with different lengths and with different MO garnet materials can be designed and fabricated to get further confirmation, and better repeatable performances should be expected.

	Substrate 1				Substrate 2			
	500nm SOI				340nm SOI			
Garnet	$L_m(\text{mm})$	$\Theta_m(\text{rad})$	$d_c(\text{dB})$	$L_{\text{optimal}}(\text{mm})$	$L_m(\text{mm})$	$\Theta_m(\text{rad})$	$d_c(\text{dB})$	$L_{\text{optimal}}(\text{mm})$
Bi-TIG	5.4	$0.28\pi$	0.88	19.3	3.4	$0.83\pi$	11.57	4.1
Bi-TIG+TIG	NA	NA	NA	NA	3.7	$0.81\pi$	10.63	4.57
Ce-TIG	6	$0.816\pi$	10.9	7.35	4.5	$0.32\pi$	1.15	14
Ce-YIG/YIG	4.07	$0.74\pi$	8.02	5.5	5.74	$0.10\pi$	0.11	57.4
Ce-YIG/MgO	7	$0.51\pi$	3.1	13.7	NA	NA	NA	NA

**Table 5-2. Summary of the measurement results of all the NR-PMC devices fabricated on both 500 nm SOI and 340 nm SOI. In the table,  $L_m$  - Measured Device Length,  $\Theta_m$  – Measured Stokes vectors angle,  $d_c$  – Calculated Isolation ratio based on  $\Theta_m$ ,  $L_{\text{optimal}}$  - Device Length Needed to achieve  $\pi$  between Stokes vectors. The best results are highlighted in red.**

Below, Figure 5-16 (a), (b), (c), and (d) present the relationship between isolation vs wavelength of the four best results highlighted in red in Table 5-2. Isolation was calculated by the method and equation 5.11 described in 1.2.3, while the relationship between the Isolation Ratio and Stokes Vector Angle based on equation 5.11 is described in Figure 5-17. Figure 5-17 (a) shows the periodic relationship between the isolation ratio and Stokes vector angle according to equation 5.11 with the period of  $2\pi$ . The maximum value, which tends to be infinite, is obtained at Stokes Vector Angle =  $(2n+1)\pi$ ,  $n=0,1,2,\dots$ , where the two modes are orthogonal to each other. Figure 5-17 (b) presents the relationship between the Isolation Ratio and Stokes Vector Angle for half a period ( $0-\pi$ ), and points out the best results described in Table 5-2.

$$d = -10 \log \left( \cos \frac{\theta}{2} \right)^2 \quad (5-11)$$

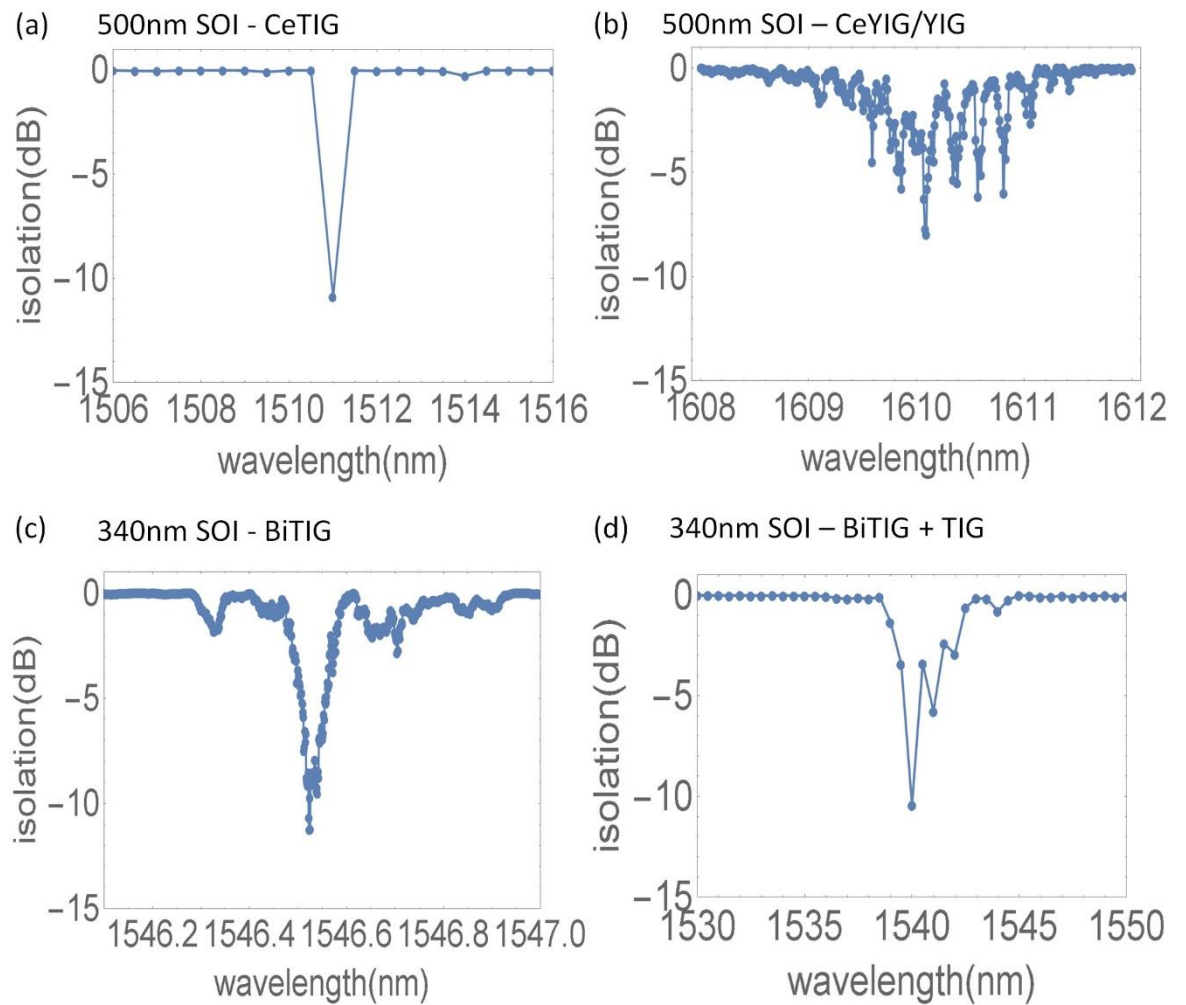


**Figure 5-16.**(a), (b), (c), and (d). The relationship between isolation vs wavelength for the four best results highlighted in red in Table 5-2. The isolation was calculated by the method and equation 5.11 described in 5.4.4.

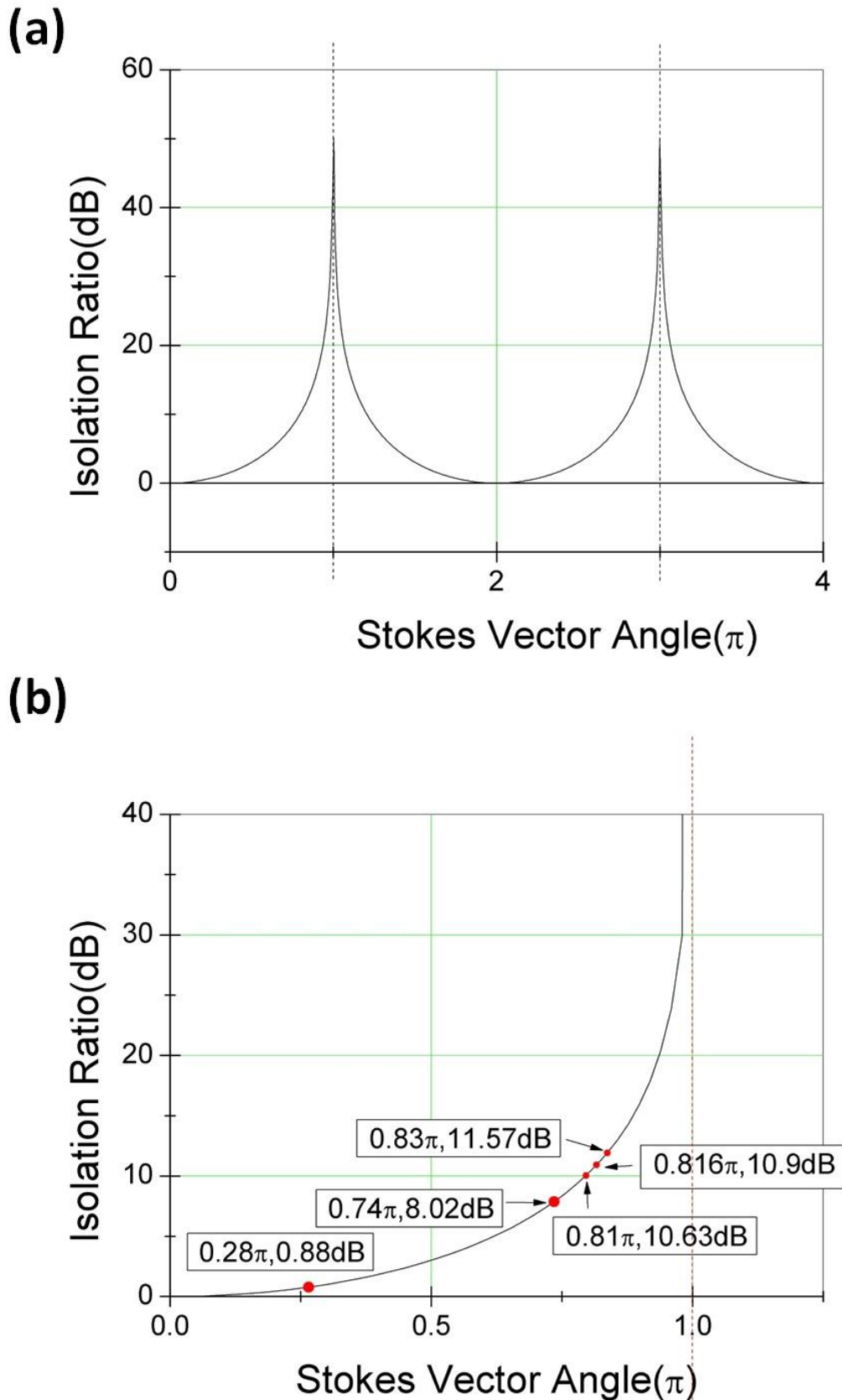


Figure 5-17.(a) describes the relationship between the Isolation Ratio and Stokes Vector Angle according to equation 5.11, which clearly shows a periodic trend with the period of  $2\pi$ . The maximum value, which tends to be infinite, is obtained at Stokes Vector Angle =  $(2n+1)\pi$ ,  $n=0,1,2,\dots$ , where the two modes are orthogonal to each other. (b) presents the relationship between the isolation ratio and Stokes vector angle for half a period, and points out the best results described in Table 5-2.

## **6 Chapter 6—Design, Fabrication, and Optical Measurement for Reciprocal Polarisation Mode Converter**

### **6.1 Introduction**

Chapters 3, 4, and 5 discussed the simulation, design, fabrication, and optical measurement of the NR-PMC part. This chapter is going to describe the simulation, design, fabrication, and optical measurement of the R-PMC (reciprocal polarisation mode conversion) part. Here, an L-shaped structure was adopted to achieve reciprocal polarisation mode conversion, similar to the trench structure. The asymmetric profile of the L-shaped waveguide effectively rotates the optical axis of the waveguide, such that, when a single mode from a symmetric waveguide is incident upon this asymmetric section, it excites both polarisation modes within the asymmetric structure. Beating between these two excited modes results in a modification of the state of the polarization that varies with propagation through the asymmetric section. Thus, through careful design of the length and degree of asymmetry of this section, various desired polarisation state conversions may be achieved.

The trench structure has been realised in III-V materials by Electrical Beam Lithography (EBL) and the Reactive Ion Etching (RIE) lag effect [96] [157] where, after the same amount of etch time, the etched depth of patterns with smaller feature sizes is smaller than those of bigger feature sizes. But, primarily due to its smaller dimensions, but also due to the etch parameters adopted for Si, the control of the RIE-lag approach is not straightforward in Si. The left pic of Figure 6-1 presents the cross-section profile of trenches of different widths after being deep etched for 20 mins, where it is clear that not much difference in etched depth vs trench width is obtained. The 5  $\mu\text{m}$ -wide trench is etched down 54  $\mu\text{m}$ , while the 10  $\mu\text{m}$ -wide trench is etched down 60  $\mu\text{m}$ . The right pic of Figure 6-1 includes four sets of data reflecting the change of etch depth of different trench widths after being etched for 20 mins, 60 mins, 80 mins, and 100 mins,

respectively. We can see that for the same trench width range, the difference in etch depth increases with the increase of the etch time. The RIE lag effect is small even for features of both the trench width and the trench depth at the 100  $\mu\text{m}$  scale. It will become much smaller for our case, where the width and depth of the trench is only at the 500 nm scale.

Therefore, an equivalent structure, the L-shaped profile, achieved through a two-step etch and re-mask process, is adopted to achieve the required asymmetry and reciprocal polarisation mode conversion.

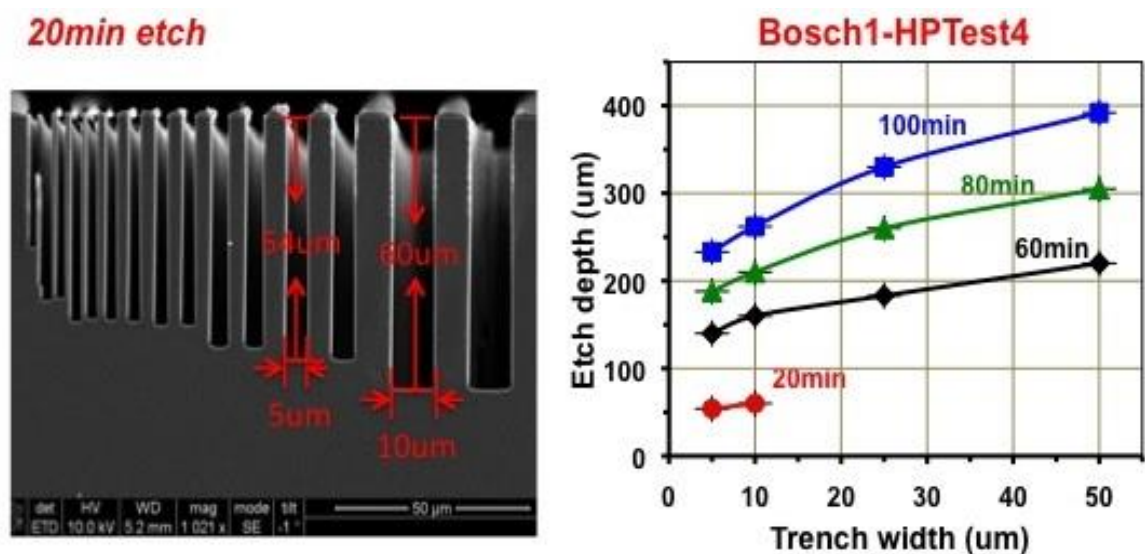


Figure 6-1. The left pic of Figure 6-1 presents the cross-section profile of trenches of different widths after being deep etched for 20 mins, where it is clear that not much difference in etched depth is obtained. The 5  $\mu\text{m}$ -wide trench is etched down 54  $\mu\text{m}$ , while the 10  $\mu\text{m}$ -wide trench is etched down 60  $\mu\text{m}$ . The right pic of Figure 6-1 includes four sets of data reflecting the change of etch depth of different trench widths after being etched for 20 mins, 60 mins, 80 mins, and 100 mins, respectively. These results are reprinted with the kind permission of Dr. Haiping Zhou [158].

## 6.2 Simulation and Design on 500 nm SOI and 340 nm SOI

### 6.2.1 500 nm SOI

The Reciprocal Polarisation Mode Converter (R-PMC) is designed to be made in an L-shaped (Figure 6-2b) cross-section on 500 nm SOI, where a big dimension gives more fabrication tolerance and offers enough space for modes conversion compared to thinner core SOI platforms. Simulation is conducted in a modesolver

program [137] in MATLAB<sup>®</sup> to ascertain the whole width ( $=W_1+W_2$ ) of the waveguide and also  $W_1$ ,  $W_2$ , and  $h_1$ , the depth to be etched down to. Here, 50%, not 100%, modes polarization conversion (i.e., the equivalent of a half-waveplate orientated at  $22.5^\circ$ ) has been previously identified as better implementation for the integrated isolator. The Stokes vectors relating to the effective optic axis orientations are  $S = \left(\frac{1}{\sqrt{2}}, \pm \frac{1}{\sqrt{2}}, 0\right)$  and  $S = \left(-\frac{1}{\sqrt{2}}, \pm \frac{1}{\sqrt{2}}, 0\right)$ , respectively [86].

First of all, an initial simulation was carried out to find out the width range for single-mode guided 500nm-thick waveguides. The cross-section profile is shown in Figure 6-2 (a). The height of waveguide  $H$  is 500 nm. The relationship between the effective refractive index of the two orthogonal single-lobed fundamental modes and the width of the waveguide is described in Figure 6-3, from which we can obtain the width range of single mode waveguides, 150 nm-300 nm. Then, for the L-shaped simulation, 250 nm, half of the whole Si core thickness, was chosen as the etched-down depth  $h_1$ . The cross-section profile is shown in Figure 6-2 (b). Based on the obtained single-mode width range and the etched depth  $h_1$ , simulations were conducted to find the proper dimensions to achieve 50% mode conversion by varying  $W_1$  and  $W_2$ . The single-mode width range 150 nm-300 nm was used as the width range for  $W_1$ . By increasing the value of  $W_2$ , structures with different optic axis orientations, which also only allow the guiding of the single-mode, can be found from the Stokes vectors. The simulation result is summarized in Table 6-1.

In the actual e-beam mask design, a wider range of widths for  $W_2$  were chosen for each  $W_1$  value to accommodate any fabrication error/difference. Taking  $W_1 = 150$  nm as an example, the simulated value for  $W_2$  was 168 nm, while 165 nm-175 nm was chosen for  $W_2$  when designing the e-beam mask. Three lengths of the L part were chosen based on the half-beat length  $L_\pi$  to achieve a different percent of mode conversion,  $L_\pi$ ,  $1.5L_\pi$ , and  $2L_\pi$ , from which a 50%, 35.36% ( $= \frac{\sqrt{2}}{2} \cdot 50\%$ ), and 0% mode conversion should be expected.

As the waveguides were thin, in order to ensure they were guiding the light and avoiding bad facets of these thin waveguides after the cleaving process, a linear Si adiabatic taper coupler was added to both sides of the waveguides, as shown in Figure 6-4. Here ‘adiabatic’ means that the taper changes so slowly that the power is maintained in the two fundamental modes, and the power that couples to other higher order modes is nearly negligible [159][160][161]. A long

and gently changing taper is one solution to achieve adiabatic coupling [161]. An adiabatic taper coupler does not require a precise power-transfer length [162] as long as it is long enough to satisfy the adiabatic condition. The width of the taper varied from  $W_1$  to  $2\ \mu\text{m}$  through a  $350\ \mu\text{m}$  length on an SOI platform [163]. In actual design, waveguides with adiabatic tapers of different lengths can be designed and tested. Additionally, tapers of two forms, the triangle and the quarter circle, were also added to both ends of the L-part to avoid the sudden change and incontinuity, as seen in Figure 6-5. Also, there is an overlap between the layer of the L-part and the layer of the straight waveguide to allow for a greater fabrication tolerance.

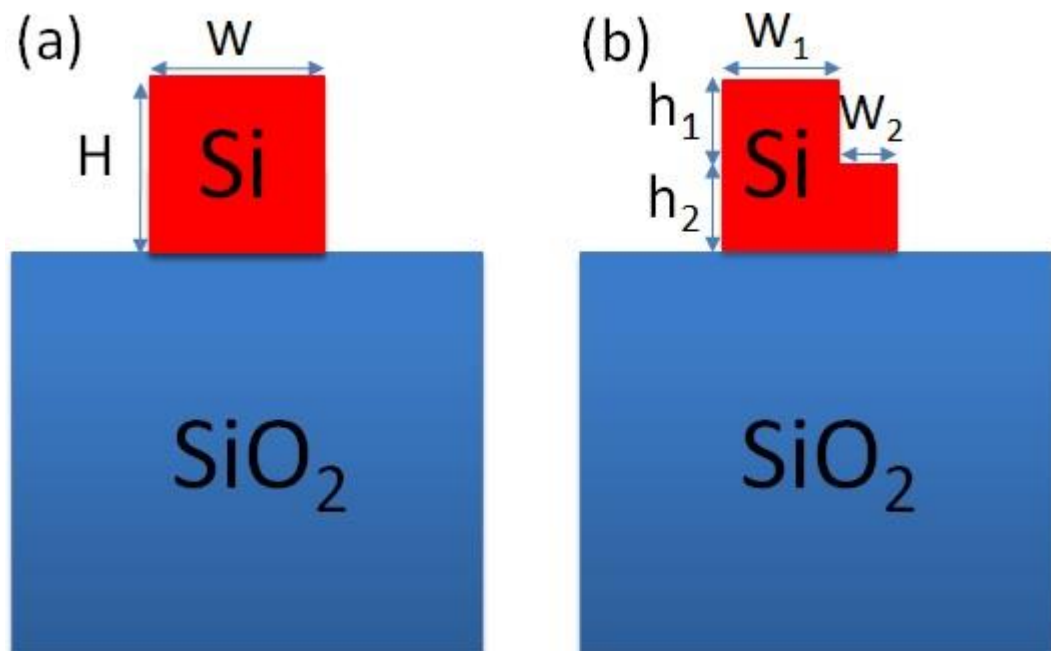


Figure 6-2. (a) The Cross-Section Profile of a 500 nm-thick single-mode waveguide, while (b) is the Cross-Section Profile of the L-shaped design.

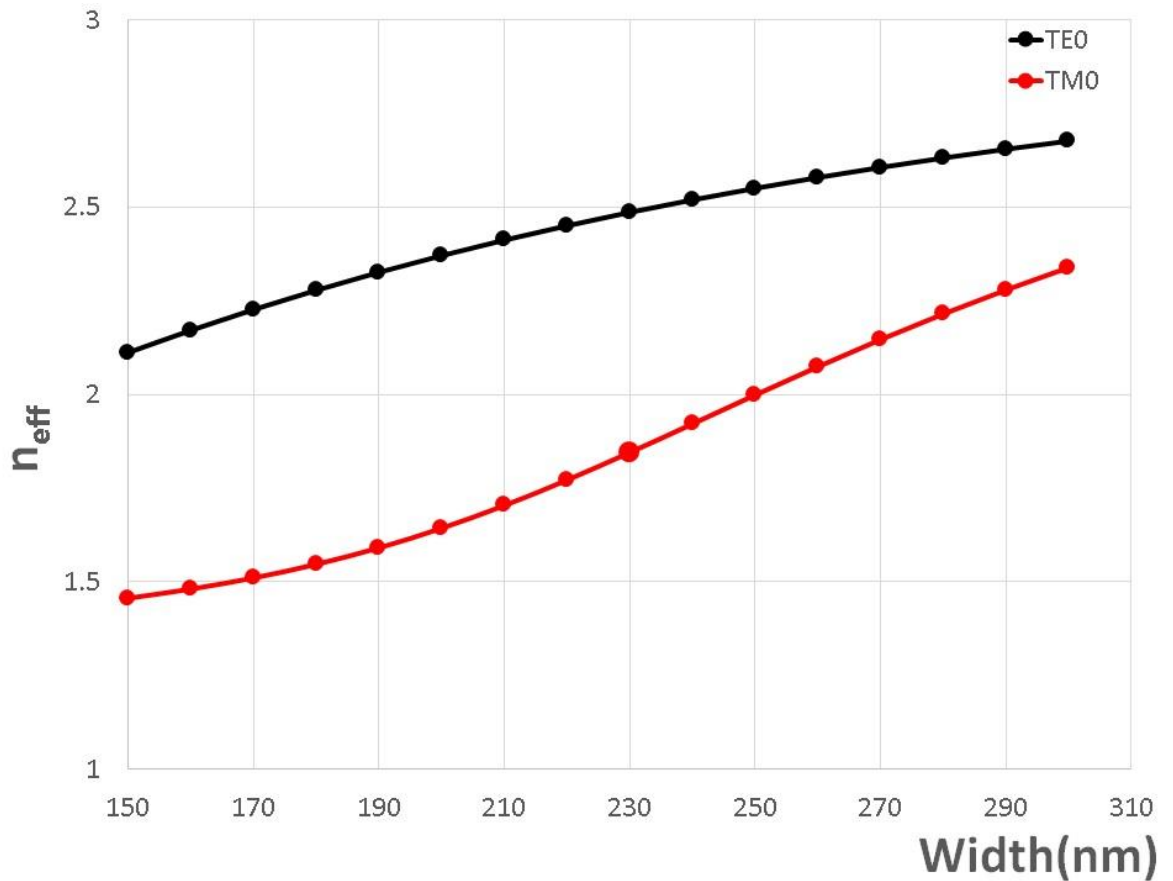


Figure 6-3. The relationship between the effective refractive index of the two fundamental modes and the width of the waveguide.

$h_1$ (nm)	$W_1$ (nm)	$W_2$ (nm)	$W$ (nm)	$L\pi$ ( $\mu$ m)	$S_1(1)$	$S_2(1)$	$S_1(2)$	$S_2(2)$
250	150	168	318	2.5384	0.7009	0.6041	-0.7080	-0.5722
250	160	168	328	2.6596	0.6979	0.6099	-0.7013	-0.5772
250	170	165	335	2.7276	0.7079	0.6026	-0.7076	-0.5716
250	180	165	345	2.8816	0.7054	0.6083	-0.7020	-0.5782
250	190	165	355	3.0536	0.7027	0.6142	-0.6965	-0.5856
250	200	163	363	3.1713	0.7113	0.6086	-0.7029	-0.5833
250	210	163	373	3.3820	0.7074	0.6159	-0.6971	-0.5928

Table 6-1. The optimised parameters of the L-shaped waveguide of each specific width to achieve a 50% mode conversion on 500 nm SOI.

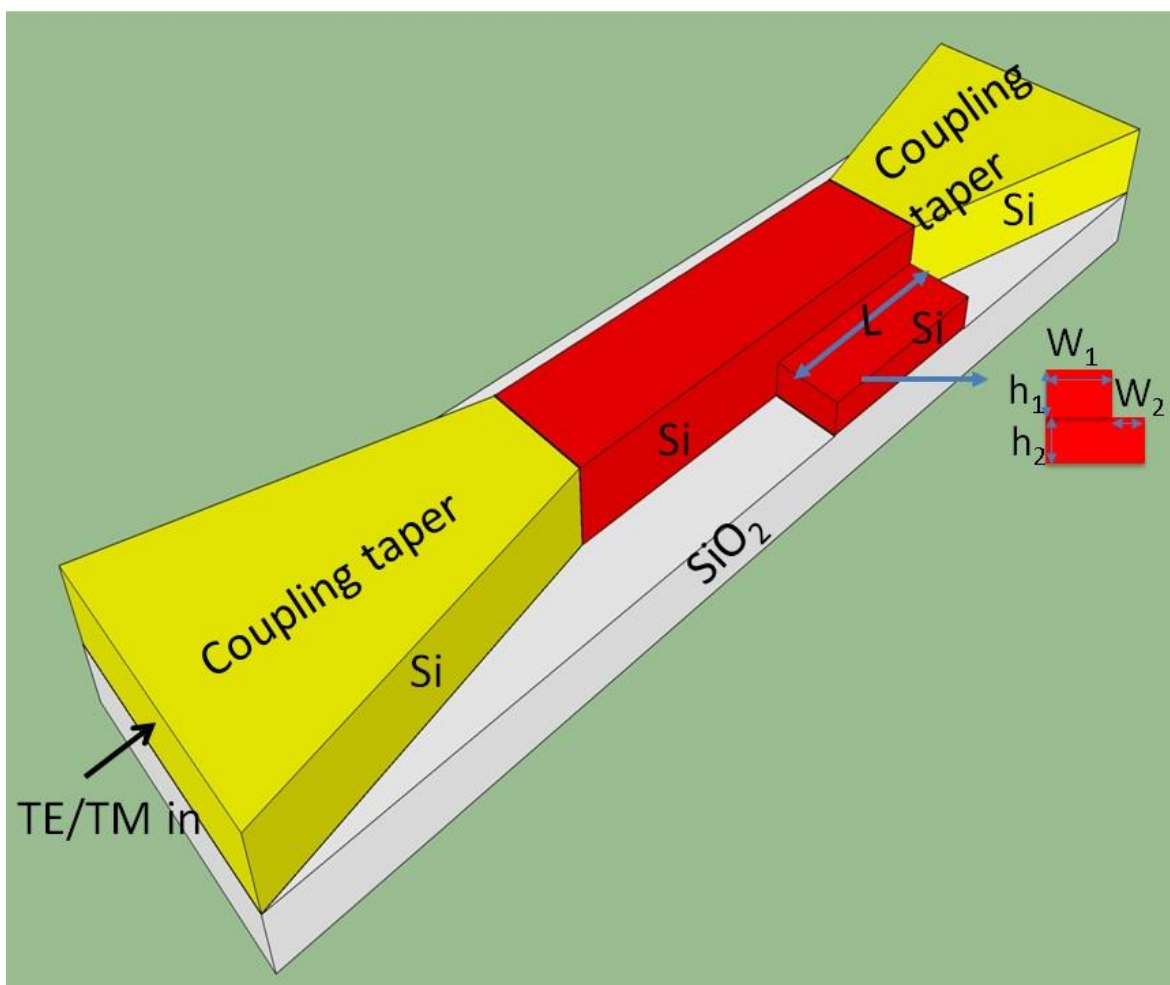


Figure 6-4. The structure of the L shape with Si adiabatic taper coupler.

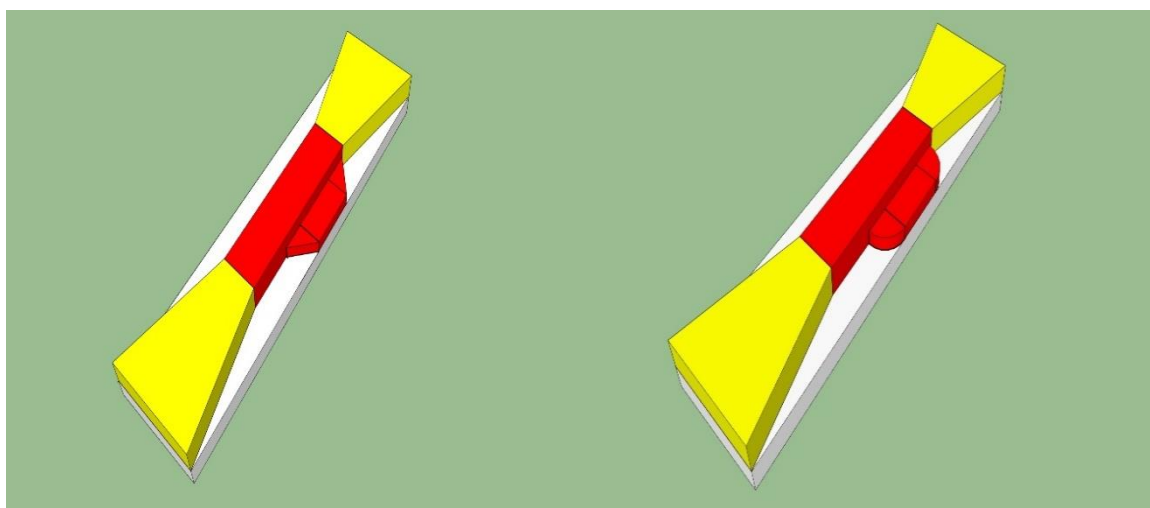


Figure 6-5. The triangle and the quarter circle added to both ends of the L-part to avoid the sudden change and in-continuity.

### 6.2.2 340 nm SOI

The same rules and methods apply to the simulation and design of the L-shaped design on the 340 nm SOI platform, except that the thickness of the core Si layer is now 340 nm and not 500 nm. Figure 6-6 indicates the relationship between the effective refractive index of the two fundamental modes and the width of the waveguide, from which we can get the width range of single mode waveguides, 200 nm-400 nm. Interestingly, there is a crossover for square cross-section guides.

For waveguides with widths less than 340 nm, represented by the points at the left side of the crossover point (340,340) in Figure 6-6, the difference in the effective refractive index between the two fundamental modes decreases with the increase of the width in the horizontal dimension. This means that the half-beat length increases and the difference becomes 0 when the width in the horizontal dimension equals the height in the vertical dimension.

For waveguides with widths more than 340 nm, represented by the points at the right side of the crossover point (340,340) in Figure 6-6, the difference in the effective refractive index between the two fundamental modes increases with the increase of the width in the horizontal dimension. Meanwhile, the height in the vertical dimension stays the same, at 340 nm; hence, the half-beat length decreases. For waveguides with a fixed value of the vertical dimension (height), the bigger the difference between the horizontal dimension (width) and the vertical dimension (height), the bigger the effective refractive index between the two fundamental modes, the shorter the half-beat length.

For the L-shaped simulation, 170 nm, half of the whole Si core thickness, was chosen as the etched down depth  $h_1$ . Here, no proper 50% mode conversion structures were found in waveguides where  $W_1$  was wider than 320 nm, as the horizontal dimension ( $W_1 + W_2$ ) is much bigger than the vertical dimension ( $h_1 + h_2 = 340$  nm), and there is always more power scattered in the horizontal dimension than in the vertical dimension. The simulation result is summarized in Table 6-2.

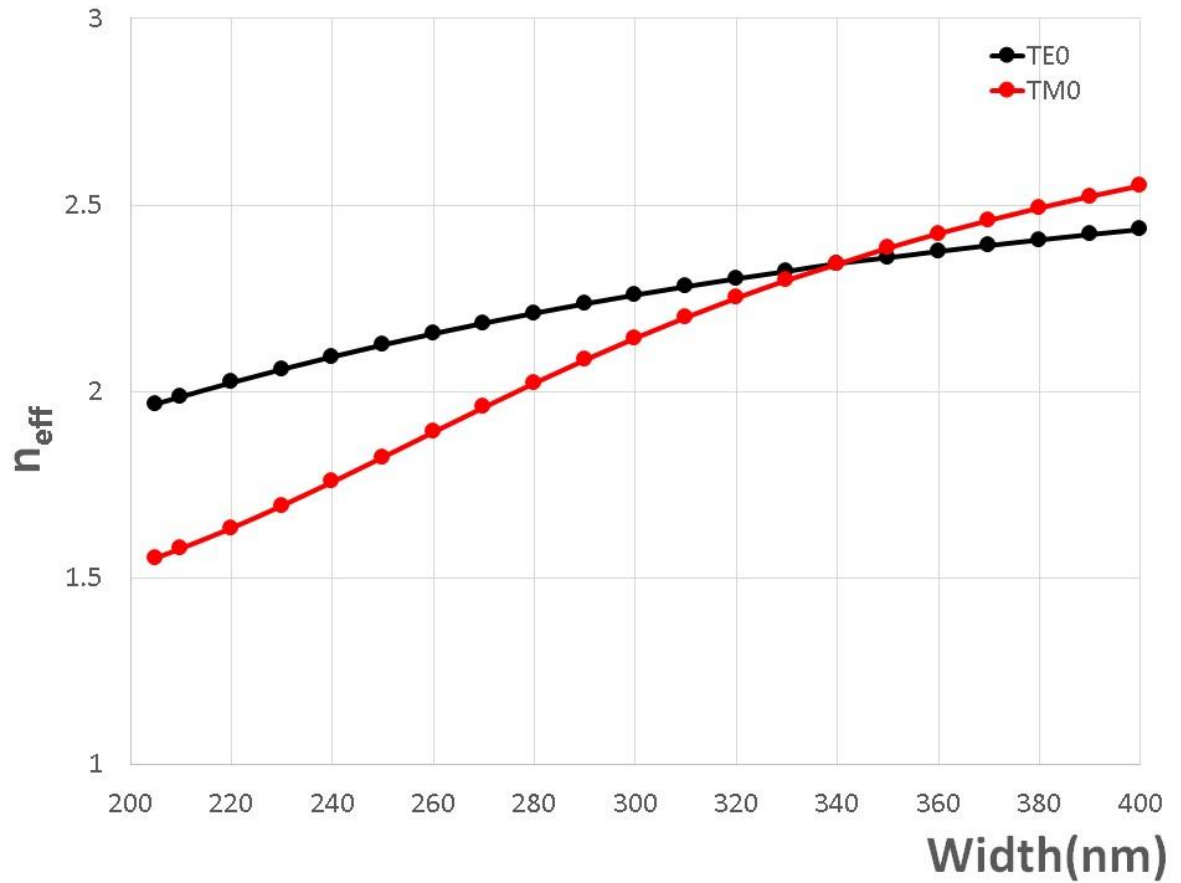


Figure 6-6. The relationship between the effective refractive index of the two fundamental modes and the width of the waveguide.

$h_1$ (nm)	$W_1$ (nm)	$W_2$ (nm)	$W$ (nm)	$L\pi$ ( $\mu$ m)	$S_1(1)$	$S_2(1)$	$S_1(2)$	$S_2(2)$
170	200	90	290	2.6592	0.6837	0.6185	-0.6943	-0.6327
170	210	85	295	2.7996	0.6879	0.6169	-0.6965	-0.6306
170	220	80	300	2.9899	0.6898	0.6177	-0.6970	-0.6304
170	230	75	305	3.2401	0.6891	0.6211	-0.6953	-0.6324
170	240	70	310	3.5642	0.6853	0.6276	-0.6909	-0.6373
170	250	65	315	3.9830	0.6774	0.6378	-0.6828	-0.6457
170	260	60	320	4.5266	0.6643	0.6525	-0.6696	-0.6586
170	270	50	320	5.1111	0.7039	0.6144	-0.7107	-0.6183
170	280	45	325	6.0714	0.6838	0.6367	-0.6907	-0.6387
170	290	40	330	7.4204	0.6510	0.6689	-0.6584	-0.6690
170	300	30	330	9.2702	0.6997	0.6228	-0.7082	-0.6200
170	310	25	335	12.5990	0.6404	0.6795	-0.6506	-0.6745
170	320	15	335	19.0707	0.7124	0.6109	-0.7247	-0.6007

Table 6-2. The optimised parameters of the L-shaped waveguide of each specific width to achieve a 50% mode conversion on a 340 nm SOI.

### 6.3 Fabrication

First of all, etched markers used for alignment between layers were prepared using e-beam lithography. Two layers of 12% 2010 PMMA were used as the etch resist mask, and written at a dose of  $1000 \mu\text{C}/\text{cm}^2$  with a 64 nA e-beam current along with a VRU (variable resolution unit) of 16 under 100 kV. The sample was developed in 2.5:1 IPA: MIBK for 140 s followed by 45 s IPA at 23.5 Degrees. These markers are sets of  $20 \mu\text{m} \times 20 \mu\text{m}$  of 4 squares plus  $700 \mu\text{m} \times 20 \mu\text{m}$  crosses. A Si etch tool (STS-ICP, Estrelas, or ICP-180) was used to etch the markers down into the Si layer to the  $\text{SiO}_2$ , which was confirmed using the end-point detector to get the interferometer trace. Therefore, all these markers are 500nm/340nm deep, the same thickness as that of the Si core layer. Overnight soaking in hot acetone (50 Degrees C) and then 2 mins Oxygen Plasma ash were adopted to remove the remnant PMMA resist.

Afterwards, 1:1 MIBK diluted HSQ (Hydrogen silsesquioxane)-negative resist was spun at 2000 rpm and baked on a hotplate for 15 mins before being sent to the e-beam to write the waveguides patterns. Only the straight waveguide part and the taper couplers were written this time as the first layer. The patterns were written with a 2 nA beam with VRU as 6 and at a dose of  $1350 \mu\text{C}/\text{cm}^2$ . At the same time, the cover strips to cover the markers, to protect them from being damaged in the subsequent dry etch procedure, were written.

Afterwards, the mask was developed in neat TMAH for 30 s followed by a 30 s rinse in RO (de-ionised) water, another 30 s in RO (de-ionised) water and 45 s in IPA. Then, an Si dry etch tool was used to etch away half of the core Si layer, using an end-point detector, 250 nm deep for the 500 nm SOI and 170 nm deep for the 340 nm SOI. Then, an acetone, IPA rinse, and an oxygen ash were carried out to remove any 'etch residues' on the sample surface, after which a second layer of 1:1 MIBK diluted HSQ resist was applied on the sample, to have the second layer of the L-part written, without stripping off the remaining HSQ, which was used as the dry etch mask for the second etch as well. The same spinning speed, bake time, e-beam beam size, VRU, dose, and develop condition were used as in the first layer. Then, the device was etched down another half thickness of the Si core layer in the Si etch tool. The device was completed and ready for cleaving.

Before cleaving, a layer of photoresist was spun on top without any hot-plate curing. Careful cleaving was carried out using the scribe+cleave tool to get a 4-5mm-long device with straight edges. Finally, a 5 mins acetone rinse was applied to remove the photoresist on top, and the device was ready for measurements. Figure 6-7 indicates the structure of the L-shape under SEM. The left and the middle pics show the top-down view of the L-part with a triangle and quarter-circle taper, respectively, while the right pic presents the cross-section profile of the L-part.

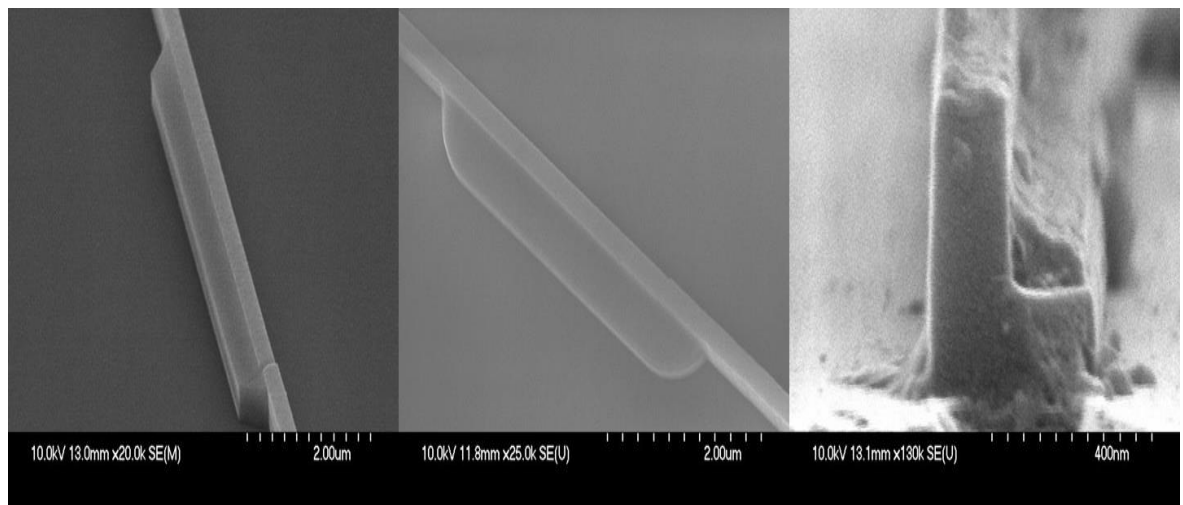


**Figure 6-7.** The structure of the L-shape under SEM. The left and the middle pics show the top-down view of the L-part with a triangle and quarter-circle taper, respectively, while the right pic presents the cross-section profile of the L-part.

During the fabrication process, the alignment between the layers is very critical as there is very small fabrication tolerance in this design. Only misalignment under  $W_1/2$  (75 nm-105 nm for a 500 nm SOI and 100 nm-160 nm for a 340 nm SOI) is allowed if a  $W_1/2$  wide overlap is placed between the first straight waveguide layer and the second L-part layer, while the normal drift in the VB6 tool is ~30 nm every 15 mins [164]. So, in order to achieve a good alignment, a recalibration every 15 mins is needed during the e-beam job-writing process, or a job shorter than 15 mins should be designed by varying the e-beam mask, e-beam spot size, or VRU.

Another fabrication problem will be the stitch error (Figure 6-8), resulting when the whole e-beam mask is divided into many 1.2 mmx1.2 mm or 1 mmx1 mm subfields [164]. Therefore, there will be many stitches between the sub-fields, and it becomes worse when there is drift in the process of switching fields. To

avoid the stitch error, overlap can be placed in the mask between subfields if the mask is too large to be put in a single subfield, and an effort should be made to design the mask to be in a single subfield if it is within a single subfield size.

A cell registration process can be developed to solve the alignment issue and the stitch error where the whole mask is divided into small cells whose mask-writing time is shorter than 15 mins, and there is a re-calibration between two cells writing and a bit of mask overlap between two cells. As the mis-alignment for the last set of devices fabricated is within the tolerance range because of the good performance of the EBL tool, the cell registration process is not applied in the fabrication process of the R-PMC part yet. However, in the future, the cell registration process, which guarantees the good alignment between layers regardless of the performance of the EBL tool, is a must, and has to be applied in the fabrication process of the L-shape device.

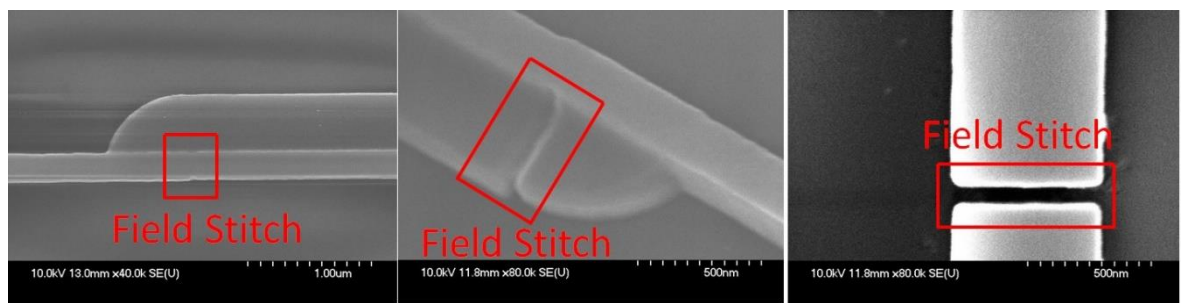


Figure 6-8. Field stitch errors

## 6.4 Optical Measurements

The measurements method for the R-PMC part is much the same as that described for the NR-PMC part in Chapter 5. The same free space end-coupling method was adopted with pure TE injected in, and TM and TE modes of the output measured by the photodiode detector together with the lock-in amplifier system. The whole setup of the measurement system is shown in Figure 6-9.

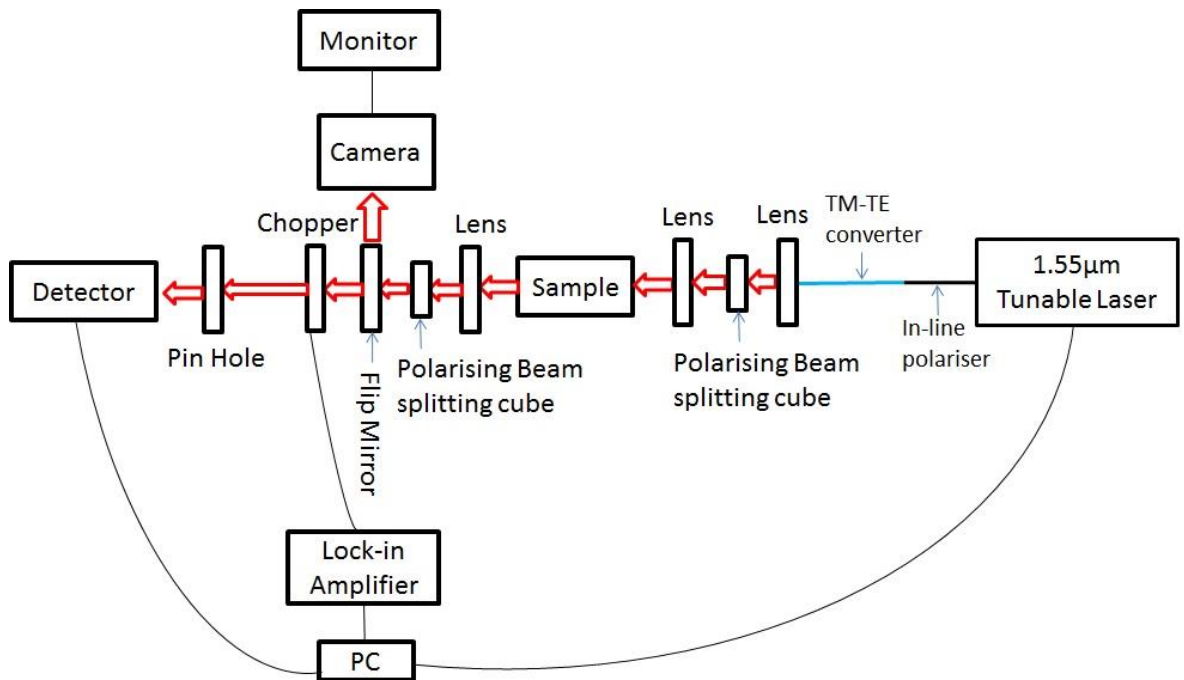


Figure 6-9. Measurement rig set-up for the R-PMC part.

Figure 6-10 shows the measurement results of TM output vs wavelength of three devices on a 500 nm SOI, where  $W_1=200$  nm,  $W_2=163$  nm, and  $h_1=250$  nm; the only difference between the three devices is the length of the L-part with the three different values as  $L_1=L_\pi$ ,  $L_2=1.5L_\pi$ , and  $L_3=2L_\pi$ , from which we should expect 50%, 35.36% ( $=\frac{\sqrt{2}}{2} \cdot 50\%$ ), and 0% mode conversion. We can see that there is a trend whereby, with the increase of the L-part length, the TM output power increases, which hints that there is more mode conversion. However, there is not one outstanding obvious peak in any results of the devices of different L-part lengths. The peaks are quite randomly scattered. There are also fringes resulting from the Fabry-Perot cavity of the device in the traces. Similar results are obtained from devices of different lengths in the L-part on the 340 nm SOI (Figure 6-11), where  $W_1=280$  nm,  $W_2=50$  nm, and  $h_1=170$  nm.

Later, the reason why the measurement results did not match what should be expected was discovered: there was a problem with the designs we had for both the 500 nm SOI and 340 nm SOI platforms. From the dimension parameters of the structure designs on the 500 nm SOI and 340 nm SOI in Tables 6.1 and 6.2, respectively, we can see that, in the L-part, the total width ( $w$ ) of the waveguide is smaller than the height of the waveguide (500 nm for a 500 nm SOI and 340 nm for a 340 nm SOI), while, in the adiabatic taper section, the input/output side, 2µm wide, is larger than the height of the waveguide. Thus, there will be a square

cross-section part in the design where the width of the waveguide equals the height, which leads to polarisation scattering between the modes with a similar effective refractive index, and random polarisation states will be obtained.

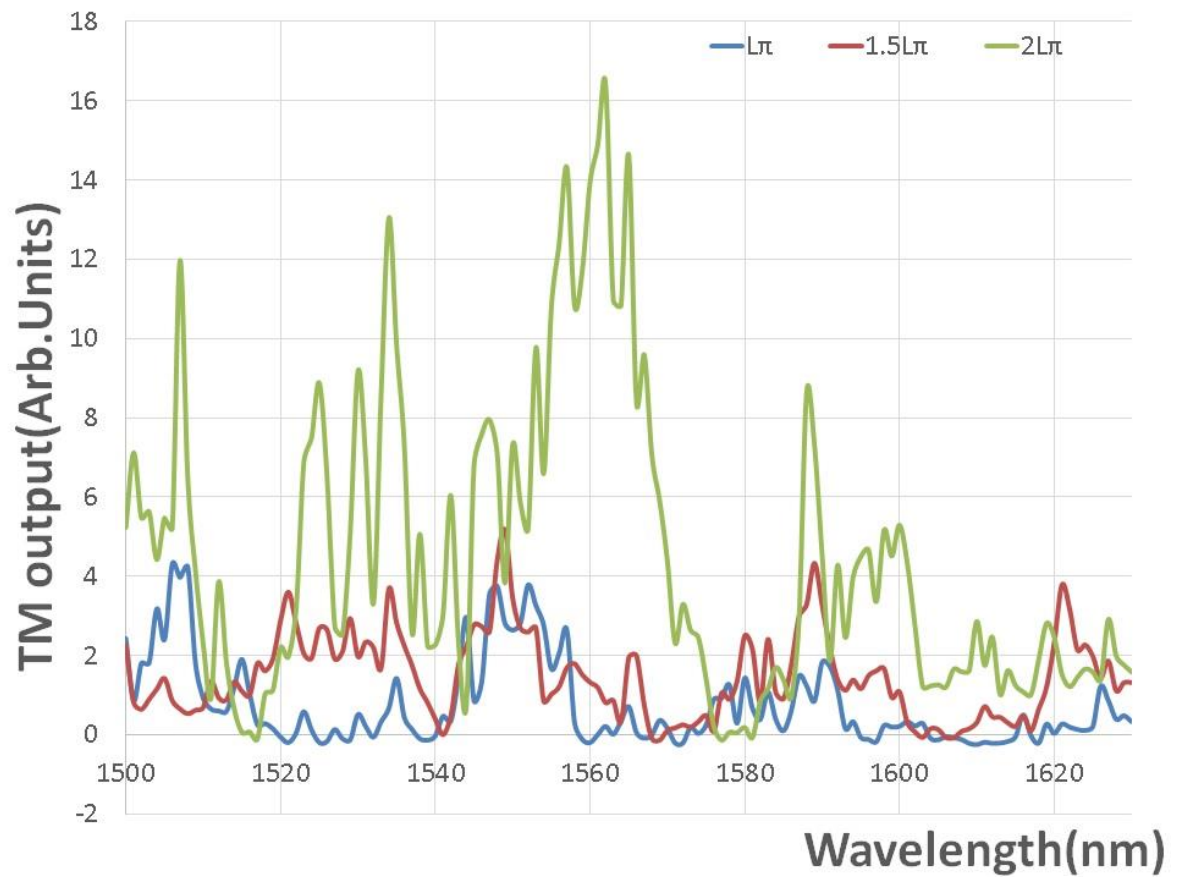


Figure 6-10. The measurement results of TM output vs wavelength of three devices on a 500 nm SOI.

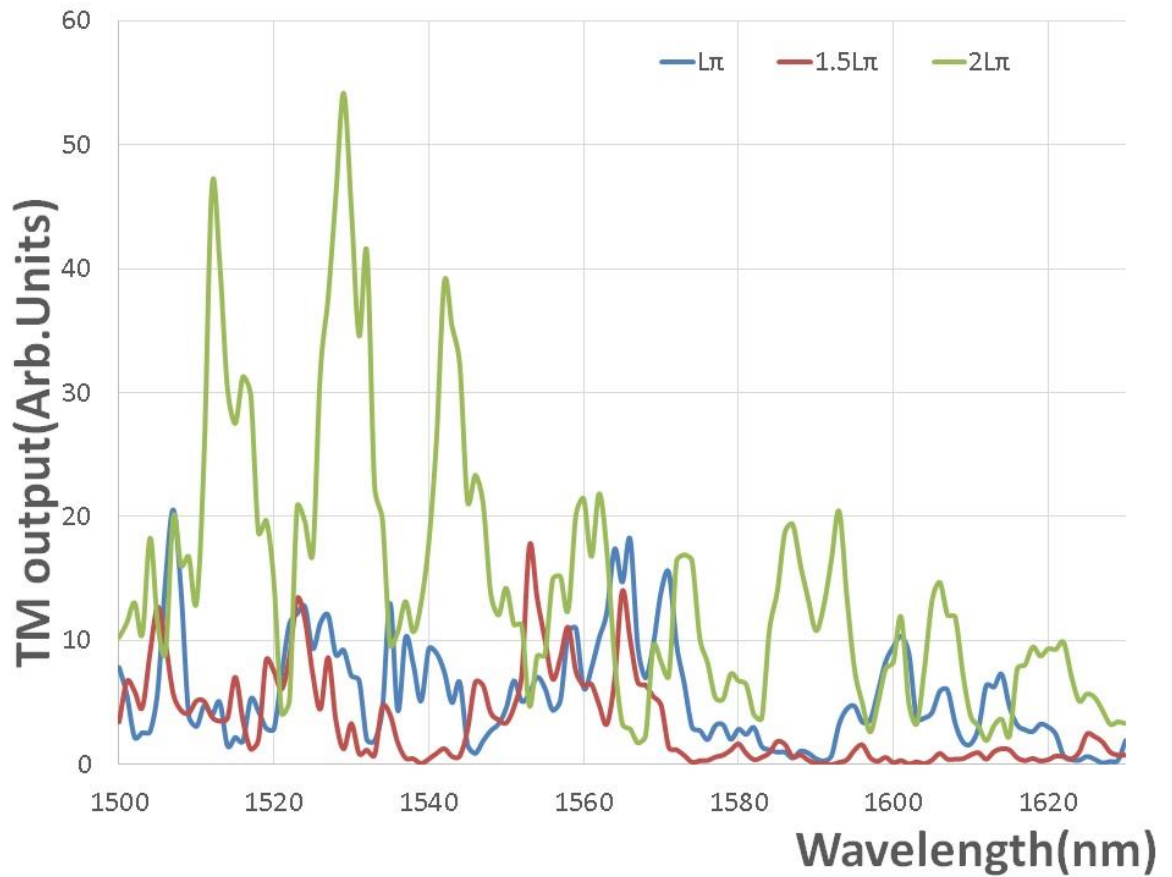


Figure 6-11. The measurement results of TM output vs wavelength of three devices on a 340 nm SOI.

## 6.5 Discussion and Future Work

More work needs to be done in order to develop a working R-PMC device in the future. On one hand, in order to remove the Fabry-Perot fringes noise, an anti-reflection coating (ARC) can be applied to both facets of the devices after cleaving. The existence of the anti-reflection coating layer creates a double interface, which, thus, leads to two reflected waves, as seen in Figure 6-12. When the coating layer is a quarter-wavelength thick  $d = \frac{\lambda}{4n}$  with a refractive index of  $n = \sqrt{n_1 n_{air}}$  [165], there will be a  $\pi$  phase difference between the two waves, so the two waves will completely cancel each other.  $\text{Si}_x\text{N}_y$  with a refractive index of around 2-2.1 at the infra-red wavelength range is a good candidate for the AR coating. According to the reflectivity equation,  $R = \left(\frac{n_1 - n}{n_1 + n}\right)^2$ , only 4% of the wave is reflected.

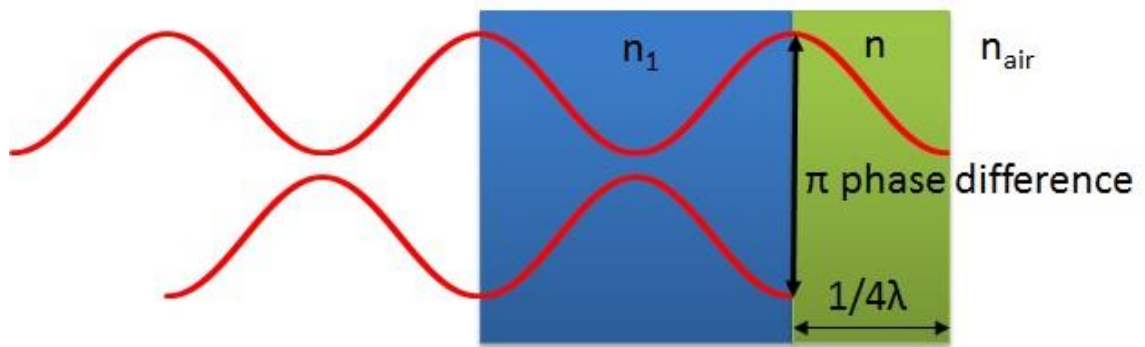


Figure 6-12. The existence of the anti-reflection coating layer creates a double interface, which, thus, leads to two reflected waves.

On the other hand, a defect was found in the design of the L-shape. Between the wide taper (2-3  $\mu\text{m}$  wide) and the straight waveguide (200-300 nm), there is a part where the width of the waveguide equals the height of the waveguide, which makes it a total square waveguide (500x500 nm for a 500 nm SOI and 340x340 nm for a 340 nm SOI). This leads to unwanted mode conversion between the guided modes as it can be either mode component. The mode scattering at the square cross-section part gives a random incoherent polarisation state.

Later measurements carried out in a polarimeter system can be done to identify whether the output is a polarisation coherent state or a polarisation mode scattering state, which is an incoherent state that can result from a structure with total square cross-section dimensions. Polarisation coherent state outputs are represented by points on the Poincare sphere, and the relationship of the Stokes parameters of the points can be expressed by equations about Stokes parameters, as discussed in Chapter 5. The polarisation mode scattering states are described by random points in the middle of the Poincare sphere, and the relationship of the Stokes parameters is not coherent. Revisions need to be made to avoid the total square area, including making the taper area a half-etch down by applying a wider second layer, as seen in Figure 6-13. Also, waveguides with adiabatic tapers of different lengths can be designed and tested. Besides, the QPM periodic loading on top of the Si waveguide can be another promising option, as observed and discussed in Chapter 5.

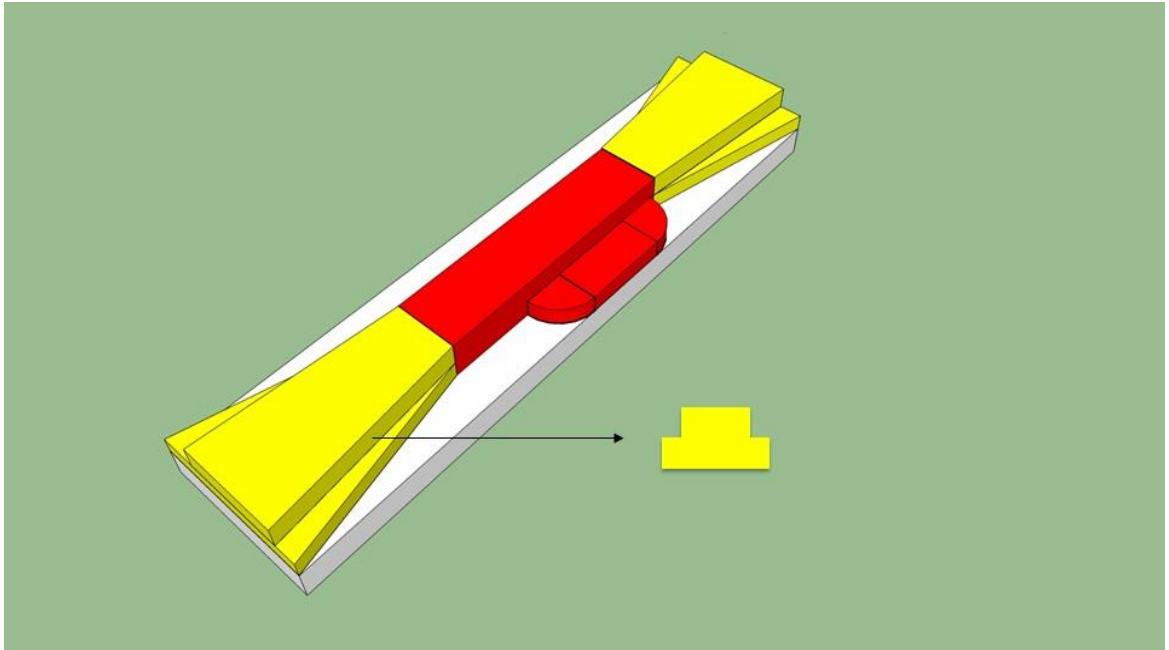


Figure 6-13. The structure of a potential working L-shaped R-PMC device; a wider second layer can be added to the coupler to avoid the total square waveguide.

## 7 Chapter 7—Discussions, Conclusions, and Future Work

As an indispensable component in optical circuits/systems, an optical isolator helps to keep the performance of the whole system stable, by preventing and blocking reflected light signals that occur at interfaces. The isolator also prevents undesired interference and interactions between connected devices and pathways/routes from coming back to the optical source, which will make the source suffer and lead to instabilities. To date, the optical isolator is the most significant device that has not been successfully commercialised.

The core technique of the integrated isolator requires non-reciprocity. There are commonly two approaches taking advantage of magneto-optical (MO) garnet material in waveguides: the Faraday Effect (longitudinal) - Nonreciprocal Polarisation Mode Conversion (NR-PMC), and the transverse approach - Nonreciprocal Phase Shift (NPS), where a phase shift between forward and backward traveling light is generated, but which only normally applies to TM mode designs.

Currently, almost all of the research into the development of integrated isolators correspond to TM (Transverse Magnetic) modes by applying NPS in structures like ring isolators [64]-[67] and MZI (Mach-Zehnder Interferometers) [29][31][69]-[73]. This, however, does not match the needs of many integrated systems, like PICs (Photonic Integrated Circuits) or OEICs (Opto-Electronic Integrated Circuits), as most of the lasers within these systems emit TE (Transverse Electric)-polarised light as a result of quantum-well selection rules. A detailed literature review can be found in Chapter 1.

A few TE mode integrated optical isolators have been proposed based upon NPS [31] [32] [84] [110]. To date, the only two TE polarised light optical isolators were realized by Ghosh et al. [31] and Shoji et al. [32]. In these experiments, MO garnet material was adhesively bonded on top of the waveguide and the NPS

approach, together with a complicated optical serpentine circuit or complicated design of asymmetric coupled waveguides for TE-TM mode conversion, was employed, although the controllability of the thickness of the adhesive bonding layer remains an issue of concern.

Obstacles remain in the integration of MO garnet material on semiconductor substrates. In most cases, adhesive bonding or direct bonding is utilized for the integration [29][65]-[67][69]-[73], which is sensitive to any thermal expansion and currently unsuitable for mass production.

This project aimed to realise the integration of an optical waveguide isolator that works for both TE and TM modes on the Silicon-on-Insulator platform. We have targeted a design with two core components that are required to build such an isolator. One is a 45 ° NR-PMC (Nonreciprocal Polarisation Mode Conversion), where the NR-PMC approach, which works for both TE and TM modes, is adopted. The other is a 45° R-PMC (Reciprocal Polarisation Mode Conversion), where an asymmetric structure, with an L-shaped cross-section waveguide is employed, so that the resultant rotation of the optical axis of the guide enables the excitation of hybrid modes from an injected linear polarisation mode and reciprocal mode conversion between the two modes.

For the NR-PMC part, in order to resolve the problems of phase matching and the integration of MO garnet material on the SOI substrate, a bilayer PMMA lift-off mask was developed to form a periodic loading MO garnet segments pattern in order to achieve quasi-phase matching. This was achieved by forming MO segments that alternate with  $\text{Si}_x\text{N}_y$  segments, or by forming MO segments (+) with a positive Faraday rotation coefficient alternating with MO segments (-) with a negative Faraday rotation coefficient. Radio-frequency (RF) material deposition techniques were adopted, followed by a rapid thermal annealing process (RTA) to achieve crystallinity of the MO garnet. This section of the project was in collaboration with Professor Bethanie Stadler's group from the University of Minnesota. All the MO garnet materials deposition and all the material characterisation with VSM, XRD, EBSD, and Faraday rotation measurements were carried out in Minnesota, where I spent several weeks.

## 7.1 Nonreciprocal Polarisation Mode Converter (NR-PMC)

### 7.1.1 Conclusions

On the NR-PMC part, different SOI substrates with the Si core layer thicknesses of 220 nm, 340 nm, 400 nm, and 500 nm, together with different MO garnet materials (YIG, Ce-YIG on MgO, Ce-YIG on YIG, Ce-TIG, Bi-TIG, and TIG) were chosen to be researched. Among them, Ce-TIG, which possesses a considerable Faraday rotation coefficient, and, additionally, does not require a buffer/seed layer to achieve crystallinity, was the most promising garnet.

As there was a quality problem with the 220 nm SOI and 400 nm SOI wafers we were supplied with, simulation has only been conducted on these two substrate platforms, and devices have only been fabricated and optically characterized on 340 nm SOI and 500 nm SOI platforms.

First of all, simulation of the structure with MO garnet on top was carried out in WGMODES<sup>®</sup> [137], a Modesolver<sup>®</sup> package based in MATLAB<sup>®</sup>, primarily to get the parameters of the effective refractive index, half-beat length, and Stokes parameters. The effect of the seed layer (YIG) and buffer layer (MgO) on the MO behaviour of different garnets was also simulated. Then, an e-beam mask was designed in L-Edit<sup>®</sup>, based upon the obtained parameters from MATLAB<sup>®</sup>. Afterwards, a nanofabrication process, including e-beam lithography, plasma processing, RF sputtering, and RTA, mainly conducted in the James Watt Nanofabrication Center (JWNC) of the University of Glasgow, was used for the device definition. The development of a suitable bilayer undercut PMMA lift-off layer for periodic loading MO garnet islands and the optimisation of the crystallinity of the MO garnet materials have been critical steps during the process. Once fabricated, the two sides of the device can be cleaved to form an Fabry-Perot (FP) cavity, and used for free space measurement.

During the measurement, pure TE mode light was injected into the waveguide. In the beginning, TM output separated by a polarisation splitting cube was measured by a Lock-in amplifier under situations when the waveguide was

unsaturated. It was then magnetically saturated in the forward and backward directions, where only the remanent magnetization of the garnet was used, so that the quasi-phase matching (where a peak should appear) wavelength, together with the MO Faraday effect, can be identified.

Devices were saturated using a permanent magnet providing a ~1200 Gauss magnetic field. A pair of Helmholtz coils were also employed as a source of variable magnetic field and placed at the two sides of the device under measurement, which also enables simultaneous measurements with changing magnetic fields. Later, they were abandoned as they could only produce a relatively weak magnetic field of ~200 Gauss, and also for undesirable thermal effects upon propagation modes, arising from the heating of the coils.

Afterwards, the total output of the waveguides where quasi-phase matching occurred was analysed by the Thorlabs© polarimeter system, in which various parameters of the output mode can be obtained, such as Stokes parameters, azimuth, and ellipticity. Later, further analysis was done on these parameters to present the nonreciprocity of the device.

The angle between the two Stokes vectors of opposite magnetization directions was elected as the optimum index to show the nonreciprocity and isolation of the measured device. Here, an angle of  $\pi$  indicates that the two output modes of opposite magnetization saturation directions are completely orthogonal and, as such, demonstrates that it could achieve 100% isolation with appropriate polarisers and waveplates.

A nonreciprocal isolation performance has been found in devices with many kinds of MO garnets on both 340 nm SOI and 500 nm SOI platforms. Among these, more than a  $3/4\pi$  Stokes vector angle was observed in devices with Bi-TIG and Bi-TIG + TIG as MO periodic cladding on a 340 nm SOI, and Ce-YIG on YIG and Ce-TIG as MO periodic cladding on a 500 nm SOI, which corresponded to about an 11 dB isolation ratio if combined with proper polarisers. The length of these devices ranged between 3mm and 6 mm.

Also, in this design, the number of periods of the alternating MO segments and  $\text{Si}_x\text{N}_y$  segments or MO segments (+) with a positive Faraday rotation coefficient and MO segments (-) with a negative Faraday rotation coefficient decides the isolation ability of the device. Thus, 100% isolation can be achieved in every device where quasi-phase matching is satisfied and nonreciprocal behaviour is identified, as long as an appropriate length of the device is designed.

### 7.1.2 Future Work

So far, a producible device fabrication process and optical characterisation and analysis process have been fully developed for the NR-PMC part, and isolation has been demonstrated in devices on both 500 nm SOI and 340 nm SOI platforms. However, effort is still required to optimize the performance of the device and make the fabrication process more controllable.

Firstly, research can be conducted on SOI platforms with different thicknesses of Si core layer to find the optimum platform. Thinner cores of SOIs, 340 nm SOI and 220 nm SOI, have been used to make waveguides that enable more interaction between the mode and the garnet on top, as modes become less confined/more radiative and pushed up in thinner core waveguides. However, more evanescent wave interaction in thinner core SOI waveguides can also lead to more propagation loss as more light is confined in the garnet layer. Usually, garnet waveguides are quite lossy [156], while less interaction in thicker core SOI waveguides requires a longer device length to achieve an equivalent amount of rotation, which also increases the propagation loss. Therefore, a compromise might be needed according to the relationship between the Faraday rotation and propagation loss.

There is a large mis-alignment problem in the processing of 340 nm SOI, as mentioned in Chapter 4, while the 220 nm SOI wafer we were supplied with was of poor quality, resulting from manufacturing defects from the producer. Actually, 400 nm SOI was first considered as it is also practical for the R-PMC. However, there was the same material problem with the new 400 nm SOI wafers as with the 220 nm SOI wafers. As such, fabrication parameters need to be optimised on 400 nm SOI, 340 nm SOI, and 220 nm SOI of good quality. Also, the whole fabrication and optical measurement process will be carried out, from which the best structure can be decided based on the results of the figure of merit (isolation ratio/propagation loss) of waveguides on SOI platforms of different core thicknesses.

Secondly, from the aspect of MO garnet material, an increase in the crystalline percentage of the garnet segments, ideally fully crystallized, are to be achieved.

Thirdly, optical characterisation-wise, the measurement results are to be improved by removing the FP fringes noise found in the optical measurements of the devices currently fabricated. Tapers and polymer couplers can be added to both the input and output of the waveguides. Also, anti-reflection coating (AR) can be applied to both sides of the cleaved facets.

Besides, in all measurements in this work, TE polarised light is used as input, as the majority of the lasers used in optical systems are TE-polarised as a result of the quantum mechanical selection rule to demonstrate the feasibility of the design of the NR-PMC part and R-PMC part, and the nonreciprocity of the NR-PMC device, the integrated Faraday rotator. Here, we have successfully demonstrated the achievement of an integrated Faraday rotator by integrating periodic magneto-optic garnet as cladding on top of the waveguide, which acts as the nonreciprocal part of the designed isolator device. In the future, the same optical characterisation methodology can be applied for TM-input or circularly-input to further confirm the feasibility of the integrated Faraday rotation device and support the claim that it can work for light with arbitrary polarisation.

Fourthly, from the aspect of specific application, though isolation has been achieved in the current devices, the required  $45^\circ$  mode conversion devices for the integrated waveguide isolator are not realised yet. Waveguides with different numbers of quasi-phase matching periods can be designed to find out the right number of periods/device length to achieve a  $45^\circ$  mode conversion.

## **7.2 Reciprocal Polarisation Mode Converter (R-PMC)**

### **7.2.1 Conclusions**

On the R-PMC part, an asymmetric structure, an L-shape waveguide, was chosen so that the rotation of the optical axis could enable the excitation of hybrid modes from an injected linear polarisation mode and reciprocal mode conversion between the two modes. The L-shape design is similar to the trenches structure

due to the RIE (Reactive Ion Etching) lag effect [157], which is not applicable in our situation, as the RIE lag effect is less flexible in Si etching and even less so for shallow etching.

R-PMC might be able to be accomplished in a 500 nm SOI, 400 nm SOI, or 340 nm SOI, but not on a 220 nm SOI as it is too thin (here, possibly, we can deposit amorphous Si selectively on top of a section of the waveguides to increase the thickness of the core layer to complete the whole device on a 220 nm SOI wafer [31]).

To start with, simulations in MATLAB<sup>®</sup> were formed to acquire the half-beat length and the right dimensions - the widths and height of each section of the L-shaped part. Then, a similar method of mask design, device nanofabrication, and optical characterisation process was applied. Designs of waveguides were made with different lengths of the L-shaped part, at both sides of which an inverted adiabatic Si taper was placed in order for better light coupling in/out. During the device fabrication process, the alignment between the two mask layers was very critical for the success of the device. The same free space measurement setup was used to measure the reciprocal mode conversion. The only difference is that an external magnetic field is not needed any more.

The measurement results turned out to be quite different from what was expected. The mismatch between the measured and expected results led to a re-check in the design of the device, where it was discovered that a total square cross-section waveguide part was included in the design, where the two modes cross with one another and, thus, the polarisation got messed up. A new design was proposed for further research by making an inverted adiabatic taper area a half-etch down by applying a wider second layer to avoid the total square cross section.

### **7.2.2 Future Work**

Initial simulation and fabrication of the L-shaped design have been conducted to show that more trials and efforts are required in order to create a working reciprocal 45° mode converter.

On one side, optimization can be done to the simulation, fabrication, and optical measurements of the design, as suggested at the end of Chapter 6. To start

with, simulation in R-soft<sup>®</sup> is to be conducted to find out the optimized dimensions. Then, during the fabrication process, cell registration in e-beam lithography can be used to achieve critical layer-to-layer alignment. Additionally, an AR coating can also be applied to both sides of the cleaved facets to avoid the FP fringes noise.

On the other side, from the optical measurements of the NR-PMC part, it is verified that offsetting the quasi-phase matching loading periods on top of the waveguides can lead to reciprocal mode conversion. There are both reciprocal and non-reciprocal mode conversions in the waveguides with magneto-optical (MO) garnet material as periodic upper cladding at the presence of an external magnetic field, and an offset between the waveguide and the upper garnet cladding layer. The device itself can be an isolator when a proper half-beat length and the right number of quasi-phase matching loading periods are defined.

### **7.3 Integration of the NR-PMC Part and R-PMC Part**

When success has been made in both the 45° NR-PMC part and 45° R-PMC part, the optimized NR-PMC section and the R-PMC section will be combined and integrated together with polarisers to make an integrated isolator. A quarter-wave plate also needs to be integrated between the NR-PMC and R-PMC parts to provide the necessary phase shift to convert between linear polarization and circular polarization [138]. Also, a SmCo permanent magnet layer [136] or a metallic strip (Ti/Au) [68] can be added on top of the garnet cladding layer to help bias the garnet layer for Faraday rotation, which exempts the presence of an external magnetic field and makes the optical system more integrated.

In addition, by deciding the length of each part, control of the arbitrary angle can be achieved. There will be 30 deg, 45 deg, and 60 deg polarisation converters made to confirm the control of arbitrariness. Also, a complete optimum recipe with good repeatability will be created for integration with other optical devices' fabrication processes and, later, even massive production in industry. For example, tapers will also be made on the same device to help couple in from the laser and couple out the signal to another optical device.

Furthermore, the garnet lift-off technique where tapers can be added to the garnet pattern can be transferred for other applications, like ring isolators

[64]-[68] and the MZI (Mach-Zehnder Interferometer) [29][31][69]-[73] to avoid the discontinuity brought by adhesive bonding [32][72][73] or direct bonding [29][65][68]-[71]. Therefore, rings and the MZI with magneto-optical garnets on top, which adopt the non-reciprocal phase shift theorem, are also considered to achieve light isolation, and can be investigated in the future.

## 7.4 Conclusions

This thesis presented research work to realise the integration of an optical waveguide isolator that works for both TE and TM modes on the Silicon-on-Insulator platform. Two core components are required to build such an isolator. One is a 45° NR-PMC (Nonreciprocal Polarisation Mode Conversion), where the NR-PMC approach, which works for both TE and TM modes, is adopted and periodic magneto-optical (MO) rare-earth doped yttrium iron garnet (RE-YIG) segments are deposited on top of the Si waveguides as upper cladding to achieve quasi-phase matching. The other is a 45° R-PMC (Reciprocal Polarisation Mode Conversion), where an asymmetric structure, with an L-shaped cross-section waveguide, is employed. This is so that the resultant rotation of the optical axis of the guide enables the excitation of hybrid modes from an injected linear polarisation mode, and reciprocal mode conversion between the two modes.

On the NR-PMC part, different SOI substrates with the Si core layer thicknesses of 220 nm, 340 nm, 400 nm, and 500 nm, together with different MO garnet materials (YIG, Ce-YIG on MgO, Ce-YIG on YIG, Ce-TIG, Bi-TIG, and TIG) were chosen to be researched. Nonreciprocal isolation performance has been found in devices with many kinds of MO garnets on both 340 nm SOI and 500 nm SOI platforms.

Among these, more than a  $3/4\pi$  Stokes vector angle was observed in devices with Bi-TIG and Bi-TIG + TIG as MO periodic cladding on a 340 nm SOI, and Ce-YIG on YIG and Ce-TIG as MO periodic cladding on a 500 nm SOI, which corresponded to about an 11 dB isolation ratio if combined with proper waveplates and polarisers. The length of these devices ranged between 3 mm and 6 mm.

However, the isolation ratio we got here from the measurements is not the optimised performance each device should have. Here, the isolation ratio depends on the number of QPM (Quasi-Phase Matching) periods on the device. Thus, the

longer the device, the more the QPM periods. When the device is cleaved at the proper length, a Stokes vector angle of  $\pi$  is expected, where the lightwaves of opposite propagation directions are orthogonal to each other and 100% isolation, ideally more than 60 dB, can be achieved integrated with some other necessary components, like wave-plates and polarisers, as discussed before.

On the R-PMC part, an asymmetric structure, an L-shaped waveguide, was chosen so that the rotation of the optical axis enables the excitation of hybrid modes from an injected linear polarisation mode and reciprocal mode conversion between the two modes. Devices have been fabricated on both 500 nm SOI and 340 nm SOI platforms. However, the measurement results turned out to be quite different from what was expected. A new design was proposed for further research by making an inverted adiabatic taper area a half-etch down by applying a wider second layer to avoid the total square cross section.

In summary, this work has successfully realised the first integrated SOI polarisation-independent Faraday rotator, which works for both TE and TM modes, based on nonreciprocal polarisation mode conversion (NR-PMC) on both 500 nm SOI and 340 nm SOI platforms. Both the performance and the footprint are promising and suitable for optical integration. Instead of bonding, RF sputtering was adopted to integrate MO garnet materials on an SOI substrate, which improves the controllability and is more favourable in massive production.

By contrast, all other isolators realised nowadays are based on nonreciprocal phase shift (NPS) and usually employ either direct bonding or adhesive bonding to achieve MO garnet integration, which suggests that these isolators can only work on either TE mode light or TM mode light, which has limits in mass production. The TM isolators cannot accommodate the isolation needs as the vast majority of semiconductor lasers used in the integrated optical system emit TE rather than TM due to quantum mechanical selection rules. The TE isolators based on NPS need a complicated optical serpentine circuit or a complicated design of asymmetric coupled waveguides for TE-TM mode conversion, which leads to a large footprint.

## Appendix A – Observed Promising Results on 340 nm SOI Platforms with Different Garnets on Top

1. 340 nm SOI platform with Bi-TIG, Bi-TIG+TIG, Ce-TIG, and Ce-YIG on YIG as cladding layer

Figure a-1 and Figure a-2 display measurement results of a device with 300 nm Bi-TIG as cladding. Figure a-1 shows the relative fraction of the TM-polarised output as a function of input wavelength when the sample is not saturated, and saturated in a forward direction and back direction; a peak at  $\lambda=1546.5$  nm is observed. Figure a-2 presents the Stokes vector angle of opposite magnetic saturation at a resolution of 0.001 nm, where an angle of more than  $3/4\pi$  is observed.

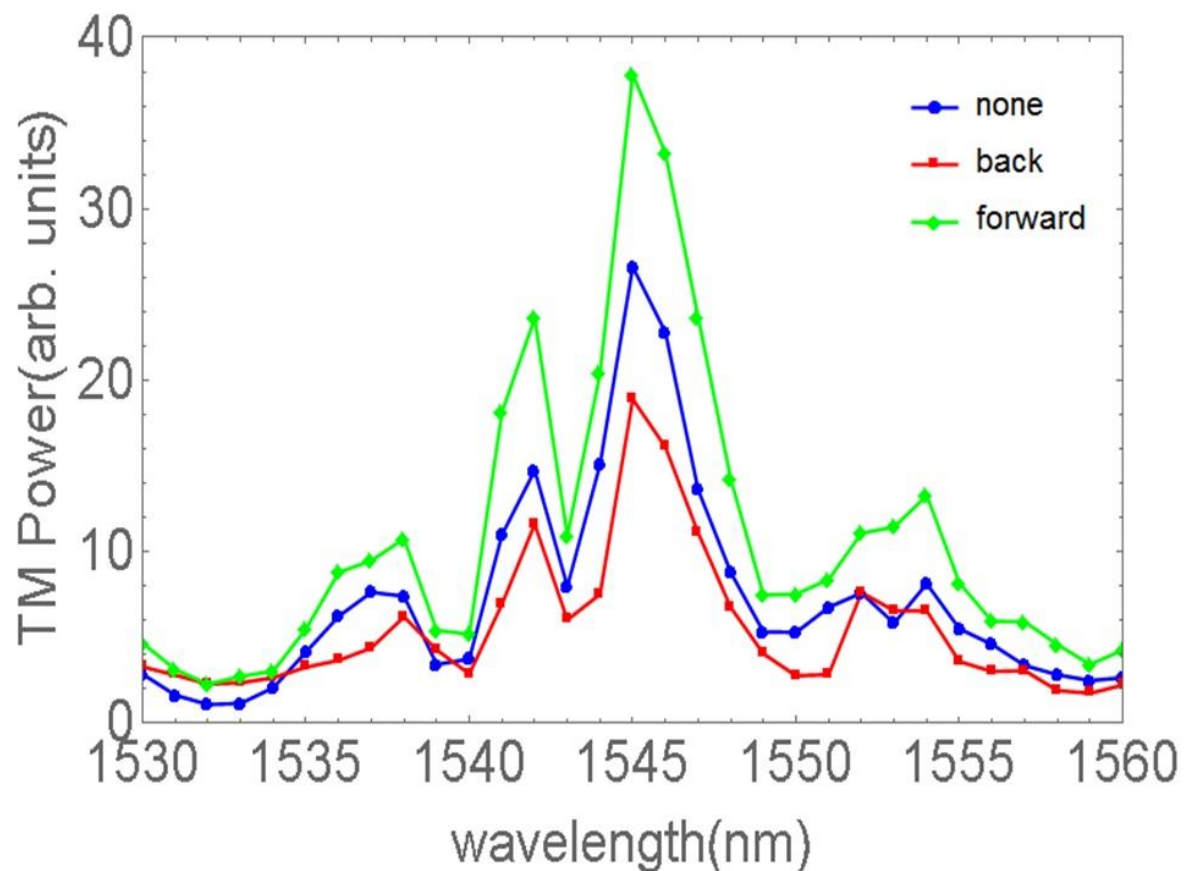


Figure a-1. Device with Bi-TIG cladding on 340 nm SOI platform: it shows the relative fraction of the TM-polarised output as a function of input wavelength when sample is not saturated, and saturated in a forward direction and back direction; a peak at  $\lambda=1546.5$  nm is observed.

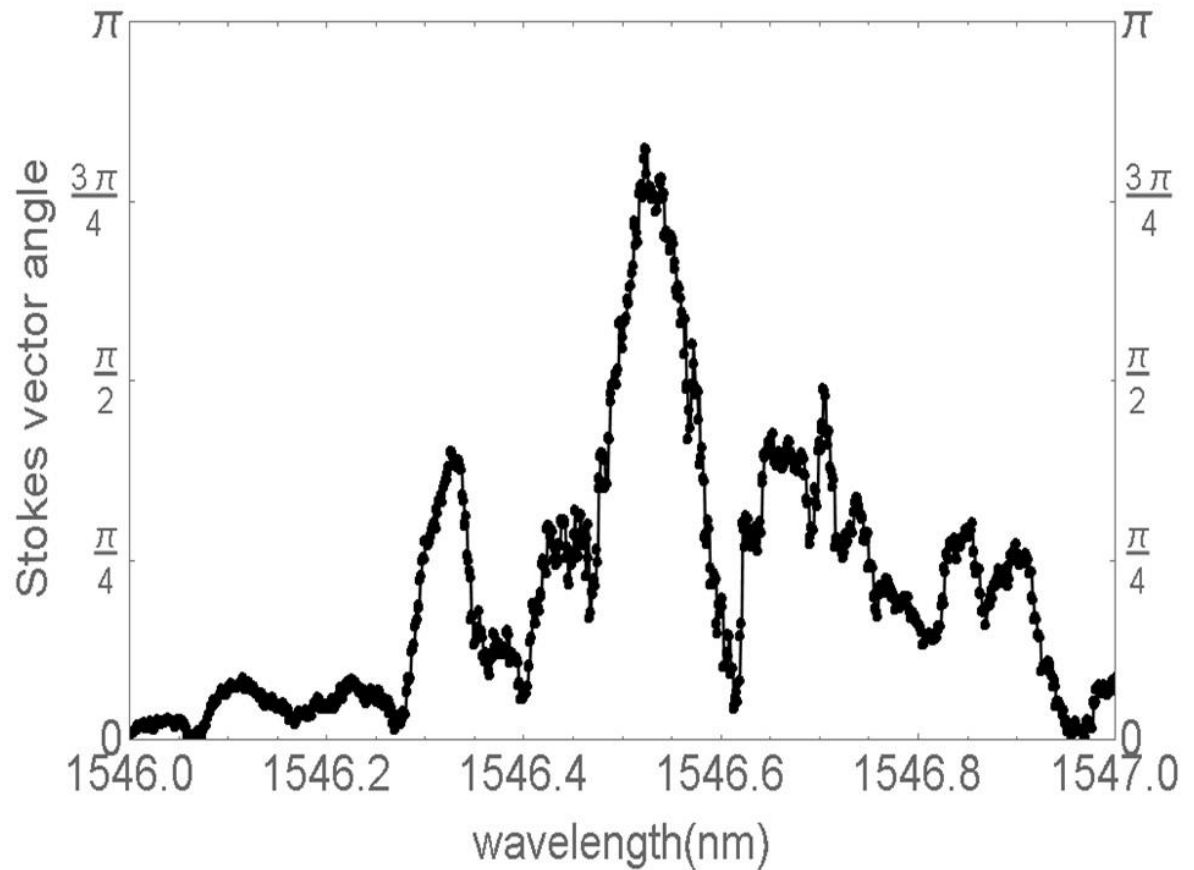


Figure a-2. Device with Bi-TIG cladding on 340 nm SOI platform: it presents the Stokes vector angle of opposite magnetic saturation at resolution of 0.001 nm, where an angle of more than  $3/4\pi$  is observed.

Figure a-3 and Figure a-4 display measurement results of a device with 300 nm Bi-TIG and 300 nm TIG as cladding, the MO(+) + MO(-) design. Figure a-3 shows the relative fraction of the TM-polarised output as a function of input wavelength when the sample is not saturated, and saturated in a forward direction and back direction; a peak at  $\lambda=1541$  nm is observed. Figure a-4 presents the Stokes vector angle of opposite magnetic saturation at 0.5 nm resolution, where an angle of more than  $3/4\pi$  is observed.

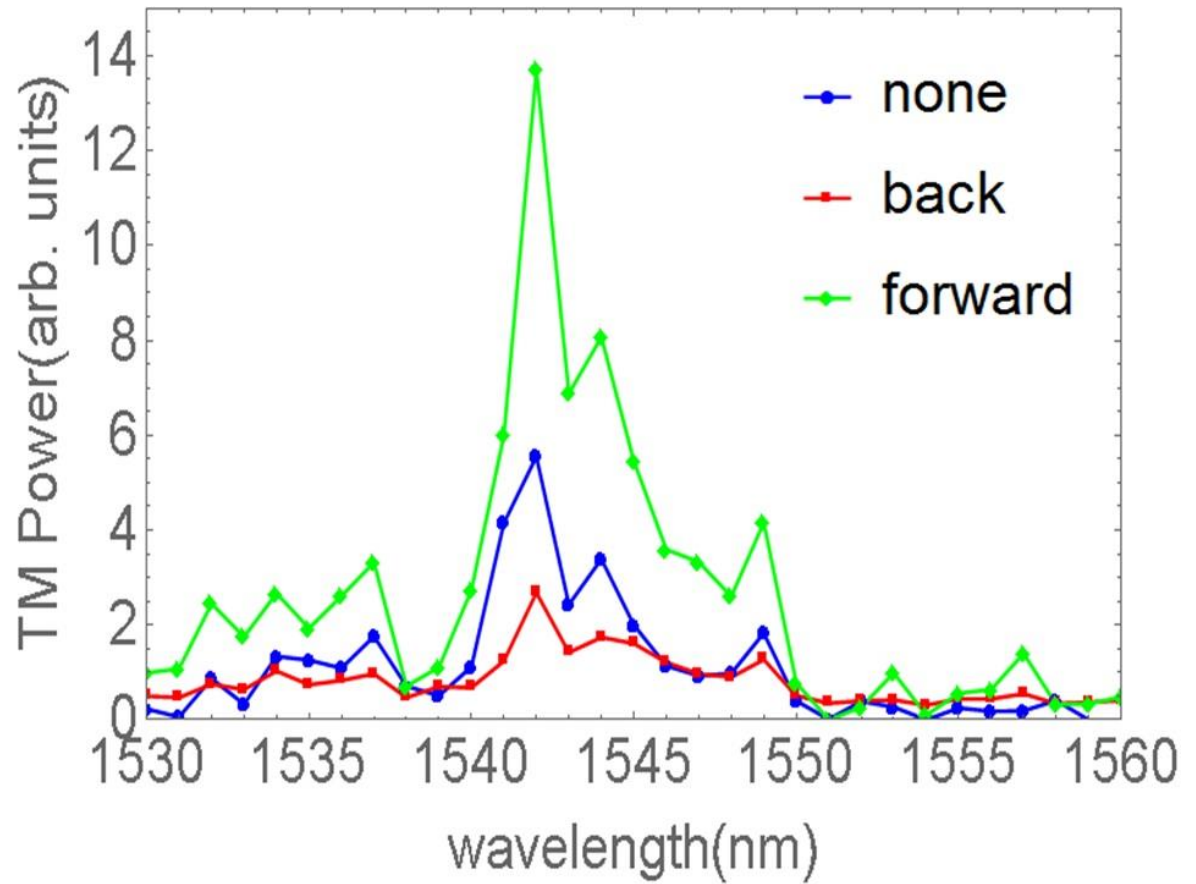


Figure a-3. Device with Bi-TIG + TIG as cladding on a 340 nm SOI platform: it shows the relative fraction of the TM-polarised output as a function of input wavelength when the sample is not saturated, and saturated in a forward direction and back direction; a peak at  $\lambda=1541$  nm is observed.

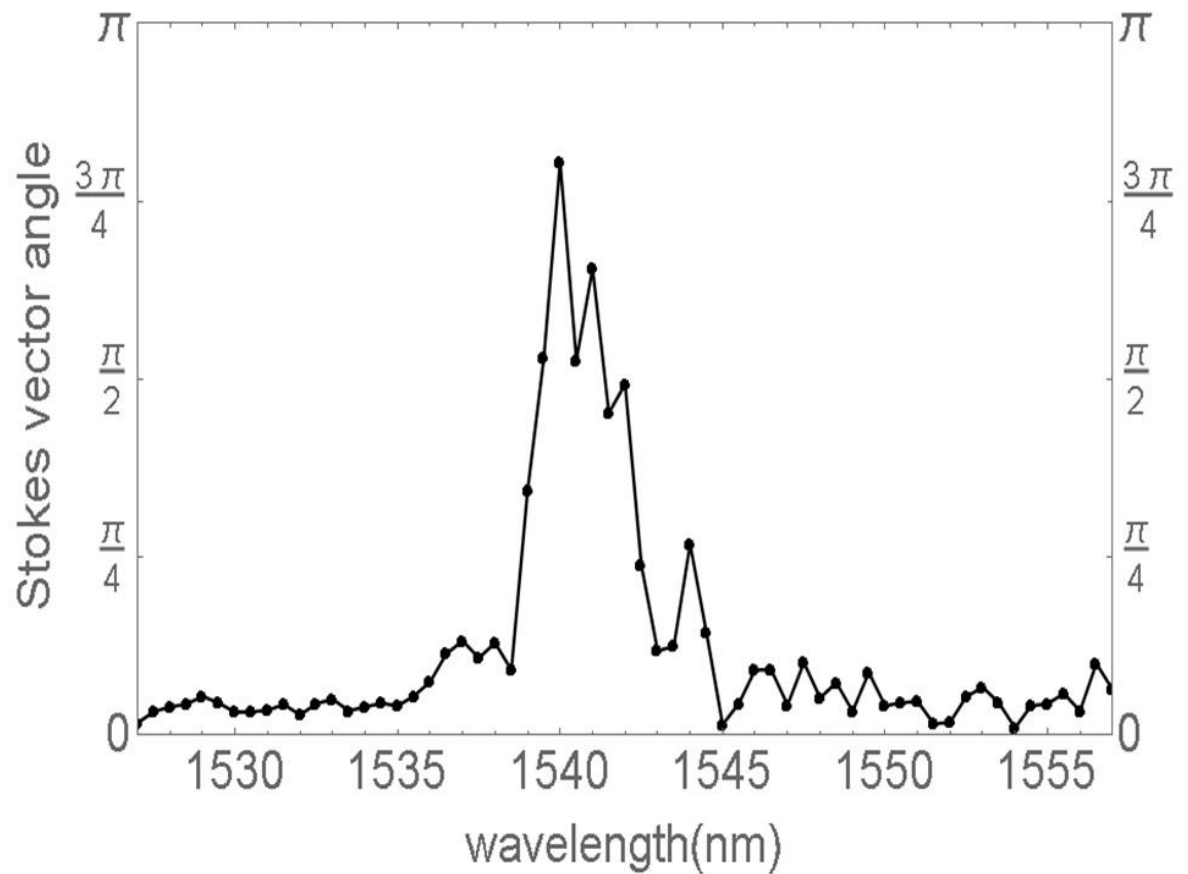


Figure a-4. Device with Bi-TIG + TIG as cladding on a 340 nm SOI platform: it presents the Stokes vector angle of opposite magnetic saturation at 0.5 nm resolution, where an angle of more than  $3/4\pi$  is observed.

Figure a-5 and Figure a-6 display measurement results of a device with 300 nm Ce-TIG as cladding. Figure a-5 shows the relative fraction of the TM-polarised output as a function of input wavelength when the sample is not saturated, and saturated in a forward direction and back direction; a peak at  $\lambda=1548$  nm is observed. Figure a-6 presents the Stokes vector angle of opposite magnetic saturation at a resolution of 0.01 nm, where an angle of more than  $1/4\pi$  is observed.

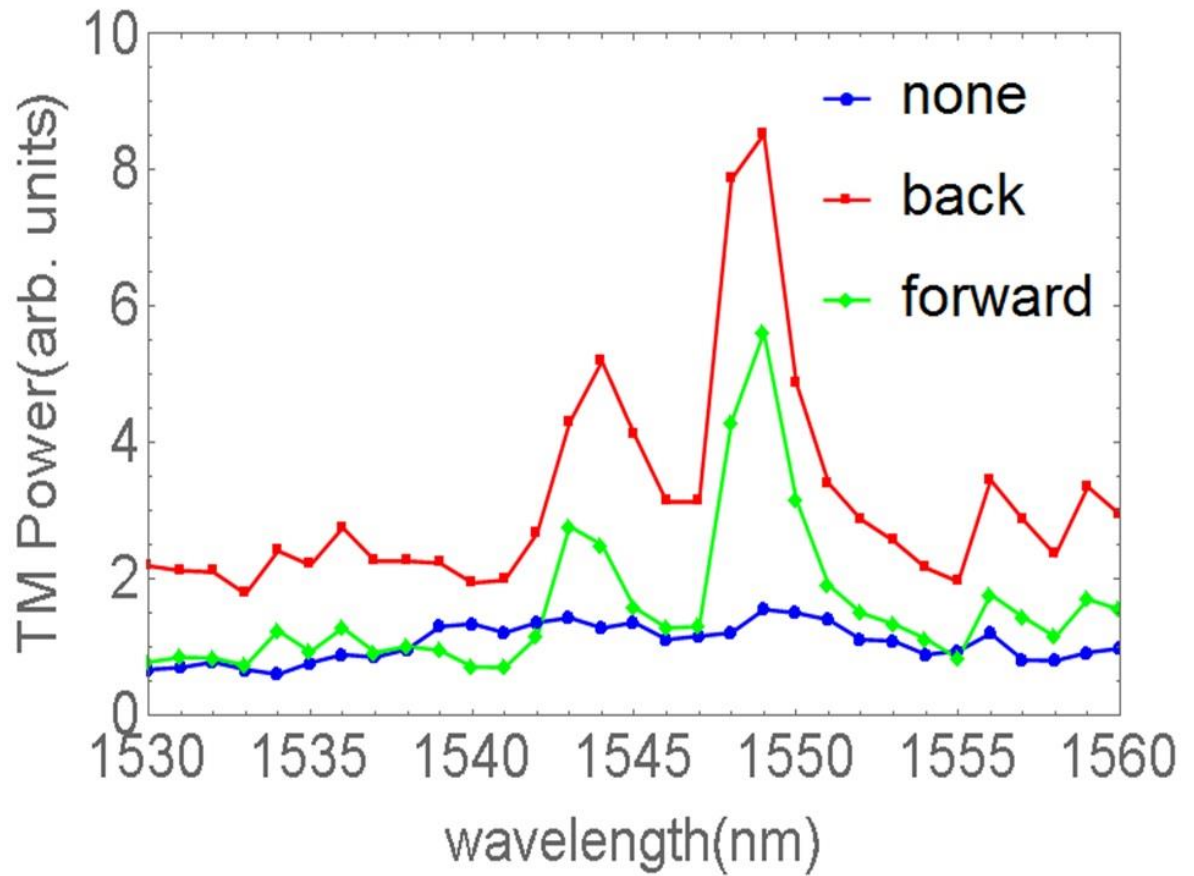


Figure a-5. Device with Ce-TIG cladding on a 340 nm SOI platform: it shows the relative fraction of the TM-polarised output as a function of input wavelength when the sample is not saturated, and saturated in a forward direction and back direction; a peak at  $\lambda=1548$  nm is observed.

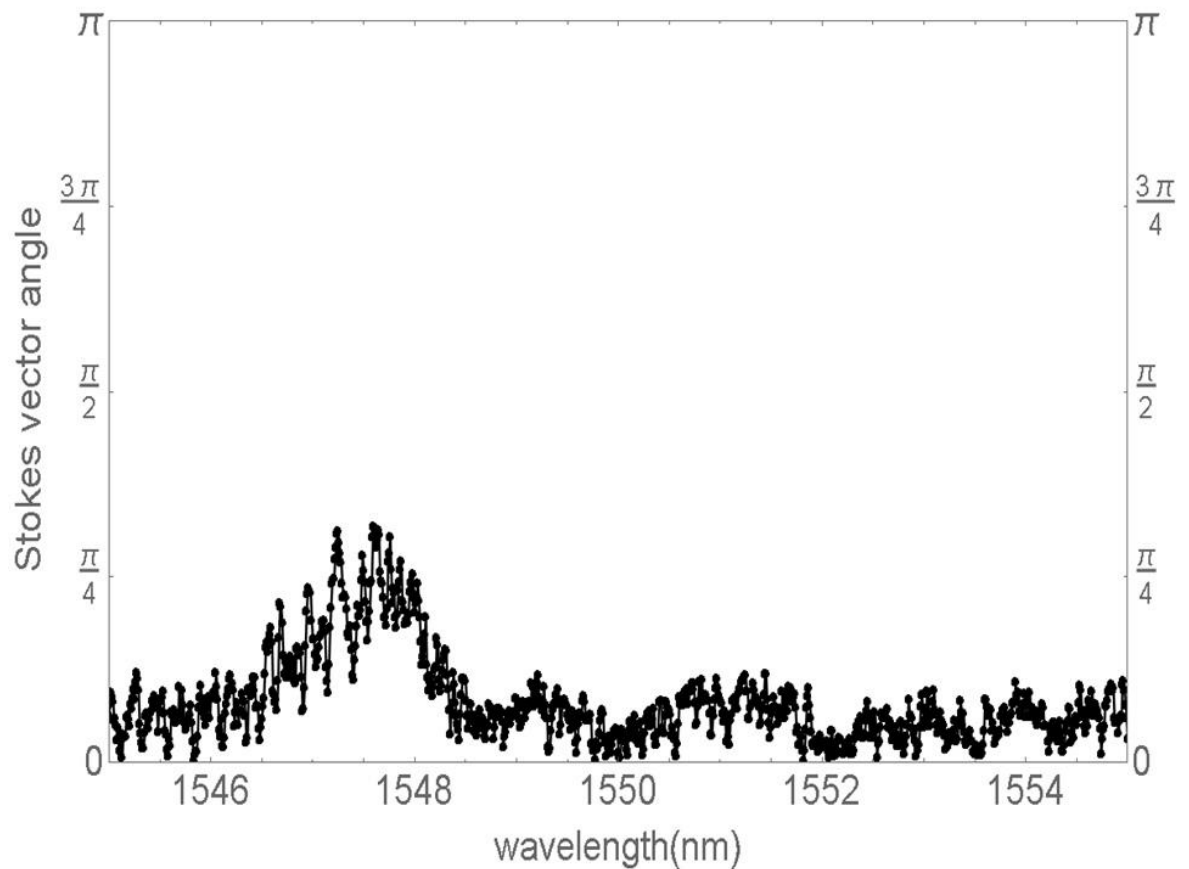


Figure a-6. Device with Ce-TIG cladding on a 340 nm SOI platform: it presents the Stokes vector angle of opposite magnetic saturation at a resolution of 0.01 nm, where an angle of more than  $1/4\pi$  is observed.

Figure a-7 and Figure a-8 display measurement results of a device with 330 nm Ce-YIG on 50 nm YIG as cladding. Figure a-7 shows the relative fraction of the TM-polarised output as a function of input wavelength when the sample is not saturated, and saturated in a forward direction and back direction; a peak at  $\lambda=1524$  nm is observed. Figure a-8 presents the Stokes vector angle of opposite magnetic saturation at 0.5 nm resolution, where an angle of about  $1/8\pi$  is observed.

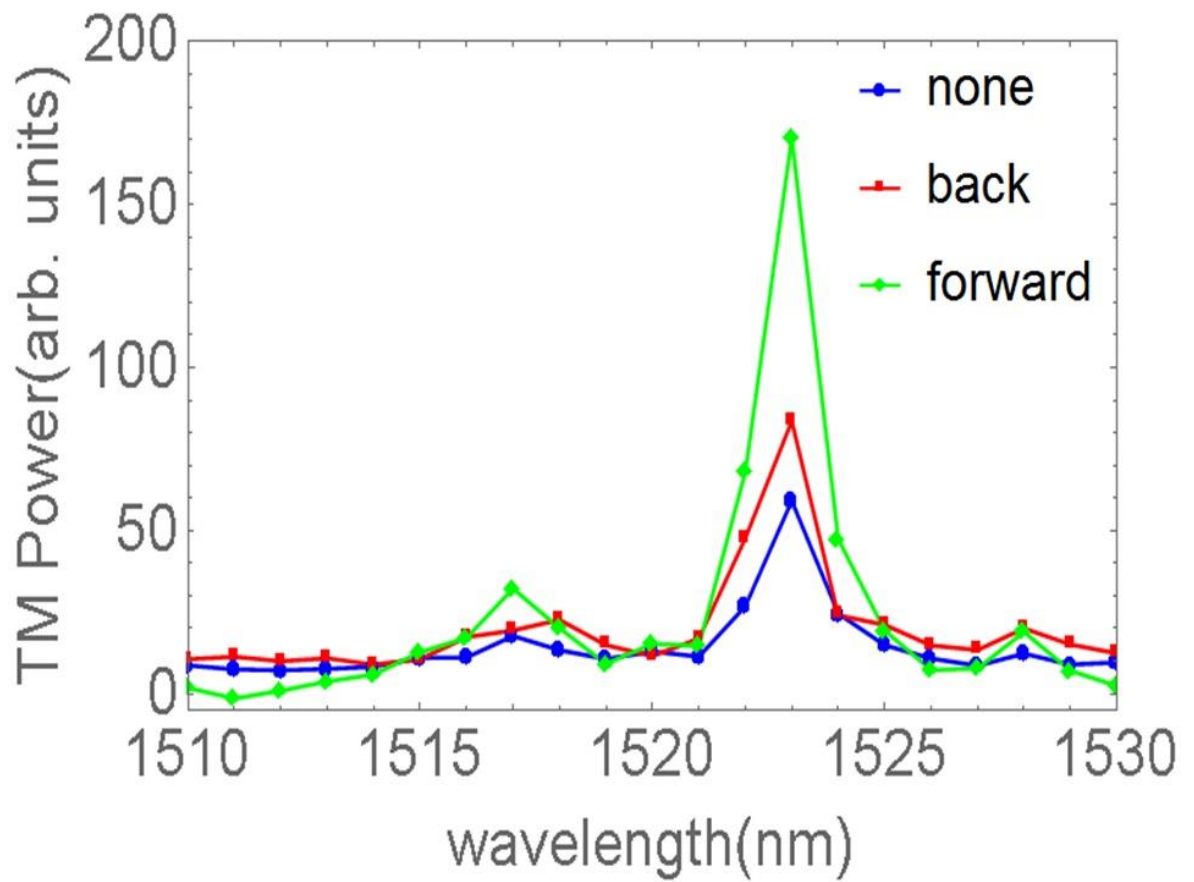


Figure a-7. Device with Ce-YIG on YIG cladding on 340 nm SOI platform: it shows the relative fraction of the TM-polarised output as a function of input wavelength when the sample is not saturated, and saturated in a forward direction and back direction; a peak at  $\lambda=1524$  nm is observed.

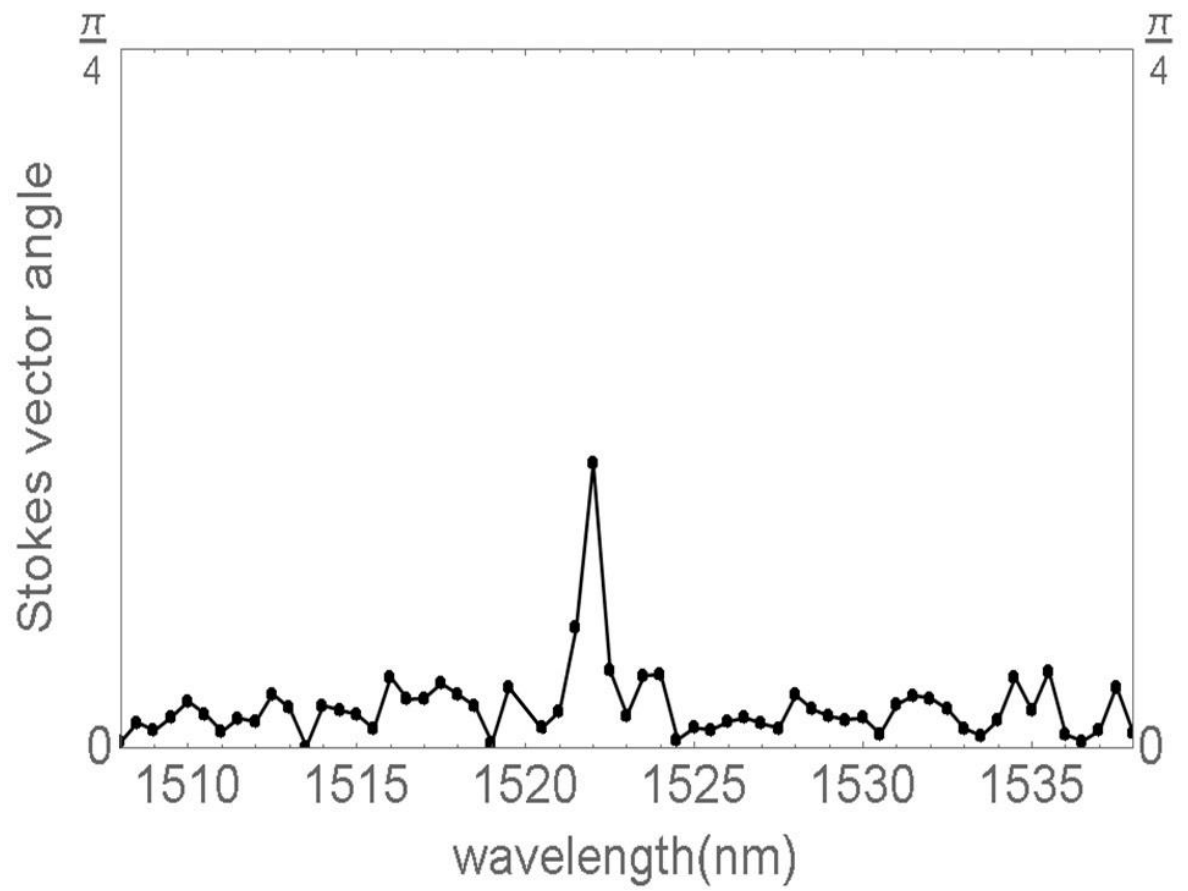


Figure a-8. Device with Ce-YIG on YIG cladding on 340 nm SOI platform: it presents the Stokes vector angle of opposite magnetic saturation at 0.5 nm resolution, where an angle of about  $1/8\pi$  is observed.

## **Appendix B – Failed Fabrication on 220 nm SOI, 340 nm SOI, and 400 nm SOI**

The same method of simulation, design, and fabrication process is applied on thinner core SOIs platforms, like 220 nm SOI, 340 nm SOI, and 400 nm SOI, where the guided mode is more pushed up and there is more interaction between the evanescent tail of the guided mode and the MO garnet layer so that a stronger MO Faraday effect can be expected.

For the 220 nm SOI and 400 nm SOI samples, the wafer itself was of poor quality resulting from a mistake in the manufacturing process. The interface between the Si and SiO<sub>2</sub> box layer was too rough, which led to huge propagation loss. Before the actual fabrication process, wafer-quality tests were carried out. It turned out that the 500 nm wide waveguides on 400 nm core SOI are not guiding light at all, while those on 220 nm core SOI have a much larger loss for both the TE mode and TM mode than a normal good-quality 500x220 nm waveguide. The 340 nm SOI turned out to be of very good quality, and the plain 500x340 nm waveguides give a loss of around 1 dB/cm for the TE mode and around 2 dB/cm for the TM mode.

In spite of the large propagation loss in the 220 nm SOI, the actual experiment was carried out on both the 220 nm SOI and 340 nm SOI. However, the introduction of the MO garnet also substantially gave rise to the propagation loss [156], which leads to none of the waveguides devices on the 220nm SOI guiding light when integrated with MO material.

For the 340 nm SOI devices, the misalignment between e-beam layers resulting from the shift in the mask-writing process became a serious problem where the MO segments would not get crystallized when the second layer of MO material, like Ce-YIG, was not aligned with the first seed layer/buffer layer (YIG/MgO), or there was huge propagation loss when the HSQ mask layer was not aligned with the MO segment layer (Figure b-1). There is about 30 nm drift in 15 mins writing time of the VB6 tool resulting from heat, flatness of the sample, the alignment between the sample and the holder, etc., which can be reduced by automatically re-calibrating the whole system every 15 mins. Compared to the e-

beam mask of the 500 nm SOI, that of the 340 nm SOI is much larger and it takes much longer to write, which means the drift is also much larger because of the accumulation effect of the drift. In order to reduce the drift and improve the alignment between the e-beam layers, the size of the e-beam mask can be reduced, or the mask can be divided into small cells, and cell registration can be applied in the future.

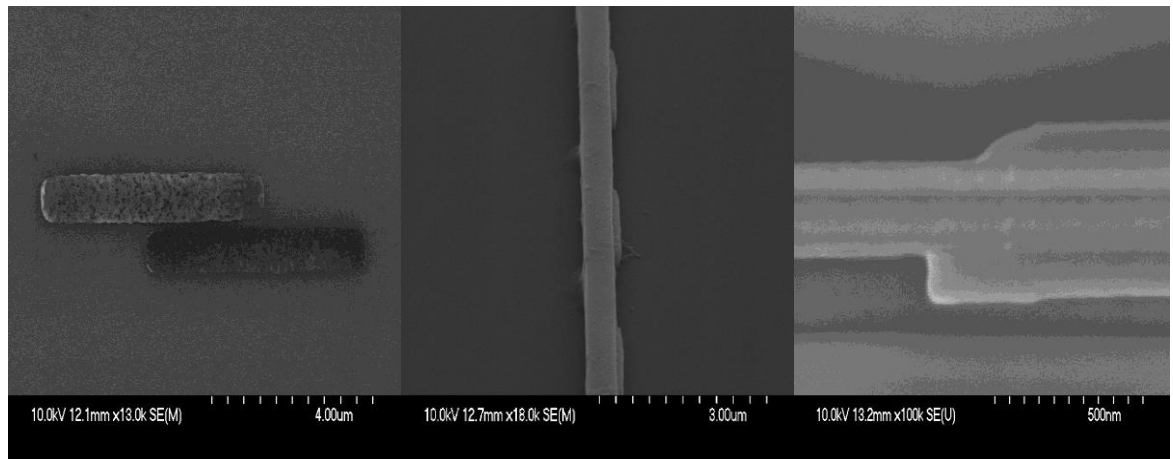


**Figure b-1. Mis-alignment between e-beam layers.**

## List of References

- [1] Stewart E. Miller, "Integrated Optics: An Introduction," *bell Syst. Tech. J.*, vol. 48, no. 7, pp. 2059-2069.
- [2] R. G. Hunsperger, *Integrated optics Theory and Technology Sixth Edition*, Sixth Edit., vol. 2. Springer Science+Business Media, 2009.
- [3] B. Jalali, S. Yegnanarayanan, T. Yoon, T. Yoshimoto, I. Rendina, and F. Coppinger, "Advances in Silicon-on-Insulator Optoelectronics," *IEEE J. Sel. Top. Quantum Electron.*, vol. 4, no. 6, pp. 938-947, 1998.
- [4] Z. Fang and C. Z. Zhao, "Recent Progress in Silicon Photonics: A Review," *ISRN Opt.*, vol. 2012, pp. 1-27, 2012.
- [5] L. M. Augustin, S. Member, J. J. G. M. Van Der Tol, R. Hanfoug, W. J. M. De Laat, M. J. E. Van De Moosdijk, P. W. L. Van Dijk, Y. Oei, and M. K. Smit, "A Single Etch-Step Fabrication-Tolerant Polarization Splitter," *J. Light. Technol.*, vol. 25, no. 3, pp. 740-746, 2007.
- [6] P. Splittedswitch, M. Okuno, A. Sugita, K. Jinguji, and M. Kawachi, "Birefringence Control of Silica Waveguides on Si and Its Application to a Polarisation-Beam Splitter/Switch," *J. Light. Technol.*, vol. 12, no. 4, 1994.
- [7] D. Liang and J. E. Bowers, "Photonic integration: Si or InP substrates?," *Electron. Lett.*, vol. 45, no. 12, pp. 10-12, 2009.
- [8] B. Jalali, "Silicon-on-Insulator Photonic Integrated Circuit ( SOI-PIC ) Technology," vol. 2997, pp. 60-71.
- [9] B. Schuppert, J. Schmidtchen, A. Splett, U. Fischer, T. Zinke, R. Moosburger, and K. Petermann, "Integrated optics in silicon and SiGe-heterostructures," *J. Light. Technol.*, vol. 14, no. 10, pp. 2311-2322, 1996.
- [10] H. Demir, V. Sabnis, O. Fidaner, J. Harris, D. Miller, and J.-F. Zheng, "Dual-diode quantum-well modulator for C-band wavelength conversion and broadcasting.," *Opt. Express*, vol. 12, no. 2, pp. 310-316, 2004.
- [11] D. Hofstetter, B. Maisenhölder, and H. P. Zappe, "Quantum-well intermixing for fabrication of lasers and photonic integrated circuits," *IEEE J. Sel. Top. Quantum Electron.*, vol. 4, no. 4, pp. 794-802, 1998.
- [12] A. Birner, R. B. Wehrspohn, U. M. Gosele, and K. Busch, "Silicon-based photonic crystals," *Adv. Mater.*, vol. 13, no. 6, pp. 377-388, 2001.
- [13] T. F. Krauss, R. Wilson, R. Baets, W. Bogaerts, M. Kristensen, P. I. Borel, L.

- H. Frandsen, M. Thorhauge, B. Tromborg, A. Lavrinenko, R. D. La Rue, H. Chong, L. Socci, M. Midrio, B. Stefano, and D. Gallagher, "Photonic Integrated Circuits using Crystal Optics(PICCO)," 2003.
- [14] Jeppix, "Jeppix platform capabilities." [Online]. Available: <http://www.jeppix.eu/platforms.html>. [Accessed: 08-Aug-2016].
- [15] Lionix, "TripleX Integrated Optics." [Online]. Available: <http://www.lionixbv.nl/triplex-integrated-optics/>. [Accessed: 08-Aug-2016].
- [16] D. J. Moss, R. Morandotti, A. L. Gaeta, and M. Lipson, "New CMOS-compatible platforms based on silicon nitride and Hydex for nonlinear optics," *Nat. Photonics*, vol. 7, no. July, pp. 597-607, 2013.
- [17] Z. Fang, Q. Y. Chen, and C. Z. Zhao, "A review of recent progress in lasers on silicon," *Opt. Laser Technol.*, vol. 46, no. 1, pp. 103-110, 2013.
- [18] H. Rong, R. Jones, A. Liu, O. Cohen, D. Hak, A. Fang, and M. Paniccia, "A continuous-wave Raman Silicon laser," *Nature*, vol. 433, no. 7027, pp. 725-728, 2005.
- [19] O. Boyraz and B. Jalali, "Demonstration of a silicon Raman laser," *Opt. Express*, vol. 12, no. 21, p. 5269, 2004.
- [20] R. Chen, T.-T. D. Tran, K. W. Ng, W. S. Ko, L. C. Chuang, F. G. Sedgwick, and C. Chang-Hasnain, "Nanolasers grown on silicon," *Nat. Photonics*, vol. 5, no. February, pp. 1-18, 2011.
- [21] Y. Huo, H. Lin, R. Chen, Y. Rong, T. I. Kamins, and J. S. Harris, "MBE growth of tensile-strained Ge quantum wells and quantum dots," *Front. Optoelectron.*, vol. 5, no. 1, pp. 112-116, 2012.
- [22] J. E. Bowers, H. Park, A. W. Fang, R. Jones, O. Cohen, and M. J. Paniccia, "A technology for integrating active photonic devices on SOI wafers," *2006 Int. Conf. Indium Phosphide Relat. Mater. Conf. Proc.*, vol. 1, pp. 218-221, 2006.
- [23] G. Roelkens, J. Brouckaert, D. Van Thourhout, R. Baets, R. No"tzsel, and M. Smit, "Adhesive Bonding of InP/InGaAsP Dies to Processed Silicon-On-Insulator Wafers using DVS-bis-Benzocyclobutene," *J. Electrochem. Soc.*, vol. 153, no. 12, pp. 1015-1019, 2006.
- [24] S. J. Koester, S. Member, J. D. Schaub, G. Dehlinger, and J. O. Chu, "Germanium-on-SOI Infrared Detectors for Integrated Photonic Applications," *IEEE J. Quantum Electron.*, vol. 12, no. 6, pp. 1489-1502, 2006.
- [25] B. Snyder, B. Corbett, and P. O'Brien, "Hybrid integration of the wavelength-

- tunable laser with a silicon photonic integrated circuit,” *J. Light. Technol.*, vol. 31, no. 24, pp. 3934-3942, 2013.
- [26] G. Roelkens, L. Liu, D. Liang, R. Jones, A. Fang, B. Koch, and J. Bowers, “III-V/silicon photonics for on-chip and intra-chip optical interconnects,” *Laser Photonics Rev.*, vol. 4, no. 6, pp. 751-779, 2010.
- [27] T. Aalto, M. Harjanen, M. Kapulainen, S. Ylino, J. Ollila, V. Vilokkinen, L. Mörl, M. Möhrle, and R. Hamelin, “Integration of InP-based optoelectronics with silicon waveguides,” *Integr. Opt. Devices, Mater. Technol. XIII*, vol. 7218, pp. 1-14, 2009.
- [28] I. Z. Mitrovic, O. Buiu, S. Hall, D. M. Bagnall, and P. Ashburn, “Review of SiGe HBTs on SOI,” *Solid. State. Electron.*, vol. 49, no. 9 SPEC. ISS., pp. 1556-1567, 2005.
- [29] T. Mizumoto, R. Takei, and Y. Shoji, “Waveguide optical isolators for integrated optics,” *IEEE J. Quantum Electron.*, vol. 48, no. 2, pp. 252-260, 2012.
- [30] B. J. H. Stadler and T. Mizumoto, “Integrated magneto-optical materials and isolators: A review,” *IEEE Photonics J.*, vol. 6, no. 1, 2014.
- [31] S. Ghosh, S. Keyvaninia, Y. Shirato, T. Mizumoto, G. Roelkens, and R. Baets, “Optical isolator for TE polarized light realized by adhesive bonding of Ce:YIG on silicon-on-insulator waveguide circuits,” *IEEE Photonics J.*, vol. 5, no. 3, 2013.
- [32] Y. Shoji, A. Fujie, and T. Mizumoto, “Silicon Waveguide Optical Isolator Operating for TE Mode Input Light,” *IEEE J. Sel. Top. Quantum Electron.*, no. c, pp. 1-1, 2016.
- [33] E. M. Randone and S. Donati, “Mitigation of the back-reflection disturbances in semiconductor lasers taking advantage of the self-mixing signal properties,” *Proc. SPIE*, vol. 7022, p. 70220H-70220H-10, 2007.
- [34] K. E. Stubkjaer and M. B. Small, “Noise Properties of Semiconductor Lasers Due to Optical Feedback,” *IEEE J. Quantum Electron.*, vol. QE-20, no. 5, pp. 472-478, 1984.
- [35] L. Pauling, T. Nature, and C. Bond, “Impact of multiple reflection noise in Gbit/s lightwave systems with optical fibre amplifiers,” *Electron. Lett.*, vol. 25, no. 2, pp. 600-602.
- [36] M.Z.IQBAL, J.L.GIMLETT, M.M.CHOY, A.YI-YAN, M.J.ANDREJCO, L.CURTIS, M.A.SAIFI, C. LIN, and N.K.CHEUNG, “An 11Gbit/s, 151 km Transmission Experiment Employing a 1480nm Pumped Erbium-Doped In-line Fiber Amplifier,” *IEEE Photonics Technol. Lett.*, vol. 1, no. 10, pp. 334-336, 1989.

- [37] M. Tsubokawa, N. Shibata, S. Seikai, and T. Higashi, "BULK OPTICAL ISOLATOR TUNABLE FROM 1.2 $\mu$ m TO 1.7 $\mu$ m," *Electron. Lett.*, vol. 21, no. 18, pp. 28-29, 1985.
- [38] L. J. C. Rivera, S. Pandit, S. Pieski, R. Cobian, M. Cherif, and B. J. H. Stadler, "Integrated Isolators for Opto-Electro-Mechanical Systems and Devices, (Invited)," *Proc. SPIE*, vol. 4284, pp. 29-42, 2001.
- [39] Thorlabs, "IR Free-Space Isolators (1110 - 2100 nm)." [Online]. Available: [https://www.thorlabs.de/newgrouppage9.cfm?objectgroup\\_id=4916](https://www.thorlabs.de/newgrouppage9.cfm?objectgroup_id=4916). [Accessed: 31-Jul-2016].
- [40] Thorlabs, "IR Fiber Optic Isolators with PM Fiber (1290 - 2010 nm)." [Online]. Available: [https://www.thorlabs.de/newgrouppage9.cfm?objectgroup\\_id=6763](https://www.thorlabs.de/newgrouppage9.cfm?objectgroup_id=6763). [Accessed: 31-Jul-2016].
- [41] Thorlabs, "IR Fiber Optic Isolators with SM Fiber (1290 - 2010 nm)." [Online]. Available: [https://www.thorlabs.de/newgrouppage9.cfm?objectgroup\\_id=6178](https://www.thorlabs.de/newgrouppage9.cfm?objectgroup_id=6178).
- [42] C. Wang, X.-L. Zhong, and Z.-Y. Li, "Linear and passive silicon optical isolator.," *Sci. Rep.*, vol. 2, p. 674, 2012.
- [43] L. Feng, M. Ayache, J. Huang, Y.-L. Xu, M.-H. Lu, Y.-F. Chen, Y. Fainman, and A. Scherer, "Nonreciprocal light propagation in a silicon photonic circuit.," *Science*, vol. 333, no. 6043, pp. 729-733, 2011.
- [44] D. Jalas, A. Petrov, M. Eich, W. Freude, S. Fan, Z. Yu, R. Baets, M. Popović, A. Melloni, J. D. Joannopoulos, M. Vanwolleghem, C. R. Doerr, and H. Renner, "What is – and what is not – an optical isolator," *Nat. Photonics*, vol. 7, no. 8, pp. 579-582, 2013.
- [45] Wikipedia, "Reciprocity ( electromagnetism )," *ACCSEED 2016-07-03*, vol. V. pp. 1-7, 2004.
- [46] Y. Okamura, M. Ishida, and S. Yamamoto, "Magneto-optic rib waveguides in YIG: an experiment," *Appl. Opt.*, vol. 23, no. 1, pp. 2-4.
- [47] T. Shintaku, T. Uno, and M. Kobayashi, "Magneto-optic channel waveguides in Ce-substituted yttrium iron garnet," *J. Appl. Phys.*, vol. 74, no. 8, p. 4877, 1993.
- [48] H. Yokoi, T. Mizumoto, and Iwasaki.H, "Nonreciprocal TE-TM mode converter with semiconductor guiding layer," *Electron. Lett.*, vol. 38, no. 25, pp. 1670-1672, 2002.
- [49] D. C. Hutchings, "Prospects for the implementation of magneto-optic elements in optoelectronic integrated circuits: a personal perspective," *J.*

- Phys. D. Appl. Phys.*, vol. 36, no. 18, pp. 2222-2229, 2003.
- [50] T. Okuda, N. Koshizuka, a. Murata, Y. Yokoyama, and K. Ando, "Control of birefringence in LPE-grown magnetic garnet films," *J. Appl. Phys.*, vol. 55, no. 6, p. 2176, 1984.
- [51] R. Wolfe, V. J. Fratello, and M. McGlashan-Powell, "Elimination of birefringence in garnet films for magneto-optic waveguide devices," *Appl. Phys. Lett.*, vol. 51, no. 16, p. 1221, 1987.
- [52] E. Pross, H. Dammann, and W. Tolksdorf, "Light guidance and mode conversion in magneto-optic buried channel waveguides," *J. Appl. Phys.*, vol. 68, no. 8, p. 3849, 1990.
- [53] R. Wolfe, V. J. Fratello, and M. McGlashan-Powell, "Thin-film garnet materials with zero linear birefringence for magneto-optic waveguide devices (invited)," *J. Appl. Phys.*, vol. 63, no. 8, p. 3099, 1988.
- [54] R. Wolfe, J. Hegarty, J. F. Dillon, L. C. Luther, G. K. Celler, L. E. Trimble, and C. S. Dorsey, "Thin-film waveguide magneto-optic isolator," *Appl. Phys. Lett.*, vol. 46, no. 9, p. 817, 1985.
- [55] M. Lohmeyer, N. Bahlmann, O. Zhuromskyy, H. Dötsch, and P. Hertel, "Phase-matched rectangular magneto-optic waveguides for applications in integrated optics isolators: numerical assessment," *Opt. Commun.*, vol. 158, no. 1-6, pp. 189-200, 1998.
- [56] J. P. Castera, P. L. Meunier, J. M. Dupont, and a. Carencio, "Phase matching in magneto-optic YIG films by waveguide temperature control," *Electron. Lett.*, vol. 25, no. 5, p. 297, 1989.
- [57] H. Dammann, E. Pross, G. Rabe, W. Tolksdorf, and M. Zinke, "Phase matching in symmetrical single-mode magneto-optic waveguides by application of stress," *Appl. Phys. Lett.*, vol. 49, no. 26, p. 1755, 1986.
- [58] T. Mizumoto, H. Yamazaki, and Y. Naito, "Phase-Matched Waveguide Using the Artificial Anisotropic Structure and its Application to Mode Converter," *MTT-S Int. Microw. Symp. Dig.*, vol. 84, pp. 502-504, 1984.
- [59] M. Kawachi, "Silica waveguides on silicon and their application to integrated-optic components," *Opt. Quantum Electron.*, vol. 22, no. 5, pp. 391-416, Sep. 1990.
- [60] S. C.-C. Tseng, A. Reisinger, Giess.E.A, and Powell.C.G, "Mode conversion in magneto-optic waveguides subjected to a periodic Permalloy structure," *Appl. Phys. Lett.*, vol. 24, no. 6, p. 265, 1974.
- [61] Y. Shani, R. Alferness, T. Koch, U. Koren, M. Oron, B. I. Miller, and M. G. Young, "Polarization rotation in asymmetric periodic loaded rib

- waveguides,” *Appl. Phys. Lett.*, vol. 59, no. 11, p. 1278, 1991.
- [62] W. Huang and Z. . Mao, “Polarization Rotation in Periodic Loaded Rib Waveguides,” *J. Light. Technol.*, vol. 10, no. 12, pp. 1825-1831, 1992.
- [63] B. M. Holmes and D. C. Hutchings, “Towards the Monolithically Integrated Optical Isolator on a Semiconductor Laser Chip,” vol. 1, pp. 897-898, 2006.
- [64] L. Bi, J. Hu, P. Jiang, D. H. Kim, G. F. Dionne, L. C. Kimerling, and C. a. Ross, “On-chip optical isolation in monolithically integrated non-reciprocal optical resonators,” *Nat. Photonics*, vol. 5, no. 12, pp. 758-762, Nov. 2011.
- [65] M.-C. Tien, T. Mizumoto, P. Pintus, H. Kromer, and J. E. Bowers, “Silicon ring isolators with bonded nonreciprocal magneto-optic garnets,” *Opt. Express*, vol. 19, no. 12, pp. 11740-11745, 2011.
- [66] N. Kono, K. Kakihara, K. Saitoh, and M. Koshiya, “Nonreciprocal microresonators for the miniaturization of optical waveguide isolators,” *Opt. Express*, vol. 15, no. 12, pp. 7737-7751, 2007.
- [67] X. Y. Sun, Q. Du, T. Goto, M. C. Onbasli, D. H. Kim, N. M. Aimon, J. Hu, and C. A. Ross, “Single-Step Deposition of Cerium-Substituted Yttrium Iron Garnet for Monolithic On-Chip Optical Isolation,” *ACS Photonics*, vol. 2, no. 7, pp. 856-863, 2015.
- [68] D. Huang, P. Pintus, C. Zhang, and Y. Shoji, “Electrically Driven and Thermally Tunable Integrated Optical Isolators for Silicon,” *IEEE J. Sel. Top. Quantum Electron.*, no. c, 2016.
- [69] H. Yokoi, T. Mizumoto, and Y. Shoji, “Optical nonreciprocal devices with a silicon guiding layer fabricated by wafer bonding,” *Appl. Opt.*, vol. 42, no. 33, 2003.
- [70] R. L. Espinola, T. Izuhara, M.-C. Tsai, R. M. Osgood, and H. Dötsch, “Magneto-optical nonreciprocal phase shift in garnet/silicon-on-insulator waveguides,” *Opt. Lett.*, vol. 29, no. 9, pp. 941-3, May 2004.
- [71] Y. Shoji, T. Mizumoto, H. Yokoi, I. W. Hsieh, and R. M. Osgood, “Magneto-optical isolator with silicon waveguides fabricated by direct bonding,” *Appl. Phys. Lett.*, vol. 92, no. 7, 2008.
- [72] S. Ghosh, S. Keyvavinia, W. Van Roy, T. Mizumoto, and G. Roelkens, “Ce : YIG / Silicon-on-Insulator waveguide optical isolator realized by adhesive bonding,” vol. 20, no. 2, pp. 1839-1848, 2012.
- [73] S. Ghosh, S. Keyvaninia, Y. Shoji, W. Van Roy, T. Mizumoto, G. Roelkens, and R. G. Baets, “Compact Mach-Zehnder interferometer Ce:YIG/SOI optical isolators,” *IEEE Photonics Technol. Lett.*, vol. 24, no. 18, pp. 1653-1656, 2012.

- [74] Y. Shoji, I. W. Hsieh, R. M. Osgood, and T. Mizumoto, "Polarization-independent magneto-optical waveguide isolator using TM-mode nonreciprocal phase shift," *J. Light. Technol.*, vol. 25, no. 10, pp. 3108-3113, 2007.
- [75] Y. Shirato, Y. Shoji, and T. Mizumoto, "High Isolation in Silicon Waveguide Optical Isolator Employing Nonreciprocal Phase Shift," *Opt. Fiber Commun. Conf. Fiber Opt. Eng. Conf. 2013*, p. OTu2C.5, 2013.
- [76] Y. Shoji, Y. Shirato, and T. Mizumoto, "Silicon Mach-Zehnder interferometer optical isolator having 8 nm bandwidth for over 20dB isolation," *Jpn. J. Appl. Phys.*, vol. 53, no. 2 PART 1, 2014.
- [77] D. C. Hutchings, B. M. Holmes, C. Zhang, P. Dulal, A. D. Block, S.-Y. Sung, N. C. a. Seaton, and B. J. H. Stadler, "Quasi-Phase-Matched Faraday Rotation in Semiconductor Waveguides With a Magneto-optic Cladding for Monolithically Integrated Optical Isolators," *IEEE Photonics J.*, vol. 5, no. 6, pp. 6602512-6602512, Dec. 2013.
- [78] C. Zhang, B. M. Holmes, and D. C. Hutchings, "Faraday Polarisation Rotation in Semiconductor Waveguides Incorporating Periodic Garnet Claddings," *Conf. Lasers Electro-Optics 2014*, vol. SM4G.3, pp. 4-5, 2014.
- [79] D. C. Hutchings, C. Zhang, B. M. Holmes, P. Dulal, A. D. Block, and B. J. H. Stadler, "Faraday polarisation mode conversion in semiconductor waveguides incorporating periodic garnet claddings," in *Proc. SPIE*, 2016, vol. 9750, no. 0, p. 97500V.
- [80] Y. Shoji, M. Ito, Y. Shirato, and T. Mizumoto, "MZI optical isolator with Si-wire waveguides by surface-activated direct bonding," *Opt. Express*, vol. 20, no. 16, p. 18440, 2012.
- [81] B. M. Holmes, M. A. Naeem, D. C. Hutchings, J. H. Marsh, and A. E. Kelly, "A semiconductor laser with monolithically integrated dynamic polarization control.," *Opt. Express*, vol. 20, no. 18, pp. 20545-50, Aug. 2012.
- [82] J. J. Bregenzer, S. McMaster, M. Sorel, B. M. Holmes, and D. C. Hutchings, "Compact Polarization Mode Converter Monolithically Integrated Within a Semiconductor Laser," *J. Light. Technol.*, vol. 27, no. 14, pp. 2732-2736, 2009.
- [83] B. M. Holmes, J. J. Bregenzer, and D. C. Hutchings, "Enabling Technologies for the Monolithic Integration of Semiconductor Lasers and Waveguide Optical Isolators," *2007 Conf. Lasers Electro-Optics*, pp. 1-2, 2007.
- [84] P. Pintus, F. Di Pasquale, and J. E. Bowers, "Design of transverse electric ring isolators for ultra-low-loss Si<sub>3</sub>N<sub>4</sub> waveguides based on the finite element method.," *Opt. Lett.*, vol. 36, no. 23, pp. 4599-601, 2011.

## List of References

- [85] J. F. Bauters, M. J. R. Heck, D. John, D. Dai, M.-C. Tien, J. S. Barton, A. Leinse, R. G. Heideman, D. J. Blumenthal, and J. E. Bowers, "Ultra-low-loss high-aspect-ratio Si<sub>3</sub>N<sub>4</sub> waveguides," *Opt. Express*, vol. 19, no. 4, pp. 3163-3174, 2011.
- [86] D. C. Hutchings and B. M. Holmes, "A Waveguide Polarization Toolset Design Based on Mode Beating," *IEEE Photonics J.*, vol. 3, no. 3, pp. 450-461, Jun. 2011.
- [87] S. Yamamoto and T. Makimoto, "Circuit theory for a class of anisotropic and gyrotropic thin-film optical waveguides and design of nonreciprocal devices for integrated optics," *J. Appl. Phys.*, vol. 45, no. 2, p. 882, 1974.
- [88] D. C. Hutchings and B. M. Holmes, "Quasi-Phase Matching Magneto-Optical Waveguides," in *MRS Proceedings*, 2011, vol. 1291, no. July.
- [89] B. M. Holmes and D. C. Hutchings, "Demonstration of quasi-phase-matched nonreciprocal polarization rotation in III-V semiconductor waveguides incorporating magneto-optic upper claddings," *Appl. Phys. Lett.*, vol. 88, no. 6, pp. 3-5, 2006.
- [90] V. P. Tzolov and M. Fontaine, "A passive polarization converter free of longitudinally-periodic Structure," *Opt. Commun.*, vol. 4018, no. 96, pp. 7-13, 1996.
- [91] B. M. . Rahman, S. S. . Obayya, N. Somasiri, M. Rajarajan, K. T. . Grattan, and H. A. E. Mikathi, "Design and Characterization of Compact Single-Section Passive Polarization Rotator," *J. Light. Technol.*, vol. 19, no. 4, pp. 512-519, 2001.
- [92] J. Z. Huang, R. Scarmozzino, G. Nagy, M. J. Steel, and R. M. Osgood, "Realization of a Compact and Single-Mode Optical Passive Polarization Converter," *IEEE Photonics Technol. Lett.*, vol. 12, no. 3, pp. 317-319, 2000.
- [93] H. El-Refaei, D. Yevick, and T. Jones, "Slanted-Rib Waveguide InGaAsP-InP Polarization Converters," *J. Light. Technol.*, vol. 22, no. 5, pp. 1352-1357, May 2004.
- [94] C. Brooks, P. E. Jessop, H. Deng, D. O. Yevick, and T. Garry, "Passive silicon-on-insulator polarization-rotating waveguides," *Opt. Eng.*, vol. 45, no. 4, p. 44603, 2006.
- [95] T. Takamori, L. a. Coldren, and J. L. Merz, "Angled etching of GaAs/AlGaAs by conventional Cl<sub>2</sub> reactive ion etching," *Appl. Phys. Lett.*, vol. 53, no. 25, p. 2549, 1988.
- [96] F. Ayazi, K. Najafi, and A. Arbor, "HIGH ASPECT-RATIO POLYSILICON MICROMACHINING TECHNOLOGY," in *Presented at 10th International Conference on Solid State Sensors and*

*Actuators(Transducers'99),Sendai,Japan,Jun1999, 1999.*

- [97] J. Bransky, "Magneto optic effects and applications," *Air Force Wright Aeronaut. Lab.*, p. 38, 1981.
- [98] B. Neite and H. Dötsch, "Dynamical conversion of optical modes in garnet films induced by ferrimagnetic resonance," *J. Appl. Phys.*, vol. 62, no. 2, pp. 648-652, 1987.
- [99] K. Ando, "Waveguide optical isolator: a new design.," *Appl. Opt.*, vol. 30, no. 9, pp. 1080-4, 1991.
- [100] J. P. Castera and G. Hepner, "ISOLATOR IN INTEGRATED OPTICS USING THE FARADAY AND COTTON-MOUTON EFFECTS," *IEEE Trans. Magn.*, vol. 1.MAG-13, no. 5, pp. 5-7, 1977.
- [101] K. Ando, T. Okoshi, and N. Koshizuka, "Waveguide magneto-optic isolator fabricated by laser annealing," *Appl. Phys. Lett.*, vol. 53, no. 1, pp. 4-6, 1988.
- [102] H. Hemme, H. Dobtsch, and H. . Menzler, "Optical isolator based on mode conversion in magnetic garnet films," *Appl. Opt.*, vol. 26, no. 18, pp. 3811-3817, 1987.
- [103] D. D. Stancil, "Optical-Magnetostatic Wave Coupled-Mode Interactions in Garnet Heterostructures," *IEEE J. Quantum Electron.*, vol. 27, no. 1, pp. 61-70, 1991.
- [104] J. J. Bregenzler, "Integrated polarisation rotators," Univeristy of Glasgow, 2010.
- [105] S. Yamamoto and T. Makimoto, "Circuit theory for a class of anisotropic and gyrotropic thin-film optical waveguides and design of nonreciprocal devices for integrated optics," *J. Appl. Phys.*, vol. 45, no. 2, pp. 882-888, 1974.
- [106] F. Auracher and H. H. Witte, "New Design for an Integrated Optical Isolator," *Opt. Commun.*, vol. 13, no. 4, pp. 435-438, 1975.
- [107] M. Wallenhorst, M. Niemoller, H. Dotsch, P. Hertel, R. Gerhardt, and B. Gather, "Enhancement of the nonreciprocal magneto-optic effect of TM modes using iron garnet double layers with opposite Faraday rotation," *J. Appl. Phys.*, vol. 77, no. 7, pp. 2902-2905, 1995.
- [108] O. Zhuromskyy, H. Dötsch, M. Lohmeyer, L. Wilkens, and P. Hertel, "Magneto-optical Waveguides with Polarization- Independent Nonreciprocal PhaseShift," *IEEE J. Light. Technol.*, vol. 19, no. 2, pp. 214-221, 2001.
- [109] A. F. Popkov, M. Fehndrich, M. Lohmeyer, and H. Dötsch, "Nonreciprocal TE-mode phase shift by domain walls in magneto-optic rib waveguides,"

*Appl. Phys. Lett.*, vol. 72, no. 20, pp. 2508-2510, 1998.

- [110] H. Dotsch, N. Bahlmann, O. Zhuromskyy, M. Hammer, L. Wilkens, R. Gerhardt, P. Hertel, and A. F. Popkov, "Applications of magneto-optical waveguides in integrated optics: review," *J. Opt. Soc. Am. B*, vol. 22, no. 1, p. 240, 2005.
- [111] M. Levy, "The on-chip integration of magneto-optic waveguide isolators," *IEEE J. Sel. Top. Quantum Electron.*, vol. 8, no. 6, pp. 1300-1306, 2002.
- [112] G. Winkler, *Magnetic Garnets*, vol. 5, no. May. 1981.
- [113] L. Pearson, F. Chong, J. Zingg, J. H. Hoper, M. Stewart, A. Turczyn, A. Smay, and A. Adomines, "A Survey of Magneto-optic Effects," pp. 305-314, 1966.
- [114] G. F. Dionne, G. A. Allen, P. R. Haddad, C. A. Ross, and B. Lax, "Circular Polarization and Nonreciprocal Propagation in Magnetic Media," vol. 15, no. 2, pp. 323-340, 2005.
- [115] D. C. Hutchings, M. SHEIK-BAHAE, D.J.HAGAN, and E. W. V. STRYLAND, "Kramers-Kronig relations in nonlinear optics," *Opt. Quantum Electron.*, vol. 24, pp. 1-30, 1992.
- [116] Y. Yazaki, Y. Shoji, and T. Mizumoto, "Demonstration of interferometric waveguide optical isolator with a unidirectional magnetic field," *Japanese J. Appl. Physics, Part 1 Regul. Pap. Short Notes Rev. Pap.*, vol. 46, no. 8 B, pp. 5460-5464, 2007.
- [117] T. Mizumoto, K. Oochi, T. Harada, and Y. Naito, "Measurement of Optical Nonreciprocal Phase Shift in a Bi-Substituted Gd<sub>3</sub>Fe<sub>5</sub>O<sub>12</sub> Film and Application to Waveguide-Type Optical Circulator," *J. Light. Technol.*, vol. LT-4, no. 3, 1986.
- [118] T. Mizumoto, "Optical Isolator: Application to Photonic Integrated Circuits," *IEEE Photonics Soc. distinguished lecture*, 2010. [Online]. Available: <http://slidegur.com/doc/17988/presentation-of-the-keynote-address>. [Accessed: 28-Aug-2016].
- [119] Wolfgang Kleemann, "Magneto-optical Materials," in *Handbook of Magnetism and Advanced Magnetic Materials Vol.4 Novel Materials*, H. Kronmuller and S. Parkin, Eds. John Wiley & Sons Ltd, 2007, pp. 2342-2356.
- [120] V. FRATELLO and R. WOLFE, "Epitaxial Garnet Films for Nonreciprocal Magneto-Optic Devices," in *Handbook of Thin Film Devices*, no. January, 2000, pp. 93-141.
- [121] B. J. H. Stadler, R. Cobian, L. J. Cruz Rivera, N. Kim, S. Sung, and X. Qi, "Magneto-Optic Materials for Integrated Photonics," *IEEE LEOS*, 2008. [Online]. Available:

<http://photonicsociety.org/newsletters/apr03/university.html>.  
[Accessed: 18-Aug-2016].

- [122] J. J.F.DILLON, "Origin and uses of the faraday rotation in magnetic crystals," *J. Appl. Phys.*, vol. 39, no. 2, pp. 922-929, 1968.
- [123] P. Dulal, A. D. Block, H.Haldren, D. C. Hutchings, and B. J. H. Stadler, "Effects of different seedlayers on the magneto-optic properties of rare earth iron garnets grown on semiconductor substrates," in *2016 Joint MMM-Intermag Conference, January 11, 2016, San Diego, CA*.
- [124] S. Geller, "Crystal chemistry of the garnets," *Zeitschrift fur Krist. - New Cryst. Struct.*, vol. 125, no. 125, pp. 1-47, 1967.
- [125] Ü. Özgür, Y. Alivov, and H. Morkoç, *Microwave ferrites, part 1: Fundamental properties*, vol. 20, no. 9. 2009.
- [126] P. Hansen and J. P. Krumme, "Magnetic and magneto-optical properties of garnet films," *Thin Solid Films*, vol. 114, no. 1-2, pp. 69-107, 1984.
- [127] S. Y. Sung, X. Qi, and B. J. H. Stadler, "Integrating yttrium iron garnet onto nongarnet substrates with faster deposition rates and high reliability," *Appl. Phys. Lett.*, vol. 87, no. 12, pp. 1-3, 2005.
- [128] A. D. Block, P. Dulal, B. J. H. Stadler, and N. C. a. Seaton, "Growth Parameters of Fully Crystallized YIG, Bi:YIG, and Ce:YIG Films With High Faraday Rotations," *IEEE Photonics J.*, vol. 6, no. 1, pp. 1-8, 2014.
- [129] B. J. H. Stadler and a. Gopinath, "Magneto-optical garnet films made by reactive sputtering," *IEEE Trans. Magn.*, vol. 36, no. 6, pp. 3957-3961, 2000.
- [130] B. El-Dasher and A. Deal, "Chapter 6 Application of Electron Backscatter Diffraction to Phase Identification," in *Electron Backscatter Diffraction in Materials Science*, 2009, p. 81,231.
- [131] W. Zhou and Z. L. Wang, *Scanning Microscopy for Nanotechnology Techniques and Applications*. 2006.
- [132] J. I.Goldstein, D. E.Newbury, P. Echlin, D. C.Joy, C. E.Lyman, E. Lifshin, L. Sawyer, and J. R.Michael, "Chapter 1 Introduction," in *Scanning Electron Microscopy and X-ray Microanalysis Third Edition*, vol. 158, no. 1, 2003, p. 19.
- [133] V. Randle, "Chapter 2 Theoretical Framwork for Electron Backscatter Diffraction," in *Electron Backscatter Diffraction in Materials Science*, 2000.
- [134] J. I.Goldstein, D. E.Newbury, P. Echlin, D. C.Joy, C. E.Lyman, E. Lifshin, L. Sawyer, and J. R.Michael, "Chapter 5 Special Topics in Scanning Electron Microscopy," in *Scanning Electron Microscopy and X-ray Microanalysis Third*

Edition, 2003.

- [135] S. Y. Sung, X. Qi, and B. J. H. Stadler, "Fabrication of garnet waveguides and polarizers for integrated optical isolators," *Conf. Lasers Electro-Optics, 2007, CLEO 2007*, pp. 5-6, 2007.
- [136] S.-Y. Sung, A. Sharma, A. Block, K. Keuhn, and B. J. H. Stadler, "Magneto-optical garnet waveguides on semiconductor platforms: Magnetics, mechanics, and photonics," *J. Appl. Phys.*, vol. 109, no. 7, p. 07B738, 2011.
- [137] A. B. Fallahkhair, K. S. Li, and T. E. Murphy, "Vector finite difference modesolver for anisotropic dielectric waveguides," *J. Light. Technol.*, vol. 26, no. 11, pp. 1423-1431, 2008.
- [138] D. C. Hutchings and B. M. Holmes, "A waveguide polarization toolset design based on mode beating," *IEEE Photonics J.*, vol. 3, no. 3, pp. 450-461, 2011.
- [139] E. Collett, "Chapter 3-The Observables of Polarized Light," in *Field Guide to Polarization*, no. 1, 2005, pp. 12-15.
- [140] W. H. McMaster, "Matrix representation of polarization," *Rev. Mod. Phys.*, vol. 33, no. 1, pp. 8-28, 1961.
- [141] W. H. McMaster, "Polarization and the Stokes Parameters," *Am. J. Phys.*, vol. 22, no. 6, p. 351, 1954.
- [142] E. Collett, "Chapter 2-The Wave Theory of Light," in *Field Guide to Polarization*, 2005, pp. 10-11.
- [143] H. Dammann, E. Pross, G. Rabe, and W. Tolksdorf, "45 ° waveguide isolators with phase mismatch," vol. 1302, no. May 2013, pp. 1-4, 1990.
- [144] G.N.RAMACHANDRAN and S.RAMASESHAN, "Magneto-Optic Rotation in Birefringent Media Application of the Poincaré Sphere," *Opt. Prop. Count. diamonds*, vol. 165, no. January, 1952.
- [145] R. Scarmozzino, a. Gopinath, R. Pregla, and S. Helfert, "Numerical techniques for modeling guided-wave photonic devices," *IEEE J. Sel. Top. Quantum Electron.*, vol. 6, no. 1, pp. 150-162, 2000.
- [146] Wikipedia, "Beam Propagation Method," *ACCSEED 2016-04-12*. [Online]. Available: [https://en.wikipedia.org/wiki/Beam\\_propagation\\_method](https://en.wikipedia.org/wiki/Beam_propagation_method). [Accessed: 12-Apr-2016].
- [147] E. J. Tarsa, M. De Graef, D. R. Clarke, a. C. Gossard, and J. S. Speck, "Growth and characterization of (111) and (001) oriented MgO films on (001) GaAs," *J. Appl. Phys.*, vol. 73, no. 7, p. 3276, 1993.
- [148] M. Z. Tseng, S. Y. Hu, Y. L. Chang, W. N. Jiang, and E. L. Hu, "Minimum

- thickness MgO buffer layers for YBa<sub>2</sub>Cu<sub>3</sub>O<sub>7-x</sub>/GaAs structures: Assessment using photoluminescence of multiple-quantum-well structures,” *Appl. Phys. Lett.*, vol. 63, no. 7, p. 987, 1993.
- [149] T. Goto, M. C. Onbaşlı, and C. a Ross, “Magneto-optical properties of cerium substituted yttrium iron garnet films with reduced thermal budget for monolithic photonic integrated circuits.,” *Opt. Express*, vol. 20, no. 27, pp. 28507-17, Dec. 2012.
- [150] C.-C. Yang and W.-C. Chen, “The structures and properties of hydrogen silsesquioxane (HSQ) films produced by thermal curing,” *J. Mater. Chem.*, vol. 12, no. 4, pp. 1138-1141, 2002.
- [151] S. Thoms, “Resists and nanofabrication,” *Univ. Glas. Nanosci. Nanotechnol. MSc Core course - Nanofabrication JWNC ebeam user Train*.
- [152] M. M. Mirza, H. Zhou, P. Velha, X. Li, K. E. Docherty, A. Samarelli, G. Ternent, and D. J. Paul, “Nanofabrication of high aspect ratio (~50:1) sub-10 nm silicon nanowires using inductively coupled plasma etching,” *J. Vac. Sci. Technol. B Microelectron. Nanom. Struct.*, vol. 30, no. 6, p. 06FF02, 2012.
- [153] M. A. Mohammad, M. Muhammad, S. K. Dew, and M. Stepanova, “Chapter 2 Fundamentals of Electron Beam Exposure and Development,” in *Nanofabrication*, Springer-Verlag/Wien, 2012.
- [154] MicroChem, “NANO PMMA and Copolymer™,” 2001.
- [155] X. C. Tong, “Advanced Materials for Integrated Optical Waveguides, Chapter 2 Characterization Methodologies of Optical Waveguides,” vol. 46, Springer International Publishing Switzerland, 2014.
- [156] L. Bi, J. Hu, P. Jiang, H. S. Kim, D. H. Kim, M. C. Onbasli, G. F. Dionne, and C. A. Ross, “Magneto-optical thin films for on-chip monolithic integration of non-reciprocal photonic devices,” *Materials (Basel)*, vol. 6, no. 11, pp. 5094-5117, 2013.
- [157] B. M. Holmes and D. C. Hutchings, “Realization of Novel Low-Loss Monolithically Integrated Passive Waveguide Mode Converters,” *IEEE Photonics Technol. Lett.*, vol. 18, no. 1, pp. 43-45, 2006.
- [158] Z. Haiping, “Bosch 1-HP Test4 Deep Trench etch result.” [Online]. Available: <http://jwnc.eng.gla.ac.uk/index.php?module=dryetch&cmd=>. [Accessed: 16-May-2016].
- [159] Y. Fu, T. Ye, W. Tang, and T. Chu, “Efficient adiabatic silicon-on-insulator waveguide taper,” *Photonics Res.*, vol. 2, no. 3, p. A41, 2014.
- [160] J. . Love, W. M. Henry, W. J. Stewart, R. J. Black, S. Lacroix, and F.

Gonthier, "Tapered single-mode fibres and devices Part 1: Adiabaticity criteria," *October*.

- [161] F. Xia, V. M. Menon, and S. R. Forrest, "Photonic Integration Using Asymmetric Twin-Waveguide (ATG) Technology: Part I – Concepts and Theory," *IEEE J. Sel. Top. Quantum Electron.*, vol. 11, no. 1, pp. 30-42, 2005.
- [162] X. Sun, H. Liu, and A. Yariv, "Adiabaticity criterion and the shortest adiabatic mode transformer in a coupled-waveguide system," vol. 34, no. 3, pp. 280-282, 2009.
- [163] D. Dai, Y. Tang, and J. E. Bowers, "Mode conversion in tapered submicron silicon ridge optical waveguides," *Opt. Express*, vol. 20, no. 12, p. 13425, 2012.
- [164] U. K. Leica Microsystems Lithography Ltd, "Leica Vectorbeam Series Vectorbeam Operator Manual."
- [165] H. K. Raut, V. A. Ganesh, A. S. Nair, and S. Ramakrishna, "Anti-reflective coatings: A critical, in-depth review," *Energy Environ. Sci.*, vol. 4, no. 10, p. 3779, 2011.